Low temperature microwave optomechanics : anomalous force noise and optomechanically induced transparency

Sumit Kumar

THÈSE

Pour obtenir le grade de

DOCTEUR DE L'UNIVERSITÉ GRENOBLE ALPES

Spécialité : Physique de la Matière Condensée et du Rayonnement

Arrêté ministériel : 25 mai 2016

Présentée par

Sumit KUMAR

Thèse dirigée par **Eddy COLLIN**,Chercheur, Université Grenoble Alpes
et codirigée par **Andrew FEFFERMAN**, CNRS

préparée au sein du **Laboratoire Institut Néel**
dans **l'École Doctorale Physique**

Optomécanique des micro-ondes à basse température : bruit de force anormal et transparence induite par l'optomécanique

Low temperature microwave optomechanics: anomalous force noise and optomechanically induced transparency

Thèse soutenue publiquement le **13 septembre 2021**,
devant le jury composé de :

Monsieur ALESSANDRO MONFARDINI
DIRECTEUR DE RECHERCHE, CNRS DELEGATION ALPES, Président
Monsieur ADRIAN BACHTOLD
PROFESSEUR, Institute of Photonic Sciences, Examinateur
Monsieur NICOLAS ROCH
CHARGE DE RECHERCHE, CNRS DELEGATION ALPES, Examinateur
Monsieur ANDREW ARMOUR
PROFESSEUR, The University of Nottingham, Rapporteur
Monsieur GARY STEELE
PROFESSEUR, DELFT University of Technology, Rapporteur
Monsieur LAURENT SAMINADAYAR
PROFESSEUR DES UNIVERSITES, UNIVERSITE GRENOBLE ALPES, Examinateur

Université Grenoble Alpes

Doctoral Thesis

Low temperature microwave optomechanics: anomalous force noise and optomechanically induced transparency

---

Author:
Sumit Kumar

Supervisor:
Dr. Andrew Fefferman

A thesis submitted in fulfillment of the requirements for the degree of Doctor of Philosophy

in the

Ultra Low Temperature Group
Insitut Néel/CNRS

November 11, 2021

Acknowledgements

Foremost, I would like to express my sincere gratitude to my advisor Dr. Andrew Fefferman for his continuous support during my Ph.D. and research. His valuable guidance has not only helped me in my research but also in other aspects of academia like giving presentations, writing, and many more. I am also indebted to my co-advisor Dr. Eddy Collin for his motivation, valuable suggestions, and of course humor. I would also like to offer my special thanks to Dr. Xin Zhou for advising me on fabrication and RF measurements. I have also greatly benefited from usual conversations with my colleagues (Dylan, Baptiste, Ilya, David, Annina, Razul) in the lab. Special thanks to Thierry Crozes, Bruno, Jeff, Gwénaëlle, and other members of the nanofabrication facility for their insightful suggestions. I appreciate the continuous help from the cryogenics and the electronics team. Advice and comments given by Dr. Nicolas Roch and Dr. Clemens Winkelmann during the thesis monitoring meeting every year were invaluable. I would like to thank the jury members (Dr. Andrew Armour, Dr. Gary Steele, Dr. Nicolas Roch, Dr. Alessandro Monfardini, Dr. Adrian Bachtold, Dr. Laurent Saminadayar) for their patience to read my thesis. I appreciate the feedback and meticulous comments from them during my defense. Lastly, I would like to thank my family and friends (Akshay, Hemant, Karthik, Rahul, Saransh, Sanu, Vivekanand), without their moral support this would not have been possible. Special mention to Rachaiyata for her persistent encouragement.

UNIVERSITÉ GRENOBLE ALPES

Abstract

Ultra Low Temperature Group
Insitut Néel/CNRS

Doctor of Philosophy

Low temperature microwave optomechanics: anomalous force noise and optomechanically induced transparency

by Sumit Kumar

Most of the terrestrial matter is made of glassy or amorphous materials. The low-temperature properties of these materials, particularly below 1 kelvin, are intriguing. For instance, the thermal conductivity of amorphous materials was initially believed to behave the same way as crystalline materials, but experimental findings modeled the thermal conductivity with T^2 dependence instead of T^3 dependence, where T is the temperature of the material measured. The internal friction of the amorphous materials does not show any dependence on temperature around 1 kelvin and at lower temperatures drops off with T^3 dependence. In the regime where the internal friction does not depend on T, all amorphous materials with few exceptions shows quantitative similarity in internal friction within a factor of 20. A phenomenological model known as the tunneling two-level system model (TTLS model) was proposed by Philips [58] and Anderson *et al.* [5] independently in 1972. They postulated two or more positional degenerate states exist for entities like atoms, ions, or even molecules to tunnel between them. They explained the anomalous low-temperature properties of amorphous materials qualitatively and predicted various nonlinear phenomena like saturation, echoes, hole burning, etc. According to the TTLS model, the internal friction of amorphous materials can be explained by TLS-phonon interactions via resonant and relaxation processes. Resonant and relaxational interactions between TLS and phonons are discussed in detail in *Chapter 1*. The contribution of resonant interaction to internal friction is negligible when $\hbar\omega << k_bT$, where k_b is the Boltzmann constant and ω is the measurement frequency. Many experimental findings showed slight deviations in the measurements of internal friction and relative change in the speed of sound from the predicted behavior by the TTLS model. However, the variations were explained by including some corrections in the TTLS model. For example, in the measurement of internal friction by Fefferman *et al.* [26], the linear dependence on temperature below 10 mK was explained by accounting for Intra-TLS interactions. Leggett *et al.* [42] argued that discrepancies not predicted by the TTLS model could not be fixed by mere minor modification. The TTLS model and its success was based on the interaction of TLSs (as an ensemble) with phonons, yet the microscopic nature of TLS remains elusive to us. Leggett *et al.* [42] further suggested that the measurement of internal friction of amorphous materials when $\hbar\omega >> k_bT$ will be an ultimate test in favor of the TTLS model and existence of TLSs since only non-negligible contribution to internal frictions comes from the resonant process. However, reaching the regime, where $\hbar\omega >> k_bT$, is not easy. To measure the internal friction using mechanical suspended structures, the resonant frequency of the fundamental mode should be more than 60 MHz at 5 millikelvins to reach the regime mentioned above. NEMS (nano-electromechanical system) can support such high resonance frequency.

With the advent of semiconductor technologies and, in turn, the development of novel processes in nanofabrication facilities, many different types of NEMS were realized. Cantilevers,

drums, doubly clamped nanobeams are a few of them. A doubly clamped nanobeam made of silicon nitride (SiN) is a promising candidate for our measurement of internal friction. Few arguments in support of SiN doubly clamped nanobeam are, a) SiN is an amorphous material, and the properties are expected to behave in accord with TTLS model and b) Typically SiN is deposited on Si wafer using LPCVD (Low-pressure chemical vapor deposition), tweaking the parameters of deposition controls the stress developed in the thin film of SiN on Si. The stress in the doubly clamped nanobeams is proportional to the square of resonance frequency. Thus we can achieve high resonance frequency by developing high stress in SiN thin film during deposition. The SiN doubly clamped nanobeams with various dimensions were fabricated in the nanofabrication facility at Institut Néel. The nanobeams were initially characterized using magntomotive actuation and detection scheme in a ^{4}He cryostat. However, the thermal motion of the nanobeam is small and is difficult to measure at low temperatures.

We are witnessing a paradigm shift in NEMS's applications from being an ultrasensitive detector of motion to testing various quantum theories by coupling NEMS to an optical cavity or superconducting microwave cavity. The field is called ***cavity optomechanics*** and has paved the way for sensitive detection of the position of NEMS and control of its mechanical characteristics. Teufel *et al.* [73] were able to cool the fundamental mode of a micron-sized drum coupled to a superconducting microwave cavity to its quantum ground state using the radiation pressure forces. We will confine ourselves in detecting the position of NEMS instead of controlling its mechanical behavior since studying the intrinsic mechanical characteristics at low temperature is our objective. However, controlling the mechanical characteristics using radiation pressure forces can help determine the coupling constant between NEMS and the cavity. Therefore, we fabricated the doubly clamped nanobeam made of SiN with a thin layer of Aluminum coupled to a superconducting microwave cavity to facilitate the cavity optomechanical measurements at low temperatures in commercial BlueFors dilution cryostat.

Chapter 1 concerns our motivation to test the theory of the TTLS model. The chapter begins with various experimental findings suggesting anomalous properties of amorphous materials at low temperatures in contrast with the predictions of the Debye model. The TTLS model and TLS-phonon interactions governing the low-temperature properties of amorphous materials are discussed in detail. We will then discuss the fallacies associated with the TTLS model and its failure to explain discrepancies in many experimental findings. Following Leggett *et al.* to test the validity of the TTLS model and the existence of TLSs, we will explain the relevance of NEMS. To detect the motion of NEMS, we use the principles of cavity optomechanics. We will discuss in brief the various principles of this field and talk about multiple cavity optomechanical measurements done to date.

The analytical expression for the resonance frequency of doubly clamped nanobeam can be derived from Euler-Bernoulli's principle. *Chapter 2* starts with the analytical expression for calculating the resonance frequency of the doubly clamped nanobeam, which depends on the stress in the material and its dimensions. Further, the resonance frequency from the analytical expression can be compared with finite element simulation (COMSOL). As discussed before, coupling the nanobeam to a superconducting microwave cavity facilitates the former's sensitive measurements of thermal motion. The thermal motion of the nanobeam can be extracted from the noise spectrum coming out of the cavity. We derive the noise spectrum from the first principles using the Heisenberg-Langevin equation of motion. The output field from the cavity can be written in terms of an input field and the field inside the cavity using Input-Output formalism, which we have discussed in detail. All the experimental calibrations and techniques will be discussed in *chapter 3*. The first step is to fabricate the devices in a nanofabrication facility. We will discuss the fabrication steps of making NEMS on Silicon/Silicon Nitride chip and the superconducting microwave cavity made of Niobium or Aluminum. The various obstacles we faced while fabricating these devices will be analyzed. The circuitry for characterizing the NEMS in 4-kelvin cryostat and the microwave circuitry in the commercial dilution cryostat will be explained with all calibration issues.

High-quality microwave amplifiers and notch filters can be made from microwave optomechanical systems. These amplifiers and filters can rely on optomechanically induced transparency (OMIT) and absorption (OMIA), respectively. Such devices can amplify microwave signals with large, controllable gain, high dynamic range, and very low noise. Furthermore, extremely narrowband filters can be constructed with this technique. We briefly review previous measurements of microwave OMIT and OMIA before reporting our measurements in *Chapter 4*. Our measurements cover a large parameter space than has been explored in previous works. We find excellent agreement between our measurements and the predictions of input/output theory, thereby guiding further development of microwave devices based on nanomechanics.

Although microwave optomechanics is a powerful technique for measuring the thermal vibrations of nanomechanical modes all the way down to the quantum ground state, not all the observed phenomena can be explained in the framework of the optomechanical theory. In particular, Zhou *et al.* reported anomalous fluctuations in the apparent vibration amplitude of a nanomechanical mode that could not be explained by thermal agitation [87]. These fluctuations, called 'spikes', appeared below 200 mK. Such spikes have also been observed in the apparent vibration amplitude of other nanomechanical devices with varying magnitudes and onset temperatures. In *Chapter 5*, we report detailed measurements of the spikes in the device of Zhou

et al. It consists of 50 μm $\times$ 120 nm $\times$ 300 nm Al on SiN string coupled to a high impedance Nb microwave cavity. At 250 mK, the device behaved in agreement with predictions of the optomechanical theory. With the sample cell at 10 mK, we applied a pump tone at microwave resonance frequency $\frac{\omega_c}{2\pi} = 6$ GHz and monitored the output power around $\omega_c + \Omega_m$, where $\frac{\Omega_m}{2\pi} = 4$ MHz is the mechanical resonance. At constant pump power, we observed spikes in the output power with a decay time of 100 msec. Quiet periods with no spikes lasting thousands of seconds were also observed. These spikes were only observed at $\omega_p \pm \Omega_m$ where ω_p is the pump frequency, demonstrating that their origin must involve the motion of the nanomechanical string. We will further discuss plausible reasons responsible for such anomalous spikes in detail.

Most NEMS measured at low temperatures are either made of amorphous insulator with a thin layer of metal or made of pure metal. To probe the dyanamics of TLS-phonon interaction in amorphous material, it is relevant to measure the NEMS made of bare amorphous insulator. We have developed a dual-chip technique where NEMS on-chip will be actuated dielectrically and measured by coupling it microwave cavity on another chip. The complete experimental scheme of this dual-chip technique and our latest result will be discussed in *Chapter 6*.

Contents

List of Figures

Chapter 1

Motivation

Phil Anderson quoted [11] that *"one of the deepest and most interesting unsolved problems in solid-state theory is probably the nature of glass and the glass transition"*. So what is so special about glasses? First of all, most of the terrestrial matter is made of glassy or amorphous materials. Secondly, the static shear modulus is nonzero for all practical purposes below the glass transition temperature, but there is no long-range order. The static shear modulus is zero for an ergodic amorphous state (liquids), *glasses are liquids that cannot flow*. There is a huge literature on glass transitions, and the thermodynamic properties of glasses at ambient temperatures [44]. The low-temperature properties of glasses are even more interesting, and this thesis focuses on probing the same. Peter debye in 1912 developed the Debye model [24] estimating the phonon contribution to the specific heat of the solids. He correctly predicted the $\sim T^3$ dependence of specific heat at low temperatures, assuming high energy phonons' contribution (shorter wavelength phonons) to be negligible. According to the model, the long wavelengths phonons are the main contributors to carry heat. The low-temperature thermal and mechanical properties of amorphous materials, particularly below 1 kelvin, are intriguing and are very different from the properties of crystals. Naively, one might expect that amorphous materials should have the same properties as crystals at low temperatures since the long-wavelength phonons should be insensitive to disorder at length scales comparable to inter-particle spacing.

Pohl *et al.* [85] measured the thermal conductivity and specific heat of SiO_2, Se, silica, and germanium-based glasses. They observed that the thermal conductivity in these materials below 1 kelvin goes as $\sim T^n$ where $n \sim 1.8$, which is in sharp contrast with the thermal conductivity varying as $\sim T^3$ in crystalline solids in the case of temperature independent phonons [7]. They also observed the same characteristic plateau in thermal conductivity, around 10 kelvin for all these materials. The different properties of glasses like thermal conductivity and specific heat, elastic and dielectric properties have been studied extensively after the above-mentioned experiment. Figure 1.1 (left) shows the thermal conductivity of different amorphous materials (taken from [18]) below 1 kelvin. The two dashed lines shown in the same figure are proportional to T^2 and also outline the range spanned by practically all amorphous materials. These lines

are separated by a factor of 20, and the range is called *glassy range*. This is the first evidence of the universal behavior of glasses.

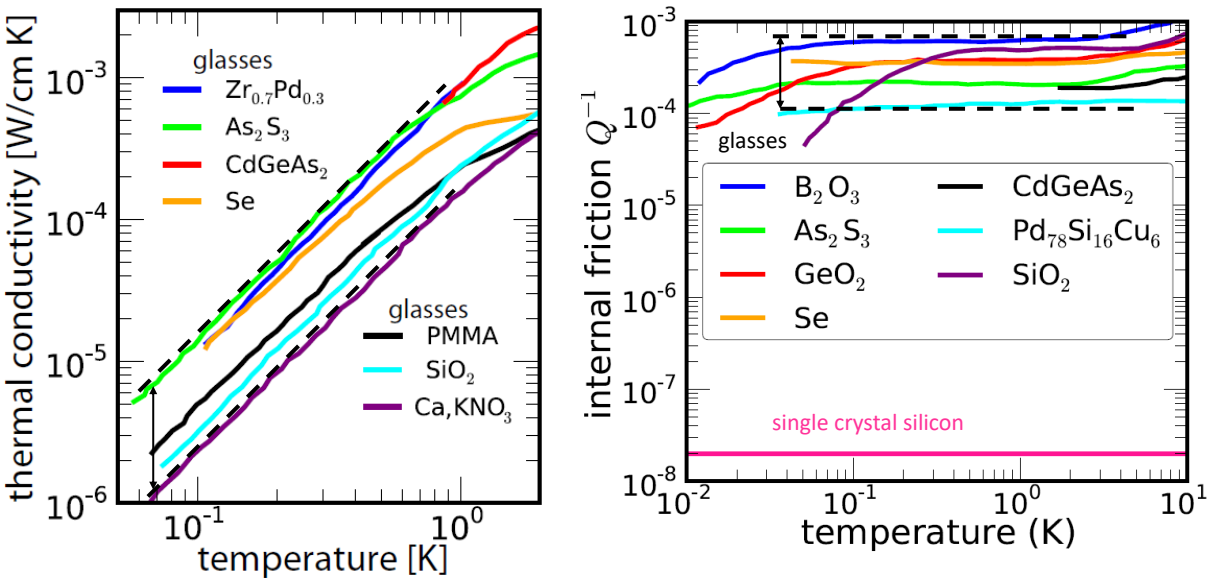

FIGURE 1.1: (left) Thermal conductivity versus Temperature which goes as T^2 below 1 kelvin (right) Internal friction versus Temperature which is independent of T around 1 kelvin but then drops off as temperature is reduced

Figure 1.1 (right) (taken from [75]) shows the internal friction Q^{-1} of amorphous solids below 10 kelvin. The internal friction is temperature independent in the temperature range shown in the figure and then shows a drop-off at lower temperatures. The drop-off at the lower temperatures depends on the frequency of measurement. The drop-off will occur at lower temperatures with decreasing measuring frequency. The two dashed lines separated by an arrow shown in the figure mark the range spanned by all the amorphous solids in the plateau region studied to date. The range spanned is again a factor of 20 as in thermal conductivity. However, thin films of a-Si, a-Ge, and, a-C have also shown plateaus below the *glassy range* [60].

Many experiments confirmed the similar anomalous low-temperature properties of glasses. One of the plausible explanations is the existence of localized low energy excitation states (LEEs) in glassy materials given by Philips [58], and by Anderson *et al.* [5] independently. They incorporated this idea in their TTLS (Tunneling two-level system) model. The TTLS model postulated that in amorphous materials, there exist nearly degenerate states, and entities like single atoms, groups of atoms, or even molecules can tunnel between them. The TTLS model was successful in explaining many properties of glasses, including specific heat, thermal conductivity, elastic susceptibility, etc., although qualitatively. In addition, the TTLS model makes qualitative predictions of a variety of nonlinear phenomena (saturation, echoes,

hole burning) that are all seen experimentally. As discussed before in the *glassy range*, the properties of amorphous materials are similar not only qualitatively but also quantitatively independent of the chemical composition or preparation of the amorphous materials. The quantitative similarity referred to as *universality* is not a part of the standard TTLS model. Many different theoretical effort have been put out focusing mainly on interaction between tunneling defects by Leggett *et al.* [41], [83], Burin *et al.* [17] to explain the universality.

I will commence this chapter by giving a brief review of the TTLS model and its implications on the properties of glasses. I will then summarize various experiments measuring the mechanical dissipation in mechanical resonators (made of amorphous materials) at low temperatures. A recent paper titled '*The "Tunneling Two level Systems" Model of the Low-Temperature Properties of Glasses: Are "Smoking-Gun" Tests possible?* by Leggett *et al.* [42] explains the fallacies in the TTLS model and proposes a definitive test of the model. I will then discuss the role of dimensionality of the oscillators and why we need miniature oscillators for probing the TTLS model. With the advent of the semiconductor industry and, in turn, nanofabrication facilities, many novel devices were fabricated. One such device is NEMS (nano-electromechanical system). These mechanical resonators are typically made of dielectric materials (SiN, SiO_2) or metals (e.g., Aluminum). These devices have shown various applications, i.e., from being an ultrasensitive detector of motion to its applications in quantum information processing. Therefore it is critical to understand the dissipation in these mechanical resonators. The recent field of cavity optomechanics has not only helped to detect the thermal motion of NEMS at low temperatures but also paved the way to demonstrate various quantum optics experiments such as sideband cooling of NEMS to its quantum ground state, optomechanically induced transparency, etc. I will then highlight the various achievements in the field of cavity optomechanics to date.

Many experiments have been carried out with NEMS made of dielectric materials showing the variation of mechanical dissipation with temperature. Although these materials are made of dielectrics, typically SiN and SiO_2, they usually have a thin layer of metal on top for contacts. The interface between dielectric and metal provides an additional channel for dissipation. Measuring NEMS made of dielectrics but without metal will give us an insight into the distribution of two-level systems inside the material and its role in dissipation. I will then illustrate a novel technique that we are developing in our lab for measuring the bare SiN NEMS. I will then delve into our recent progress on probing the dynamics of an individual two-level defect in NEMS, which remains important.

1.1 TTLS model

In a regular lattice of a crystal, all atoms and molecules occupy a well-defined position, thus allowing a single configuration. The TTLS model incorporates the fact that in amorphous materials or glasses, there exist at least two configurational degenerate states embedded randomly. Figure 1.2 depicts the configuration of amorphous SiO_2 where silicon atom and oxygen atom are represented in blue and white, respectively. Various positional changes available (which form nearly degenerate states) for atoms to tunnel is also shown in colored circles.

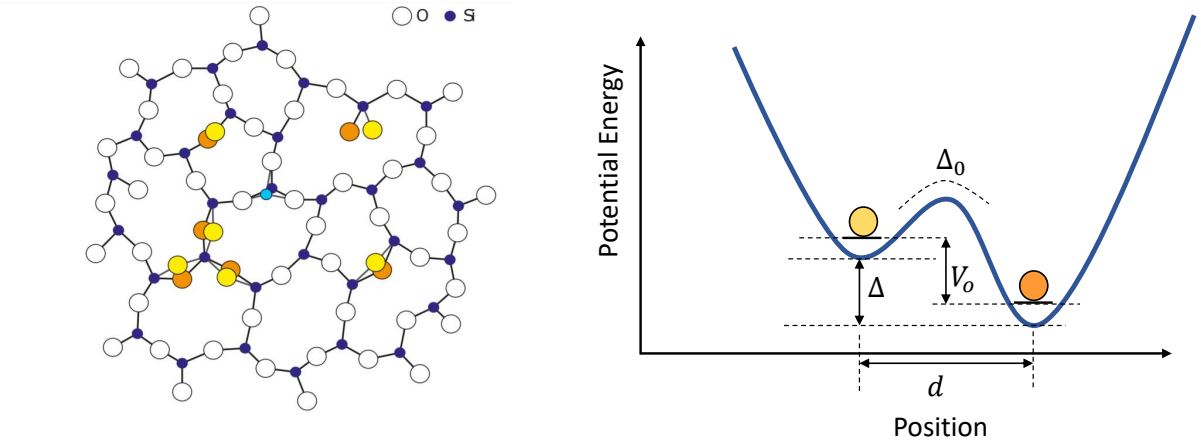

FIGURE 1.2: (inset) Schematic of amorphous SiO_2 at low temperatures. Several possible tunneling systems are indicated with their two possible positions indicated in orange and yellow (oxygen) or dark and light blue (silicon) respectively (image taken from [45]) (right) TLS model showing two minima separated by a potential Δ and the tunneling amplitude Δ_0

The two nearly degenerate states can be modeled as double potential energy well separated by a barrier as shown in figure 1.2. There is a series of vibrational states separated by an energy $\hbar\Omega$, which is of the order of the Debye energy in each of the wells. At low temperatures, we are interested in the ground states of this double potential well which are denoted as $\psi_l(x)$ and $\psi_r(x)$. The TTLS model is valid for temperatures where thermal transitions between different states can be ignored, and the only possible position change is through quantum mechanical tunneling through an energy barrier. The hamiltonian of the single individual TLS in the position basis is given by,

$$H_{TLS} = \frac{1}{2}\begin{pmatrix} \Delta & \Delta_0 \\ \Delta_0 & -\Delta \end{pmatrix} \tag{1.1}$$

where Δ is the difference in energy of two minima also called asymmetry energy and $\Delta_0 = \hbar\Omega e^{-\lambda}$ is the tunneling strength between two potentials. The tunneling parameter $\lambda = d(2mV_0/\hbar^2)^{\frac{1}{2}}$ represents the overlap of the wave functions $\psi_1(x)$ and $\psi_2(x)$, d is the separation between the two wells, m is the effective mass of the tunneling particles and V_0 is the barrier between two

minima. $\hbar\Omega$ is approximately equal to $\frac{E_l+E_r}{2}$ where E_l and E_r are ground state energies of state $\psi_l(x)$ and $\psi_r(x)$. Diagonalizing the matrix is straightforward and we end up with two energy eigenstates as

$$E_{\pm} = \pm\frac{1}{2}\sqrt{\Delta^2 + \Delta_0^2} \tag{1.2}$$

Therefore the energy splitting between two eigenstates is $E = E_+ - E_- = \sqrt{\Delta^2 + \Delta_0^2}$. Also the hamiltonian of a single TLS H_{TLS} can be written in terms of Pauli's matrices as $H_{TLS} = \frac{\Delta}{2}\sigma_z + \frac{\Delta_0}{2}\sigma_x$.

One of the features of the TTLS model is, in amorphous material, there exists an ensemble of TLSs leading to the distribution of energy asymmetries Δ and tunneling amplitudes Δ_0. In the case of asymmetry Δ, the distribution function is assumed to be symmetric as both positive and negative values of Δ are equally likely [59]. The scale of energy variation of the asymmetry is set by glass transition temperature, typically between 200 kelvin and 1000 kelvin. At low temperatures, the relevant tunneling states have asymmetries much less than 1000 kelvin; the distribution on asymmetries can be considered constant. The primary dependence of the energy density of states comes from the WKB exponent. A small change in λ leads to a large shift in tunneling amplitude Δ_0. At low temperatures, the range of Δ_0 spanned is small, the distribution on λ parameter is assumed to be roughly uniform. The probability distribution is thus,

$$P(\Delta, \lambda)d\Delta d\lambda = P_0 d\Delta d\lambda \tag{1.3}$$

where P_0 is number of TLS per unit energy per unit volume. We can further write the distribution on asymmetries and tunneling matrix elements by doing a simple variable change as,

$$P(\Delta, \Delta_0) = \frac{P_0}{\Delta_0} \tag{1.4}$$

1.2 Dynamics: TLS and its coupling with strain field

We have discussed the tunneling two-level system and the density of TLSs in amorphous materials in the previous section. However, they interact with thermal phonons and externally applied excitations. The experimental observables are the internal friction Q^{-1} and the relative change in sound speed $(v - v_0)/v_0 = \dfrac{\delta v}{v_0}$ where v_0 is the sound speed at an arbitrary reference temperature. TLS-phonon interactions contribute to the experimental observables through two different processes, namely resonant and relaxational. In the resonant process, the externally applied field at ω_0 are scattered by TLSs with energy splitting $E = \hbar\omega_0$ driving the phonon population back to thermal equilibrium. Thus the internal friction depends on the phonon scattering rate, and the change in sound velocity can be calculated using Kramers-Kroenig

relation. On the other hand, in the relaxational process, the externally applied sound wave interacts with TLSs by perturbing the potential energy and thus changing the energy splitting of the latter. The phonons then interact with TLSs driving them back to thermal equilibrium from their perturbed energy state. The externally applied perturbations can be via strain and electric fields. In this section, we will mainly focus on the strain field as an electric field can be realized in a similar way. The strain can lead to the change of Δ and Δ_0. The coupling between stain field $e(t)$ and tunneling system can be written as

$$H_{coup} = \begin{pmatrix} \gamma_\Delta & \gamma_{\Delta_0} \\ \gamma_{\Delta_0} & -\gamma_\Delta \end{pmatrix} e(t) \tag{1.5}$$

where γ_Δ and γ_{Δ_0} is the change in asymmetry and tunneling amplitude, respectively. We also assume that strain field only couples to the asymmetry such that $\gamma_\Delta >> \gamma_{\Delta_0}$. From here on, we will denote γ_Δ as γ. We can rewrite the total Hamiltonian of the system in the basis of TTLS energy eigenvalues based on the assumption that TTLS-phonon coupling is diagonal as,

$$H = H_{ph} + \frac{1}{2}\begin{pmatrix} E & 0 \\ 0 & -E \end{pmatrix} + \frac{\gamma}{2}\begin{pmatrix} \frac{\Delta}{\epsilon} & \frac{\Delta_0}{\epsilon} \\ \frac{\Delta_0}{\epsilon} & -\frac{\Delta}{\epsilon} \end{pmatrix} e(t) \tag{1.6}$$

In the above equation, H_{ph} is the hamiltonian of the phonons present in the system, the second term is the hamiltonian of the TLS in energy basis, whereas the third term represents the coupling of TLS and strain field. The diagonal elements of the third term illustrate the change in the energy eigenvalue due to external perturbation, while the off-diagonal matrix element stands for transitions between different eigenstates.

All the equations from here follows from the reference [27]. Consider the transition from TTLS energy state 1 with energy $+E$ to state 2 with energy $-E$ due to an external phonon field. Let's denote the transition probability rate from state 1 to state 2 as ω_{12} and ω_{21} for state 2 to state 1. The change in the occupation probability of state 1 and state 2 denoted by $\dot{P}_1$ and $\dot{P}_2$ is governed by the following rate equations,

$$\begin{aligned} \dot{P}_1 &= -P_1\omega_{12} + P_2\omega_{21} \\ \dot{P}_2 &= P_1\omega_{12} - P_2\omega_{21} \end{aligned} \tag{1.7}$$

The above two equations lead to the following equation,

$$\dot{P}_1 = -P_1(\omega_{12} + \omega_{21}) + \omega_{21} \tag{1.8}$$

Also $\dot{P}_1 = -\frac{P_1}{\tau}$ where τ is the relaxation rate of two level system and is further given by

$\tau^{-1} = \omega_{12}(1 + e^{\beta E})$ where $\beta = \frac{1}{k_b T}$, k_b being the boltzmann constant. The transition rate ω_{21} can be further calculated using the Fermi's golden rule,

$$\omega_{12} = \sum_{\alpha=l,t} \frac{2\pi}{\hbar^2} |\langle\psi_1| H_{coup} |\psi_1\rangle|^2 \frac{g(E)}{e^{\beta\epsilon} - 1} \tag{1.9}$$

where α is the phonon polarization and $g(E)$ is the phonon density of states. Therefore one gets the relaxation time of TLS with (Δ,Δ_0) as

$$\tau^{-1}(E) = \sum_{\alpha} \frac{\gamma_\alpha^2}{v_\alpha^5} \frac{E\Delta_0^2}{2\pi\rho\hbar^4} \coth(\frac{1}{2}\beta E) \tag{1.10}$$

The above equation can be further written by omitting the summation over the different polarization of phonon. One can assume the $\frac{\gamma}{v}$ and v do not considerably depend on polarization. Thus,

$$\tau^{-1}(E) = \frac{3\gamma^2}{v^5} \frac{E\Delta_0^2}{2\pi\rho\hbar^4} \coth(\frac{1}{2}\beta E) \tag{1.11}$$

The factor of 3 accounts for the one longitudinal and two transverse polarization of phonon field. Let us consider that the TLS are in thermal equilibrium and the phonon population at frequency ω has been perturbed from thermal equilibrium. The phonon scattering rate is given as

$$\tau_{ph}^{-1}(\Delta, \Delta_0) = \frac{\pi\gamma^2\omega}{\rho v^2} \frac{\Delta_0^2}{E^2} \tanh(\frac{1}{2}\beta E) \tag{1.12}$$

However due to an ensemble of TLSs one has to sum over all the TLSs with different Δ_0 ranging from $-E$ to E to obtain the relaxation rate of phonons due to all the TLSs,

$$\tau_{ph}^{-1}(\Delta, \Delta_0) = \pi\omega C \tanh(\frac{1}{2}\beta E) \tag{1.13}$$

where we define the tunneling strength as $C = \frac{P_0\gamma^2}{\rho v^2}$. One can also calculate the change in the sound velocity using Kramers-Kroenig relation,

$$\left[\frac{\delta v}{v_0}\right]_{res} = C \ln(T/T_0) \tag{1.14}$$

where T_0 is some reference temperature, where sound velocity is v_0. In the relaxational process, the phonon population is assumed to be in thermal equilibrium barring the drive photons, and the drive photons change the energy splitting of the TLSs. Here the energy splitting of TLS need not be equal to drive frequency. In this process, the drive photons interact with all the TLS changing their asymmetry. Resonant interactions between thermal phonons and the TLS can bring the TLSs back to thermal equilibrium. These two types of interaction mechanisms

lead to an anelastic response of the amorphous material. In anelastic material, stress and strain are related by a complex modulus. In an amorphous solid, the complex modulus is given as,

$$M = \frac{\sigma}{e} = M_0 + M_{rel} + M_{res} \tag{1.15}$$

where σ is the stress, e is the strain, M_0 is contribution from non TLSs processes, M_{rel} is the contribution from relaxational process and M_{res} is the contribution from resonant process. M_0 is temperature independent at low temperatures and the dissipative part is small. M_{rel} and M_{res} are only relevant contribution to complex modulus at low temperatures. Since we have already discussed about the experimental observables related to resonant mechanism, the experimental observables related to relaxational mechanism can be derived in terms of M_{rel}. One can now the derive the Maxwell-like relation which links strain dependence of the total energy to the dependence of the stress on the population of the TLS excited state and consider n being the volume density of TLS with parameters Δ and Δ_0. The relaxational contribution to the stress is given by,

$$\sigma_{rel,i,j} = 2n\frac{\Delta}{E}\gamma_{i,j}dP_1 \tag{1.16}$$

where $\sigma_{rel,i,j}$ is the relaxational second order stress tensor, $\gamma_{i,j} = \frac{1}{2}\frac{d\Delta}{de_{i,j}}$ is the change in asymmetry due to second order strain tensor $e_{i,j}$ and P_1 is the occupation probablity of state 1 (also the repeated subscripts in stress and strain tensor indicate summation). The detail derivation of the above expression can be found in Fefferman's thesis [27]. To find an expression for relaxational contribution we need to write dP_1 in terms of strain e. Due to periodic perturbation of the applied strain the instantaneous equilibrium position P_1^i changes continuously. We can further write,

$$\begin{aligned} P_1^i &= P_1^0 + \frac{dP_1^0}{d\Delta}\frac{d\Delta}{de_{kl}}e_{kl} \\ &= P_1^0 + 2\frac{dP_1^0}{d\Delta}\gamma_{k,l}e_{kl} \end{aligned} \tag{1.17}$$

Defining $\delta P_1 = P_1 - P_1^0$ and taking $\dot{P}_1 = -\frac{P_1 - P_1^i}{\tau}$ we have,

$$\sigma_{rel,i,j} = n\frac{\Delta}{E}\gamma_{i,j}\frac{dP_1^0}{d\Delta}\gamma_{k,l}\frac{e_{k,l}}{1+i\omega\tau} \tag{1.18}$$

Again one can further refer to [27] for detailed discussion. Now $M_{rel,ijmn} = \frac{\sigma_{rel,i,j}}{e_{mn}}$. Simplifying the expression for $M_{rel,ijmn}$ by omitting the tensor nature of elastic fields we get $M_{rel} = \frac{M_{rel}(0)}{1+i\omega\tau}$

where $M_{rel}(0) = n\gamma^2 \frac{\Delta}{E} \frac{dP_1^0}{d\Delta}$. On further simplification we get,

$$M_{rel} = -\frac{n\gamma^2}{k_b T} \left(\frac{\Delta}{E}\right)^2 \text{sech}^2 \left(\frac{E}{2k_b T}\right) \frac{1}{1 + i\omega\tau} \tag{1.19}$$

Deriving the experimental observables i.e. internal friction and relative change in sound velocity in terms of M_{rel} is given in [27]. However a summary of results is given in next section.

1.3 Validity of TTLS model

Summarizing the results of the above section, the temperature dependence of internal friction can be classified into two limiting cases. In the extreme low-temperature limit, the maximum relaxation rate of TLS $\tau_{max}^{-1} << \omega$ where ω is the angular frequency of the applied strain or perturbation. The occupations of TLS are incapable of reaching the thermal equilibrium in the time scale of oscillations leading to T^3 dependence of internal friction. At higher temperatures, the TLS can relax quickly in the time scale of oscillation, and thus, the internal friction remains constant. Thus,

$$\begin{aligned} Q^{-1} &= \frac{\pi^4}{12} C \left[\frac{T}{T_{CO}}\right]^3 \text{ for } T << T_{CO} \\ Q^{-1} &= \frac{\pi}{2} C \text{ for } T >> T_{CO} \end{aligned} \tag{1.20}$$

where $C = \frac{P_0 \gamma^2}{\rho v}$ and the crossover temperature between two regimes is denoted by T_{CO}. The tunneling strength C is obtained by simply fitting the internal friction to a constant value in the regime $T >> T_{CO}$. The value of T_{CO} can be obtained by fitting the data in the regime where $T << T_{CO}$ where there is $\sim T^3$ dependent roll-off from the plateau region of internal friction. The tunneling model also predicts the change in the speed of sound outlined below,

$$\begin{aligned} \frac{\delta v}{v_0} &= C \ln T \text{ for } T << T_{CO} \\ \frac{\delta v}{v_0} &= -\frac{C}{2} \ln T \text{ for } T >> T_{CO} \end{aligned} \tag{1.21}$$

The tunneling strength C appearing in the temperature dependence of internal friction and relative change in the sound speed also appears in the low-temperature thermal conductivity predicted by the TTLS model. Comparing the tunneling strength, C extracted from the measurements of sound attenuation and thermal conductivity in glasses is one way to understand the validity of the TTLS model. Figure 1.3 taken from [60] compares the tunneling strength C_t from acoustic attenuation and thermal conductivity measurements for a wide variety of glasses

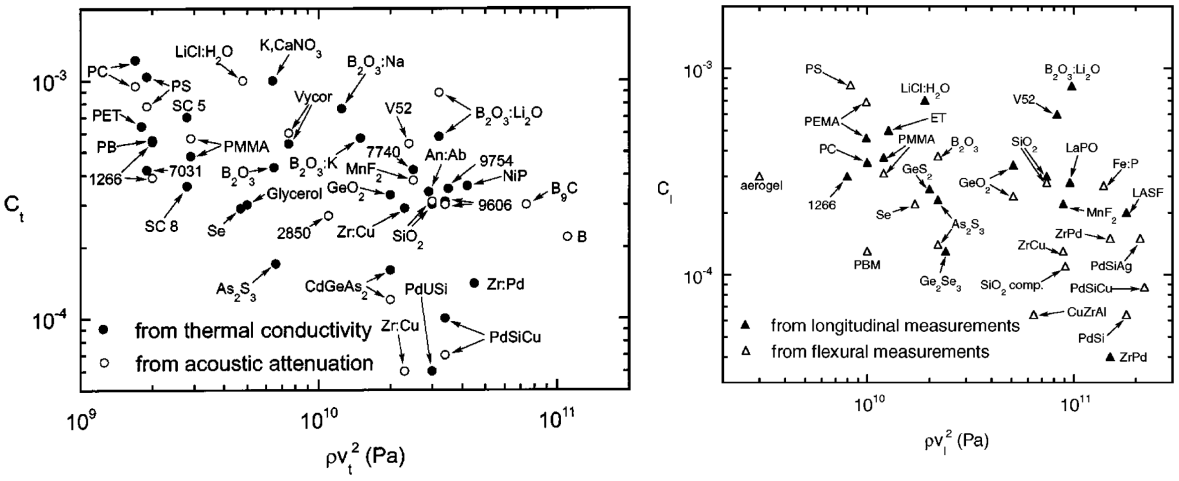

FIGURE 1.3: (left) Plot comparing the tunneling strength C_t (transverse waves) obtained from thermal conductivity and acoustic attenuation (right)Plot comparing the tunneling strength C_l obtained from longitudinal measurements and flexural measurements

(except a-Si, a-Ge, and a-C). The elastic constant ρv_t^2 covers two orders of magnitude from 2 $\times 10^9$ to 2.2 $\times 10^{11}$, yet the plot shows how little the tunneling strength changes. Also, the similarity in the values of C_t from thermal conductivity and acoustic attenuation measurements is the remarkable success of the TTLS model, where t in C_t stands for tunneling strength in transverse direction. The tunneling strengths C_l and C_t are very similar in magnitudes, also shown in figure 1.3 independent of the samples and the measuring techniques, where. Pohl *et al.* [60] also mentioned following key features about the tunneling strength, where l in C_l stands for tunneling strength in longitudinal direction.

a) They observed the small systematic increase of C with the acoustic frequency used for the measurements. Over the five orders of frequencies range studied, C has been found to increase by a factor of 3. Such a variation is not included in the tunneling model.

b) The tunneling strength C appears to be independent of impurities used in a-SiO_2. The variation of OH contents from less than 1 ppm to 1000 ppm does not influence C measured using acoustic attenuation and shows a 10 % decrease in the thermal conductivity measurements.

c) Heat treatment also has little influence on the tunneling strength C.

The experimental findings reviewed in [60] can be explained in the framework of the TTLS model with tunneling strength $C \sim$ lying between 10^{-4} to 10^{-3} for all the amorphous materials. The TTLS model also predicts the dependence of T_{CO} with the frequency of measurement. In the figure 1.4 taken from [75] shows the dependence of internal friction on temperature. T_{CO} is the crossover temperature where the maximum relaxation rate of TLS is equal to the angular

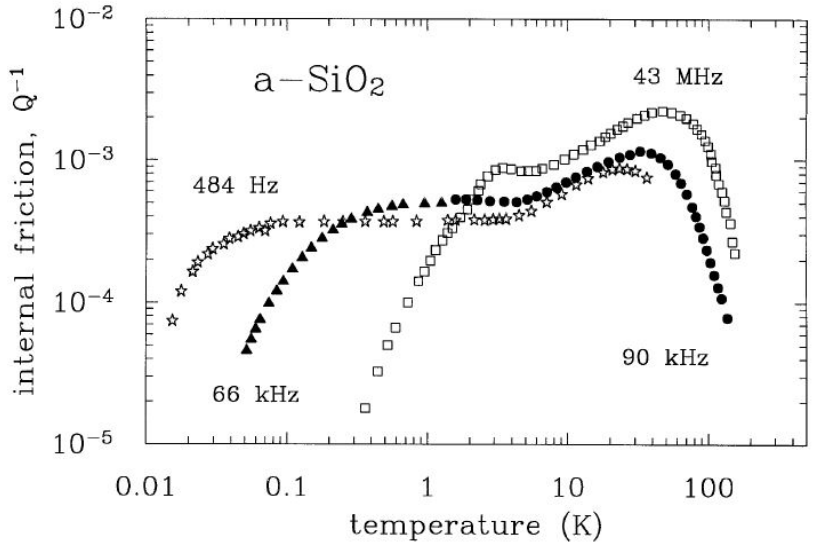

FIGURE 1.4: Internal friction of a-SiO_2 versus temperature measured at different frequencies

frequency used in the measurement. The data shows the clear variation of T_{CO} with $\omega^{\frac{1}{3}}$ dependence predicted by the TLS model.

There is an extensive literature on various measurements in favor of the TTLS model. Discussing them is beyond the scope of this thesis. It is more interesting to highlight the fallacies of the TTLS model and various results in contradiction with the predicted outcome of the TTLS model. *So what is wrong with this model ?*

In this part, I will reiterate the arguments made by Leggett *et al.* in [42]. Leggett argued that if the TTLS model is able to explain some of the experimental findings of the properties of glasses at low temperatures does mean it is correct. He then reviews various predictions of the TTLS model and talks about the fallacies associated with it.

The various non-linear phenomena (such as saturation, echoes, hole-burning) predicted by the TTLS model have been experimentally verified. Leggett argues that these non-linear phenomena are not unique to TLSs, but any model with the system energy levels and stress matrix elements other than familiar, simple harmonic oscillators are sufficient to reproduce the results. The TTLS model is also phenomenological and lacks quantitative calculations. TTLS model predicts that the specific heat of amorphous materials is linearly dependent on temperature. However, experimental findings suggest T^n where $n \sim 1.2 - 1.3$ dependence is inconsistent with the theory. The universal quantitative behavior of glasses, e.g., the internal friction of the amorphous solid in the regime where $T >> T_{CO}$, i.e., in the plateau region, is of the order

of $(3\pm 2)\times 10^{-4}$ for almost all amorphous materials which are striking. Leggett further argues this universality can be attributed to a mind-boggling degree of coincidence as the internal friction depends on four different independent parameters. He then further commented that ultrasonic absorption might be *smoking gun* to test the existence of TLSs in amorphous materials.

As outlined in the previous section, the TLS-phonon interaction occurs via two mechanisms (resonant and relaxation). In the relaxation mechanism, the phonon modulates the energy splitting of the TLS, perturbing the TLS population away from the equilibrium distribution. The TLS relax by exchanging energy with sound waves leading to damping of the sample's vibration. As mentioned before, the internal friction varies as $\sim \left(\frac{T}{T_{CO}}\right)^3$ for $T << T_{CO}$ and $Q^{-1} = \frac{\pi}{2}C$ for $T >> T_{CO}$. Fefferman *et al.* [26] measured the internal friction and change in sound velocity of oscillators made of vitreous silica as shown in figure 1.5. The measurement was done at three different frequencies, and they observed another crossover temperature at 10 millikelvin where Q^{-1} goes from $\sim T^3$ dependence to $\sim T$ dependence. The T dependence of the internal friction is not in accord with the standard TTLS model. However, the T dependence can be predicted by the model if interactions between pairs of TLS are accounted for. It is argued that the existence of such 4-particle clusters leads to a relaxation rate linear in temperature [16]. Also, the ratio of $\frac{d\frac{\delta v}{v_0}}{d\log 10T}$ is 1:-1 for both high and low temperature, which is in sharp contrast with the ratio predicted by the TTLS model, i.e., 2:-1. They also highlighted that $\frac{\delta v}{v_0}$ departs from the usual $d\log 10T$ dependence below 3 mK. According to them, the slope ratio can be accounted for by modifying the distribution function of the TLSs. Thus measurement of internal friction and relative change in the sound velocity in the relaxational regime is not the test for the TTLS model as the discrepancies not predicted by the TTLS model cannot be fixed by mere minor modifications, argues Leggett.

In the high frequency, low temperature regime ($\hbar\omega >> k_bT$) the only non-negligible contribution to internal friction comes from the resonant mechanism, where the internal friction is given by $Q^{-1} = \pi\omega C\tanh(\frac{1}{2}\beta E)$. To enter into this regime, one needs oscillators with high resonance frequency. For instance, at $T = 5$mK, one needs to have the resonance frequency of the order of ~ 60 MHz. The only way to achieve such a high frequency is to reduce the size of the oscillators. With the rapid improvement in nanofabrication, one can now make these small oscillators referred to as NEMS (doubly clamped nanobeams, cantilevers, drums, etc.) from amorphous materials capable of reaching the desired resonance frequency. Also, coupling these NEMS with superconducting microwave cavities has opened up the path to detect the motion of NEMS at low temperatures. The field is called ***Cavity Optomechanics***.

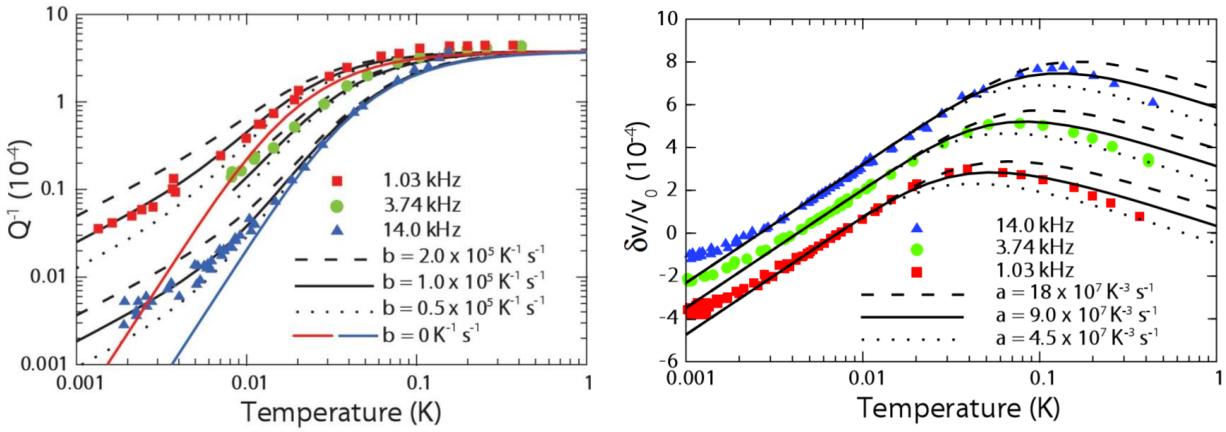

FIGURE 1.5: (left) Internal friction versus Temperature for three different measuring frequencies and the parameter 'b' is the fitting parameter for $\sim T$ depedence of the internal friction below 10 millikelvin (taken from [26]) (right) Change in sound velocity versus temperature for three different measuring frequencies (again taken from [26])

Another aspect of the TTLS model which remains elusive to us is the microscopic nature of TLSs. Ramos *et al.* [62] proposed a scheme to probe the individual TLS using cavity optomechanics. They postulated that under some conditions, there might be a strong coupling between single TLS and the mechanical mode inducing Jaynes Cummings like hamiltonian leading to the splitting of the mechanical mode. The output spectrum can be measured using the microwave cavity coupled to the mechanical resonator. Thus with the developing field of cavity optomechanics, it is possible to test the validity of the TTLS model and probe an individual TLS. However, there are other complications related to the technique of cavity optomechanics prohibiting us from measuring the internal friction and change in the sound velocity in NEMS at low temperatures. The concepts behind cavity optomechanics are discussed in the next section. I will also discuss the current problems we are facing and the prospect of measuring the NEMS just made of amorphous material.

1.4 Cavity Optomechanics

The field of cavity optomechanics [51], [8] is a rapidly growing field with its applications in detecting the small motion of mechanical resonators, quantum information processing, and testing various quantum theories. In a cavity optomechanical setup, a mechanical resonator is coupled to an electromagnetic cavity. The field of cavity optomechanics encompasses a large range of mechanical frequencies i.e., from 100 kHz to 1 GHz, and electromagnetic fields from GHz to THz range. We can span such a large range of mechanical and electromagnetic frequencies due to various designs and fabrication of the above entities in nanofabrication facilities. Coupling

the mechanical resonator to an electromagnetic cavity gives us information about the position of the former. On the other hand, the radiation pressure forces (due to standing waves inside the cavity) on the mechanical resonator influence the mechanical properties.

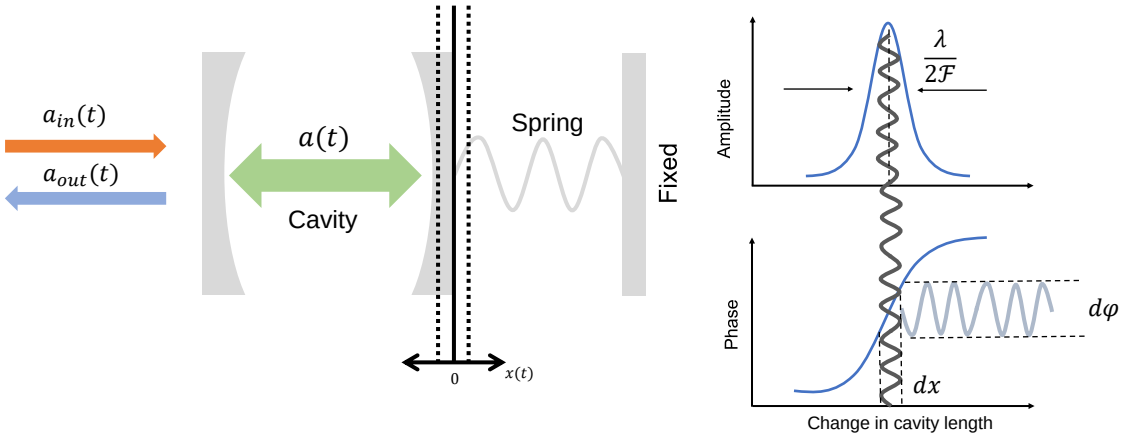

FIGURE 1.6: (left) Schematic showing an optical cavity with a mechanically compliant resonator (right) The small motion of the mechanically compliant mirror induces a large change in the phase of the output signal

The basic cavity optomechanical setup consists of a mechanical resonator coupled to an optical (microwave) cavity as shown in figure 1.6. The cavity consists of one highly reflective (right) and a partially reflecting mirror (left) separated by a distance l. The cavity can be modeled as a simple Fabry Perot resonator. The cavity undergoes a series of resonances with angular frequencies give as $\omega_c \approx m\pi\frac{c}{l}$ where c is the speed of light, and m is an integer mode number. The cavity is also characterized by its finesse which gives the average number of round trips before the photons leave the cavity. The optical finesse is given as $\mathcal{F} = \frac{\Delta\omega_{FSR}}{\kappa}$ where $\Delta\omega_{FSR} = \pi\frac{c}{l}$ is the free spectral range of the cavity and κ^{-1} is the photon lifetime (cavity loss rate). The cavity loss rate for an optical cavity can further be decomposed into κ_{ext} and κ_i such that $\kappa = \kappa_{ext} + \kappa_i$. κ_{ext} characterizes the coupling or the loss rate associated with waveguide and resonator, and κ_i is related to absorption of light inside the cavity. Now the quantum mechanical model of any cavity can be given in terms of input-output theory which relates the output field $a_{out}(t)$ (either reflected or transmitted from the cavity) in terms of input field $a_{in}(t)$ and the field inside the cavity $a(t)$. The evolution of the field inside the cavity is generally given by Heisenberg-Langevin equation of motion. We will analyze the Heisenberg-Langevin equation and its solution in the chapter dedicated to theory.

As shown in figure 1.6, one of the mirrors is not fixed. For a general optomechanical system, the movable mirror can have a mechanical degree of freedom about any direction subject to

boundary conditions. For the schematic shown in the figure, we assume the mirror is only free in a single direction, i.e., x. The motion of this mirror changes the length of the cavity, which in turn changes the resonance frequency of the cavity. For the fundamental mode of the cavity, the resonance frequency is now given as $\omega_c = \omega_0 + Gx$ where ω_0 is the resonance frequency of the cavity when the mirror is at its equilibrium position, and $G = \dfrac{\partial \omega_c}{\partial x}$ is the change in resonance frequency of the cavity with the displacement of the movable mirror. The change in the resonance frequency imparts a change in the phase of the outgoing field $a_{out}(t)$. As shown in figure 1.6 a slight change in the length of the cavity induces a significant change in the phase of the outgoing field. The sensitivity of the measurement can further be increased by fabricating cavities with low losses.

Most of the optomechanical experiments rely on this simple Fabry Perot resonator with movable mirror, or the electrical setup of a mechanically compliant variable capacitance in microwave cavities [63]. Recent progress has led to various other optomechanical setups such as microtoroid [67] resonator which supports whispering-gallery optical modes around its circumference. The mechanical mode can change the circumference, thereby changing the resonance frequency of the optical modes. Then there is a mechanical beam that has been patterned with photonic crystal structure [66] such that photonic and phononic modes exist and couple in a single structure.

1.4.1 Mechanical control by dynamical radiation pressure forces

The basic idea behind the radiation pressure force is simple to understand. If a continuous electromagnetic wave with power P is continuously reflected from a surface, then the force on the surface will be $F = \dfrac{dP}{dt} = \dfrac{2P}{c}$ where c is the speed of light. The phase with which radiation pressure force acts on the mechanical resonator can cause the amplification or damping of its harmonic motion.

For a simple optomechanical system such as Fabry Perot resonator with one mirror partially reflecting and other fully reflecting separated by distance l resonates at frequency $\omega_c = \dfrac{\pi c}{l}$. The total loss associated with the resonator is κ. The energy stored in the cavity can be characterized by the number of photons stored in the cavity given as $n_d = \dfrac{E}{\hbar \omega_d}$ where ω_d is the frequency of light entering the resonator. On the other hand, the full reflecting mirror is mechanically compliant characterized by its mechanical resonance frequency Ω_m. The mechanical dissipation rate is given by Γ_m. We can now define a detuning parameter $\Delta = \omega_d - \omega_c$. The various regimes of cavity optomechanical experiments can be classified depending on the sign

of Δ. When $\Delta \approx -\Omega_m$ we observe the damping of mechanical mode resonating with Ω_m. This scheme of pumping the optical cavity is called red detuned pumping. We can also observe the anti-damping of mechanical mode when $\Delta \approx +\Omega_m$ and the scheme of pumping is called blue detuned pumping. The resonant in cavity pumping where $\Delta = 0$ does not influence the mechanical damping rate. Figure 1.7 shows the three different pumping schemes. Each of the

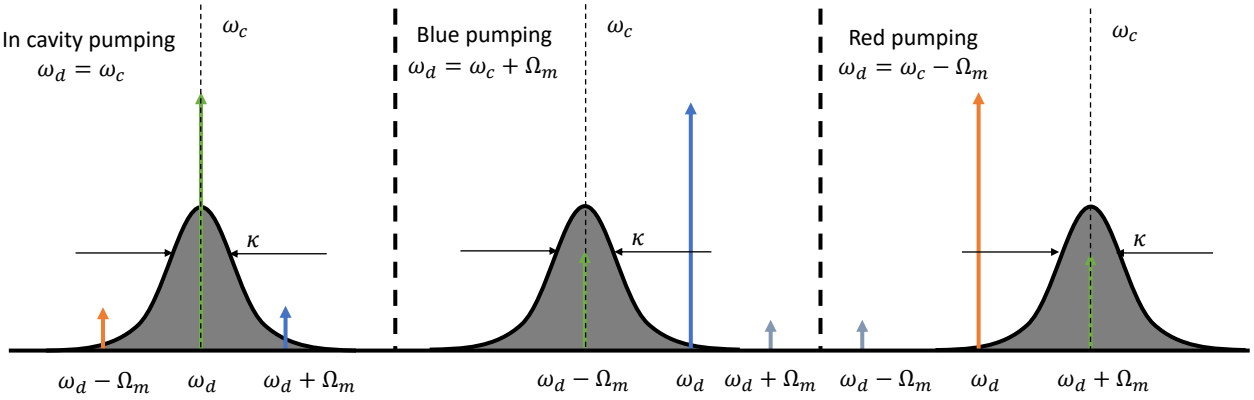

FIGURE 1.7: The schematic showing three different pumping schemes (left) in-cavity pumping (center) Blue pumping and (right) red pumping

schemes shown in figure 1.7 have cavity lineshape with κ denoting its linewidth and ω_c its resonance frequency. The tallest arrow represents the drive/pump field, and the smaller arrows represent the two sidebands in the noise spectrum due to the motion of the mechanically compliant mirror. When $\omega_d = \omega_c$ the areas under two sidebands are same if $k_b T >> \hbar\Omega_m$ where k_b is the Boltzmann constant and T is the temperature under consideration. For blue pumping, $\omega_d \approx \omega_c + \Omega_m$. The lower sideband for this pumping shown in green will be enhanced to cavity density of state, and the upper sideband will be suppressed. The pump down-converts the photon by giving a phonon to the mechanical resonator. Therefore, blue detuned pumping preferentially gives energy to the mechanical resonator, thus amplifying its motion. On the other hand, when $\omega_d \approx \omega_c - \Omega_m$, there is up-conversion of phonon from the mechanical resonator to photon in the cavity, thus removing energy from the mechanical resonator (in turn cooling the mechanical mode of interest). The quantitative description of cavity optomechanics is given in chapter 2 (Theory: quantum noise in microwave optomechanics).

One of the long-standing goals in the field of cavity optomechanics is the cooling of mechanical mode to its quantum ground state as it is a prerequisite to many experiments in the field of quantum information processing and tests for quantum theories. Teufel *et al.* [73]

were able to cool down the mechanical mode resonating at 10.56 MHz of their mechanical resonator (Aluminum drum) to its quantum ground state using active cooling technique of cavity optomechanics. The Aluminum drum was coupled inductively to a superconducting LC circuit (microwave cavity). The resonance frequency of the fundamental mode of the cavity was 7.54 GHz. They demonstrated the average final occupancy of their mechanical mode was ≈ 0.3.

Inspired by the above exciting result encouraged the notions that mechanical resonators may perform useful functions in the processing of quantum information and superconducting circuits. Palomaki *et al.* [56] demonstrated coherent transfer of the state of microwave field transferred into, stored in, and retrieved from a mechanical resonator with amplitudes at a single quanta level. Zhou *et al.* [88] realized the slowing and advancing of microwave signals with millisecond distortion-free and negligible losses using the technique of optomechanically induced transparency which is a characteristic of any optomechanical setup. Chapter 4 is dedicated to measurements of optomechanically induced transparency and absorption. Wollman *et al.* [80] utilized the microwave radiation pressure to prepare their mechanical resonator in the quantum ground state and then manipulated its thermal fluctuations to produce a quadrature squeezed state. The variance of one motional quadrature was 0.8 times the zero-point level. Barzanjeh *et al.* [12] used reservoir engineered optomechanical interactions to demonstrate on-chip magnetic free circulators, which could pave the way for superconducting qubit processors with multiplexed on-chip signal processing and readout.

The success of superconducting microwave optomechanics gave us an impetus to measure the dissipation and frequency shift of the mechanical resonator based on glassy materials with temperature. Therefore we coupled the suspended nanobeam made of SiN capacitively to a superconducting microwave cavity. The design features of the microwave cavity and NEMS are given in detail in the chapter on experimental techniques. The devices were fabricated at nano-fabrication facilities in Institut Neel/CNRS. For our experiments aiming at the careful characterization of mechanical properties at different temperatures, we need the whole system to be in thermal equilibrium. The mechanical beam, as well as its mode, should be in equilibrium with the temperature of the cryostat. The chip containing the mechanical resonator and the microwave cavity was installed in a cell made of annealed Cu. The cell is pressed against the mixing chamber plate of our cryogen-free dilution cryostat. Inside the cell, the input and the output coaxial transmission lines are soldered to gold coplanar waveguides (CPW) on a circuit board, which in turn is micro bonded to the ends of a niobium CPW on the chip. The pump tone was generated by microwave generators at room temperature. The signal then passes through a series of attenuators, which decrease the thermal noise level, and a bandpass filter before reaching the input port of the experimental cell. The transmitted signal that exits

the cell passes through two circulators, which prevent noise traveling down the detection line from entering the output of the cell. The resulting signal was amplified by a series of two high electron mobility transistors (HEMT) at 4-kelvin plate and room temperature before being measured by spectrum analyzer or lock-in amplifier.

In a simple experiment, the microwave cavity is pumped by a pump tone, and mechanical characteristics are determined by demodulating the signal at sidebands. With in-cavity pumping where $\omega_d = \omega_c$ we can measure the signal at both $\omega_c + \Omega_m$ and $\omega_c - \Omega_m$ thus deducing the intrinsic linewidth or the mechanical dissipation rate Γ_m. However, the signal corresponding to the frequencies at $\omega_c \pm \Omega_m$ are suppressed. At lower temperatures, it is impossible to characterize the sideband due to the small amplitude of the signal corresponding to the small thermal motion of the mechanical resonator. We can further take advantage of red or blue pumping with smaller pumping drives such that damping and anti-damping due to radiation pressure forces are negligible. The upper sideband is amplified due to cavity density of state while pumping red, whereas the lower sideband is amplified while pumping blue. We measured the sidebands and deduced the mechanical characteristics, which are in agreement with the theory above T>200 mK, where T is the temperature of the mixing chamber plate of the cryostat. Below $T < 200$ mK the signal is marred by anomalous force noise, prohibiting us from measuring the signal accurately. We observe very large amplitude fluctuations (spikes) below $T < 200$ mK and get worse for lower temperatures regardless of the pumping schemes. The statistics of these fluctuations or events are complex and are subject to chapter Anomalous force noise of mechanical resonators. However, I will mention few key points here. These spikes are only detected on mechanical sidebands, and sometimes these spikes trigger the self-oscillation. We cannot attribute the fluctuations to the input field as one of the plausible reasons. With higher power due to the input field, the nanobeam would subsequently be heated to higher temperatures leading to broad peaks which are shifted in frequency. These anomalous amplitude fluctuations are rarely mentioned in the literature. Massel *et al.* [49] mentioned intermittent heating in their beam devices below 150 mK. There is also a mention of anomalous force noise by Rocheleau *et al.* [64], where they also used Aluminum beam devices for their cavity optomechanical measurements.

The cause of these spikes remains elusive to us. One of the plausible causes could be strongly coupled TLSs since these TLSs are responsible for low-temperature properties of glasses governing the damping, frequency shifts, and phase fluctuations within the standard tunneling model. Our results are also similar to those of [53] obtained with macroscopic mechanical glass sample, where spiky events were attributed to the interaction of mechanical resonator with gamma rays. The different possible sources of these spiky events will be discussed in detail in

Chapter 5.

1.5 Dielectric actuation of SiN nanobeam

The superconducting microwave cavity optomechanics so far has been limited to measurements of mechanical resonators made of metals (typically Aluminum) or dielectrics (Si, SiN) with a thin layer of metal on top. As discussed before it is imperative to measure the mechanical properties of resonators made just of the dielectric to study the interactions of TLSs with phonons. It is difficult to couple a mechanical resonator made of dielectric to a microwave cavity owing to fabrication as well as measurement challenges. We have developed a novel dual-chip scheme where the chip with MWC will be coupled to the chip with NEMS through wire bonds as shown in figure 1.8. This scheme was inspired by Faust *et al.* [25]. While

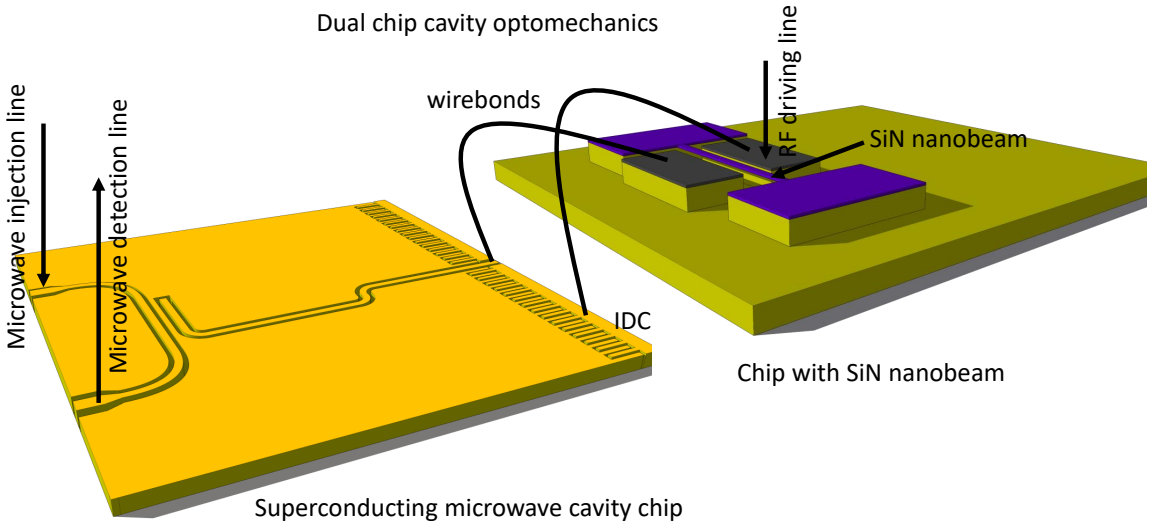

FIGURE 1.8: Schematic showing the dual-chip technique

previous works mostly relied on capacitive coupling between the cavity and metalized resonator, in this scheme, we take advantage of dielectric gradient forces. When a dielectric beam is placed in between two electrodes, its vibration will induce periodic modulation of their mutual capacitance. The capacitative modulation will thus alter the response of the microwave cavity connected to one of the electrodes via a wire bond. The response of the microwave cavity can be demodulated to probe the position of the mechanical resonator. This scheme will not be limited to just measuring the thermal motion of the mechanical resonator but also have the capability to actuate the motion by applying an RF drive to an electrode at a frequency near its resonance. Apart from measuring the dissipation and frequency shift of mechanical resonator with temperature, we would also be able to test our hypothesis i.e., if the spikes (random amplitude fluctuations) as discussed in the previous section are due to the presence of metal. The detail of these experiments is given in *Chapter 6.*

Chapter 2

Theory: quantum noise in microwave optomechanics

2.1 Introduction

In the previous chapter, we discussed the substantial applications of optomechanical systems i.e. from being an ultrasensitive detector of motion to their ubiquitous nature in quantum information applications and tests for quantum theory. We also discussed our motivation to cool down the mechanical resonator to its quantum ground state to explore the dissipation and decoherence due to thermal bath and probe the individual intrinsic two level defects. We also discussed why cooling the environment along with the mechanical mode of interest is vital. In this chapter, we are concerned with the equations governing the mechanical resonators and optomechanical systems. We will commence this chapter by deriving the resonance frequency of the nanobeam which depends on its dimension, stress and Young's modulus of the material [72] using Euler Bernouilli's theory of beam. Although the theory predicts the resonance frequency of the beam precisely it does not take into account the undercut in the devices made in the cleanroom which influences the resonance frequency. Simulation of mechanical objects using finite element methods thus become pivotal in determining the same. We will then switch to the classical equation of motion for a damped harmonic oscillator and derive the amplitude of motion of the center of mass of nanobeam. Using the Fluctuation-Dissipation theorem we will then calculate the spectral density of position fluctuation which will be crucial to link it to the spectral density of the output field in the optomechanical systems. Quantum mechanical models for both NEMS and MWC will also be addressed.

We will then shift our attention to the quantum langevin equation of motion for coupled MWC and NEMS interacting with multiple heat baths. For deriving the equations we will follow the input-output formalism from Gardiner and Zoller [29]. Several optomechanical properties such as optical spring effect, heating and cooling of the mechanical mode by following various pumping schemes i.e. pumping at MWC's resonance frequency or detuned from MWC's

resonance frequency by mechanical resonance frequency will be mentioned. The spectral density of the output field which is the measurable quantity will be extracted from solving the quantum langevin equation for various pumping schemes which is important for quantitative description of characteristics of the mechanical object at different temperatures.

2.2 Mechanical Resonators

The various eigenmodes of a resonator can be calculated by solving the linear theory of elasticity using appropriate boundary conditions. For beam we can use Euler Bernoulli's beam equation [13]. Consider a rectangular beam of length l, width w and thickness t such that $l >> w, t$ shown in figure 2.1 (z is along the length of the beam, y is along the width and x is out of plane); the Euler Bernoulli equation is given by,

$$EI\frac{\partial^4 u(z,t)}{\partial z^4} + \rho A\frac{\partial^2 u(z,t)}{\partial t^2} - \sigma A\frac{\partial^2 u(z,t)}{\partial z^2} = 0 \tag{2.1}$$

where E is Young's modulus, $A = wt$, I is the second moment of area ($I = wt^3/12$), ρ is the mass density, σ is the inbuilt stress and $T = \rho A$. The displacement field $u(z,t)$ can be separated into displacement profile $\psi(z)$ and time dependent oscillation of the center of mass, $x(t)$. The oscillation is considered sinusoidal here, so $x(t) = x_0 e^{i\omega t}$.

$$u(z,t) = \psi(z)x(t) \tag{2.2}$$

Substituting (2.2) in (2.1) we get,

$$EI\frac{\partial^4 \psi(z)}{\partial z^4} - \rho A\omega^2\psi(z) - \sigma A\frac{\partial^2 \psi(z)}{\partial z^2} = 0 \tag{2.3}$$

The displacement profile can be approximated as,

$$\psi(z) = c_1\sinh(\frac{Mz}{l}) + c_2\cosh(\frac{Mz}{l}) + c_3\sin(\frac{Nz}{l}) + c_4\cos(\frac{Nz}{l}) \tag{2.4}$$

where c_1, c_2, c_3, c_4,M,N are real and constants.
Substituting (2.4) in (2.3) we get,

$$[EI(\frac{M}{l})^4 - T(\frac{M}{l})^2 - \rho A\omega^2][c_1\sinh(\frac{Mz}{l}) + c_2\cosh(\frac{Mz}{l})] + [EI(\frac{N}{l})^4 + T(\frac{N}{l})^2 - \rho A\omega^2][c_3\sin(\frac{Nz}{l}) + c_4\cos(\frac{Nz}{l})] = 0 \tag{2.5}$$

Since $c_1\sinh(\frac{Mz}{l}) + c_2\cosh(\frac{Mz}{l})$ and $c_3\sin(\frac{Nz}{l}) + c_4\cos(\frac{Nz}{l})$ cannot be zero in (2.5), we have

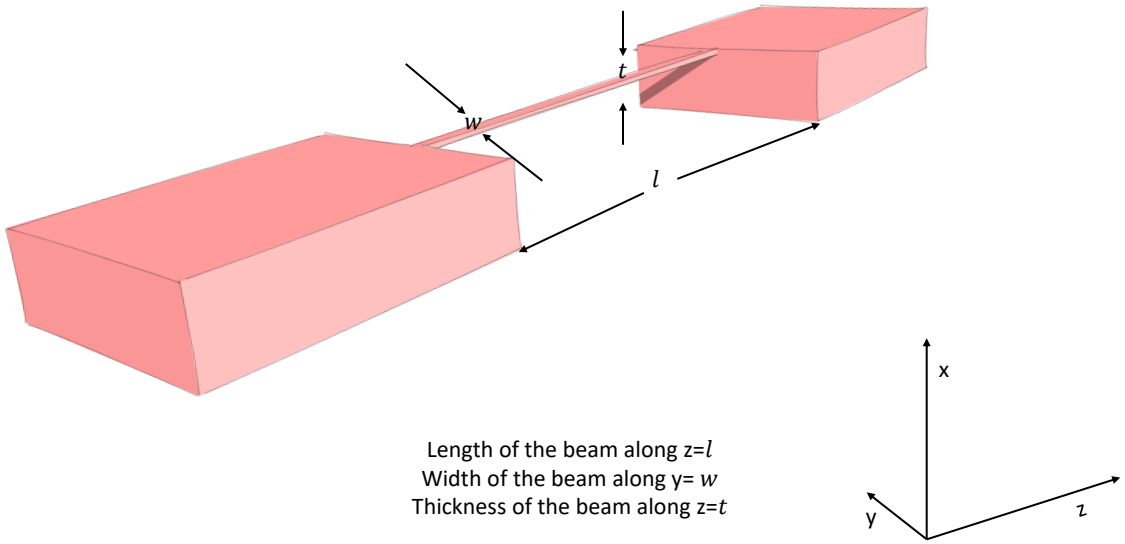

FIGURE 2.1: A schematic showing the length, width and thickness of nanobeam

$EI(\frac{M}{l})^4 - T(\frac{M}{l})^2 - \rho A\omega^2 = 0$ and $EI(\frac{N}{l})^4 + T(\frac{N}{l})^2 - \rho A\omega^2 = 0$ thus giving

$$M = l(\frac{T + \sqrt{T^2 + 4\rho\omega^2 AEI}}{2EI})$$

$$N = l(\frac{-T + \sqrt{T^2 + 4\rho\omega^2 AEI}}{2EI})$$

Since we are considering the doubly clamped beam, following are the boundary conditions imposed,

$$\psi(0) = 0, \psi(l) = 0$$

$$\frac{d\psi(z)}{dz}|_{z=0} = 0, \frac{d\psi(z)}{dz}|_{z=l} = 0$$

Imposing these boundary conditions on (2.4) we get the following 4 equations,

$$c_2 + c_4 = 0$$

$$c_1 \sinh(M) + c_2 \cosh(M) + c_3 \sin(N) + c_4 \cos(N) = 0$$

$$c_1 M + c_2 N = 0$$

$$c_1 M \cosh(M) + c_2 M \sinh(M) + c_3 N \cos(N) - c_4 N \sin(N) = 0$$

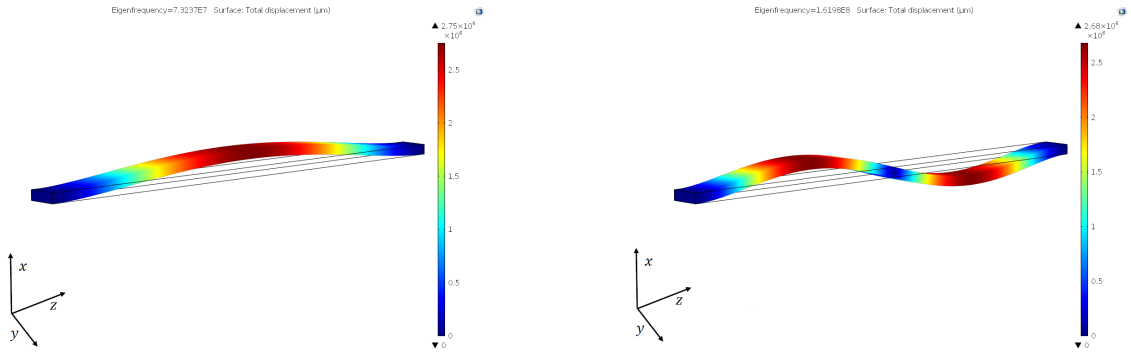

FIGURE 2.2: Comsol simulation of a beam with dimensions given in the text and showing two eigenmodes corresponding to motion in direction x. The colors represent the displacement of the beam from the equilibrium position

The constants c_1, c_2, c_3 and c_4 can be eliminated giving the following transcendental equation,

$$(M^2 - N^2)\sin(M)\sin(N) + 2MN - 2MN\cosh(M)\cos(N) = 0 \tag{2.6}$$

Since M and N depend only on frequency ω and the rest of the parameters are known, we can plot the function $P(\omega)$ where $P(\omega) = (M^2-N^2)\sin(M)\sin(N)+2MN-2MN\cosh(M)\cos(N)$ and look for the points where $P(\omega) = 0$ thus giving the eigenfrequencies of the doubly clamped beam.

Taking $l = 5$ μm, $w = 300$ nm, $t = 120$ nm, $E = 250$ MPa, $\sigma = 0.9$ GPa, $\rho = 2.8$e3 Kg/m^3, $P(\omega)$ is plotted in figure 2.3. The values of the parameters taken are typical values of the actual device. The values of frequency where the function takes the value 0 are the resonant mode frequencies. The resonant frequencies matches within 1% as calculated from the finite element simulation of nanobeam as shown in figure 2.2.

2.2.1 Time dependence of damped harmonic oscillator

The temporal evolution of $x(t)$ can be calculated using the basic equation of motion for the damped harmonic oscillator.

$$m_{eff}\frac{\partial^2 x(t)}{\partial t^2} + m_{eff}\Gamma_m\frac{\partial x(t)}{\partial t} + m_{eff}\Omega_m^2 x(t) = F(t) \tag{2.7}$$

The above equation can be written for different eigenmodes of the mechanical resonator. We will deal with fundamental eigenmode here. The effective mass of the mechanical resonator is $m_{eff} = \rho A \int \psi(z)^2 dz$ [68], where $\psi(z)$ is the shape factor defined in above section and ρ is the mass density and $A = wt$. Γ_m is the damping rate of mode and Ω_m is its resonance

frequency. The above equation can easily be solved in frequency space. Let the actuating force be $F(t) = F_0 e^{-i\omega t}$ such that the motion of the NEMS also follows sinusoidal motion i.e. $x = x_0 e^{-i\omega t} e^{-i\phi}$ where ϕ is the phase difference. x_0 is the vibration amplitude of the mechanical resonator. Putting $F(t)$ and $x(t)$ in (2.7) we get,

$$x_0 e^{-i\phi} = \frac{F_0}{m_{eff}(\Omega_m^2 - \omega^2 - i\omega\Gamma_m)} \tag{2.8}$$

The two quadratures of the motion are thus the real and the imaginary parts of the x_0. The real and imaginary parts of $x_0 e^{-i\phi}$ is given as $\Re(x_0 e^{-i\phi}) = X(\omega) = \frac{F_0}{m_{eff}} \frac{\Omega_m^2 - \omega^2}{(\Omega_m^2 - \omega^2)^2 + \Gamma_m^2\omega^2}$ and $\Im(x_0 e^{-i\phi}) = Y(\omega) = \frac{F_0}{m_{eff}} \frac{\Gamma_m\omega}{(\Omega_m^2 - \omega^2)^2 + \Gamma_m^2\omega^2}$ describing the motion of mechanical resonator in complex plane. $X(\omega)$ is called the absorption part of the mechanical response and $Y(\omega)$ the dispersion part. If the force is applied at mechanical resonance frequency then $Y(\omega) = \frac{F_0}{m_{eff}\Gamma_m\Omega_m}$ and $X(\omega) = 0$. The mechanical response has the lorentzian line shape with vibration amplitude given as $|x_0| = \sqrt{(X(\omega)^2 + Y(\omega)^2)}$.

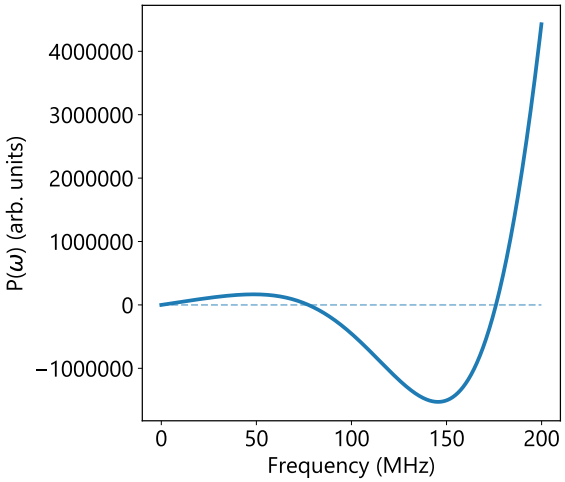

FIGURE 2.3: Plotting the transcendental function, $P(\omega)$ derived from Euler-Bernouill's beam theory and extracting the resonance frequency

2.2.2 Quantum mechanical treatment of mechanical resonator

In the above section, we considered the classical equation of motion to deduce the vibration amplitude of the mechanical resonator. Considering the mechanical resonator as a harmonic oscillator we can write the hamiltonian as,

$$H = \hbar\Omega_m b^\dagger b + \frac{1}{2}\hbar\Omega_m \tag{2.9}$$

In the above equation, $b^\dagger$ and b are the phonon creation and annihilation operators and $\frac{1}{2}\hbar\Omega_m$ is the zero-point energy of the harmonic oscillator corresponding to the zero-point fluctuation. The position operator $x = x_{zpf}(b + b^\dagger)$ and the momentum operator $p = -im_{eff}\Omega_m x_{zpf}(b - b^\dagger)$ satisfy the commutation relation $[x, p] = i\hbar$. $x_{zpf} = \sqrt{\frac{\hbar}{2m_{eff}\Omega_m}}$ is the zero-point fluctuation of the mechanical resonator corresponding to its ground state. We have not yet discussed the effects of dissipation in this quantum mechanical treatment. An exhaustive quantum mechanical

treatment of mechanical resonator interacting with thermal bath inducing dissipation is done in section 2.3.

Spectral density is an indispensable quantity in the study of random signals which is a measure of intensity of signal at a given frequency. Consider a random signal $V(t)$ characterized by mean $\langle V(t)\rangle = 0$ and autocorrelation function $G_{vv}(t, t+\tau) = \langle V(t)V(t+\tau)\rangle$. $\langle V(t)V(t+\tau)\rangle$ is average of product of instantaneous values of $V(t)$ at two different time instances t and t'. We also assume $V(t)$ is Gaussian distributed therefore the mean and autocorrelation function completely specify the statistics and probability distribution of $V(t)$. We also assume that signal is stationary which means $\langle V(t)\rangle$ and $G_{vv}(t, t+\tau)$ do not vary as t varies. Therefore the autocorrelation function is dependent only on time displacement i.e. $G_{vv}(t, t+\tau) = G_{vv}(\tau)$.

According to the Wiener-Khinchin theorem spectral density is the fourier transform of the autocorrelation function [22].

$$S_{vv}[\omega] = \int_{-\infty}^{\infty} dt e^{i\omega t} G_{vv}(t) \tag{2.10}$$

Once we have defined the spectral density classically we can lay emphasis on calculating the position spectral density of the mechanical resonator [22]. The position operator of the mechanical resonator can be written in terms of two quadratures X and Y describing the smooth envelope of the motion.

$$x(t) = X\cos(\Omega_m t) + Y\sin(\Omega_m t) \tag{2.11}$$

We can write the momemtum operator as,

$$p(t) = [-X\sin(\Omega_m t) + Y\cos(\Omega_m t)]m_{eff}\Omega_m \tag{2.12}$$

X and Y can thus be solved using above equations yielding

$$\begin{aligned} X &= x(t)\cos(\Omega_m t) - \frac{p(t)}{m_{eff}\Omega_m}\sin(\Omega_m t) \\ Y &= x(t)\sin(\Omega_m t) + \frac{p(t)}{m_{eff}\Omega_m}\cos(\Omega_m t) \end{aligned} \tag{2.13}$$

Therefore we can write $x(t) + i\dfrac{p(t)}{m_{eff}\Omega_m} = [X + iY]e^{-i\Omega_m t}$. X and Y are canonically conjugate variables and hence do not commute with each other. They are hermitian and thus observables. $X + iY$ is the quantum-mechanical analog of the resonator's classical complex amplitude. It's now straightforward to show that $[X, Y] = \dfrac{i\hbar}{m_{eff}\Omega_m} = 2ix_{xpf}^2$ since the position and momentum operator follows $[x, p] = i\hbar$. At time $t = 0$, $x(0) = X$ and $p(0) = Ym_{eff}\Omega_m$. $x(t)$ and $p(t)$ can

be further written in terms of their values at time $t = 0$:

$$\begin{aligned} x(t) &= x(0)\cos(\Omega_m t) + \frac{p(0)}{m_{eff}\Omega_m}\sin(\omega t) \\ p(t) &= p(0)\cos(\Omega_m t) - x(0)\sin(\Omega_m t) m_{eff}\Omega_m \end{aligned} \tag{2.14}$$

Considering the case where the mechanical oscillator is not perturbed by any dissipation and is completely isolated from the environment, the autocorrelation function is

$$G_{xx}(t) = \langle x(t)x(0)\rangle = \langle x(0)x(0)\rangle\cos(\Omega_m t) + \langle p(0)x(0)\rangle\frac{1}{m_{eff}\Omega_m}\sin(\Omega_m t) \tag{2.15}$$

Quantum mechanically there must be some correlation between x and p as they are canonically conjugate variables. The following equation holds true for x and p which can easily be evaluated by converting them to creation and annihilation operators.

$$\langle x(0)p(0)\rangle - \langle p(0)x(0)\rangle = i\hbar \tag{2.16}$$

Also $\langle p(0)x(0)\rangle = -i\frac{\hbar}{2}$ and $\langle x(0)p(0)\rangle = i\frac{\hbar}{2}$ [22]. We can write $\langle x(0)x(0)\rangle = x_{zpf}^2\{n_b(\hbar\Omega_m) + [n_b(\hbar\Omega_m)+1]\}$ since $x(0) = x_{zpf}(b+b^\dagger)$. Putting the values of $\langle x(0)x(0)\rangle$ and $\langle p(0)x(0)\rangle$ in equation (2.15) we get,

$$\begin{aligned} G_{xx}(t) &= x_{zpf}^2\left[n_b(\hbar\Omega_m) + n_b(\hbar\Omega_m) + 1\right]\cos(\Omega_m t) - i\frac{\hbar}{2}\frac{1}{m_{eff}\Omega_m}\sin(\Omega_m t) \\ &= x_{zpf}^2\left[(n_b(\hbar\Omega_m) + n_b(\hbar\Omega_m) + 1)\cos(\Omega_m t) - i\sin(\Omega_m t)\right] \\ &= x_{zpf}^2\left[(n_b(\hbar\Omega_m) + n_b(\hbar\Omega_m) + 1)\cos(\Omega_m t) + i(n_b(\hbar\Omega_m) - n_b(\hbar\Omega_m) - 1)\sin(\Omega_m t)\right] \\ &= x_{zpf}^2(n_b(\hbar\Omega_m)e^{-i\Omega_m t} + (n_b(\hbar\Omega_m)+1)e^{i\Omega_m t}) \end{aligned} \tag{2.17}$$

where $n_b(\hbar\Omega_m) = \frac{1}{e^{\hbar\Omega_m/k_bT} - 1}$ is bose einstein occupation number which depends on temperature and the harmonic oscillator's resonance frequency. The spectral density which is the fourier transform of the $G_{xx}(t)$ is not symmetric in frequency and is given as,

$$S_{xx}[\omega] = 2\pi x_{zpf}^2\left[n_b\delta(\omega+\Omega_m) + (n_b+1)\delta(\omega-\Omega_m)\right] \tag{2.18}$$

When $k_bT >> \hbar\Omega_m$ i.e. in the classical limit $n_b \approx n_b{+}1$ and spectral density becomes symmetric in frequency.

2.2.3 Fluctuation-Dissipation Theorem

In the previous section, we have derived the position spectral density when the harmonic oscillator is isolated from the environment. In reality, NEMS is not isolated from the environment. It is coupled to different temperature baths comprising clamps, two-level defects, electrons in the metallic layer, external impedances, etc. This coupling of NEMS to external degrees of freedom can be characterized by its dissipation rate denoted as $\Gamma_m = \sum_i \Gamma_i$ where Γ_i is dissipation through a particular bath. According to the fluctuation-dissipation theorem, the quantum position spectral density is given as [69],

$$S_{xx}[\omega] = \frac{2\hbar}{(1 - e^{-\hbar\omega/k_bT})} \Im(\chi_m(\omega)) \tag{2.19}$$

In the above equation $\chi_m(\omega)$ is mechanical susceptibility which we have derived in 2.8. The imaginary part of mechanical susceptibilty is ,

$$\Im(\chi_m(\omega)) = \frac{\Gamma_m \omega}{m_{eff}[(\omega^2 - \Omega_m^2)^2 + (\Gamma_m^2 \omega^2)]} \tag{2.20}$$

Thus,

$$S_{xx}[\omega] = \frac{2\hbar}{(1 - e^{-\hbar\omega/k_bT})} \frac{\Gamma_m \omega}{m_{eff}[(\omega^2 - \Omega_m^2)^2 + (\Gamma_m^2 \omega^2)]} \tag{2.21}$$

which is not symmetric in frequency as

$$\frac{S_{xx}[\omega]}{S_{xx}[-\omega]} = \frac{(1 - e^{\hbar\omega/k_bT})}{(1 - e^{-\hbar\omega/k_bT})} \tag{2.22}$$

For the NEMS with the high quality factor, $\omega \approx \Omega_m$ and $\Im(\chi_m(\omega))$ can be approximated as,

$$\Im(\chi_m(\omega)) \approx \frac{\Gamma_m}{4m_{eff}\Omega_m[(\omega - \Omega_m)^2 + (\Gamma_m/2)^2]} \tag{2.23}$$

The quantum position spectral density is now,

$$S_{xx}[\omega] \approx \frac{2\hbar}{(1 - e^{-\hbar\omega/k_bT})} \frac{\Gamma_m}{4m_{eff}\Omega_m[(\omega - \Omega_m)^2 + (\Gamma_m/2)^2]} \tag{2.24}$$

In the classical limit where $k_bT >> \hbar\omega$, the expression $\frac{1}{(1 - e^{-\hbar\omega/k_bT})}$ can be approximated as $\frac{\hbar\omega}{k_bT}$. Thus classical position spectral density is,

$$S_{xx}[\omega] \approx \frac{k_bT}{2m_{eff}\Omega_m^2} \frac{\Gamma_m}{[(\omega - \Omega_m)^2 + (\Gamma_m/2)^2]} \tag{2.25}$$

In experiments we are concerned with single sided position spectral density which is twice the double sided spectral density. Thus single side spectral density is,

$$S_x[\omega] \approx \frac{k_b T}{m_{eff}\Omega_m^2} \frac{\Gamma_m}{[(\omega - \Omega_m)^2 + (\Gamma_m/2)^2]} \tag{2.26}$$

2.3 Input-output formalism

Input-output formalism is one of the ways to describe the quantum mechanical behavior of any system coupled to multiple heat baths comprising of a continuum of harmonic oscillators with different frequencies [30]. More specifically input-output formalism relates the field emitted by a system to the input field and the field inside the system. If the system under consideration is a microwave cavity, then both signal (coherent microwave drive from the generator) and noise (fluctuations in the microwave drive, fluctuations due to heat baths, etc.) may be embodied together as an input drive. The derivation of the input-output formalism follows from [29]. The ideal Hamiltonian can be written as,

$$H = H_{sys} + H_{bath} + H_{int} \tag{2.27}$$

$$H_{bath} = \sum_l \hbar \int_{-\infty}^{\infty} d\omega \; \omega b_l^\dagger(\omega) b_l(\omega) \tag{2.28}$$

In equation (2.28), l represents one of the multiple heat baths and $b_l(\omega)$ the boson annihilation operator of that bath with $[b_l(\omega), b_l^\dagger(\omega)] = \delta(\omega - \omega')$. The heat bath operator $b_l(\omega)$ is coupled to c_l where c_l is one of the system's operator. If the coupling between heat bath and the system's operator is linear, the interaction hamiltonian can be written as,

$$H_{int} = i\hbar \sum_l \int_0^{\infty} d\omega \gamma_l(\omega)[b_l^\dagger(\omega) + b_l(\omega)][c_l - c_l^\dagger] \tag{2.29}$$

Applying rotating wave approximation to equation (2.29) we get the interaction hamiltonian as,

$$H_{int} = i\hbar \sum_l \int_{-\infty}^{\infty} d\omega \gamma_l(\omega)[b_l^\dagger(\omega) c_l - c_l^\dagger b_l(\omega)] \tag{2.30}$$

where $\gamma_l(\omega)$ is the coupling constant. In equation (2.30) we have dropped the terms $b_l(\omega)c_l$ and $b_l^\dagger(\omega)c_l^\dagger$ as they are fast oscillating compared to other terms. If the system's operator $c_l^\dagger$ is rotating with Ω and $b_l^\dagger(\omega)$ with ω then $b_l^\dagger(\omega)c_l^\dagger$ will have a time dependence as $e^{i(\omega+\Omega)t}$ which is rapidly oscillating compared to $b_l^\dagger(\omega)c_l$ with time dependence as $e^{i(\omega-\Omega)t}$. We have also extended the lower limit of the integral from 0 to $-\infty$. This approximation can only be made if the rotating wave approximation has already been made otherwise the terms having time

dependence term as $e^{i(\omega+\Omega)t}$ will be resonant and thus producing spurious effects.

We can now proceed by writing the Heisenberg's equation of motion for the bath's operator $b_l(\omega)$ and for an arbitrary system's operator a.

$$\dot{b_l}(\omega) = \frac{i}{\hbar}[b_l(\omega), H] \tag{2.31}$$

$$\dot{a} = \frac{i}{\hbar}[a, H] \tag{2.32}$$

Equations (2.31) and (2.32) yields,

$$\dot{b_l}(\omega) = -i\omega b_l(\omega) + \gamma_l(\omega)c_l \tag{2.33}$$

$$\dot{a} = -\frac{i}{\hbar}[a, H_{sys}] + \sum_l \int_{-\infty}^{\infty} d\omega \gamma_l(\omega)[b_l^\dagger(\omega)[a, c_l] - [a, c_l^\dagger]b_l(\omega)] \tag{2.34}$$

Equation (2.33) can be expanded as,

$$b_l(\omega) = e^{-i\omega(t-t_0)}b_{0,l}(\omega) + \gamma_l(\omega)\int_{t_0}^{t} e^{-i\omega(t-t')}c_l(t')dt' \tag{2.35}$$

where $b_{0,l}(\omega)$ is the value of $b_l(\omega)$ at time $t = t_0$. The first term denotes the time dependence of the bath operator $b_l(\omega)$ when it is not coupled to any system. The second term is due to the irradiation of waves by an arbitrary system operator c_l into the bath. Equation (2.35) can be substituted into equation (2.34) giving the following equation,

$$\begin{aligned}\dot{a} = -\frac{i}{\hbar}[a, H_{sys}] + \sum_l \int_{-\infty}^{\infty} d\omega \gamma_l(\omega)\left[b_{0,l}^\dagger(\omega)e^{i\omega(t-t_0)}[a, c_l] - [a, c_l^\dagger]e^{-i\omega(t-t_0)}b_{0,l}(\omega)\right] \\ + \sum_l \int_{-\infty}^{\infty} d\omega[\gamma_l(\omega)]^2 \int_{t_0}^{t} dt'\left[e^{i\omega(t-t')}c_l^\dagger(t')[a, c_l] - [a, c_l^\dagger]e^{-i\omega(t-t')}c_l(t')\right]\end{aligned} \tag{2.36}$$

Also we have dropped time dependence of $\dot{a}, a$ and c_l for notational convenience.

2.3.1 Markov approximation

We now make the markov approximation which assumes the coupling constant $\gamma_l(\omega)$ is constant over a range of frequencies. Therefore we can simplify $\gamma_l(\omega)$ as,

$$\gamma_l(\omega) = \sqrt{\frac{\kappa_l}{2\pi}} \tag{2.37}$$

We can simplify (2.36) using,

$$\int_{-\infty}^{\infty} d\omega e^{-i\omega(t-t')} = 2\pi\delta(t-t') \tag{2.38}$$

and

$$\int_{t_0}^{t} c_l(t')\delta(t-t')dt' = \frac{1}{2}c_l(t) \tag{2.39}$$

We can define the input field as,

$$b_{in,l}(t) = \frac{1}{\sqrt{2\pi}}\int_{-\infty}^{\infty} d\omega e^{-i\omega(t-t_0)} b_{0,l}(\omega) \tag{2.40}$$

Putting equations (2.37)-(2.40) in (2.36) we can readily derive the quantum langevin equation,

$$\begin{aligned}
\dot{a} &= -\frac{i}{\hbar}[a, H_{sys}] + \sum_l \sqrt{\kappa_l}\left[b^\dagger_{in,l}[a,c_l] - [a,c_l^\dagger]b_{in,l}(t)\right] \\
&+ \sum_l \frac{\kappa_l}{2\pi}\int_{t_0}^{t} dt'\left[2\pi\delta(t-t')c_l^\dagger(t')[a,c_l] - [a,c_l^\dagger]2\pi\delta(t-t')c_l(t')\right] \\
&= -\frac{i}{\hbar}[a, H_{sys}] + \sum_l \sqrt{\kappa_l}\left[b^\dagger_{in,l}[a,c_l] - [a,c_l^\dagger]b_{in,l}(t)\right] \\
&+ \sum_l \kappa_l\left[\frac{c_l^\dagger(t)}{2}[a,c_l] - [a,c_l^\dagger]\frac{c(t)}{2}\right]
\end{aligned} \tag{2.41}$$

Thus we have,

$$\dot{a} = -\frac{i}{\hbar}[a, H_{sys}] - \sum_l [a,c_l^\dagger][\frac{\kappa_l}{2}c_l + \sqrt{\kappa_l}b_{in,l}(t)] + \sum_l [\frac{\kappa_l}{2}c_l^\dagger + \sqrt{\kappa_l}b^\dagger_{in,l}(t)][a,c_l] \tag{2.42}$$

Once the system interacts with the input field $b_{in,l}(t)$ we get an output field $b_{out,l}(t)$. If the system does not respond to the input field, the output field will simply be the same as the input field. While if the system interacts with the input field, the output field will thus contain the waves radiated by the system. Let us consider the time t_1 in the distant future after the system has interacted with the input field. The bath operators can be written as,

$$b_l(\omega) = e^{-i\omega(t_1-t)}b_{0,l}(\omega) - \gamma_l(\omega)\int_t^{t_1} e^{-i\omega(t-t')}c_l(t')dt' \tag{2.43}$$

The above equation serves as the final condition rather than initial condition as done in equation (2.35). We define the output field as,

$$b_{out,l}(t) = \frac{1}{\sqrt{2\pi}}\int_{-\infty}^{\infty} d\omega e^{-i\omega(t_1-t)} b_{0,l}(\omega) \tag{2.44}$$

We can thus write the quantum langevin equation in terms of the output field following a procedure analogous to the one used to derive the quantum langevin equation in terms of input field.

$$\dot{a} = -\frac{i}{\hbar}[a, H_{sys}] + \sum_l [a, c_l^\dagger][\frac{\kappa_l}{2}c_l - \sqrt{\kappa_l}b_{out,l}(t)] - \sum_l [\frac{\kappa_l}{2}c_l^\dagger - \sqrt{\kappa_l}b_{out,l}^\dagger(t)][a, c_l] \tag{2.45}$$

2.3.2 Relation between input and output field

Subtracting equation (2.45) from (2.42) yields an input-output relation involving sums of contributions from different baths. More useful input-output relations, each pertaining to a single bath can be obtained by returning to equation (2.35) and its dual (2.43). We can integrate equation (2.35) and write an alternative form for $b_{in,l}(t)$.

$$\frac{1}{\sqrt{2\pi}}\int_{-\infty}^{\infty} d\omega b_l(\omega) = \frac{1}{\sqrt{2\pi}}\int_{-\infty}^{\infty} d\omega e^{-i\omega(t-t_0)}b_{0,l}(\omega) + \frac{\sqrt{\kappa_l}}{2\pi}\int_{t_0}^{t} c_l(t')dt' \int_{-\infty}^{\infty} d\omega e^{-i\omega(t-t')} \tag{2.46}$$

After simplifying the above equation we can write,

$$\frac{1}{\sqrt{2\pi}}\int_{-\infty}^{\infty} d\omega b_l(\omega) = b_{in,l}(t) + \frac{\sqrt{\kappa_l}}{2}c_l(t) \tag{2.47}$$

Similarly we can write an alternative for $b_{out,l}(t)$ by integrating equation (2.43),

$$\frac{1}{\sqrt{2\pi}}\int_{-\infty}^{\infty} d\omega b_l(\omega) = b_{out,l}(t) - \frac{\sqrt{\kappa_l}}{2}c_l(t) \tag{2.48}$$

Therefore one can relate the input and output field using equations (2.47) and (2.48),

$$b_{out,l}(t) = b_{in,l}(t) + \sqrt{\kappa_l}c_l(t) \tag{2.49}$$

2.4 Microwave cavity

In our optomechanical system, the mechanical resonator is embedded into the microwave cavity such that the motion of NEMS modulates the capacitance of the MWC and, therefore the resonance frequency. The superconducting microwave cavity can be modeled using a parallel LC circuit as shown in figure 2.4. We will discuss the design issues and simulations in the next chapter. In this section, only the quantum mechanical model of the MWC will be elaborated.

The energy stored in the circuit is

$$E_{circuit} = \frac{1}{2}Li(t)^2 + \frac{1}{2}Cv(t)^2 = \frac{1}{2}L\dot{q}^2 + \frac{1}{2}\frac{q^2}{C} \tag{2.50}$$

where $i(t) = \dfrac{\partial q(t)}{\partial t}$ is the current flowing into the inductor and $v(t)$ is the voltage across the capacitor. $q(t)$ is the charge stored in the capacitor. The lagrangian of the system is,

$$\begin{aligned} \mathcal{L}_{circuit} &= \frac{1}{2}L\dot{q}^2 - \frac{1}{2}\frac{q^2}{C} \\ \frac{\partial \mathcal{L}_{circuit}}{\partial \dot{q}} &= L\dot{q} = \phi \end{aligned} \tag{2.51}$$

where we introduce ϕ as the canonical conjugate variable to charge q. The Hamiltonian of the circuit can be written in terms of canonical conjugate variables i.e. q and ϕ,

$$\begin{aligned} H &= \frac{\phi^2}{2L} + \frac{q^2}{2C} \\ [q, \phi] &= -i\hbar \end{aligned} \tag{2.52}$$

Going further we can define the creation and annihilation operators for MWC by defining,

$$\begin{aligned} a &= \sqrt{\frac{L\omega_c}{2\hbar}}q - i\sqrt{\frac{1}{2L\omega_c\hbar}}\phi \\ a^\dagger &= \sqrt{\frac{L\omega_c}{2\hbar}}q + i\sqrt{\frac{1}{2L\omega_c\hbar}}\phi \end{aligned} \tag{2.53}$$

such that $[a, a^\dagger] = 1$ and hamiltonian of the cavity is $H = \hbar\omega_c(a^\dagger a + \frac{1}{2})$.

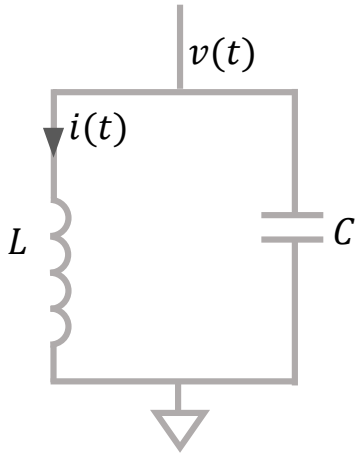

FIGURE 2.4: A superconducting microwave cavity represented as parallel LC circuit with current i flowing into the inductor and voltage v across the capacitor

2.5 Capacitively coupled NEMS and microwave cavity

Our system comprises of MWC and NEMS coupled capacitively as shown in figure 2.5 such that the resonance frequency of the MWC is modulated by the mechanical amplitude of the NEMS, x. We denote the operator corresponding to MWC as a and NEMS as b. Writing the taylor expansion of the resonance frequency of MWC up to first order we get,

$$\omega_c(x) = \omega_c + \frac{\partial \omega_c}{\partial x}x \tag{2.54}$$

In the above equation, ω_c is the resonance frequency of the MWC when the mechanical resonator is at its equilibrium position. Since both NEMS and microwave cavity are harmonic oscillators,

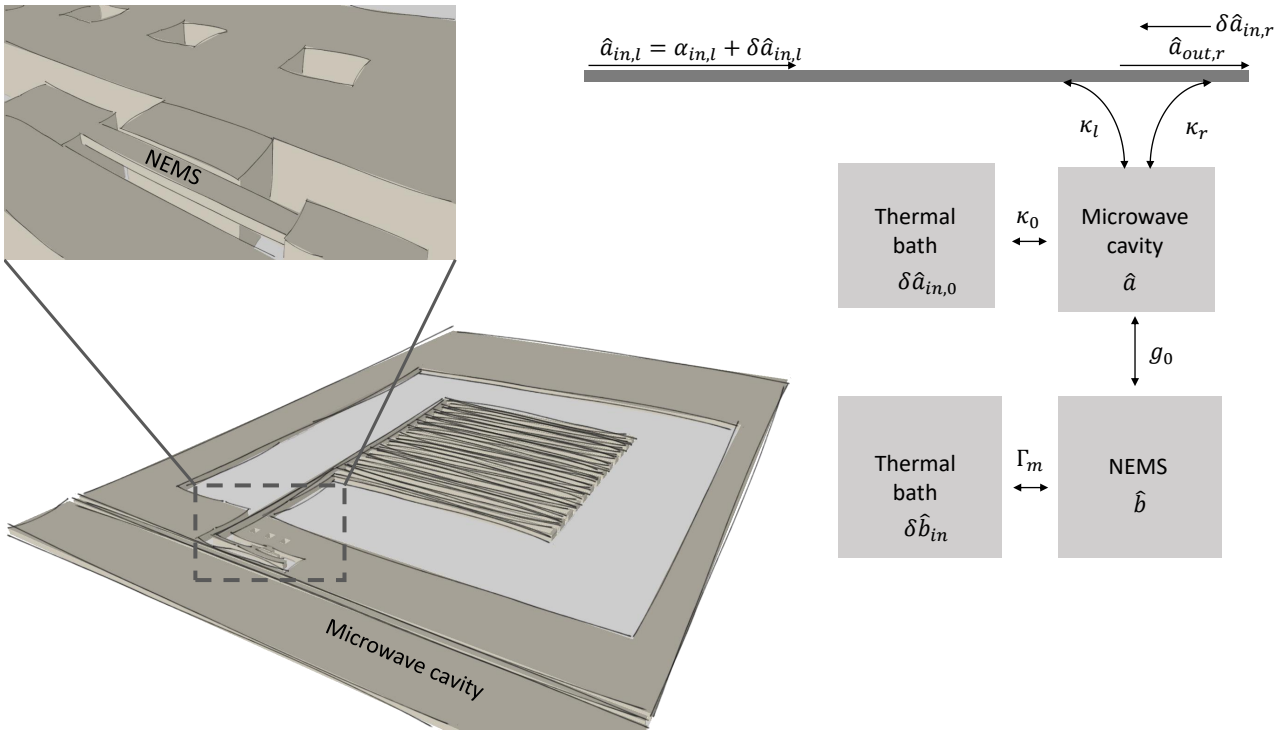

FIGURE 2.5: A schematic showing the coupling between MWC and NEMS and also the coupling of MWC and NEMS to external heat baths.

the hamiltonian of our system can be written as,

$$H_{sys} = \hbar\omega_c(x)a^\dagger a + \hbar\Omega_m b^\dagger b \tag{2.55}$$

The change in the resonance frequency of the MWC per unit displacement of the NEMS is defined as $G = \dfrac{\partial\omega_c}{\partial x}$. We can also define vacuum optomechanical coupling as $g_0 = Gx_{zpf}$ where $x_{zpf} = \sqrt{\dfrac{\hbar}{2m_{eff}\Omega_m}}$ is the zero point fluctuation of the mechanical resonantor. m_{eff} is the effective mass of the mechanical resonator when vibrating and Ω_m is the mechanical resonance frequency. Equation (2.55) can be expanded as ,

$$H_{sys} = \hbar\omega_c a^\dagger a + \hbar\Omega_m b^\dagger b + \hbar g_0(b + b^\dagger)a^\dagger a \tag{2.56}$$

where $x = x_{zpf}(b + b^\dagger)$.

2.6 Quantum langevin equations of motion

Let a be the phonon annihilation operator of microwave cavity. The input field is denoted as $a_{in,k}(t)$. Replacing c with a and $b_{in,k}(t)$ with $a_{in,k}(t)$ the quantum langevin equation (2.42) is

modified as,

$$\dot{a} = -\frac{i}{\hbar}[a, H_{sys}] - \sum_k \frac{\kappa_k}{2} a - \sum_k \sqrt{\kappa_k} a_{in,k}(t) \tag{2.57}$$

Let b be the annihilation operator for phonons occupying the mechanical mode of the nanomechanical resonator. The input field is denoted as $b_{in,k}(t)$ here. We also replace κ_k with Γ_k in equation (2.42) to have a distinction between the coupling constants of MWC and NEMS interacting separately with external thermal baths, and thus we can write the quantum Langevin equation for NEMS as,

$$\dot{b} = -\frac{i}{\hbar}[b, H_{sys}] - \sum_k \frac{\Gamma_k}{2} b - \sum_k \sqrt{\Gamma_k} b_{in,k}(t) \tag{2.58}$$

MWC will interact with transmission line through two different ports with coupling constants as κ_l and κ_r respectively and to thermal bath with coupling constant κ_0. The coupling of the mechanical resonator to external degrees of freedom is characterized by its dissipation rate as Γ_m. The thermal noise operator will be denoted as δa_l, δa_r, and δa_0 for left and right port of transmission line and cavity thermal bath, respectively. For the NEMS, it is δb.

We can further define $\kappa_{total} = \kappa_l + \kappa_r + \kappa_0$ and input field as $a_{in,l} = \alpha_{in,l} + \delta a_{in,l}$ which comprises of the driving field as well as the noise which in incident from the left port. The output field $a_{out,l}$ will always be defined to the right in the transmission geometry as shown in figure 2.5. Substituting $\kappa_{total} = \kappa_l + \kappa_r + \kappa_0$ and $a_{in,l} = \alpha_{in,l} + \delta a_{in,l}$ we can finally write the langevin equation for the MWC and NEMS with their respective coupling constants to the external thermal bath as,

$$\dot{a} = -\frac{i}{\hbar}[a, H_{sys}] - \frac{\kappa_{total}}{2} a - \sqrt{\kappa_l}\alpha_{in,l}(t) - \sum_{k=l,r,0} \sqrt{\kappa_k}\delta a_{in,k}(t) \tag{2.59}$$

For the NEMS with operator denoted as b we can write it's quantum langevin equation when it is thermal equilibrium but weakly coupled to the bath,

$$\dot{b} = -\frac{i}{\hbar}[b, H_{sys}] - \frac{\Gamma_m}{2} b - \sqrt{\Gamma_m}\delta b_{in}(t) \tag{2.60}$$

2.6.1 Solutions to equations of motion

The input field, $a_{in,l}$ comprises of driving field and the noise. The resulting field in the MWC also displaces the equilibrium position of the NEMS with a radiation pressure force. The radiation pressure force, F is simply the derivative of the interaction hamiltonian, $H_{int} = \hbar g_0 (b + b^\dagger) a^\dagger a$ between NEMS and MWC with respect to displacement.

$$F = -\frac{\partial H_{int}}{dx} = \hbar \frac{g_0}{x_{zpf}} a^\dagger a \tag{2.61}$$

In the above equation, F varies linearly with $a^\dagger a$, which is the number of photons in the MWC. The interaction can thus be enhanced by injecting more power in the MWC, thereby increasing the number of photons. The coherent drive thus induces coherent oscillations in the MWC. The cavity field, a will thus have a large component at driving frequency, ω_d and a small fluctuating term δa and the mechanical field can be split into an average shift of the equilibrium position, b_{shift} and the fluctuating term δb. Thus,

$$\begin{aligned} a_{in,l} = \alpha_{in,l} + \delta a_{in,l} = \alpha_{in} e^{-i\omega_d t} e^{-i\phi} + \delta a_{in,l} \\ a = \alpha e^{-i\omega_d t} + \delta a \\ b = b_{shift} + \delta b \end{aligned} \tag{2.62}$$

Putting (2.62) and (2.56) in (2.59) and (2.60) we get,

$$\begin{aligned} -i\omega_d \alpha e^{-i\omega_d t} + \delta\dot{a} = -(i\omega_c + \frac{\kappa_{total}}{2})(\alpha e^{-i\omega_d t} + \delta a) - ig_0(b_{shift} + \delta b + b^*_{shift} + \delta b^\dagger)(\alpha e^{-i\omega_d t} + \delta a) \\ -\sqrt{\kappa_l}(\alpha_{in} e^{-i\omega_d t} e^{-i\phi}) - \sum_{k=l,r,0} \sqrt{\kappa_k}\delta a_{in,k} \end{aligned} \tag{2.63}$$

$$\delta\dot{b} = -(i\Omega_m + \frac{\Gamma_m}{2})(b_{shift} + \delta b) - ig_0(\alpha e^{-i\omega_d t} + \delta a)(\alpha e^{i\omega_d t} + \delta a^\dagger) - \sqrt{\Gamma_m}\delta b_{in} \tag{2.64}$$

We can set all the noise terms to zero to obtain the response of the cavity which is coherent with the drive thus considering all the terms with a large component at ω_d. The above equations will give us coherent amplitude in the MWC i.e. α in terms of α_{in} and change in the equilibrium position of NEMS, b_{shift}.

$$\alpha = \frac{-\sqrt{\kappa_l}\alpha_{in} e^{-i\phi}}{i(\omega_c' - \omega_d) + \kappa_{total}/2} \tag{2.65}$$

$$b_{shift} = \frac{-ig_0\alpha^2}{i\Omega_m + \frac{\Gamma_m}{2}} \tag{2.66}$$

In above equation, $\omega_c' = \omega_c + g_0(b_{shift} + b^*_{shift})$ is the new shifted resonance frequency. From here we will denote the shifted resonance frequency ω_c' as ω_c. The coherent cavity photon numbers in the cavity is given as,

$$n_d = |\alpha|^2 = \frac{\kappa_l |\alpha_{in}|^2}{\kappa_{total}^2/4 + (\omega_c - \omega_d)^2} = \frac{4\kappa_l P_{in}}{\hbar\omega_d(\kappa_{total}^2 + 4(\omega_c - \omega_d)^2)} \tag{2.67}$$

2.6.2 Linearized equations of motion

Now we consider the noise terms in (2.63),

$$\delta\dot{a} = -(i\omega_c + \frac{\kappa_{total}}{2})\delta a - ig_0(\delta b + \delta b^\dagger)\alpha e^{-i\omega_d t} - \sum_{k=l,r,0}\sqrt{\kappa_k}\delta a_{in,k} \tag{2.68}$$

In the above equation we have neglected the terms $\delta a\delta b$ and $\delta a\delta b^\dagger$ which are very small. The term $ig_0(b_{shift} + b^\dagger_{shift})\delta a$ is merged with the term $(i\omega_c + \frac{\kappa_{total}}{2})\delta a$ and we can write $\omega_c = \omega_c + ig_0(b_{shift} + b^\dagger_{shift})$ where $ig_0(b_{shift} + b^\dagger_{shift})$ is very small shift in resonance frequency of MWC.

Similarly we can write the equation of motion for NEMS,

$$\delta\dot{b} = -(i\Omega_m + \frac{\Gamma_m}{2})\delta b - ig_0\alpha(\delta\alpha e^{i\omega_d t} + \delta a^\dagger e^{-i\omega_d t}) - \sqrt{\Gamma_m}\delta b_{in} \tag{2.69}$$

The time dependence of (2.68) and (2.69) can be eliminated by going to a rotating frame. A change of variables is done for cavity δa with new operators given by $\delta a = \delta a e^{-i\omega_d t}$,$\delta a_{in,k} = \delta a_{in,k}e^{-i\omega_d t}$ thus yielding following equations,

$$\delta\dot{a} = (i\Delta - \frac{\kappa_{total}}{2})\delta a - ig_0(\delta b + \delta b^\dagger)\alpha - \sum_{k=l,r,0}\sqrt{\kappa_k}\delta a_{in,k} \tag{2.70}$$

$$\delta\dot{b} = -(i\Omega_m + \frac{\Gamma_m}{2})\delta b - ig_0\alpha(\delta a + \delta a^\dagger) - \sqrt{\Gamma_m}\delta b_{in} \tag{2.71}$$

We will first solve the equation of motion for in-cavity pumping where $\Delta = \omega_d - \omega_c = 0$. We will call this scheme as green pumping from here on.

Green pumping scheme

Writing the linearized equations of motion with $\Delta = 0$ we get,

$$\delta\dot{a} = -\frac{\kappa_{total}}{2}\delta a - ig_0(\delta b + \delta b^\dagger)\alpha - \sum_{k=l,r,0}\sqrt{\kappa_k}\delta a_{in,k} \tag{2.72}$$

$$\delta\dot{b} = -(i\Omega_m + \frac{\Gamma_m}{2})\delta b - ig_0\alpha(\delta a + \delta a^\dagger) - \sqrt{\Gamma_m}\delta b_{in} \tag{2.73}$$

a and b are time-dependent operators, it is simple to solve the above equations in Fourier space. $a[\omega]$ and $b[\omega]$ are the Fourier transforms of a and b respectively. Writing the Fourier transforms of the above equations we get,

$$-i\omega\delta a[\omega] = -\frac{\kappa_{total}}{2}\delta a[\omega] - ig_0(\delta b[\omega] + \delta b^\dagger[\omega])\alpha - \sum_{k=l,r,0}\sqrt{\kappa_k}\delta a_{in,k}[\omega] \tag{2.74}$$

$$-i\omega\delta b[\omega] = -(i\Omega_m + \frac{\Gamma_m}{2})\delta b[\omega] - ig_0\alpha(\delta a[\omega] + \delta a^\dagger[\omega]) - \sqrt{\Gamma_m}\delta b_{in}[\omega] \tag{2.75}$$

While writing the fourier transform we have used $\mathcal{F}(\delta\dot{a}) = -i\omega\delta a[\omega]$ and $\mathcal{F}(\delta\dot{b}) = -i\omega\delta b[\omega]$ where $\mathcal{F}$ denotes the fourier transform operator. Since there are four variables i.e. $\delta a[\omega]$, $\delta b[\omega]$, $\delta a^\dagger[\omega]$, $\delta b^\dagger[\omega]$ we can take the conjugate of above two equations thus satisfying the need for four equations to solve for the variables. We have also defined $g = g_0\alpha$, $\chi_c(\omega) = \dfrac{1}{\frac{\kappa_{total}}{2} - i\omega}$ and $\chi_m(\omega) = \dfrac{1}{\frac{\Gamma_m}{2} - i(\omega - \Omega_m)}$. While taking the conjugate we have used the relation $[\delta a[\omega]]^\dagger = \delta a^\dagger[-\omega]$ and replaced $-\omega$ with ω thus yielding,

$$\delta a^\dagger[\omega] = \left[ig(\delta b[\omega] + \delta b^\dagger[\omega]) - \sum_{k=l,r,0}\sqrt{\kappa_k}\delta a^\dagger_{in,k}[\omega]\right]\chi_c^*(-\omega) \tag{2.76}$$

$$\delta b^\dagger[\omega] = \left[ig(\delta a[\omega] + \delta a^\dagger[\omega]) - \sqrt{\Gamma_m}\delta b^\dagger_{in}[\omega]\right]\chi_m^*(-\omega) \tag{2.77}$$

We can write equations (2.74), (2.75), (2.76) and (2.77) in the matrix notation such that,

$$\begin{pmatrix} 1 & 0 & ig\chi_c(\omega) & ig\chi_c(\omega) \\ 0 & 1 & -ig\chi_c^*(-\omega) & -ig\chi_c^*(-\omega) \\ ig\chi_m(\omega) & ig\chi_m(\omega) & 1 & 0 \\ -ig\chi_m^*(-\omega) & -ig\chi_m^*(-\omega) & 0 & 1 \end{pmatrix}\begin{pmatrix} \delta a[\omega] \\ \delta a^\dagger[\omega] \\ \delta b[\omega] \\ \delta b^\dagger[\omega] \end{pmatrix} = \begin{pmatrix} -\sum_{k=l,r,0}\sqrt{\kappa_k}\delta a_{in,k}[\omega]\chi_c(\omega) \\ -\sum_{k=l,r,0}\sqrt{\kappa_k}\delta a^\dagger_{in,k}[\omega]\chi_c^*(-\omega) \\ -\sqrt{\Gamma_m}\delta b_{in}[\omega]\chi_m(\omega) \\ -\sqrt{\Gamma_m}\delta b^\dagger_{in}[\omega]\chi_m^*(-\omega) \end{pmatrix} \tag{2.78}$$

which can be further written as,

$$\begin{pmatrix} \delta a[\omega] \\ \delta a^\dagger[\omega] \\ \delta b[\omega] \\ \delta b^\dagger[\omega] \end{pmatrix} = A^{-1}\begin{pmatrix} -\sum_{k=l,r,0}\sqrt{\kappa_k}\delta a_{in,k}[\omega]\chi_c(\omega) \\ -\sum_{k=l,r,0}\sqrt{\kappa_k}\delta a^\dagger_{in,k}[\omega]\chi_c^*(-\omega) \\ -\sqrt{\Gamma_m}\delta b_{in}[\omega]\chi_m(\omega) \\ -\sqrt{\Gamma_m}\delta b^\dagger_{in}[\omega]\chi_m^*(-\omega) \end{pmatrix} \tag{2.79}$$

where A^{-1} is the inverse of the matrix $A = \begin{pmatrix} 1 & 0 & ig\chi_c(\omega) & ig\chi_c(\omega) \\ 0 & 1 & -ig\chi_c^*(-\omega) & -ig\chi_c^*(-\omega) \\ ig\chi_m(\omega) & ig\chi_m(\omega) & 1 & 0 \\ -ig\chi_m^*(-\omega) & -ig\chi_m^*(-\omega) & 0 & 1 \end{pmatrix}$

Since we are interested in noise output from MWC we can solve for $\delta a[\omega]$ from above equations,

$$\begin{aligned}\delta a[\omega] = &-\sum_{k=l,r,0}\sqrt{\kappa_k}\delta a_{in,k}[\omega]\chi_c(\omega)X_1 - \sum_{k=l,r,0}\sqrt{\kappa_k}\delta a^\dagger_{in,k}[\omega]\chi_c^*(-\omega)X_2 \\ &-\sqrt{\Gamma_m}\delta b_{in}[\omega]\chi_m(\omega)X_3 - \sqrt{\Gamma_m}\delta b^\dagger_{in}[\omega]\chi_m^*(-\omega)X_4\end{aligned} \tag{2.80}$$

where,

$$X_1 = -\chi_c(\omega)\chi_m(\omega)g^2 + \chi_c(\omega)\chi_m^*(-\omega)g^2 + 1$$

$$X_2 = \chi_c(\omega)g^2(-\chi_m(\omega) + \chi_m^*(-\omega))$$

$$X_3 = -ig\chi_c(\omega)$$

$$X_4 = -ig\chi_c(\omega)$$

We can write the input-output relation for left and right coupling of transmission line to MWC,

$$\begin{aligned} a_{out,l}[\omega] &= a_{in,l}[\omega] + \sqrt{\kappa_l}a[\omega] \\ a_{out,r}[\omega] &= a_{in,r}[\omega] + \sqrt{\kappa_r}a[\omega] \end{aligned} \tag{2.81}$$

We are interested in transmission of the field, we need to calculate $a_{out,r}[\omega]$. The above input output relation can also be written in terms of noise operators such that $\delta a_{out,r}[\omega] = \delta a_{in,r}[\omega] + \sqrt{\kappa_r}\delta a[\omega]$. The state of the mechanical resonator can be characterized through its spectral density. According to the Wiener-Khinchin theorem, the spectral density of any operator is the Fourier transform of the autocorrelation function. So,

$$\begin{aligned} S_{bb}[\omega] &= \int_{-\infty}^{\infty} G_{bb}(t)e^{i\omega t}dt \\ &= \int_{-\infty}^{\infty} \langle b(t)b(0)\rangle e^{i\omega t}dt \\ &= \int_{-\infty}^{\infty} \left\langle b^\dagger(-t)b(0)\right\rangle e^{i\omega t}dt \\ &\int_{-\infty}^{\infty} \left\langle b^\dagger(0)b(t)\right\rangle e^{i\omega t}dt \end{aligned} \tag{2.82}$$

where $G_{bb}(t) = \left\langle b^\dagger(0)b(t)\right\rangle$ is the autocorrelation function. Considering $b[\omega]$ as the fourier transform of $b(t)$ we can write $\left\langle b^\dagger[\omega_2]b[\omega_1]\right\rangle$ in terms of windowed fourier transform of its time dependent analogue.

$$\begin{aligned} \left\langle b^\dagger[\omega_2]b[\omega_1]\right\rangle &= \lim_{T\to\infty}\frac{1}{T}\int_{-T/2}^{T/2}\int_{-T/2}^{T/2} e^{i\omega_2 t_2}e^{i\omega_1 t_1}\left\langle b^\dagger(t_2)b(t_1)\right\rangle dt_2 dt_1 \\ &= \lim_{T\to\infty}\frac{1}{T}\int_{-T/2}^{T/2}\int_{-T/2+t_2}^{T/2+t_2} e^{i\omega_2 t_2}e^{i\omega_1(t_2+\tau)}\left\langle b^\dagger(t_2)b(t_2+\tau)\right\rangle dt_2 d\tau \\ &= \lim_{T\to\infty}\frac{1}{T}\int_{-T/2}^{T/2}\int_{-\infty}^{\infty} e^{i\omega_2 t_2}e^{i\omega_1(t_2+\tau)}\left\langle b^\dagger(0)b(\tau)\right\rangle dt_2 d\tau \\ &= \lim_{T\to\infty}\frac{1}{T}\int_{-T/2}^{T/2} e^{i(\omega_2+\omega_1)t_2}dt_2\int_{-\infty}^{\infty} e^{i\omega_1(\tau)}\left\langle b^\dagger(0)b(\tau)\right\rangle d\tau \\ &= \delta_{\omega_2,-\omega_1}S_{bb}[\omega_1] \end{aligned} \tag{2.83}$$

The spectral density of mechanical resonator with state b can thus be defined as,

$$S_{bb}[\omega] = \left\langle b^{\dagger}[-\omega]b[\omega] \right\rangle \tag{2.84}$$

In order to infer the state of mechanical resonator from measurement, we need to relate it to the output field immediately at the output of the cavity. The spectral density of the noise field output immediately after the cavity is,

$$S_{\delta a_{out,r}\delta a_{out,r}} = \left\langle \delta a^{\dagger}_{out,r}[-\omega]\delta a_{out,r}[\omega] \right\rangle \tag{2.85}$$

We can further derive the spectrum of the output field,

$$\begin{aligned} S_{\delta a_{out,r}\delta a_{out,r}} &= \left\langle \delta a^{\dagger}_{in,r}[-\omega]\delta a_{in,r}[\omega] \right\rangle + \kappa_r \left\langle \delta a^{\dagger}[-\omega]\delta a[\omega] \right\rangle + \\ &\sqrt{\kappa_r} \left\langle \delta a^{\dagger}_{in,r}[-\omega]\delta a[\omega] \right\rangle + \sqrt{\kappa_r} \left\langle \delta a^{\dagger}[-\omega]\delta a_{in,r}[\omega] \right\rangle \\ = \left\langle \delta a^{\dagger}_{in,r}[-\omega]\delta a_{in,r}[\omega] \right\rangle &+ \sum_{k=l,r,0} \kappa_k \left\langle \delta a^{\dagger}_{in,k}[-\omega]\delta a_{in,k}[\omega] \right\rangle \chi^{*}_c(\omega)\chi_c(\omega)X_1X_1^{*}\kappa_r \\ &+ \sum_{k=l,r,0} \kappa_k \left\langle \delta a_{in,k}[-\omega]\delta a^{\dagger}_{in,k}[\omega] \right\rangle \chi^{*}_c(-\omega)\chi_c(-\omega)X_2X_2^{*}\kappa_r \\ &+ \Gamma_m\kappa_r \left\langle \delta b^{\dagger}_{in}[-\omega]\delta b_{in}[\omega] \right\rangle \chi^{*}_m(\omega)\chi_m(\omega)X_3X_3^{*} \\ &+ \Gamma_m\kappa_r \left\langle \delta b_{in}[-\omega]\delta b^{\dagger}_{in}[\omega] \right\rangle \chi^{*}_m(-\omega)\chi_m(-\omega)X_4X_4^{*} \end{aligned} \tag{2.86}$$

The expectation value of noise operators are [22],

$$\left\langle \delta a^{\dagger}_k(t)\delta a_k(t^{'}) \right\rangle = n_{k,th}\delta(t-t^{'}) \tag{2.87}$$

$$\left\langle \delta a_k(t)\delta a^{\dagger}_k(t^{'}) \right\rangle = (n_{k,th}+1)\delta(t-t^{'}) \tag{2.88}$$

where $k = (l, r, 0)$. If the bath is being probed over a narrow range of frequencies around the frequency of interest (ω_c for MWC) which we had done when we applied the Markov approximation, then the above expectation values of the noise operators are a good approximation. $n_{k,th}$ is the thermal occupancy number of the bath. Similarly, for the NEMS, we can write the expectation value of the noise operator δb as,

$$\left\langle \delta b^{\dagger}(t)\delta b(t^{'}) \right\rangle = n_b\delta(t-t^{'}) \tag{2.89}$$

$$\left\langle \delta b(t)\delta b^{\dagger}(t^{'}) \right\rangle = (n_b+1)\delta(t-t^{'}) \tag{2.90}$$

Equation (2.86) can be further expanded into noise spectrums input from left, right, internal or thermally,

$$\begin{aligned} S_{\delta a_{out,r}\delta a_{out,r}} = n_{c,r} &+ \kappa_r^2 n_{c,r}|\chi_c(\omega)|^2|X_1|^2 + \kappa_r^2(n_{c,r}+1)|\chi_c(-\omega)|^2|X_2|^2 \\ &+\kappa_r\kappa_l n_{c,l}|\chi_c(\omega)|^2|X_1|^2 + \kappa_r\kappa_l(n_{c,l}+1)|\chi_c(-\omega)|^2|X_2|^2 \\ &+\kappa_r\kappa_0 n_{c,0}|\chi_c(\omega)|^2|X_1|^2 + \kappa_r\kappa_0(n_{c,0}+1)|\chi_c(-\omega)|^2|X_2|^2 \\ &+\Gamma_m\kappa_r n_b|\chi_m(\omega)|^2|X_3|^2 + \Gamma_m\kappa_r(n_b+1)|\chi_m(-\omega)|^2|X_4|^2 \end{aligned} \tag{2.91}$$

where

$$\begin{aligned} \left\langle \delta a_{in,r}^\dagger[-\omega]\delta a_{in,r}[\omega]\right\rangle = n_{c,r} \text{ and } \left\langle \delta a_{in,r}[-\omega]\delta a_{in,r}^\dagger[\omega]\right\rangle = n_{c,r}+1 \\ \left\langle \delta a_{in,l}^\dagger[-\omega]\delta a_{in,l}[\omega]\right\rangle = n_{c,l} \text{ and } \left\langle \delta a_{in,l}[-\omega]\delta a_{in,l}^\dagger[\omega]\right\rangle = n_{c,l}+1 \\ \left\langle \delta a_{in,0}^\dagger[-\omega]\delta a_{in,0}[\omega]\right\rangle = n_{c,0} \text{ and } \left\langle \delta a_{in,0}[-\omega]\delta a_{in,0}^\dagger[\omega]\right\rangle = n_{c,0}+1 \\ \left\langle \delta b_{in}^\dagger[-\omega]\delta b_{in}[\omega]\right\rangle = n_b \text{ and } \left\langle \delta b_{in}[-\omega]\delta b_{in}^\dagger[\omega]\right\rangle = n_b+1 \end{aligned}$$

$n_{c,r}$, $n_{c,l}$, $n_{c,0}$ are the thermal occupancy of the right port, left port, internal port, thermal baths for MWC and n_b is the thermal occupancy of NEMS. We will first discuss the mechanical noise spectrum in the output noise spectrum. The last two terms in the expression for the output noise spectrum characterizes the mechanical behavior. Expanding the last two terms in the expression for output noise spectrum we get,

$$S = \frac{16\Gamma_m\kappa_r n_b g^2}{\Gamma_m^2 + 4(\omega-\Omega_m)^2}\frac{1}{\kappa_{total}^2+4\Omega_m^2} + \frac{16\Gamma_m\kappa_r(n_b+1)g^2}{\Gamma_m^2+4(-\omega-\Omega_m)^2}\frac{1}{\kappa_{total}^2+4\Omega_m^2} \tag{2.92}$$

While expanding the last two terms of (2.91) we have appoximated $|\chi_c|^2 = \dfrac{1}{(\frac{\kappa_{total}}{2})^2+\omega^2}$ as $|\chi_c|^2 = \dfrac{1}{(\frac{\kappa_{total}}{2})^2+\Omega_m^2}$ since we have made a rotating wave approximation and the derivation is done in a frame rotating with ω_c and thus $\omega \approx \Omega_m$. We can the write (2.92) in the laboratory frame as,

$$S = \frac{16\Gamma_m\kappa_r n_b g^2}{\Gamma_m^2 + 4(\omega_c-\omega-\Omega_m)^2}\frac{1}{\kappa_{total}^2+4\Omega_m^2} + \frac{16\Gamma_m\kappa_r g^2(n_b+1)}{\Gamma_m^2+4(\omega-\omega_c-\Omega_m)^2}\frac{1}{\kappa_{total}^2+4\Omega_m^2} \tag{2.93}$$

The above equation comprises of two lorentzian curves peaked at $\omega_c+\Omega_m$ and $\omega_c-\Omega_m$ as shown in figure 2.6.

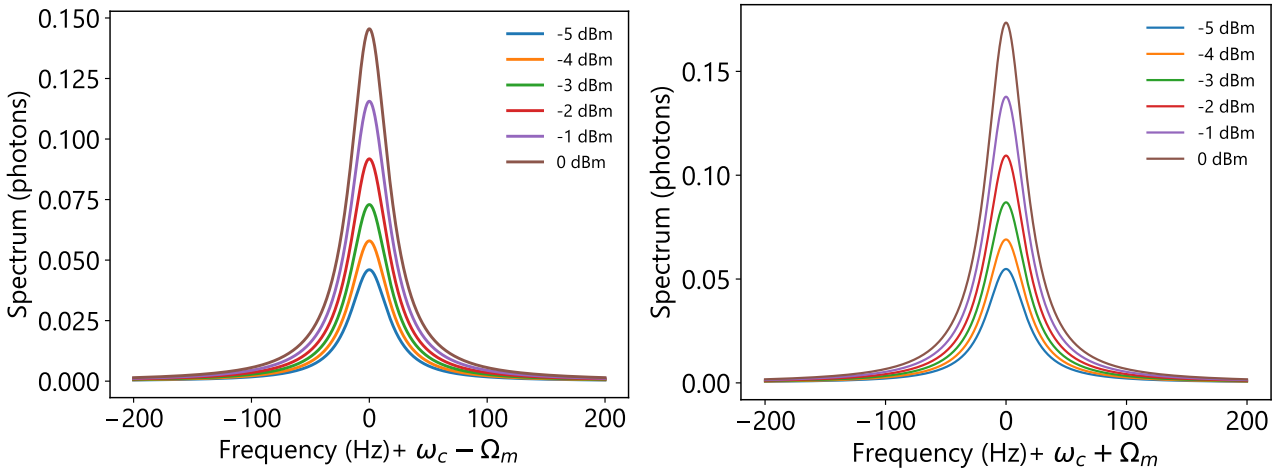

FIGURE 2.6: The mechanical noise spectrum while pumping on the MWC's resonance frequency (green pump) with different pump powers applied at the generator mentioned in the legend. The plots show two sidebands at $\omega_c - \Omega_m$ (left) and $\omega_c + \Omega_m$ (right)

Red pumping scheme

Previously in the green pumping scheme, we derived the spectrum of output cavity response when we pumped at ω_c. Various interesting phenomena can occur if we pump off-resonance particularly at $\omega_c + \Omega_m$ (blue pumping) and $\omega_c - \Omega_m$ (red pumping). We will discuss phenomena such as heating and cooling of mechanical mode after we derive the expression for the cavity output response when pumping red and blue. Starting with (2.70) and (2.71) we write the equations in Fourier space.

$$\delta a[\omega] = \left[-ig(\delta b[\omega] + \delta b^\dagger[\omega]) - \sum_{k=l,r,0} \sqrt{\kappa_k}\delta a_{in,k}[\omega]\right] \chi_c(\omega) \tag{2.94}$$

$$\delta b[\omega] = \left[-ig(\delta a[\omega] + \delta a^\dagger[\omega]) - \sqrt{\Gamma_m}\delta b_{in}[\omega]\right] \chi_m(\omega) \tag{2.95}$$

Again we define the mechanical and cavity susceptibilities as $\chi_m(\omega) = \dfrac{1}{\frac{\Gamma_m}{2} - i(\omega - \Omega_m)}$ and $\chi_c(\omega) = \dfrac{1}{\frac{\kappa_{total}}{2} - i(\omega + \Delta)}$ respectively. We have defined detuning as $\Delta = \omega_d - \omega_c$. If $\Delta < 0$ we call the pumping red detuned, and if $\Delta > 0$, the pumping is blue detuned. We will first derive the output noise spectrum for red detuned pumping while making a rotating wave approximation, and then we will follow up with blue detuned pumping. Since $\Delta \approx -\Omega_m$ for red pumping, the effective frequency of the MWC will be close to mechanical resonance frequency i.e. the cavity susceptibility is approximately $\dfrac{2}{\kappa_{total}}$. In this case terms like $b^\dagger[\omega]$ and $a^\dagger[\omega]$ can

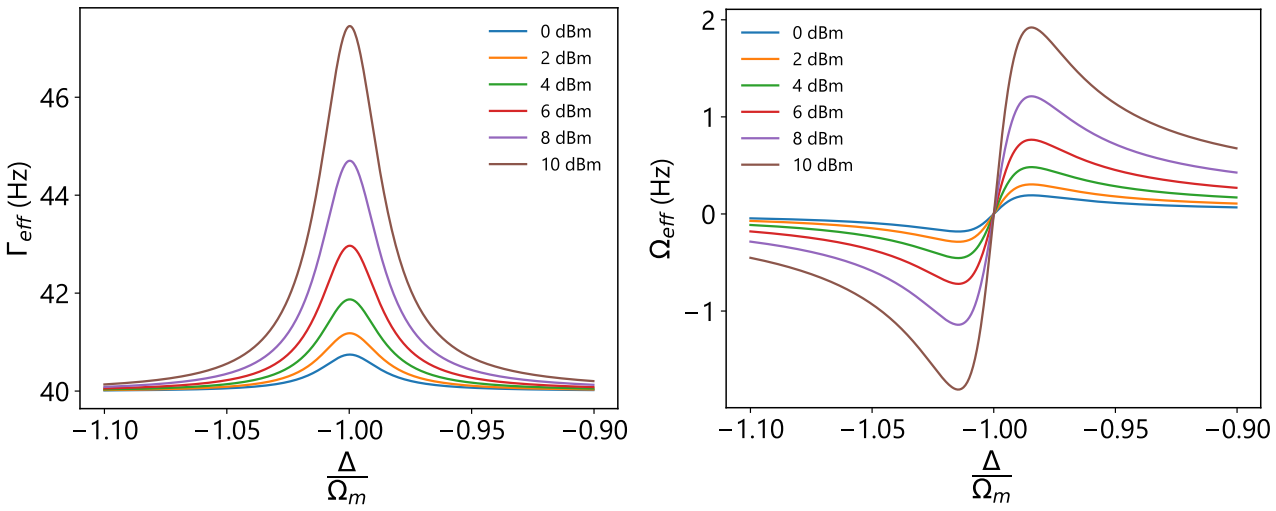

FIGURE 2.7: Theoretical plots for effective linewidth (left) and change in mechanical resonance frequency shift (right) versus relative change in the detuning (red) for different pump powers.

be ignored following rotating wave approximation. Putting (2.94) in (2.95) we get,

$$\delta b[\omega] = \frac{\chi_m(\omega)}{1 + g^2\chi_m(\omega)\chi_c(\omega)} \left[ig\chi_c(\omega) \sum_{k=l,r,0} \sqrt{\kappa_k}\delta a_{in,k}[\omega] - \sqrt{\Gamma_m}\delta b_{in}[\omega] \right] \tag{2.96}$$

Expanding the modified mechanical susceptibility we get,

$$\chi_m(\omega) = \frac{1}{\frac{\Gamma_m}{2} + \frac{g^2\kappa_{total}/2}{\kappa_{total}^2/4 + (\omega+\Delta)^2} - i(\omega - \Omega_m - g^2\frac{\Omega_m + \Delta}{\kappa_{total}^2/4 + 4(\omega+\Delta)^2})} \tag{2.97}$$

The modified dissipation rate is $\Gamma_{eff} = \Gamma_m + \frac{4g^2\kappa_{total}}{\kappa_{total}^2 + 4(\Omega_m+\Delta)^2}$ and the modified mechanical resonance frequency is $\Omega_m' = \Omega_m + \frac{4g^2(\Omega_m+\Delta)}{\kappa_{total}^2 + 4(\Omega_m+\Delta)^2}$. We also approximated $\omega \approx \Omega_m$ as term $\frac{1}{\kappa_{total}^2/4 + (\omega+\Delta)^2}$ is proportional to MWC's susceptibility which varies slowly compared to mechanical response. Thus it can be approximated by its value at the mechanical resonance. Since $\Delta \approx -\Omega_m$ we can write $\Gamma_{eff} = \Gamma_m + \frac{4g^2}{\kappa_{total}}$ and change in the mechanical resonance frequency is negligible. The plots for Γ_{eff} and change in mechanical resonance frequency versus relative change in the red detuning is shown in figure 2.7. When $\Delta \approx -\Omega_m$, χ_c can be approximated as $\frac{2}{\kappa_{total}}$. Putting $\chi_c = \frac{2}{\kappa_{total}}$ in (2.96) and (2.96) in (2.94) we can write $\delta a[\omega]$ in terms of other noise inputs.

$$\delta a[\omega] = \frac{4g^2}{\kappa_{total}^2}\chi_m(\omega)\sum_{k=l,r,i,0}\sqrt{\kappa_k}\delta a_{in,k}[\omega] + \frac{2ig}{\kappa_{total}}\sqrt{\Gamma_m}\chi_m(\omega)\delta b_{in}[\omega] - \frac{2}{\kappa_{total}}\sum_{k=l,r,0}\sqrt{\kappa_k}\delta a_{in,k}[\omega] \tag{2.98}$$

Following the input and output relation as done in Green pumping scheme, the spectral density of the noise field output after the cavity is, $S_{\delta a_{out,r}\delta a_{out,r}} = \left\langle \delta a_{out,r}^{\dagger}[-\omega]\delta a_{out,r}[\omega]\right\rangle$ which can be expanded as,

$$\begin{aligned} S_{\delta a_{out,r}\delta a_{out,r}} = &(\frac{4g^2}{\kappa_{total}^2}\chi_m(\omega) - \frac{2}{\kappa_{total}})(\frac{4g^2}{\kappa_{total}^2}\chi_m^*(\omega) - \frac{2}{\kappa_{total}})\kappa_r\sum_{k=l,r,0}\kappa_k\left\langle \delta a_{in,k}^{\dagger}[-\omega]\delta a_{in,k}[\omega]\right\rangle \\ &+(1+\frac{4g^2}{\kappa_{total}^2}\chi_m(\omega)\kappa_r - \frac{2}{\kappa_{total}}\kappa_r)(1+\frac{4g^2}{\kappa_{total}^2}\chi_m^*(\omega)\kappa_r - \frac{2}{\kappa_{total}}\kappa_r)\left\langle \delta a_{in,l}^{\dagger}[-\omega]\delta a_{in,l}[\omega]\right\rangle \\ &+4g^2\Gamma_m\frac{\kappa_r}{\kappa_{total}^2}|\chi_m(\omega)|^2\left\langle \delta b_{in}^{\dagger}[-\omega]\delta b_{in}[\omega]\right\rangle \end{aligned} \tag{2.99}$$

Since we are only concerned with the mechanical noise spectrum in the output noise spectrum of the cavity, the term relevant to us is $4g^2\Gamma_m\frac{\kappa_r}{\kappa_{total}^2}|\chi_m(\omega)|^2\left\langle \delta b_{in}^{\dagger}[-\omega]\delta b_{in}[\omega]\right\rangle$ which when expanded yields,

$$S = 4\frac{\kappa_r}{\kappa_{total}}\frac{\Gamma_{om}\Gamma_m n_b}{(\Gamma_{om}+\Gamma_m)^2 + 4(\omega-\Omega_m')^2} \tag{2.100}$$

In the above equation $n_b = \left\langle \delta b_{in}^{\dagger}[-\omega]\delta b_{in}[\omega]\right\rangle$ is the thermal occupancy of the mechanical resonator. Ω_m' is the modified resonance frequency due to optical spring effect and $\Gamma_{om} = \frac{4g^2}{\kappa_{total}}$ is the optomechanical damping rate. The spectrum S are in the units of photons and is lorentzian. The lorentian signal has to be greater than the noise floor of the measurement set up in order to be resolved. We can therefore write the spectrum as $S = nf + 4\frac{\kappa_r}{\kappa_{total}}\frac{\Gamma_{om}\Gamma_m n_b}{(\Gamma_{om}+\Gamma_m)^2 + 4(\omega-\Omega_m')^2}$ where nf is the noise floor. As discussed before position spectral density measured by spectrum analyzer $S_x = 2S_{xx} = \frac{4k_bT}{m_{eff}\Omega_m^2}\frac{\Gamma_m}{(\Gamma_{om}+\Gamma_m)^2 + 4(\omega-\Omega_m)^2}$ according to fluctuation-dissipation theorem. Therefore one can derive the position spectral density from the spectral density of the output field by replacing n_b with $\frac{k_bT}{\hbar\Omega_m}$, Γ_{om} with $\frac{4g^2}{\kappa_{total}}$ and finally g with $G\sqrt{n_d}x_{zpf}$ and

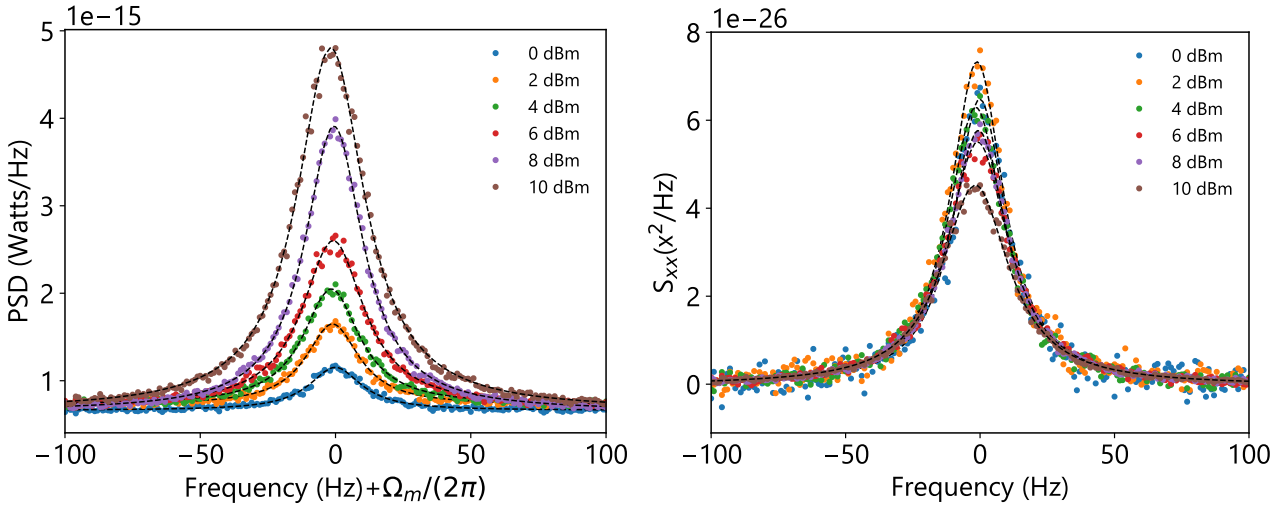

FIGURE 2.8: (left) Spectrum of the output field for red pumping at different pump powers applied at the generator at 250 mK. (right) Position spectral density of the mechanical resonator derived from the spectrum of the output field. One can refer *chapter* 4 for details about the device.

using $x_{zpf} = \sqrt{\dfrac{\hbar}{2m_{eff}\Omega_m}}$,

$$\begin{aligned} S &= nf + 4\frac{\kappa_r}{\kappa_{total}}\frac{\Gamma_{om}\Gamma_m n_b}{(\Gamma_{om}+\Gamma_m)^2 + 4(\omega-\Omega'_m)^2} \\ &= nf + 16\frac{k_b T\kappa_r g^2}{\hbar\Omega_m\kappa_{total}^2}\frac{\Gamma_m}{(\Gamma_{om}+\Gamma_m)^2 + 4(\omega-\Omega'_m)^2} \\ &= nf + 16\frac{k_b T\kappa_r G^2 n_d\hbar}{2m_{eff}\hbar\Omega_m^2\kappa_{total}^2}\frac{\Gamma_m}{(\Gamma_{om}+\Gamma_m)^2 + 4(\omega-\Omega'_m)^2} \\ &= nf + 8\frac{k_b T\kappa_r G^2 n_d}{m_{eff}\Omega_m^2\kappa_{total}^2}\frac{\Gamma_m}{(\Gamma_{om}+\Gamma_m)^2 + 4(\omega-\Omega'_m)^2} \\ &= nf + 2\frac{\kappa_r G^2 n_d}{\kappa_{total}^2}S_x \end{aligned} \tag{2.101}$$

In figure 2.8 we have plotted the spectrum of the output field with different pump power applied at the generator. With the increase in the pump power, we can see an increase in the amplitude of the signal. Also, it is expected that the linewidth of the signal will also increase with an increase in pump power due to damping of the mechanical resonator by radiation pressure forces applied by the microwave cavity. In figure **??** Linewidth of the spectrum of the output field is plotted against the power applied at the cell. Since $\Gamma_{eff} = \Gamma_m + \dfrac{4g_0^2 n_d}{\kappa_{total}}$ one can estimate the value of g_0 by extracting the slope of linear fit in figure 2.9. Here g_0 is approximately 0.45 Hz. Hence $G = g_0 x_{zpf}$ can easily be calculated as we know the dimensions of the device, and consequently, S_{xx} can be retrieved from S. Since the mechanical resonator is

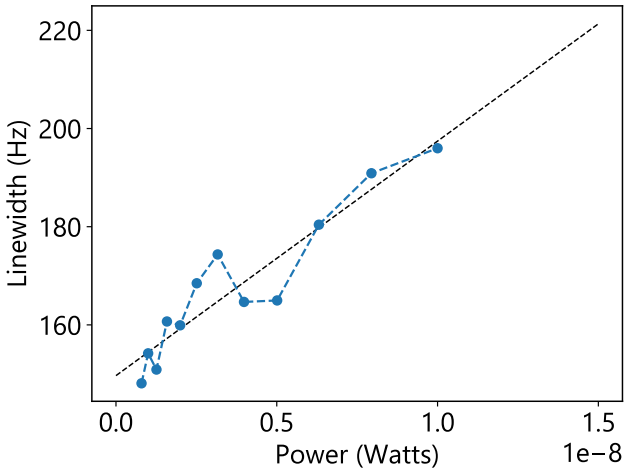

FIGURE 2.9: Linewidth of the spectral density of the output field versus Power applied to the chip. One can refer *chapter* 4 for details about the device.

damped due to radiation pressure forces, it will be cooled subsequently. This cooling process of the mechanical resonator is analogous to the Raman scattering picture. If the pump frequency is optimally detuned from the cavity, in this case, $\omega_d = \omega_c - \Omega_m$, there is a sideband asymmetry due to cavity density of states. The mechanical resonator is either cooled or heated depending on the asymmetry in the power levels of stokes and anti-stokes sidebands. If the power emitted in the stokes sideband is more than the anti-stokes sideband, the mechanical resonator is heated and cooled, if vice versa. For red detuned pumping power emitted in anti-stokes sideband is more than the stokes, so it leads to extraction of phonons from the mechanical resonator. If $\omega_d = \omega_c + \Omega_m$, blue detuned pumping, the power emitted in stokes sideband is more than the anti-stokes sideband leading to heating of mechanical resonator and consequently to self-oscillation if the asymmetry between the sidebands crosses a certain threshold.

2.6.3 Blue pumping scheme

Similarly, we can derive the spectrum of the output field when we are pumping at $\omega_d = \omega_c + \Omega_m$. As we have done for red pumping we will start with equations, (2.70) and (2.71)

$$\delta a[\omega] = \left[-ig(\delta b[\omega] + \delta b^\dagger[\omega]) - \sum_{k=l,r,0} \sqrt{\kappa_k}\delta a_{in,k}[\omega]\right] \chi_c(\omega) \tag{2.102}$$

$$\delta b[\omega] = \left[-ig(\delta a[\omega] + \delta a^\dagger[\omega]) - \sqrt{\Gamma_m}\delta b_{in}[\omega]\right] \chi_m(\omega) \tag{2.103}$$

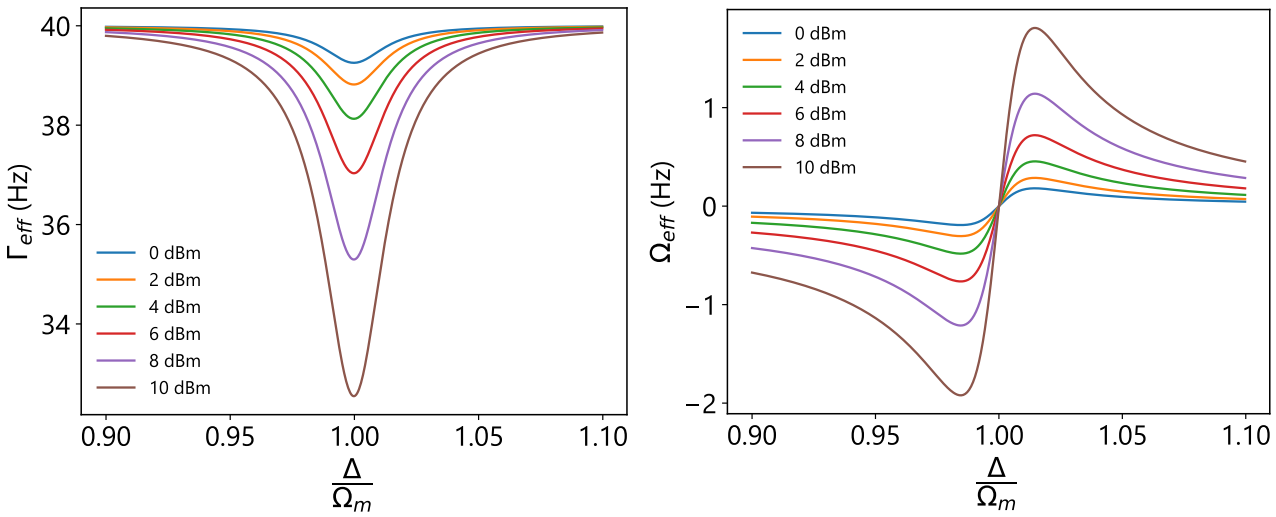

FIGURE 2.10: Theoretical plots for effective linewidth (left) and change in mechanical resonance frequency shift (right) versus relative change in the detuning (blue) for different pump powers. One can refer *chapter* 4 for details about the device.

Following the same procedure we make the rotating wave approximation and eliminate the terms like $a[\omega]$ and $b[\omega]$. Putting (2.102) in (2.103) we get,

$$\delta b[\omega] = \frac{\chi_m(\omega)}{1 - g^2\chi_m(\omega)\chi_c^*(-\omega)} \left[ig\chi_c^*(-\omega) \sum_{k=l,r,0} \sqrt{\kappa_k}\delta a_{in,k}^\dagger[\omega] - \sqrt{\Gamma_m}\delta b_{in}[\omega] \right] \tag{2.104}$$

The modified mechanical susceptibility is $\chi_m(\omega) = \dfrac{\chi_m(\omega)}{1 - g^2\chi_m(\omega)\chi_c^*(-\omega)}$ and the effective dissipation rate is $\Gamma_{eff} = \Gamma_m - \dfrac{4g^2\kappa_{total}}{\kappa_{total}^2 + 4(\Delta - \Omega_m)^2}$. For $\Delta = \Omega_m$ we can write $\Gamma_{eff} = \Gamma_m - \dfrac{4g^2}{\kappa_{total}}$. The mechanical resonance frequency will also be modified due to altered mechanical spring constant given as $\Omega_m^{'} = \Omega_m + \dfrac{4g^2(\Delta - \Omega_m)}{\kappa_{total}^2 + 4(\Delta - \Omega_m)^2}$ We can write $\delta b^\dagger[\omega]$ from equation (2.104),

$$\delta b^\dagger[\omega] = \chi_m^*(-\omega) \left[-ig\chi_c(\omega) \sum_{k=l,r,0} \sqrt{\kappa_k}\delta a_{in,k}[\omega] - \sqrt{\Gamma_m}\delta b_{in}^\dagger[\omega] \right] \tag{2.105}$$

Putting (2.105) in equation (2.102) we get,

$$\delta a[\omega] = \frac{-4g^2}{\kappa_{total}^2}\chi_m^*(-\omega) \sum_{k=l,r,0} \sqrt{\kappa_k}\delta a_{in,k}[\omega] + \frac{2ig}{\kappa_{total}}\sqrt{\Gamma_m}\chi_m^*(-\omega)\delta b_{in}[\omega] - \frac{2}{\kappa_{total}} \sum_{k=l,r,0} \sqrt{\kappa_k}\delta a_{in,k}[\omega] \tag{2.106}$$

Again following the input and output relation as done in subsection 2.6.2, the spectral density of the noise field output after the cavity is, $S_{\delta a_{out,r}\delta a_{out,r}} = \left\langle \delta a_{out,r}^\dagger[-\omega]\delta a_{out,r}[\omega] \right\rangle$ which can be

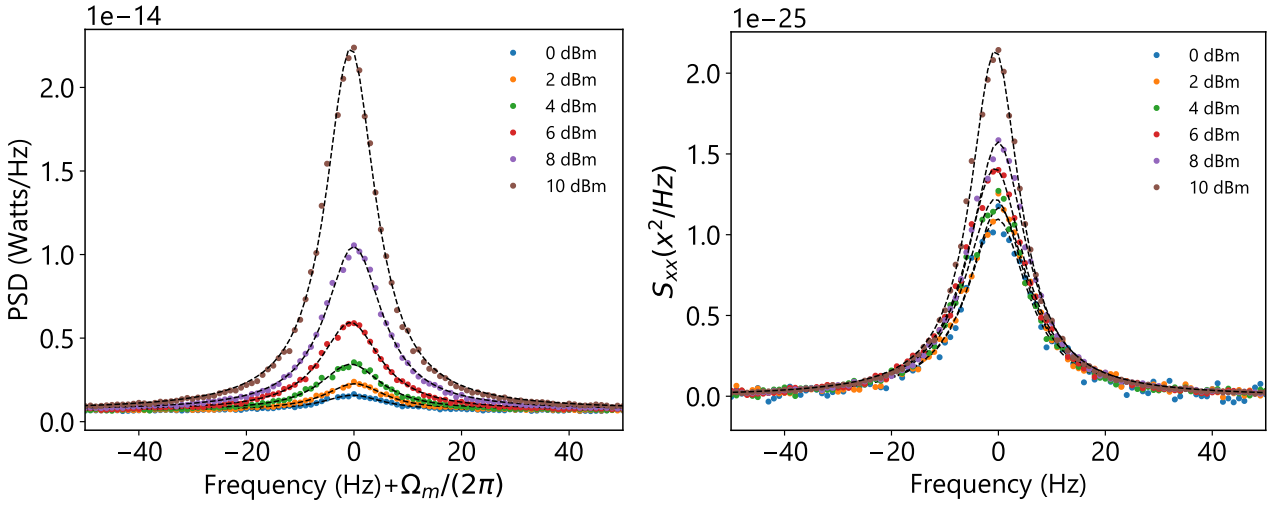

FIGURE 2.11: (left) Spectrum of the output field for blue pumping at different pump powers applied at the generator at 250 mK. (right) Position spectral density of the mechanical resonator derived from the spectrum of the output field. One can refer *chapter 4* for details about the device.

expanded as,

$$S_{\delta a_{out,r}\delta a_{out,r}} = (\frac{-4g^2}{\kappa_{total}^2}\chi_m(-\omega) - \frac{2}{\kappa_{total}})(\frac{-4g^2}{\kappa_{total}^2}\chi_m^*(-\omega) - \frac{2}{\kappa_{total}})\kappa_r \sum_{k=l,r,0} \kappa_k \left\langle \delta a_{in,k}^\dagger[-\omega]\delta a_{in,k}[\omega]\right\rangle$$
$$+(1 - \frac{4g^2}{\kappa_{total}^2}\chi_m(-\omega)\kappa_r - \frac{2}{\kappa_{total}}\kappa_r)(1 + \frac{4g^2}{\kappa_{total}^2}\chi_m^*(-\omega)\kappa_r - \frac{2}{\kappa_{total}}\kappa_r)\left\langle \delta a_{in,l}^\dagger[-\omega]\delta a_{in,l}[\omega]\right\rangle$$
$$+4g^2\Gamma_m\frac{\kappa_r}{\kappa_{total}^2}|\chi_m(-\omega)|^2\left\langle \delta b_{in}[-\omega]\delta b_{in}^\dagger[\omega]\right\rangle \tag{2.107}$$

Once again, we are interested in the mechanical noise spectrum in the output noise spectrum of the cavity. Therefore the term relevant to us if $4g^2\Gamma_m\frac{\kappa_r}{\kappa_{total}^2}|\chi_m(-\omega)|^2\left\langle \delta b_{in}[-\omega]\delta b_{in}^\dagger[\omega]\right\rangle$ which when expanded yields,

$$S = 4\frac{\kappa_r}{\kappa_{total}}\frac{\Gamma_{om}\Gamma_m(n_b+1)}{(\Gamma_{om}+\Gamma_m)^2 + 4(-\omega-\Omega_m')^2} \tag{2.108}$$

In the above equation $n_b + 1 = \left\langle \delta b_{in}[-\omega]\delta b_{in}^\dagger[\omega]\right\rangle$ where n_b is the thermal occupancy of the mechanical resonator. As done previously for the red detuned pumping we can write the mechanical noise spectral density in terms of the position spectral density in this case as,

$$S = nf + 2\frac{\kappa_r}{\kappa_{total}}\frac{G^2 n_d}{\kappa_{total}}S_x \tag{2.109}$$

In figure **??** linewidth of the output, spectrum is plotted against the power applied to the

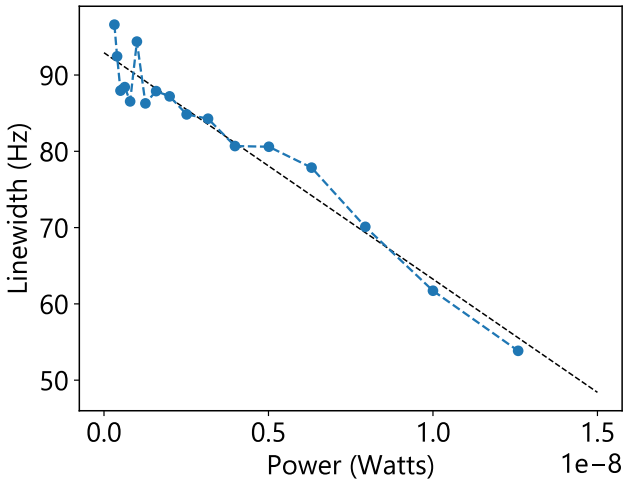

FIGURE 2.12: Linewidth of the spectral density of the output field versus Power applied to the chip. One can refer *chapter* 4 for details about the device.

transmission line. One can extract the slope of the linear fit and estimate the value of g_0, which is approximately 0.45 Hz.

Chapter 3

Experimental Techniques

3.1 Introduction

The continuous demand for faster computing has resulted in the fabrication of billions of transistors on a single chip, e.g., 7980xe has around 7 billion transistors [1]. These chips are typically fabricated in nanofabrication facilities. The nanofabrication technologies have paved the way for faster computing by fabricating smaller transistors and developing novel devices such as superconducting qubits, MEMS/NEMS etc. We will begin this chapter by discussing the fabrication steps of SiN based mechanical resonator (in our case, doubly clamped nanobeam) and superconducting microwave cavity. We will report several problems associated with the fabrication of these devices. We will then talk about the characterization of nanobeams in a 4-kelvin cryostat. We will also delve into different techniques to actuate and detect the motion of nanobeams. In particular, we will outline the ideas behind magneto-motive detection and actuation. The advent of cavity optomechanics has resulted in the sensitive detection of motion of NEMS. The majority of the experiments were done using silicon-nitride-based nanobeam capacitively coupled to the microwave cavity. The sensitivity of detecting the mechanical motion depends mainly on the quality factor of the cavity. Fabricating the superconducting cavities with high-quality factors and subsequently characterizing them is an important step. The characterization of the microwave cavities and the cavity optomechanical experiments were done in a commercial Bluefors dry dilution fridge. We will highlight the basic principles of the dilution cryostat. The circuit diagram for measurement of mechanical noise spectrum will be illustrated with all the calibrations carried out for measurement down to 7 mK. Different pumping schemes, i.e., red, blue, and in-cavity pumping, will also be discussed.

3.2 Fabrication of NEMS

NEMS comprises various suspended mechanical systems like drums, cantilevers, and nanobeams, as shown in figure 3.1. Nanobeams made of silicon nitride clamped at both ends give us an advantage of controlling the stress in the structure, which regulates the resonance frequency

of the mechanical mode. The typical approaches taken for fabricating NEMS are top-down and bottom-up. For NEMS made of graphene or carbon nanotubes (CNTs), the bottom-up approach is generally followed. We take the top-down approach to fabricate NEMS made of solid-state materials (SiN in our case). In a top-down approach, the solid-state material like SiN, Si, Al, etc., is patterned using various lithographic techniques and then etched to release the structure. This section will discuss the fabrication of doubly clamped nanobeams made of SiN with a thin layer of Aluminum on top. The process was optimized at the nanofabrication facility in Institut Néel. This process involves e-beam lithography, e-beam evaporation, reactive ion etching, and XeF_2 etching on a Silicon chip (1 cm^2) covered with 100 nm of Silicon Nitride. All the fabrication steps are illustrated in figure 3.2.

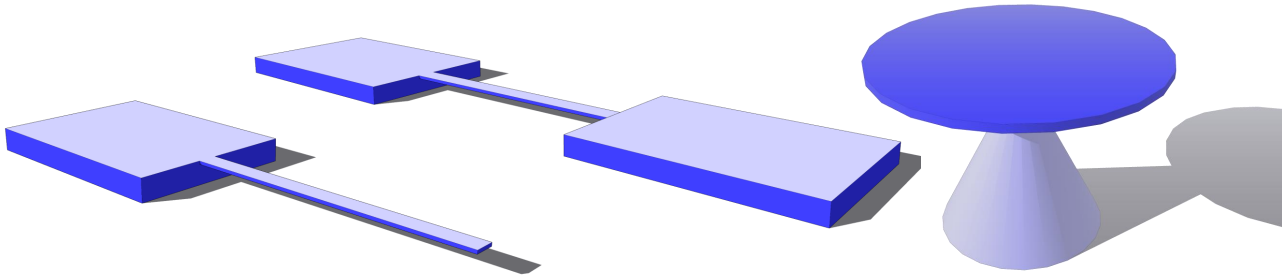

FIGURE 3.1: Different types of NEMS (left) Cantilever (middle) Doubly clamed nanobeam and (right) Toroidal whispering gallery microresonators

3.2.1 e-beam lithography

The 1 cm^2 chip is cleaned with acetone and kept in an ultrasonic bath for 5 minutes to remove any organic/oil residues. The residues left by acetone are cleaned by Isopropyl alcohol (IPA) and the chip is kept in an ultrasonic bath for 5 minutes. The chip is then rinsed with RBS solution and rinsed with abundant de-ionized water, and then exposed with O_2 plasma for 5 minutes. 250 nm of PMMA 4% resist is spin-coated on the chip at a speed of 6000 rpm with an acceleration of 4000 rpm/s for 30 s followed by baking at 180 ^{0}C.

The chip is then exposed with 20 keV electrons in a scanning electron microscope. The nanobeam is exposed with 7.5 μm aperture and the pads with 120 μm aperture. The typical dosage is around 250 $\mu C/cm^2$. The sample is then developed using MIBK: IPA (1:3) solution for 35 s and then put in IPA for 1 minute to stop the further development due to residual MIBK.

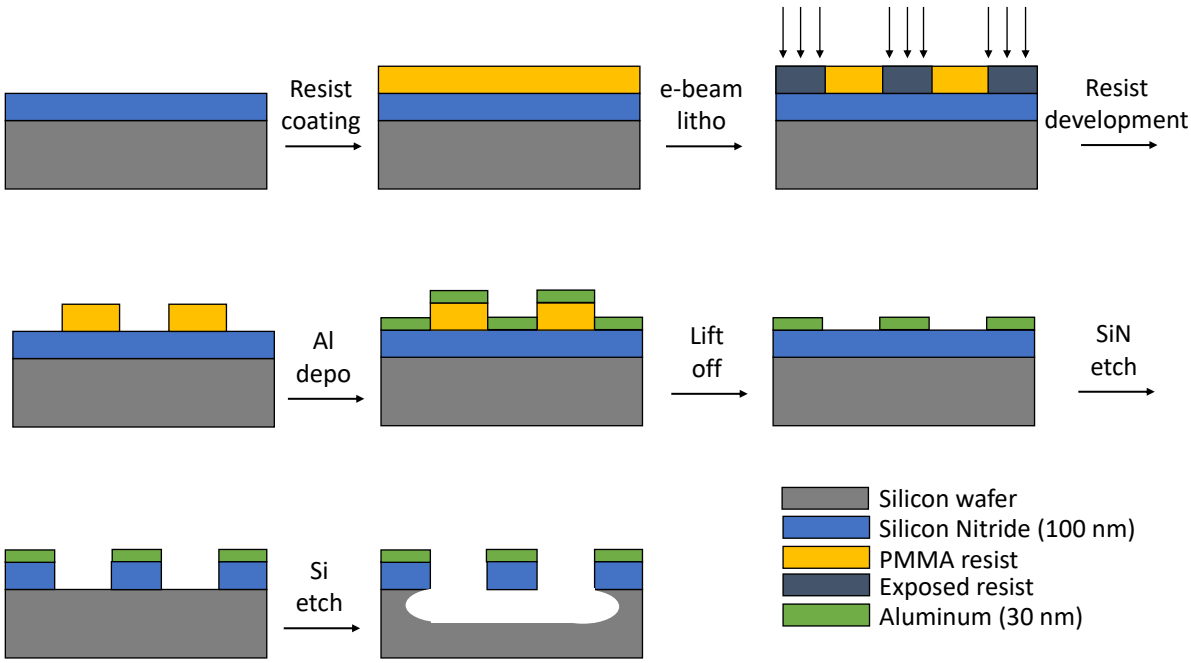

FIGURE 3.2: Schematics of fabrication process of doubly clamped nanobeam

3.2.2 e-beam evaporation

The chip is cleaned in O_2 plasma for 5 seconds to remove any residual resist before evaporating metal on the sample for electrical contacts. 30 nm of Aluminum is deposited on the sample using e-beam evaporation at a pressure of 10^{-6} torr. The rate of deposition is 0.1 nm/s. The metal outside the pattern (deposited on resist) is stripped using a lift-off process where the chip is kept in NMP solution at 80 ^{0}C for at least 2 hours. The lift-off is done by squeezing the NMP solution using a pipette directly on the chip and then slowly agitating the chip in an ultrasonic bath. The process is followed by solvent cleaning (Acetone and IPA) of the chip. One of the problems we faced during the lift-off process is the presence of holes on Aluminum pads, as shown in figure 3.3. The problem mentioned above hampered our process for further processing of chips. Some of these holes were also present on beams, thus causing a discontinuity in the metallic layer. These holes were approximately 200 nm in size. After several tests, we concluded that these holes were caused by Ag particles that we usually use for calibrating the focus while doing e-beam lithography. Once we substituted alignment marks patterned by laser lithography for the silver paste, the holes did not appear on Al pads.

3.2.3 Etching Silicon Nitride and releasing the structure

Silicon-Nitride is etched using reactive Ion etching with SF_6 chemistry. The etching rate is 40 nm/min , and thus etching is done for approximately 2 min 30 s. The etching is anisotropic and

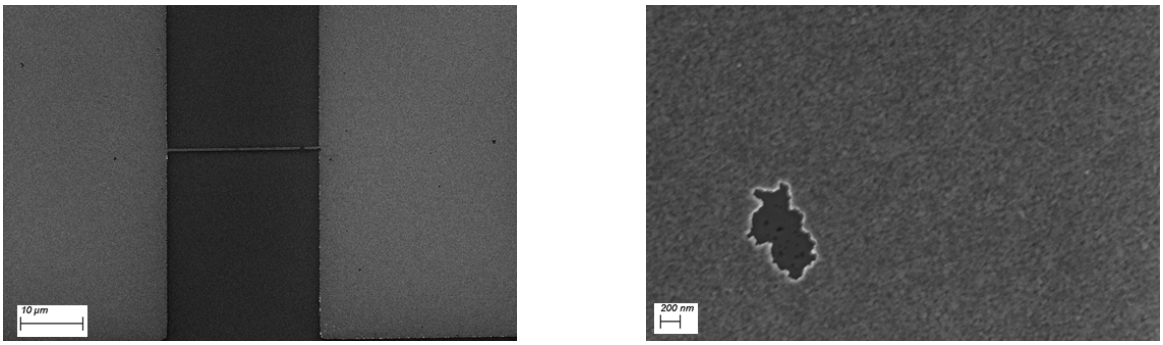

FIGURE 3.3: SEM images of Aluminum pads with holes formed due to Ag particles on chip

selective (does not etch Aluminum) and can also etch silicon. However, the process of etching silicon to release the structure using reactive ion etching is inefficient. The silicon under-etching is done using XeF_2 gas. XeF_2 has high selectivity in favor of silicon compared to silicon nitride. The silicon underneath the clamps is also etched. This part of the clamp is called an undercut. The undercut is also responsible for modifying the resonance frequency of the mechanical mode. The image depicting the released nanobeam with undercut is shown in figure 3.5. Lately, we have been facing problems with the XeF_2 etching. We are constantly seeing the transparent foils being developed underneath the nanobeam shown in figure 3.4. The problem mentioned above is one of the major hindrances in fabricating released nanobeams reliably. A careful study in collaboration with the team of Xin Zhou at IEMN in Lille implied that the foils are caused by a problem with our XeF_2 machine, not a problem with the samples. Several samples were XeF_2 etched in Grenoble or in Lille. The same XeF_2 process was used in each case. Some samples were patterned in Grenoble and others were patterned in Lille. Samples that were XeF_2 etched in Lille never had foils, regardless of where they were patterned. Samples that were XeF_2 etched in Grenoble almost always had foil, independently of where they were patterned. A further possibility, which is difficult to test but seems unlikely, is that the foils are caused by the essential, short RIE etch done just before XeF_2 etching in Grenoble. It is not desirable to make this RIE etch in Lille because the shipping time could allow the formation of oxide that inhibits the subsequent XeF_2 etch.

3.3 Magnetomotive actuation and detection

The various actuation and detection schemes for measuring the motion of NEMS are capacitive actuation and detection, dielectric detection, piezoelectric technique, and frequency modulation techniques for graphene and CNT's based mechanical resonators. The magnetomotive scheme is also a well-established technique for actuation and detection of viscometers, bolometers in superfluid ^{3}He community. Cleland and Roukes introduced this technique for actuating and

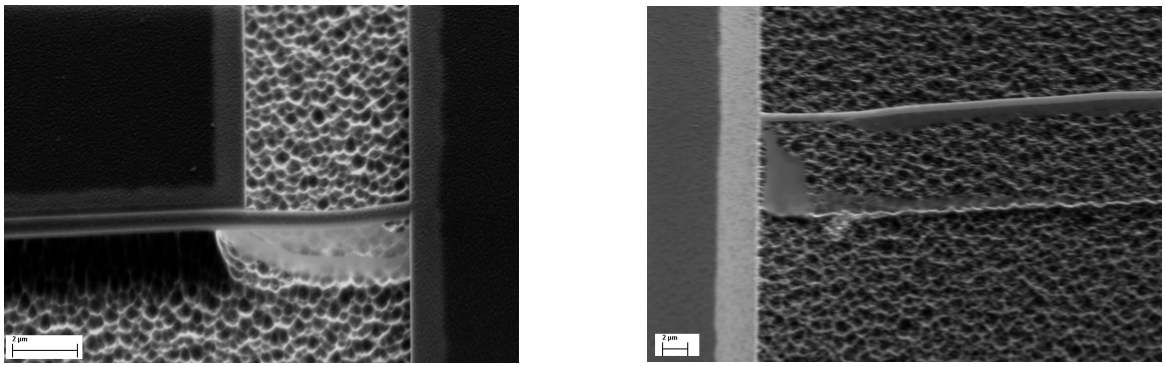

FIGURE 3.4: SEM images showing transparent foil like material hanging beneath the nanobeam

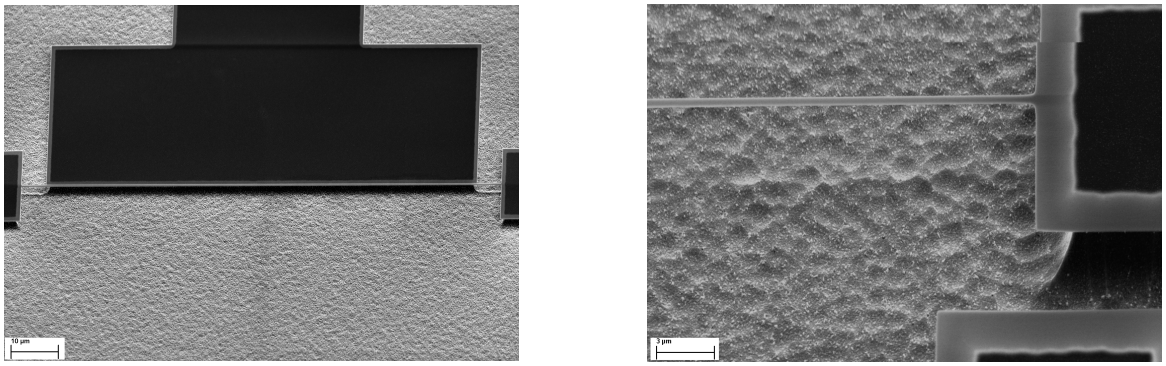

FIGURE 3.5: SEM images of the final released nanobeam with undercut

detecting NEMS [21]. Since our NEMS is made of SiN, which is amorphous and dielectric, we deposit a thin layer of Al on top of the SiN. We pass a current $I(t)$ through this thin layer of Al on suspended SiN nanobeam (along z direction as shown in figure 3.6) in a constant magnetic field, $B(y)$ (along y direction) which is perpendicular to nanobeam, the nanobeam experience a Lorentz force, F_{nems} along direction x (figure 3.6). We assume the current applied to be sinusoidal with a frequency close to the resonance frequency of nanobeam's mechanical mode. For simplicity, we assume the resonance frequency of the fundamental mode of the mechanical resonator. The length of the nanobeam is l. For the infinitesimal length of nanobeam $dl(z)$, the infinitesimal force will be,

$$dF_{nems} = I(t)dl(z) \times B(y) \tag{3.1}$$

We can further approximate $dl(z) \approx \psi(z)dz$ if the maximum displacement of the beam in direction x is much less than its length where $\psi(z)$ is the shape factor discussed in section 2.2 of *chapter 2*. Therefore integrating equation 3.1 over the length of the beam, we get total force as,

$$F_{nems} = I(t)lB \tag{3.2}$$

where $\xi = \int_{-l/2}^{l/2} \psi(z)dz$ is a factor that accounts for the fact that force is not uniform along the length of nanobeam. Due to the sinusoidal dependence of Lorentz force, the motion of NEMS will also be sinusoidal. The displacement of beam will be $u(z,t) = \psi(z)x(t)$ where $x(t)$ is the maximum displacement of the beam. An effective area is swept between the instantaneous and rest position of the beam. The magnetic flux across this differential area dA will be,

$$d^2\phi(t) = BdA(t) \tag{3.3}$$

We approximate the differential area as $dA(t) \approx \psi(z)dzx(t)$ for small maximum displacement. Integrating equation 3.3 along the length of beam we get the differential magnetic flux as,

$$d\phi(t) = \xi lBdx(t) \tag{3.4}$$

According to Faraday's law time dependent magnetic flux will induce an electromotive force given as,

$$e(t) = -\frac{d\phi}{dt} = -\xi lB\frac{dx}{dt} = -\xi lB\dot{x}(t) \tag{3.5}$$

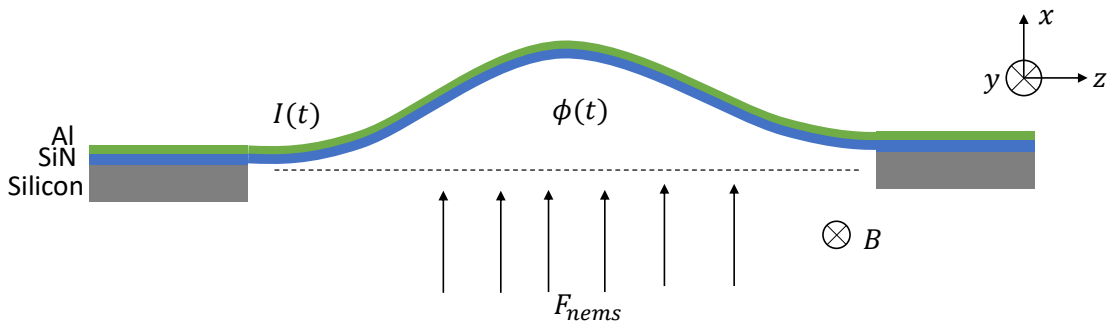

FIGURE 3.6: Schematic representation of the magnetomotive actuation and detection principle for the first flexural mode

3.3.1 Electrical circuit

The circuit diagram for magnetomotive actuation and detection is shown in figure 3.8. The sinusoidal voltage is applied using Tektronix AF3252 arbitrary function generator to NEMS with resistance R_{nems}. We have also added a bias resistor R_{bias} in the injection line to protect NEMS with low resistance. Typically, the resistance of NEMS of length 100 μm is 1 kΩ. The voltage $V(t)$ across NEMS is detected using the Stanford SR844 lockin amplifier. The current,

$I(t)$ flowing through NEMS according to ohm's law is given by,

$$I(t) = \frac{V_a(t) + e(t)}{R_{bias} + R_{nems}} \tag{3.6}$$

where $V_a(t)$ is the applied voltage by function generator. Therefore the force on NEMS will be $F_{nems} = \xi Bl \frac{V_a(t) + e(t)}{R_{bias} + R_{nems}}$. The temporal evolution of NEMS $x(t)$ can be derived by solving the equation of motion of the damped harmonic oscillator.

$$m_{eff} \frac{\partial^2 x(t)}{\partial t^2} + m_{eff} \Gamma_m \frac{\partial x(t)}{\partial t} + m_{eff} \Omega_m^2 x(t) = F_{nems} \tag{3.7}$$

Putting F_{nems} in 3.7 we get,

$$m_{eff} \frac{\partial^2 x(t)}{\partial t^2} + m_{eff} \Gamma_m \frac{\partial x(t)}{\partial t} + m_{eff} \Omega_m^2 x(t) = \xi Bl \frac{V_a(t) - \xi lB\dot{x}(t)}{R_{bias} + R_{nems}} \tag{3.8}$$

Since the motion of NEMS is sinusoidal the displacement $x(t)$ can be written as $x(t) = x_0 e^{-i\omega t}$ and $V_a(t) = V_0 e^{-i\omega t} e^{-i\phi}$ where ϕ is the phase difference between the voltage applied and the motion of NEMS. Solving for x_0 we get,

$$x_0 = \frac{\xi B L V_0 e^{-i\phi}}{m_{eff}(R_{bias} + R_{nems})} \frac{1}{(\Omega_m^2 - \omega^2) - i\omega\Omega_m Q^{-1}} \tag{3.9}$$

In the above equation, Q is the quality factor of NEMS, which is composed of intrinsic dissipation and dissipation due to the electric circuit.

$$Q^{-1} = Q_{electric}^{-1} + Q_{intrinsic}^{-1} \tag{3.10}$$

where $Q_{electric}^{-1} = \frac{\xi^2 B^2 l^2}{m_{eff}\Omega_m(R_{bias} + R_{nems})}$ and $Q_{intrinsic}^{-1} = \frac{\Omega_m}{\Gamma_m}$.

x_0 can be decomposed into real and imaginary parts which can be measured by lock in amplifier separately.

3.3.2 Cryogenics and Themometry

The sample is glued on a copper PCB using GE varnish, which facilitates thermalization. The chip is then wire bonded to the electrical tracks on PCB. The electrical tracks are further connected to RF injection and detection lines. The injection line connected to the function generator is used for driving the NEMS. The detection line is connected to the lock-in amplifier. The PCB is mounted on a copper plate which is part of stainless steel flange. The stainless steel flange is then connected to the lower part of the dipstick as shown in figure 3.9. The lower

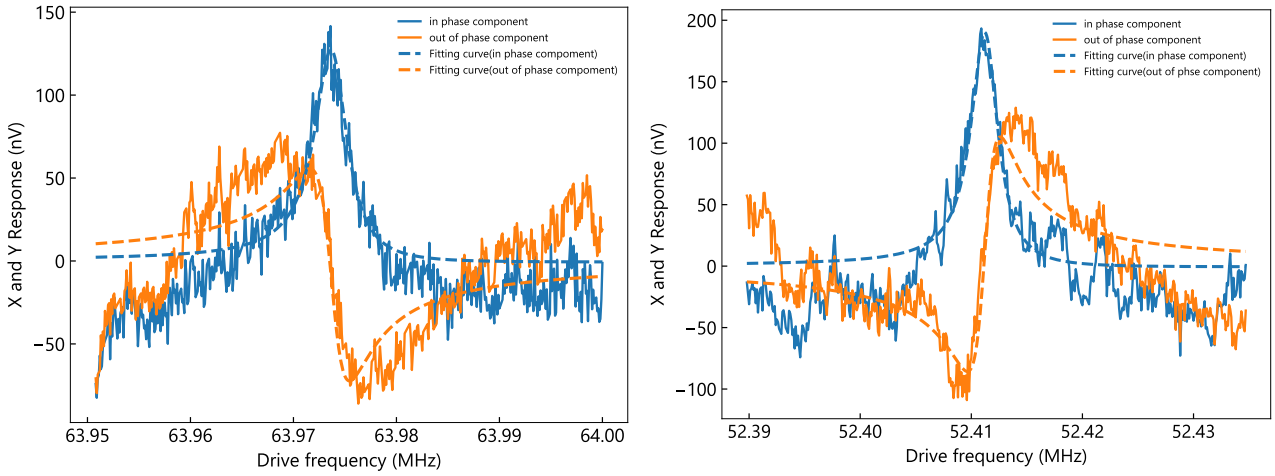

FIGURE 3.7: Typical responses of two quadratures for nanobeams of length a) 4.8 μm and b) 5.7 μm

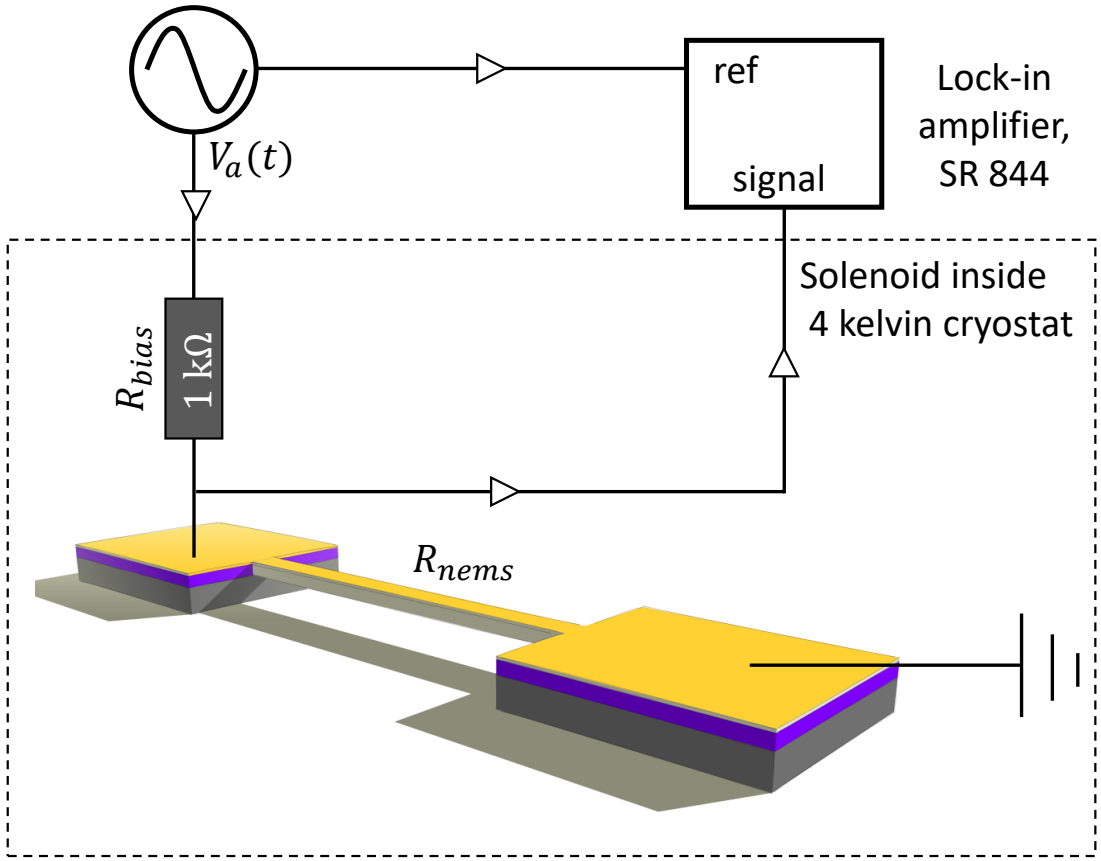

FIGURE 3.8: Schematic showing the electric circuit for actuation and detection of NEMS using magnetomotive technique

part of the dipstick also includes a solenoid. The upper part of the dipstick is connected to a room temperature flange. The cell containing the sample is sealed with an indium ring.The room temperature flange includes connectors for RF injection and detection, thermometer, and

heater. The cell containing the sample is sealed with an indium ring. The dipstick is then put inside a ^{4}He cryostat. The closed-cell is then pumped down to 1e-3 mbar using a rotary vane pump and further down to 1e-6 mbar using turbopump. The measurement of the sample under vacuum prevents the gas damping of the NEMS. The cryostat is made of stainless steel with two compartments for liquid nitrogen and ^{4}He separated by a vacuum space.The role of vacuum space is to minimize heat conduction through gas between room temperature, the liquid nitrogen reservoir and the helium reservoir. Liquid nitrogen is used for precooling and acts as a radiation shield for the inner part, thus lowering the ^{4}He boiling rate. The working temperature is 4.2 K which can be further reduced by pumping on the ^{4}He bath. However, pumping on ^{4}He bath is quite uneconomical as 40 % of liquid ^{4}He has to be evaporated to cool it from 4.2 K to 1.3 K due to significant change of its specific heat in this temperature range.

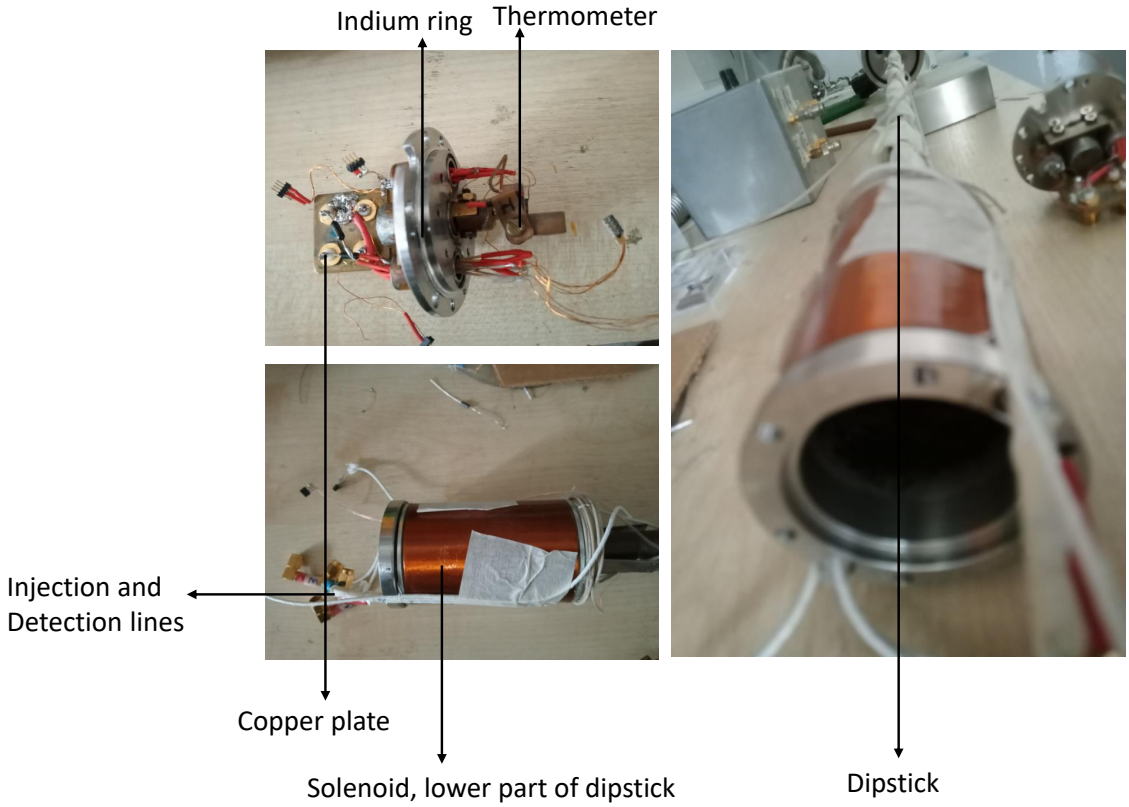

FIGURE 3.9: Image showing the part of the experimental dipstick which in immersed in ^{4}He cryostat

3.4 Superconducting microwave resonators

The microwave resonators in our experiments operate in the 4-8 GHz band designated as C band by IEEE. Operating at such high frequencies reduces the thermal excitation of our resonators.

2D geometries are preferred if we want to couple mechanical resonators to microwave cavities. Also, planar structures are easy to fabricate in the cleanroom. We have primarily used a coplanar waveguide resonator (CPW) in this work. In CPW, we have a central conductor with ground planes on both sides. The signal is fed to the resonator by capacitively coupling a CPW transmission line with an impedance of 50 ohms matched to the external feedline circuit.

3.4.1 Transmission lines

A transmission line supports the propagation of an electromagnetic wave. For TEM mode, the infinitesimal element of the transmission line can be modeled by an elementary circuit as shown in figure 3.10 where L and C are the inductance and capacitance of transmission line per unit length [61]. Let a wave is incident from a source at $z < 0$ as shown in figure 3.11 of the form $V(z) = V_0 e^{-i\beta z}$ where $\beta = \omega\sqrt{LC}$ is the propagation constant and ω is the applied frequency. The ratio of voltage to current for a traveling wave is $Z_0 = \sqrt{\frac{L}{C}}$, which is the characteristic property of any transmission line. Let us consider the line terminated by impedance Z_L (figure 3.11). At the terminal point of the line, the ratio of voltage to current must be Z_l. The total voltage on the line can be written in terms of incident and reflected wave.

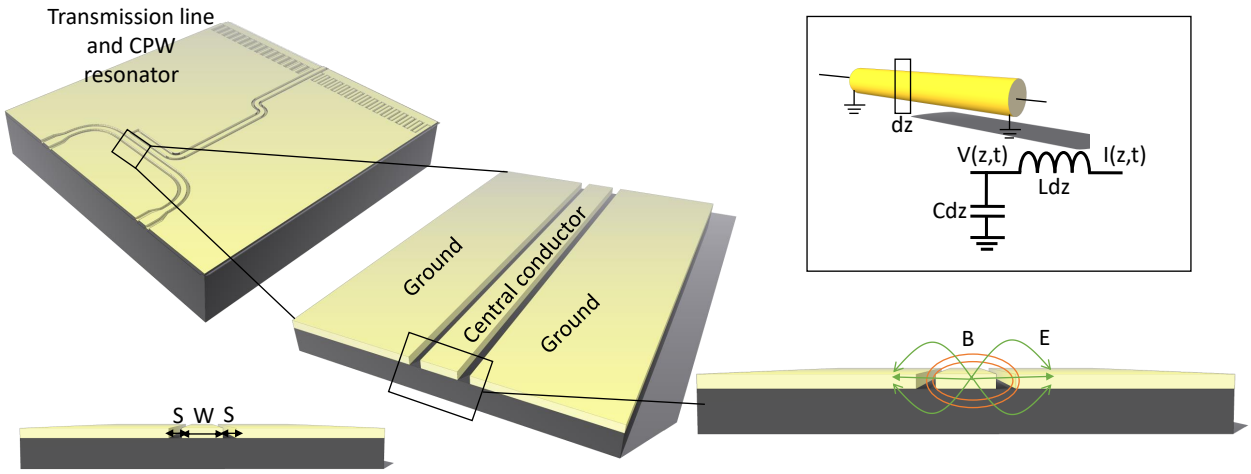

FIGURE 3.10: Schematic showing the transmission line coupled to CPW resonator (inset: Circuit model of an infinitesimal part of transmission line)

$$V(z) = V_0^+ e^{-i\beta z} + V_0^- e^{i\beta z} \tag{3.11}$$

The total current at any point on the circuit is,

$$I(z) = \frac{V_0^+}{Z_0} e^{-i\beta z} - \frac{V_0^-}{Z_0} e^{i\beta z} \tag{3.12}$$

However at $z = 0$ we have,

$$Z_l = \frac{V(0)}{I(0)} = \frac{V_0^+ + V_0^-}{V_0^+ - V_0^-} Z_0 \tag{3.13}$$

We can thus write the voltage reflection coefficient as,

$$\Gamma = \frac{V_0^-}{V_0^+} = \frac{Z_l - Z_0}{Z_l + Z_0} \tag{3.14}$$

Let the source be at $z = -l$. The input impedance seen by the source is,

$$Z_{in} = \frac{V(-l)}{I(-l)} = \frac{1 + \Gamma_l e^{-2i\beta l}}{1 - \Gamma_l e^{-2i\beta l}} Z_0 \tag{3.15}$$

Putting the value of $\Gamma_l = \frac{V_0^-}{V_0^+} = \frac{Z_l - Z_0}{Z_l - Z_0}$ we get,

$$Z_{in} = \frac{Z_l + iZ_0 tan(\beta l)}{Z_0 + iZ_l tan(\beta l)} Z_0 \tag{3.16}$$

The characteristic impedance of the external feedline circuit in our experiments is 50 Ω matched

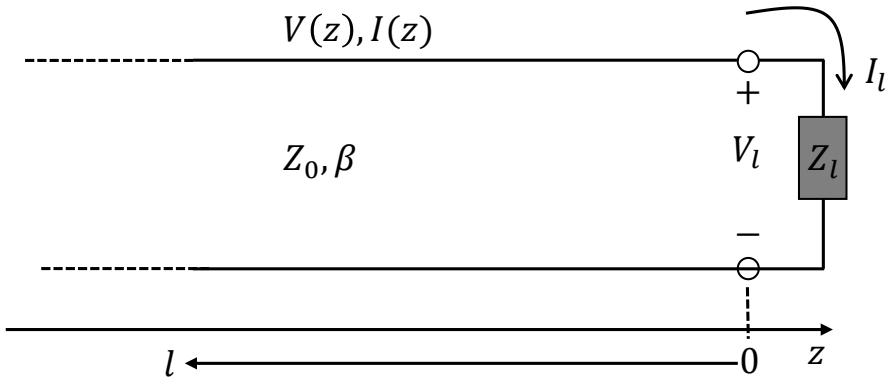

FIGURE 3.11: A transmission line terminated in a load impedance Z_l)

to the output impedance of the source (Microwave generators) and the input impedance of the measurement apparatus such as spectrum analyzer and lock-in amplifier. In most of our experiments, we are concerned with transmission measurement. Therefore it is imperative to avoid any reflections from any part of the circuit. We thus design our coplanar waveguide(CPW) transmission line to have a characteristic impedance of 50 Ω. Let W be the width of the central conductor and S be the spacing between the ground plane and the central conductor of the CPW transmission line. The impedance of the transmission line for the infinitely thick dielectric

substrate is given by [31],

$$Z_0 = \frac{30\pi}{\epsilon_{re}} \frac{K^{'}(k_1)}{K(k_1)} \tag{3.17}$$

where $\epsilon_{re} = \frac{\epsilon_r + 1}{2}$, ϵ_r is the dielectric constant of the substrate. The ration $\frac{K^{'}(k_1)}{K(k_1)}$ depends of the value of k_1 which in turn depends of S and W.

$$k_1 = \frac{S}{S + 2W} \tag{3.18}$$

$$\begin{aligned} \frac{K^{'}(k_1)}{K(k_1)} &= \frac{\pi}{ln\left[2(1+\sqrt{k_1^{'}})/(1-\sqrt{k_1^{'}})\right]} \text{ for } 0 <= k_1 <= 0.707 \\ \frac{K^{'}(k_1)}{K(k_1)} &= \frac{ln\left[2(1+\sqrt{k_1})/(1-\sqrt{k_1})\right]}{\pi} \text{ for } 0.707 < k_1 <= 1 \end{aligned} \tag{3.19}$$

Also $k_1^{'} = \sqrt{1 - k_1^2}$. The derivation is done using Schwarz-Christoffel conformal transformation. In this thesis, we are concerned with two designs shown in figure 3.12. The parameters specifying the width of the central conductor, spacing between the central conductor and the ground plane, dielectric constant of the substrate, and the impedance is shown in the table below.

Designs	W	S	ϵ_r	Z_0
1	10 μm	5 μm	11.9	50 Ω
2	150 μm	94 μm	11.9	50 Ω

TABLE 3.1: Table showing parameters of the transmission lines

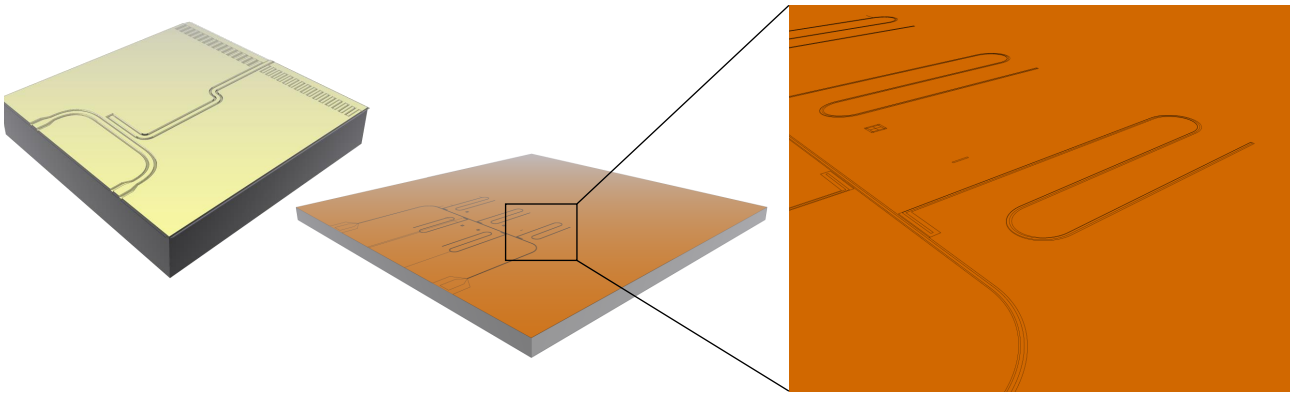

FIGURE 3.12: Designs of MWCs, left) open $\frac{\lambda}{2}$ MWC corresponding to entry 2 in the table above right) Shorted $\frac{\lambda}{4}$ MWC, the end far from the transmission line is shorted

3.4.2 CPW resonators

In the previous section, we discussed the CPW transmission line and the parameters governing its impedance. In this section, we will investigate various designs and properties of microwave resonators. These resonators are coupled capacitively or inductively coupled to the transmission line. There are different types of resonators, such as rectangular waveguide cavity resonators, circular waveguide resonators, microstrip resonators, coplanar waveguide resonators (CPW). Discussing different resonators is beyond the scope of this thesis since our designs are primarily CPW type. The CPW resonator is just a piece of CPW transmission line with a central conductor and ground plane on both sides with open or grounded terminals. The characteristic impedance of these resonators is 50 Ω. From the practical point of view, the design of the CPW resonator is classified mainly into $\lambda/2$ and $\lambda/4$ types. Also, these resonators are modeled as parallel RLC circuits. Before discussing the $\lambda/2$ and $\lambda/4$ type resonators, it is essential to highlight the properties of a parallel RLC circuit to make an analogy with these resonators [61]. For a parallel RLC circuit shown in figure 3.13 the input impedance of the circuit is,

$$Z_{in} = \left(\frac{1}{R} + \frac{1}{i\omega L} + i\omega C\right)^{-1} \tag{3.20}$$

The input impedance can be simplified by letting $\omega = \omega_0 + \Delta\omega$ where $\Delta\omega$ is very small using taylor's expansion,

$$Z_{in} \approx \frac{R}{1 + 2i\Delta\omega RC} \tag{3.21}$$

The input impedance of a shorted transmission line of length l is

$$Z_{in} = Z_0 \tanh(\alpha + i\beta)l = Z_0 \frac{1 - i\tanh\alpha l \cot\beta l}{\tanh\alpha l - i\cot\beta l} \tag{3.22}$$

where $\gamma = \alpha + i\beta$ is the complex propagation constant and $Z_0 = \sqrt{\frac{L}{C}}$ is the characteristic impedance of the transmission line. Assuming $l = \lambda/4$ and low loss transmission line such that $\alpha l << 1$, then $\tanh\alpha l \approx \alpha l$. Also let $\omega = \omega_0 + \Delta\omega$ where $\Delta\omega$ is small. Then,

$$\beta l = \frac{\omega l}{v_p} = \frac{\omega_0 l}{v_p} + \frac{\Delta\omega l}{v_p} = \frac{\pi}{2} + \frac{\pi\Delta\omega}{2\omega_0} \tag{3.23}$$

where v_p is the phase velocity and $\cot\beta l \approx \frac{-\pi\Delta\omega}{2\omega_0}$ Therefore the input impedance can now be written as,

$$Z_{in} = Z_0 \frac{1 + i\alpha l\pi\Delta\omega_0/2\omega_0}{\alpha l + i\pi\Delta/2\omega_0} \approx \frac{Z_0}{\alpha l + i\pi\Delta\omega/2\omega_0} \tag{3.24}$$

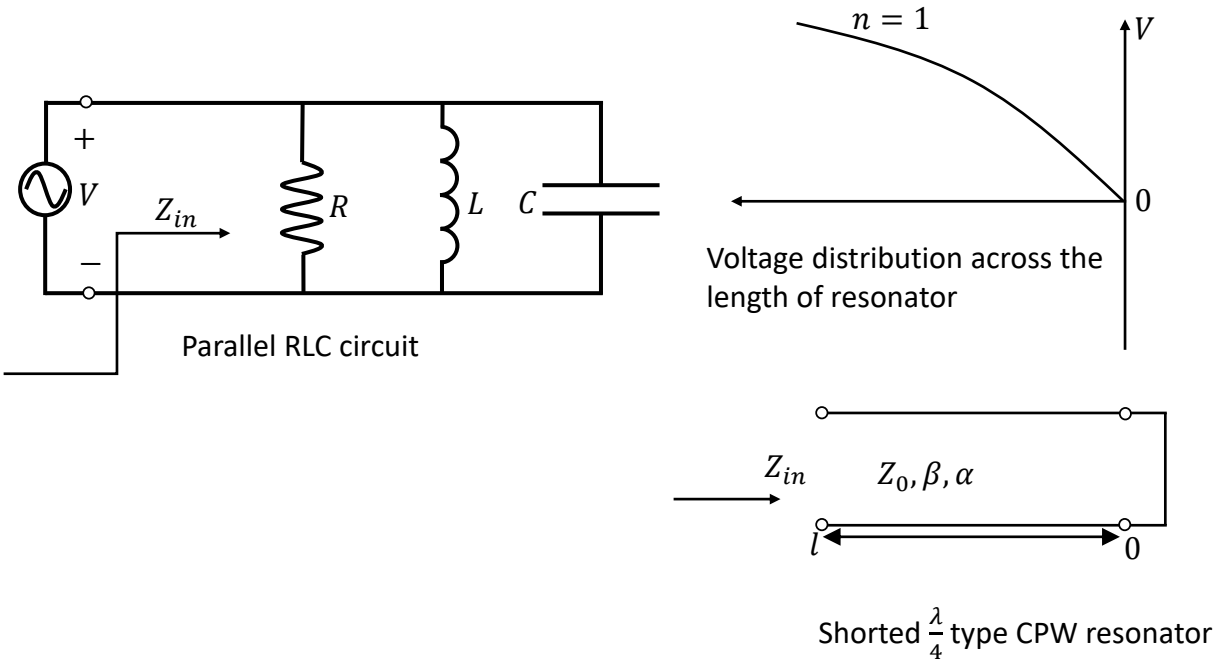

FIGURE 3.13: Voltage distribution across the length of shorted $\frac{\lambda}{4}$ resonator for the fundamental mode. Voltage is maximum at the one end and zero at the shorted end. Also the resonator can be modeled as parallel RLC circuit

The above equation is of the same form as equation 3.21 where $R = \frac{Z_0}{\alpha l}$, $C = \frac{\pi}{4\omega_0 Z_0}$ and $L = \frac{4Z_0}{\pi\omega_0}$.

Similarly we can write the input impedance of an open transmission line of length as

$$Z_{in} = Z_0 \coth(\alpha + i\beta)l = Z_0 \frac{1 + i \tanh \alpha l \tan \beta l}{\tanh \alpha l + i \tan \beta l} \tag{3.25}$$

Using the same approximations as above and considering $l = \frac{\lambda}{2}$ we can approximate input impedance as,

$$Z_{in} \approx \frac{Z_0}{\alpha l + i\pi\Delta\omega/\omega_0} \tag{3.26}$$

where $R = \frac{Z_0}{\alpha l}$, $C = \frac{\pi}{2\omega_0 Z_0}$ and $L = \frac{2Z_0}{\pi\omega_0}$

We are concerned with two designs of CPW resonators as shown in figure 3.12. Design 1, where there many CPW resonators coupled to the same transmission line, is shorted $\frac{\lambda}{4}$ type,

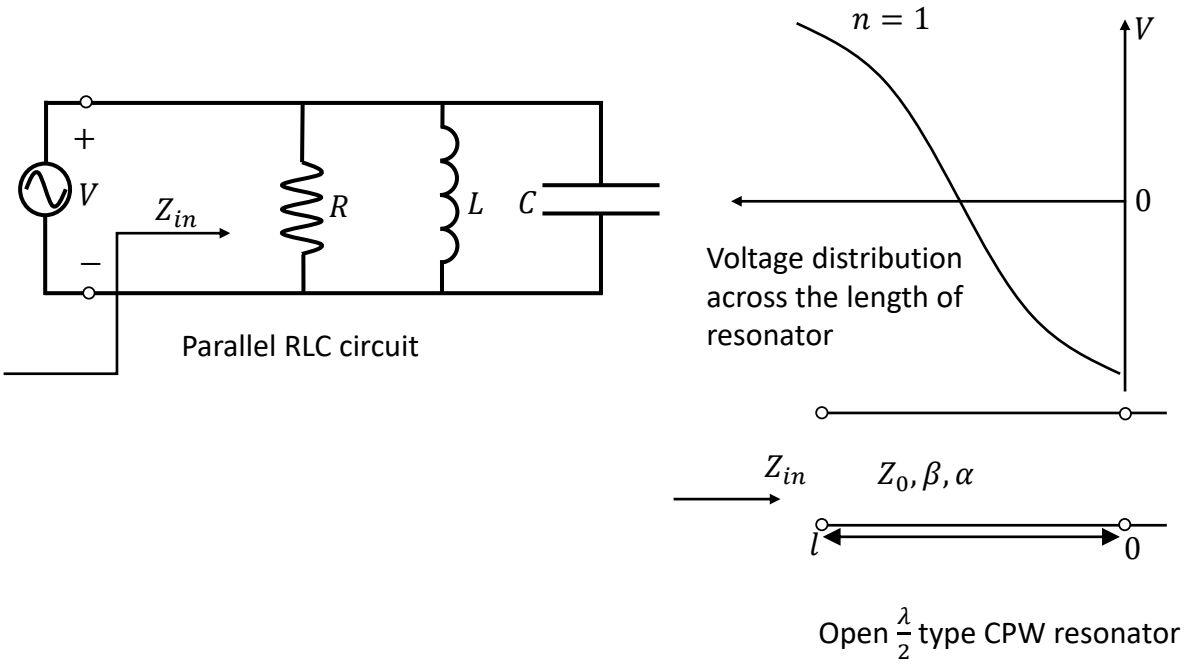

FIGURE 3.14: Voltage distribution across the length of open $\frac{\lambda}{2}$ resonator for the fundamental mode. Voltage is maximum at the two ends of resonator. Also the resonator can be modeled as parallel RLC circuit

whereas design 2 is open $\frac{\lambda}{2}$ type. Since these resonators will have NEMS capacitively coupled to them, it is vital to know the maximum of the voltages in the resonator to enhance the coupling. For design one, the nanobeam made of SiN with a thin layer of Aluminum on the top will be fabricated on the same chip, whereas design two will be used for the dual-chip technique mentioned in previous chapters. Apart from analytical calculations, these resonators are simulated using FEM (comsol) to predict the exact resonance frequency. The typical voltage distribution of open $\frac{\lambda}{2}$ type resonator is shown in figure 3.14. The next step is to fabricate these MWCs in the nano-fabrication facility. Since we are dealing with superconducting MWCs, one needs to choose the superconducting material. Conventionally these MWCs are made using Aluminum or Niobium on the dielectric substrate, but now many new materials such as TiN and NbN are also being used. We chose both Aluminum and Niobium as our superconducting material for MWC. The T_c or critical temperature of bulk Al is 1.2 kelvin, whereas, for Nb, it is 9.2 kelvin. The elevated T_c of Nb adds an added advantage to test these cavities in 4-kelvin cryostat, which is easy to cool down. The following section deals with the fabrication steps for these cavities.

3.4.3 Fabrication of Niobium microwave resonator

The first step to any fabrication process is the cleaning of the sample. The chip with silicon nitride on silicon or the silicon was cleaned by acetone kept in an ultrasonic bath for 5 mins to remove any oil/organic impurities and then by isopropyl alcohol to remove the residue left by acetone. The sample is then cleaned using RBS detergent and then rinsed in de-ionized water for 5 minutes.

The sample is then quickly transferred to an Ultra-high vacuum e-beam evaporator. The load-lock is first primarily pumped to a pressure of about 2 mbar before turning on the turbop-ump. Once the pressure in the load-lock reaches 1e-6 mbar, the sample holder is transferred into the deposition chamber, which is continuously being pumped using an ion vacuum pump, maintaining the pressure around 1e-10 mbar. The sample is then heated for 3 hours at 300^0 before depositing 120 nm of Nb.

After depositing Nb, the sample is again cleaned using RBS detergent and rinsing with de-ionized water. Acetone and IPA are used for further cleaning. The chip is then pre-baked (dehydration bake) for about 2 mins at 180 ^{0}C, thus removing moisture from the substrate. LOR 3A resist is then spin-coated on the sample at 6000 rpm for 30 s followed by a soft bake for 2 mins at 200^0. Then 420 nm of S1805 resist is coated at 6000 rpm for 30 s and again followed by a soft bake for 2 mins at200^0. Next, the microwave cavity is patterned using laser lithography. The resist is developed using the base MF26A for 1 min. The sample is then rinsed with de-ionized water and dried using N_2. 30 nm of Aluminum is deposited on the sample using an e-beam evaporator which acts as a mask while etching Nb. Al is removed using the lift-off process to expose the parts where Nb has to be etched. NMP is used as a solvent for the lift-off process at 80^0 The sample is then cleaned with usual acetone, IPA, and de-ionized water. Nb is etched using SF6 chemistry in Plassys RIE machine. The schematic of the fabrication process is shown in figure 3.15

3.4.4 Fabrication of Aluminum microwave resonator

The fabrication steps of Al-based microwave resonators are slightly different from Nb-based resonators. In the latter, Nb is deposited before lithography and then etched away since we have to heat the sample at 300^0 for 3 hours in the evaporator to remove any moisture from the substrate as Nb is very susceptible to degradation due to oxidation. However, the quality of the Al resonator is not so sensitive to oxidation (aluminum oxide forms very quickly on bare aluminum in air), and we can deposit it after lithography, followed by a lift-off process. The cleaning steps remain the same as in the case of Nb resonators. We again use LOR 3A and

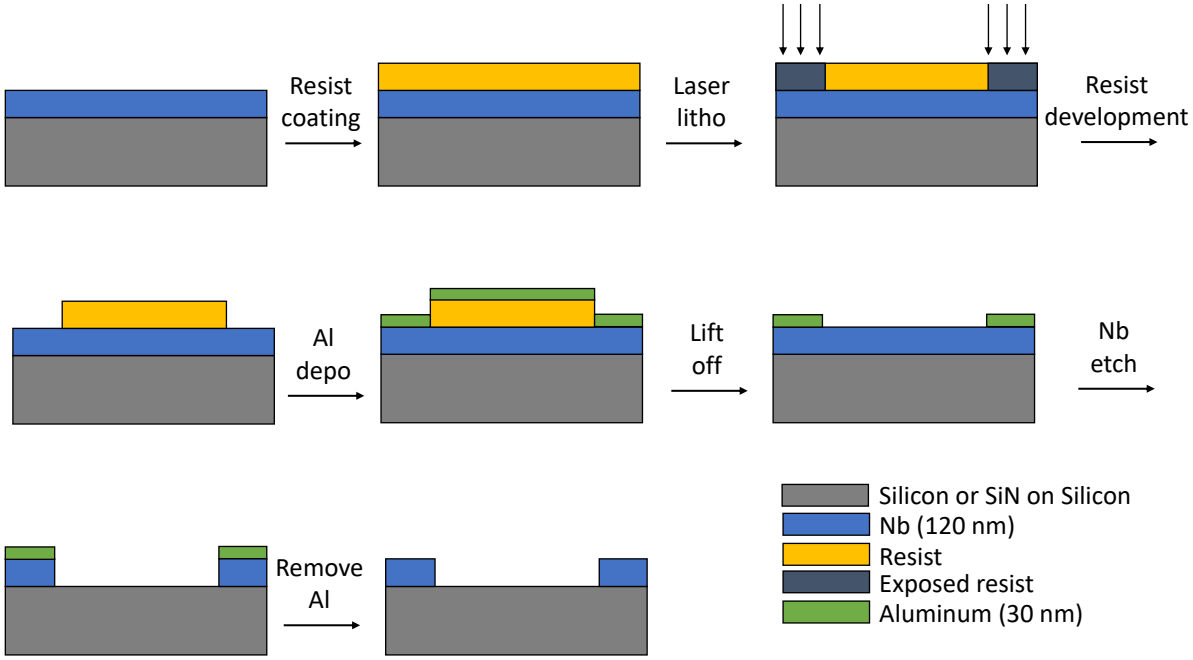

FIGURE 3.15: Schematics of fabrication process of Niobium based microwave cavity

S1805 resists with the same parameters and exposes them using laser lithography. The resist is developed with MF62A for 1 min and rinsed with deionized water. 120 nm of Al is then deposited in the e-beam evaporator at 0.1 nm/sec. The lift-off process is carried out in the NMP solution at 80^0. The schematics of the fabrication process is shown in figure 3.16

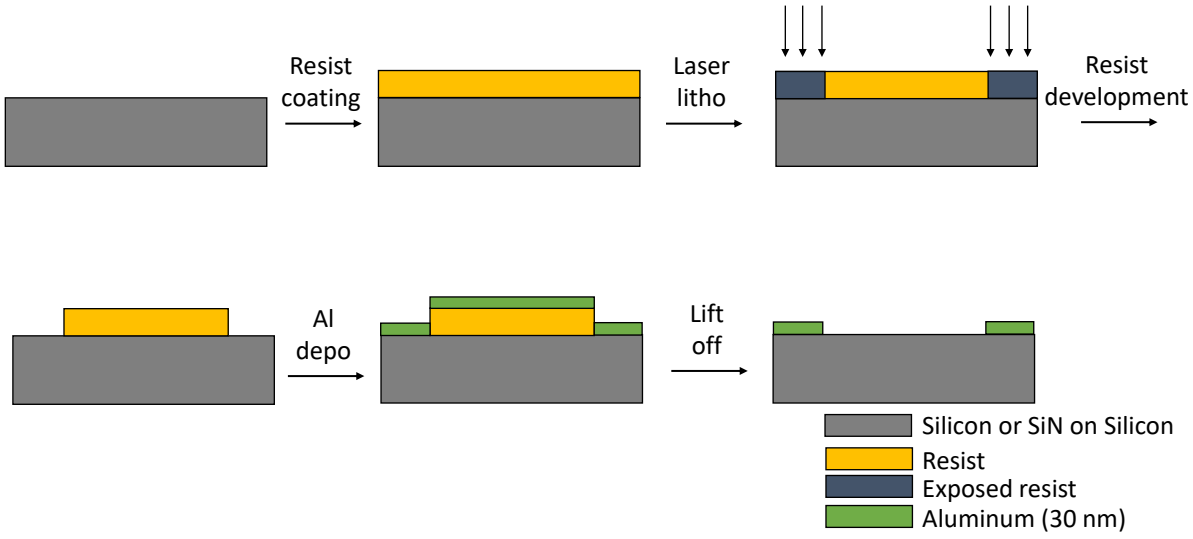

FIGURE 3.16: Schematics of fabrication process of Aluminum based microwave cavity

3.4.5 Characterization of superconducting microwave resonator

We use S-parameters to characterize the microwave cavities. For high-frequency measurements such as microwave, an ideal representation of the circuit according to the measurements, incident, reflected, and transmitted wave is given by scattering (S) matrix. For a two-port network as shown in figure 3.17, the S matrix is defined as,

$$\begin{pmatrix} V_1^- \\ V_2^- \end{pmatrix} = \begin{pmatrix} S_{11} & S_{12} \\ S_{21} & S_{22} \end{pmatrix} \begin{pmatrix} V_1^+ \\ V_2^+ \end{pmatrix} \tag{3.27}$$

where V_1^+ and V_2^+ are the amplitudes of the voltage incident on port 1 and 2 and V_1^- and V_2^-

FIGURE 3.17: A two-port network

are the amplitudes of the voltage reflected from the respective ports. In general, for a system with n ports, the specific element of the scattering matrix can be determined as

$$S_{ij} = \frac{V_i^-}{V_j^+} \tag{3.28}$$

S_{ij} is extracted by driving the port j with an incident wave of voltage V_j^+ and measuring the wave amplitude V_i^- coming out of port i. For our system, we apply the driving voltage to port 1 and measure the signal coming out of port 2. Thus we are interested in measuring the scattering parameter S_{21}. Experimentally, when we apply the voltage with a frequency near the cavity's resonance frequency to port 1 of the transmission line, the signal is partially absorbed in the cavity, and we see transmission spectra while measuring S_{21}. To fit the transmission spectra (S_{21}), we need to theoretically determine S_{21} by modeling our MWC with transmission line as an RLC circuit.

As discussed before, the CPW resonator is an analogue of a parallel RLC circuit. As shown in figure 3.18 a parallel RLC circuit (resonator) is coupled to the transmission line through a coupling capacitance C_c. R, L and C are the parameters of this RLC circuit with impedance

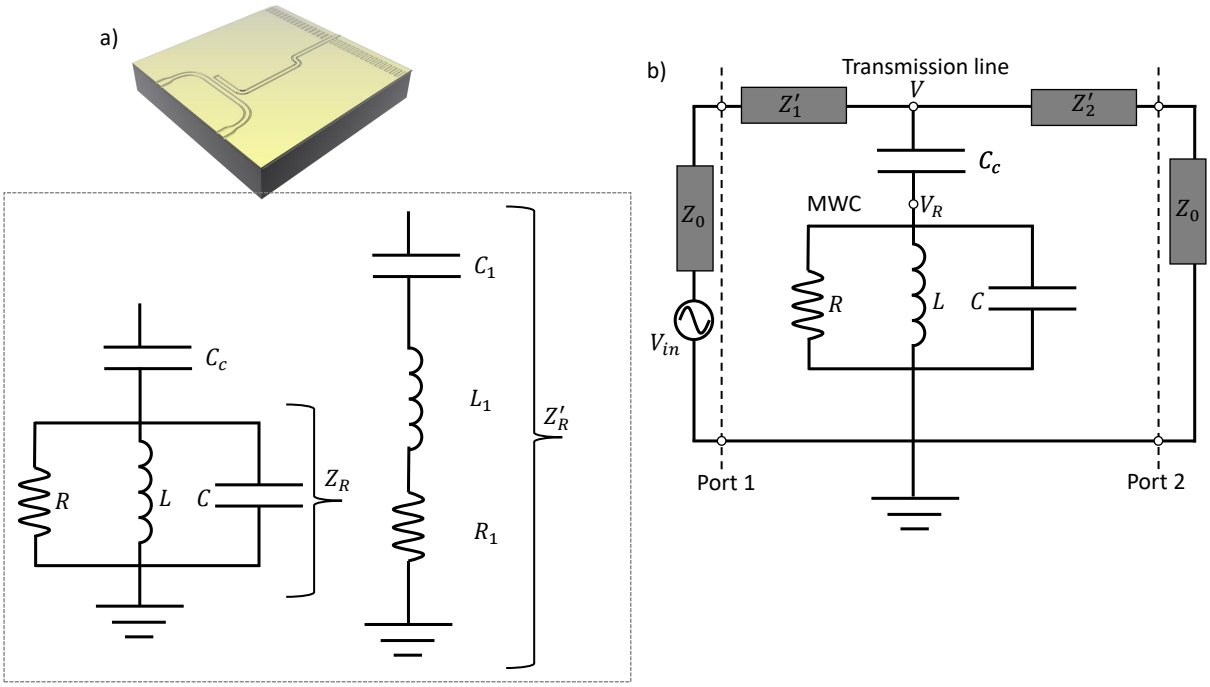

FIGURE 3.18: (left) Parallel RLC circuit with coupling capacitance C_c modeled as series RLC circuit (right) Circuit diagram of the RLC circuit coupled to the transmission line with coupling capacitance C_c

Z_R. The parallel RLC circuit along with coupling capacitance can be transformed to a series RLC circuit with parameters R_1, C_1 and L_1 with impedance $Z_R^{'}$ also shown in figure 3.18. The transformed parameters can be written in terms of original parameters as

$$\begin{aligned} L_1 &= L\left(\frac{C+C_c}{C_c}\right)^2 \\ R_1 &= L\left(\frac{C+C_c}{RC_c^2}\right) \\ C_1 &= \frac{C_c^2}{C+C_c} \end{aligned} \tag{3.29}$$

The complex impedance of the series RLC circuit is

$$Z_R^{'} = i\omega L_1 + R_1 + \frac{1}{i\omega C_1} \tag{3.30}$$

One can approximate $\omega = \omega_c + \Delta\omega$ where $\Delta\omega$ is very small and in turn appoximate the complex impedance as

$$Z_R^{'} = i\omega L_1 + R_1 + \frac{1}{i\omega C_1} + i\Delta\omega L_1 - \frac{\Delta\omega}{i\omega_c^2 C_1} = R_1 + 2i\Delta\omega L \tag{3.31}$$

In the experimental characterization, it was found that the resonant response or the absorption spectra (S_{21}) is not symmetrical around resonance frequency ω_c. This may be because of the parasitic inductances associated with the wire bonds. To include this effect we have included impedances $Z_1^{'} = iX_1Z_0$ and $Z_2^{'} = iX_2Z_0$ in our model as shown in figure 3.18 where X_1 and X_2 are reactances through which transmission line is connected to the injection and detection lines. To calculate S_{21}, one can take advantage of the impedance matrix. Similar to scattering matrix, impedance matrix's components can be defined as

$$Z_{ik} = \frac{V_i}{I_k} \tag{3.32}$$

Z_{ik} can be found by driving port k with the current I_k , opencircuiting all other ports (so $I_j = 0$ for $j \neq k$), and measuring the open-circuit voltage V_i at port i. Our circuit can be compared to T-equivalent circuit as shown in figure 3.19. Thus,

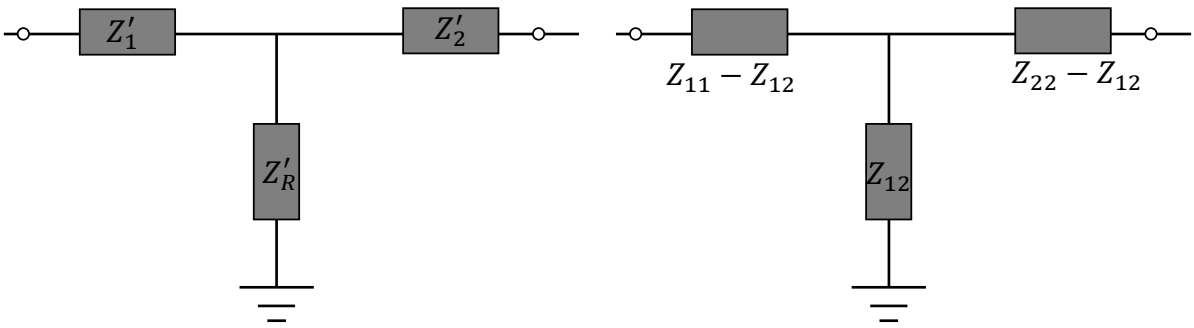

FIGURE 3.19: (left) The device under test can be represented as a tee formed by three impedances (see text). (right) The three impedances of the tee can be written in terms of the elements of the impedance matrix as shown in [61]

$$\begin{aligned} Z_{12} &= Z_R^{'} \\ Z_{11} &= Z_R^{'} + Z_1 - Z_0 \\ Z_{22} &= Z_R^{'} + Z_2 - Z_0 \end{aligned} \tag{3.33}$$

where $Z_1 = Z_1^{'} + Z_0$ and $Z_2 = Z_2^{'} + Z_0$ According to Pozar, S_{21} for T-equivalent impedance circuit is given as

$$S_{21} = \frac{2Z_{21}Z_0}{\Delta Z} \tag{3.34}$$

where $\Delta Z = (Z_{11} + Z_0)(Z_{22} + Z_0) - Z_{12}Z_{21}$ Thus,

$$S_{21} = \frac{2Z_R' Z_0}{Z_R'(Z_1 + Z_2) + Z_1 Z_2} = \frac{2Z_0}{Z_1 + Z_2}\left(1 - \frac{\frac{Z_1 Z_2}{Z_1 + Z_2}}{R_1 + 2i\Delta\omega L_1 + \frac{Z_1 Z_2}{Z_1 + Z_2}}\right) \tag{3.35}$$

We can define $\kappa_{ext} = \frac{Z_1 Z_2}{L_1(Z_1 + Z_2)}$ and $\kappa_i = \frac{R_1}{L_1}$ such that

$$S_{21} = \frac{2Z_0}{Z_1 + Z_2}\left(1 - \frac{\kappa_{ext}}{\kappa_{total} + 2i(\omega - \omega_c)}\right) \tag{3.36}$$

where $\kappa_{total} = \kappa_{ext} + \kappa_i$ If the reactances due wirebonds present in the circuit are negligible then S_{21} is simply

$$S_{21} = 1 - \frac{\kappa_{ext}}{\kappa_{total} + 2i(\omega - \omega_c)} \tag{3.37}$$

In 3.20 I have plotted the typical transmission response of the MWC measured by either VNA

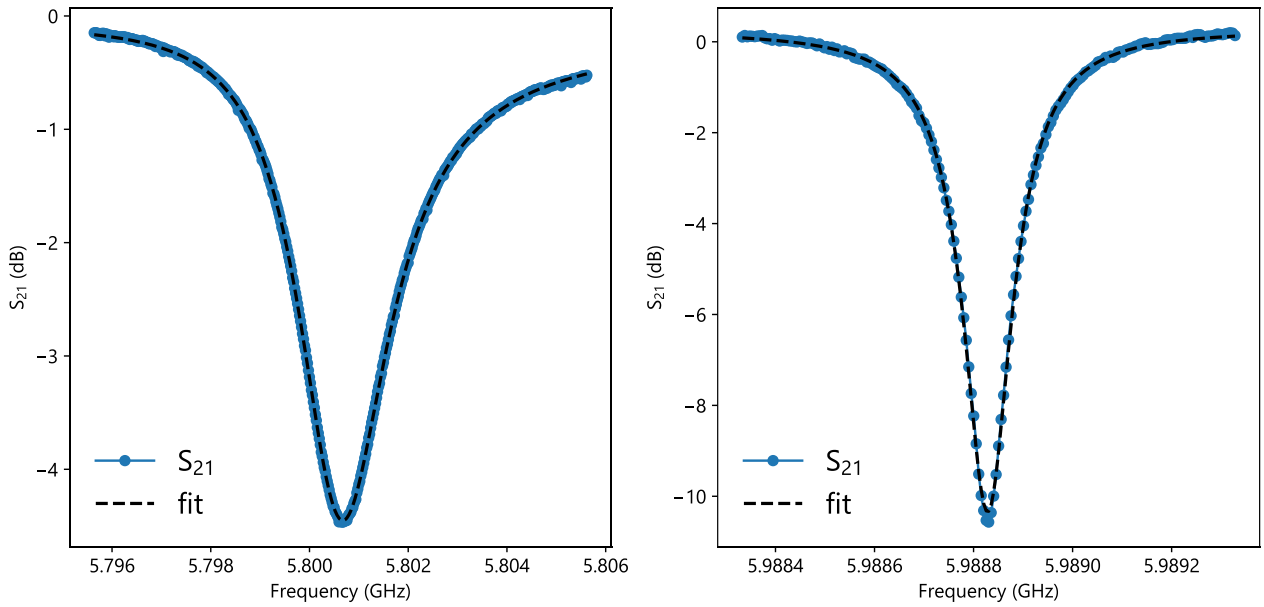

FIGURE 3.20: a) Typical transmission curve for open $\frac{\lambda}{2}$ MWC (Design 2) b) Typical transmission curve for shorted $\frac{\lambda}{4}$ MWC (Design 1)

or spectrum analyzer. The different measurement tools and schemes are subject to another section. Here we will discuss the parameters corresponding to these designs. The $\frac{\lambda}{2}$ MWC was designed to resonate at 6.2 GHz, yet we observe the cavity's resonance to be at 5.8 GHz.

This is because the central conductor of the cavity was bonded to the gate of the nanobeam which is on the other chip. The inductance and the parasitic capacitance induced due to this bonding down-shifted the resonance frequency. The κ_{ext} and κ_{total} corresponding to this cavity were approximately 500 kHz and 2.5 MHz, respectively hence a Q of 2500. The relatively low Q could be due to the presence of an interdigitated capacitor in the ground plane (see *Chapter 6*). On the other hand, the quality factor of $\frac{\lambda}{4}$ MWC was about 4×10^4. The $\frac{\lambda}{4}$ MWC was fabricated on Si wafer (thickness around 550 μm) with 100 nm of SiN on top, whereas $\frac{\lambda}{2}$ cavity is fabricated on intrinsic Si wafer (thickness around 300 μm). Both these MWCs were made using Niobium deposited in an Ultra-high vacuum e-beam evaporator. The low-quality factor of $\frac{\lambda}{2}$ cavities led us to believe that the quality of Niobium deposited was not good. One way to characterize the quality of the superconducting thin film is to measure its critical temperature. The superconducting transition temperature T_c for bulk Nb is 9.26 kelvin. The T_c was measured using PPMS (Physical property measuring system). We observed a sharp dip in the resistivity of the Nb thin film at 9.0 kelvin, which is very close to bulk T_c, and residual resistivity ratio greater than 4, as shown in figure 3.21.Considering that higher MWC Q was obtained with much lower T_c ([55]), we concluded that the quality of the Nb was sufficient. We have tested more than five $\frac{\lambda}{2}$ cavities in 4-kelvin cryostat and have not succeeded in getting quality factors above 1×10^4. One plausible reason for such a low-quality factor may be related to design. One needs to completely simulate these cavities in Sonnet or any other HFSS software to get a complete picture of different loss mechanisms leading to degradation of quality factors which is a work in progress.

The main contributors to internal losses characterized by κ_i are TLS (two-level systems)

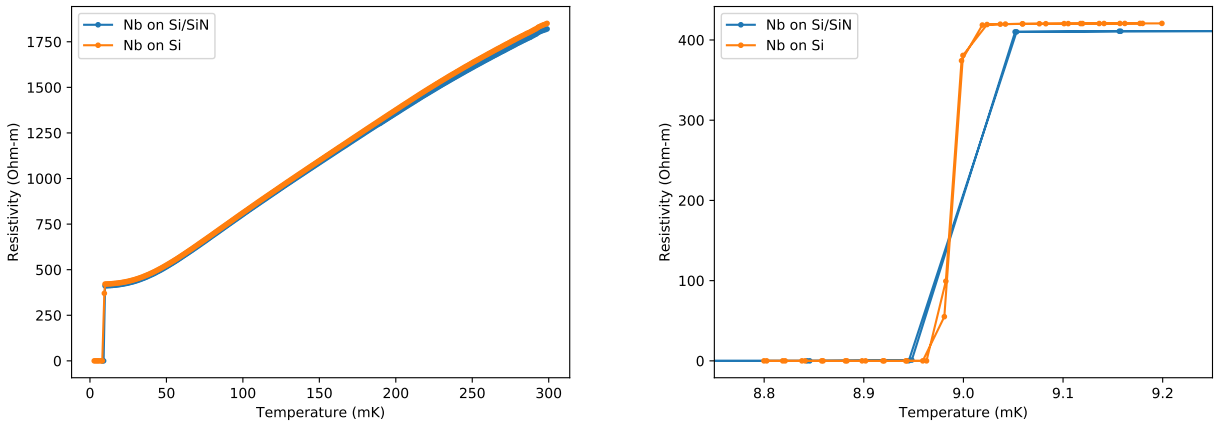

FIGURE 3.21: (left) Resistivity of Nb thin film versus Temperature (right) Resistivity of Nb this film versus Temperature around T_c

present at metal-substrate or substrate-air, or metal-air interfaces. Much effort has been put

into minimizing the TLS induced losses owing to different superconducting materials and substrates used. Also, thermal and infrared radiations induce losses in the superconducting material due to quasi-particle generation. For efficiently shielded and properly designed, MWC quality factors reaching one million can be obtained. Once the chips are fabricated, they are mounted in the cryostat for measurements. The different components of the cryostat and microwave circuitry are subject to the next section.

3.5 Experimental setup

In this section, we describe the equipment and the components that are employed in the microwave experiment. We will start by outlining the principles of dilution cryostat, and later the components installed in the dilution cryostat for microwave measurements.

3.5.1 Dilution Cryostat

It is straightforward to reach a temperature of 4 kelvin using ^{4}He cryostat where the sample mounted on the dipstick is immersed in a bath of ^{4}He. One can lower the temperature by pumping on the bath so that the energetic ^{4}He vapors are pumped out. We can reach the temperature down to 7 millikelvins by taking advantage of the dilution cryostat. The detailed principles parts of the dilution cryostat is illustrated in 3.22. Most of our experiments are carried out in a commercial BlueFors dilution cryostat. The environment is first pre-cooled to approximately 3 kelvin using a pulse tube to operate the dilution cryostat. The pulse tube cryocooler is cryogen-free, thus giving us an advantage to not replenish the ^{4}He in the cryostat regularly to maintain the environment near 3 kelvin, although the pulse tube cryocooler may add vibration to the setup. The environment inside the cryostat is also pumped down to 1×10^{-6} mbar to prevent any heat leaks. A series of thermal screens also protect the dilution unit for minimizing heat radiation.

The ^{3}He-^{4}He mixture is condensed using a compressor after the cryostat is pre-cooled to 3 kelvin. The mixture separates into two phases below 870 mK. Phase 1 is concentrated in ^{3}He, and phase 2 is diluted ^{3}He in ^{4}He, and below 200 mK, phase 1 is primarily pure ^{3}He while phase 2 contains 6.4% ^{3}He in ^{4}He. The phase boundary is at the mixing chamber plate (MXC), the coldest part of the cryostat. A pumping line connected to the still shown in figure 3.22 helps circulate the mixture. ^{3}He atoms are mostly evaporated from the mixture due to pumping owing to its higher saturated vapor pressure than ^{4}He. To maintain the concentration is phase 2 ^{3}He moves from phase 1 to phase 2. The transfer of ^{3}He from phase 1 to phase 2 is an endothermic process, thus facilitating cooling. The evaporated ^{3}He atoms from the pumping line returns to the mixing chamber via an injection line. The cooling power depends on the

flow rate of ^{3}He in the pumping line. The flow rate, in turn, depends on the heating power applied to the still plate. Once pumped out of the pumping line, the evaporated mixture goes outside the cryostat to a liquid nitrogen trap to trap any impurities before being reinjected in the cryostat. The mixture recondenses through an impedance cooling it down to 1 kelvin. The mixture is then thermalized using heat exchangers that connect the condensing and pumping line between the MXC plate and the still plate. We can reach the temperature down to 7 mK in 48 hours with dilution operation running continuously.

The temperature is measured using resistance thermometers (resistors) mounted to different plates, i.e., 50 kelvin, 4 kelvin, still, and MXC. The thermometers are not primary, and they have to be calibrated using another thermometer. These resistors are then measured by applying currents down to a few hundred pA (thus preventing heat load) by a homemade resistance bridge called TRMC2 through proper filtering lines. On the mixing chamber plate, resistors made of carbon or Ruthenium oxide are mounted. The carbon resistor is well-calibrated down to 11 mK. In addition to resistance thermometers, a noise thermometer, SQUID MFFT from Magnicon, is also installed on the MXC plate. It measures the magnetic field fluctuations due to Nyquist currents in a copper sample that is thermally coupled to the MXC plate and the integrated noise spectrum is proportional to temperature. We have measured temperatures down to 2 mK using the Magnicon MFFT.

3.5.2 Microwave lines

The commercial Bluefors dilution cryostat is also accompanied by microwave lines for carrying out high-frequency measurements. These coaxial cables can be a dominant source of heat loading in the cryostat. To minimize heat loading, microwave lines are generally made of materials with low thermal conductivity. However, with the exception of superconducting materials, these materials are also poor electrical conductors leading to dissipation when microwave signals are fed. Nevertheless, dissipation or attenuation is desired to minimize the thermal radiation coming from room temperature. These microwave lines are made of superconducting NbTi (both inner and outer conductors) and CuNi coaxial cables. CuNi coaxial cables are used from room temperature to 4-kelvin plate while superconducting NbTi coaxial cable is used from 4-kelvin plate to MXC plate. Also, the characteristic impedance of these coaxial cables is 50 Ω.

Apart from feeding the coaxial cables with high-frequency microwave signals for carrying out different quantum measurements, DC wiring is also required. The DC wiring generally serves the purpose of biasing the HEMT (high electron mobility transistor amplifier), microwave switches, or flux bias qubits on the chip. This DC wiring is made of twisted pairs of Cu based

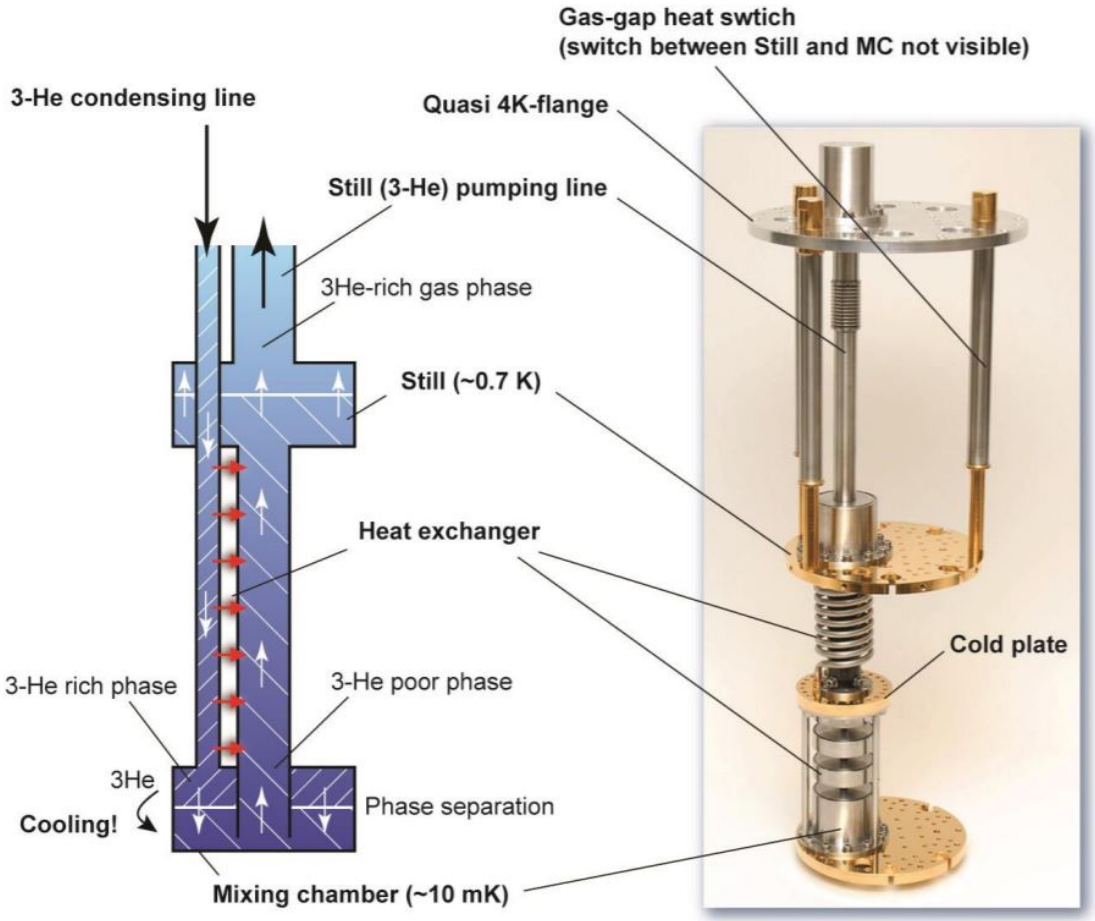

FIGURE 3.22: Dilution cryostat principle parts

alloy wires from room temperature to 4-kelvin plate due to their large thermal conductivity.

Attenuation in the microwave lines

The signal required at the chip level to measure the position of the mechanical resonator by increasing the coupling between the mechanical resonator and microwave cavity is small. However, a considerable power (orders of magnitude larger than required) is applied at the input of the dilution cryostat. This is because the signal needs to be attenuated to reduce the room temperature black body radiation present in cables at room temperature reaching the sample at mixing chamber plate. Typically $\sim$ 60 dB of attenuation is required to serve the above purpose. This black body radiation in cables is also called Johnson-Nyquist noise in electronics. Therefore, to prevent the thermal phonons running from room temperature to the coldest part of the cryostat, a cascade of attenuators is used at different stages of the cryostat.

An attenuator with an attenuation of 20 dB is analogous to a beam splitter which transmits 1 % of the incident signal power and dissipates 99 % of the signal as black body emission. In our cryostat, we have 20 dB of attenuation at 4-kelvin plate, 10 dB at still, and another 20 dB at cold plate. Distributing the attenuation enables to keep the heat load well below the cooling power at lower and colder stages.

3.5.3 Sample holder

The chip with MWC and NEMS is mounted in a sample holder (cell) made of annealed highly pure Cu. The cell comprises four SMA connectors, two on each side. The four SMA connectors can serve two purposes. First, we can mount two chips at the same time to perform the transmission measurements. Secondly, the additional two SMA connectors can be used for RF driving of NEMS in dual-chip configuration. The cell also acts as a shield protecting the superconducting material from quasi-particle generation from stray radiations. Inside the cell, the input and the output coaxial transmission lines are soldered to gold coplanar waveguides on a circuit board, which are in turn micro bonded to the ends of superconducting CPW on the chip. A Cu clamp is used to press the chip against the Cu cell for thermalization. A thin layer of indium is placed between the clamp and the chip to distribute the clamping forces and ground the chip's ground plane. The whole cell is pressed against the mixing chamber plate of the Bluefors cryogen-free dilution cryostat.

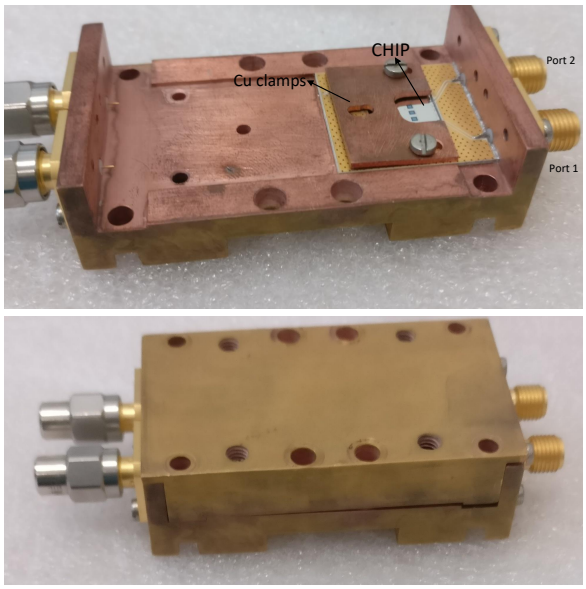

FIGURE 3.23: Cell made of highly pure Cu on which chip is mounted. Also the lid of the corresponding cell is shown at the bottom

3.5.4 RF switch

We have also installed an RF switch at the 4-kelvin plate. The switch generally serves the purpose of routing a signal to different lines corresponding to different applications. In our cryostat, it is used for bypassing the HEMT amplifier also installed at 4 kelvin. We use a commercial latching mechanical type switch from RADIALL (R577433000, 3-8 GHz). The latching type switch is a switch that, once triggered, remains in the same state even if the power that triggers the state is turned off. The characteristic impedance of the switch is 50 Ω with an insertion loss of about 1 dB. These switches have been successfully used for setups in dilution cryostat, yet the heat load from the solenoid used to move the mechanical parts can slightly increase the temperature, and then it would take some time to thermalize back to the temperature of the plate where it is installed. Since we have installed it at the 4-kelvin plate, the temperature change due to the heat load is minimal.The switch is directly connected to the HEMT amplifier in our case as shown in figure 3.24.

The switch is a 4 port network whose schematic is shown in figure 3.24. The voltage applied for switching between different states is 28 V.

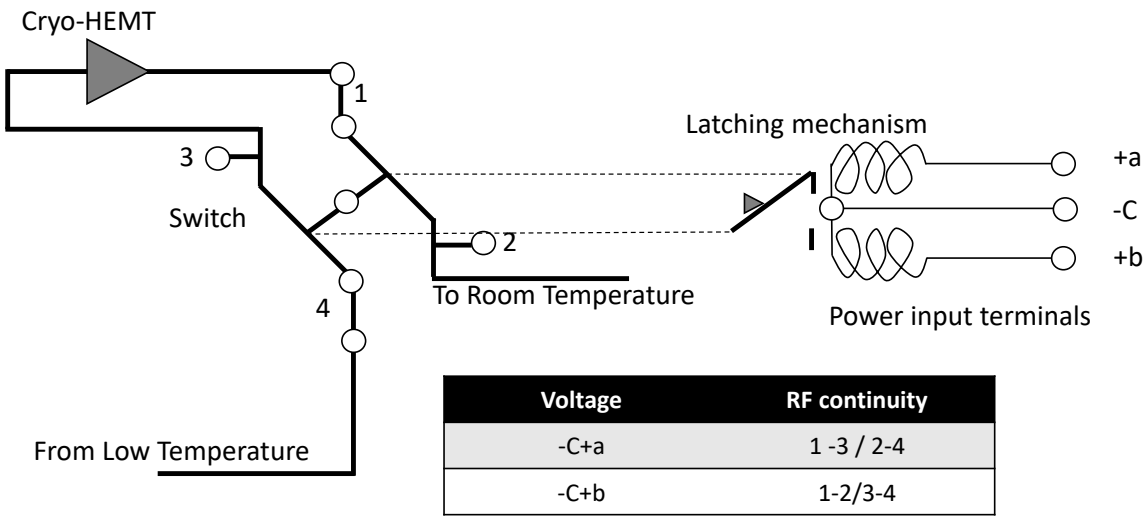

Voltage	RF continuity
-C+a	1 -3 / 2-4
-C+b	1-2/3-4

FIGURE 3.24: A schematic diagram of switch showing two different states and the latching mechanism

3.5.5 Band pass filter and Circulators

We have also installed a band-pass filter at the MXC level just before the cell, offering rejection of both low frequency and high-frequency signal, thus selecting a particular pass-band i.e., 4-8

GHz. On the other side of the cell, we installed an array of two microwave circulators. These circulators prevent the noise from the detection side from entering the output port of the cell.

3.5.6 High electron mobility transistor (HEMT) amplifier

We have installed two amplifiers based on high electron mobility transistor at 4-kelvin plate and at room temperature. These amplifiers are from Low noise factory and work in 4-8 GHz bandwidth. According to specifications from the company, the gain of cryogenic HEMT is close to 40 dB at 6 GHz. However, we measured the gain to be 34 dB at 6 GHz. The measured gain of room temperature HEMT was 40 dB at 6 GHz in accord with the specifications. During the course of our experiments, we observed a sudden drop in the gain close to $\sim$ 10 dB while measuring the transmission of the cavity. After extensive tests of the bias circuit, we concluded the problem was with the cryogenic HEMT, which we sent to the company to be repaired. After replacing the cryogenic HEMT with another HEMT, the transmission of the cavity returned to normal.

3.6 Experimental set-up

The basic circuit diagram for cavity optomechanics measurements is shown in figures 3.25 and 3.26. At room temperature, the microwave sinusoidal signal is generated by microwave generators. For our measurements, we use Keysight or Ananpico dual-channel microwave generators for pumping the cavity. The microwave pump signal with frequency ω_d is divided into two routes using a power divider. The pump signal ω_d is generally detuned from the resonance frequency of the microwave cavity ω_c by $\pm\Omega_m$, where Ω_m is the resonance frequency of the mechanical mode of interest and ω_c is the resonance frequency of the cavity. The weak microwave probe signal with frequency ω_p is combined with the pump signal at room temperature using a power combiner (3 dB of insertion loss) before being fed to the microwave coaxial cables in the cryostat. The weak probe tone is used to measure the transmission of the cavity. The combined signal is attenuated by a cascade of attenuators, as mentioned before. The signal is then filtered using a band-pass filter installed at the mixing chamber plate. The signal coming out of the cell goes through the circulators before combining with another pump signal coming from room temperature to 4-kelvin plate through an opposition line. This serves the purpose of attenuating the strong pump signal at ω_d before reaching the cryogenic HEMT amplifier at 4 kelvin. The pump signal can be canceled by tweaking the variable attenuator and phase shifter at room temperature installed on the opposition line. The cancellation of the pump signal prevents the HEMT amplifier from getting saturated. The signal is again amplified using another HEMT at room temperature. The signal is detected using a Keysight spectrum analyzer. Another way to detect signals is by using a Lockin amplifier (Zurich instruments). For cavity optomechanical

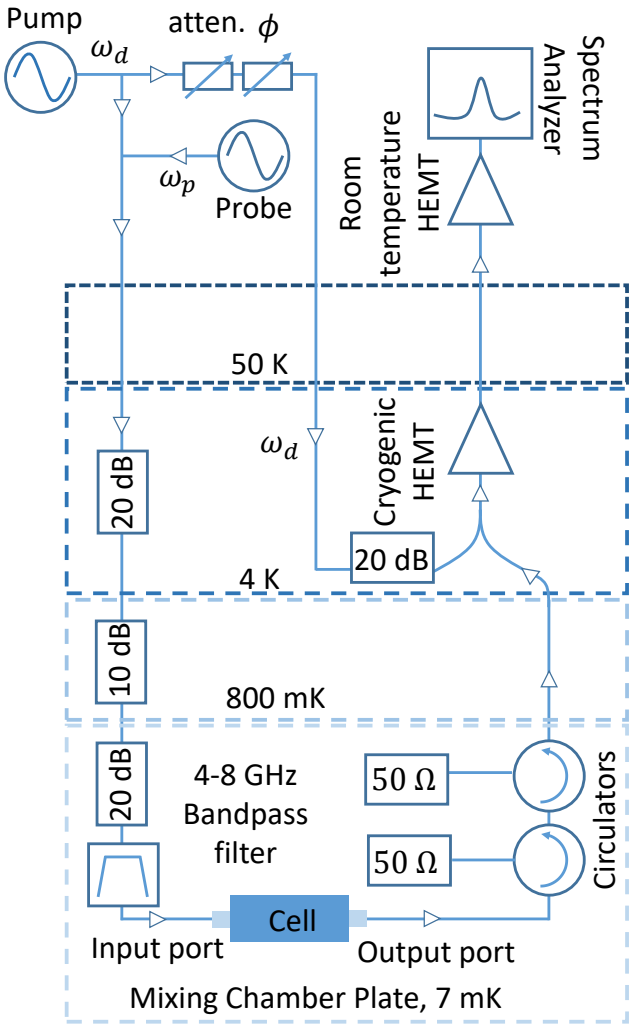

FIGURE 3.25: A schematic circuit diagram with spectrum analyzer as measuring instrument

experiments, the signal of interest is at frequency ω_c for the above-specified pump frequency. The signal coming out from the fridge is down-converted using a mixer as shown in figure 3.26. For most of our experiments, a Keysight generator is used for pump signals. Channel 1 of the Anapico dual-channel microwave generator is used for probe signal, and channel 2 is used as a local oscillator for down-conversion of the signal using a mixer. The down-converted signal is then fed to the lockin amplifier. The Zurich instrument lockin amplifier can be used in different modes, which we will discuss in chapter 5, Anomalous force noise on mechanical resonators at low temperature.

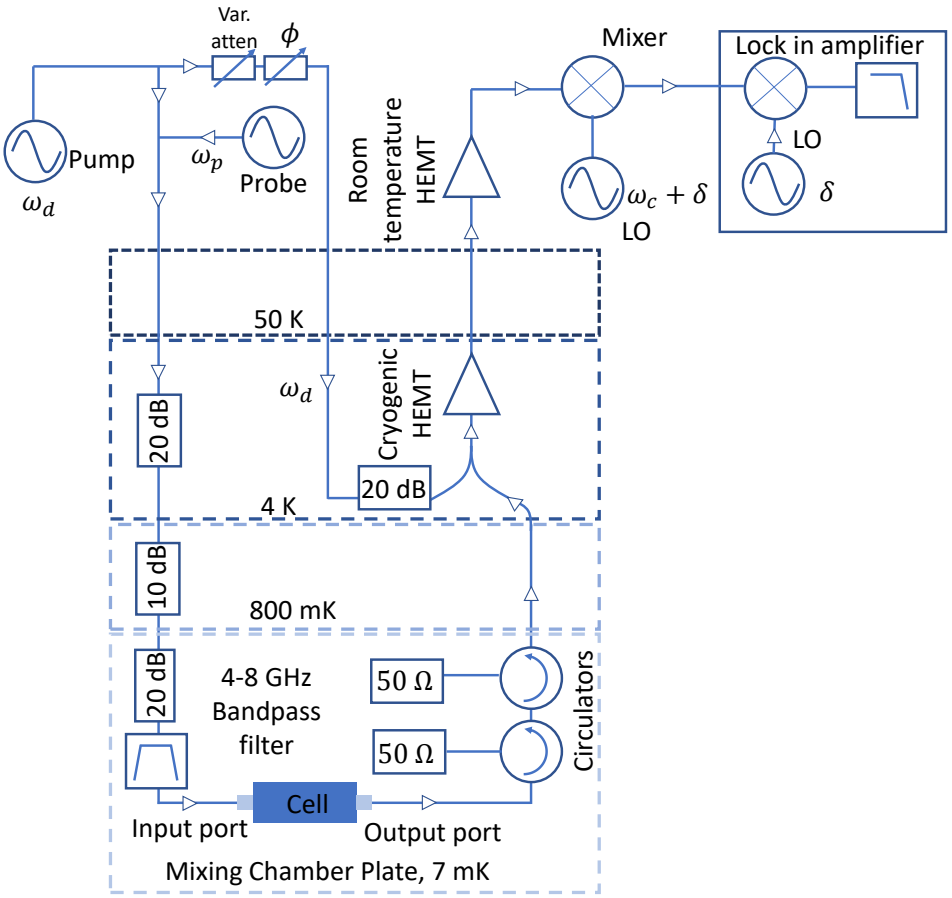

FIGURE 3.26: A schematic circuit diagram with Zurich lockin amplifier as measuring instrument

3.7 Experimental calibrations

The mechanical noise spectrum is measured using in-cavity pumping, red-detuned, and blue-detuned pumping. We have discussed the consequences of different schemes of pumping on mechanical characteristics previously. Here, we will give an experimental result based on blue-detuned pumping. 50 μm $\times$ 120 nm $\times$ 300 nm nanobeam made of SiN with a thin layer of Al is capacitively coupled to a 6 GHz shorted $\frac{\lambda}{4}$ type MWC. We apply a pump signal using one of the channels of the Anapico microwave generator. The other channel of the generator is used to generate a weak probe signal to measure the transmission of the cavity. The circuit diagram for such a measurement is shown in figure 3.25. The signal is measured using the spectrum analyzer. The plot in figure 3.27 shows the noise spectrum of power output of the MWC measured at ω_c for different pump powers applied at the generator (5 dBm, 6 dBm, 7 dBm, 8 dBm, 9 dBm, 10 dBm) at $\omega_c + \Omega_m$. The pump signal goes through a series of attenuators such that the power input at the cell installed at the mixing chamber plate is considerably smaller than at room temperature. The proper calibration is required to measure the power input at

the cell accurately. However, for this section, we will bypass these calibrations and will talk about the power applied at the generator. The gain in the circuit due to the presence of HEMTs at 4-kelvin plate and at room temperature was measured to be 65±1 dB. The measurements were done at 250 mK.

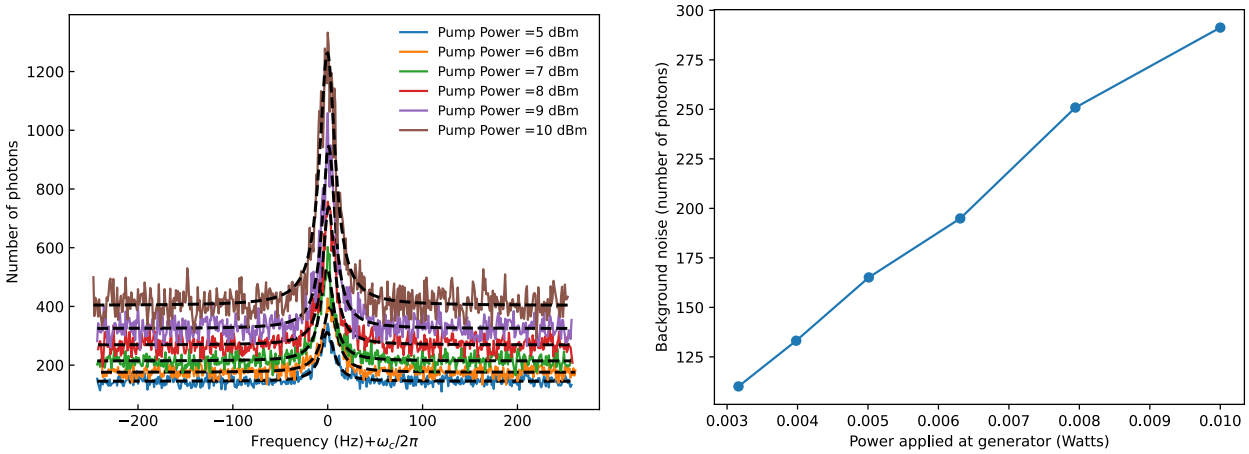

FIGURE 3.27: (left) Mechanical noise spectrum measured at ω_c for different pump powers applied at $\omega_c + \Omega_m$ (right) Background noise floor increasing with pump powers

In Chapter 2, we derived the output noise spectrum of the output power from the MWC. The output noise spectrum at ω_c for the pump power applied at $\omega_c + \Omega_m$ is given by,

$$S = nf + 2\frac{\kappa_r}{\kappa_{total}}\frac{G^2 n_d}{\kappa_{total}}S_x \tag{3.38}$$

where nf is the noise floor added by the external circuit, which is assumed to be constant. We observed that the background noise floor depends on the pump power applied at the generator. The background noise floor increased with an increase in the pump power shown in figure 3.27. We have also converted the units of noise spectrum generally measured in dBm/Hz in a 1 Hz resolution bandwidth by the spectrum analyzer to the units of the number of photons. We suspected that there is some non equilibrium population of the MWC due to some additional noise which seems to be increasing with pump power. To test our hypothesis, we measured the noise spectrum in a large span of 1 MHz with central frequency at $\frac{\omega_c}{2\pi}$ with 10 Hz resolution bandwidth using the spectrum analyzer. The plot with power spectral density in the large span is shown in figure 3.28.

The measured area under the power spectral density shown in figure 3.28 outlines the number of photons inside the cavity. Since the area under the curve increases with an increase

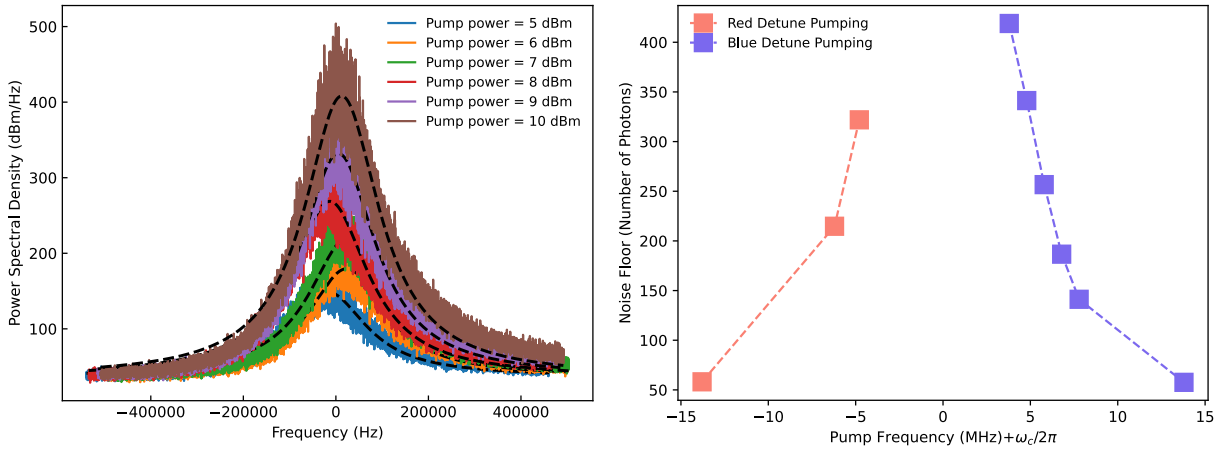

FIGURE 3.28: (left) Cavity power spectral density of the cavity resonating at 6 GHz measured by spectrum analyzer in 1 MHz span using 10 Hz resolution bandwidth for different pump powers (right) Peak of the power spectral density versus the detuning of the pump frequency from the cavity resonance

in pump power applied at the generator, we concluded that the MWC is being populated by some additional noise accompanying the pump signal. The mechanical noise spectrum sits at the peak of these curves. Therefore we attributed the change in the noise floor of the mechanical noise spectrum to the corresponding phenomena. We also characterized the peak of the cavity noise spectrum with the pump frequency detuning from the cavity resonance frequency. The results of the above measurement are shown in figure 3.28. Therefore, it is observed that the background noise floor increases if the pump frequency is closer to the cavity resonance frequency. To test the source of the heating of the MWC, i.e., if the source is present in an external circuit or is it something related to the chip itself, we measured the cavity noise spectrum of another cavity present on the chip with the resonance frequency of 6.2 GHz. We observed a similar behavior as the MWC with 6 GHz resonance frequency for the background noise dependence on the pump detuning, as shown in figure 3.29. One possibility is the heating of the chip itself due to non-equilibrium population of the cavity. We see no effect on the background noise floor of the MWC with resonance frequency of 6.2 GHz while pumping at $\omega_c + \Omega_m$ where $\omega_c = 6$ GHz and Ω_m is the mechanical resonance frequency. So the peak of the cavity spectral density or the background noise floor of the mechanical noise spectrum depends not only on the pump power but also on its detuning from the cavity resonance frequency. We, therefore, plotted the peak of the cavity spectral density with the number of drive photons n_d. The peak of the cavity spectral density is plotted versus drive photons for both the cavities (6 GHz and 6.2 GHz) shown in figure 3.30. We see that the number of photons in the cavity, not the number of photons flowing through the on-chip feedline, determines the cavity noise

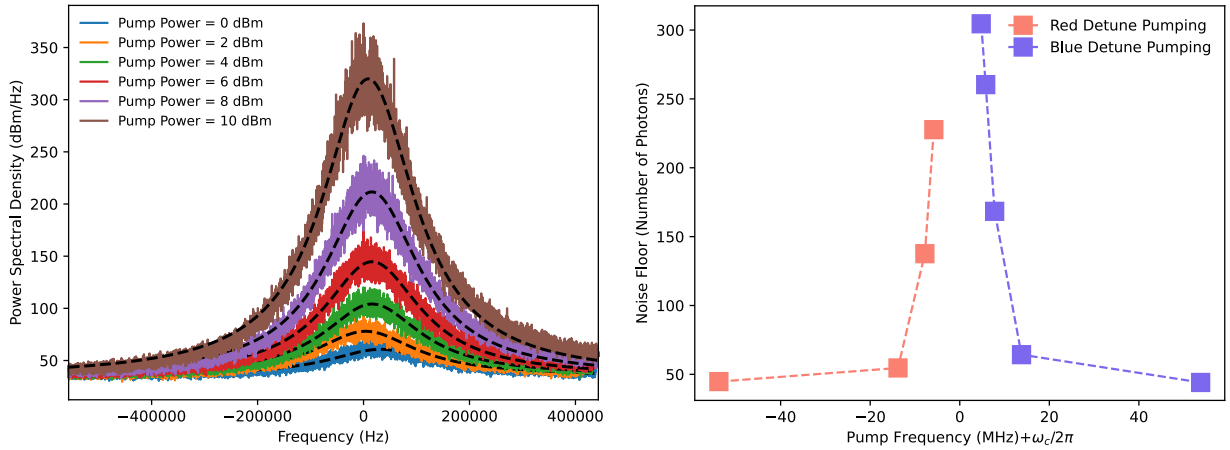

FIGURE 3.29: (left) Cavity power spectral density of the cavity resonating at 6.2 GHz measured by spectrum analyzer in 1 MHz span using 10 Hz resolution bandwidth for different pump powers (right) Peak of the power spectral density versus the detuning of the pump frequency from the cavity resonance

level. In figure 3.30, we see the peak of the cavity noise spectrum is close to 40 when the

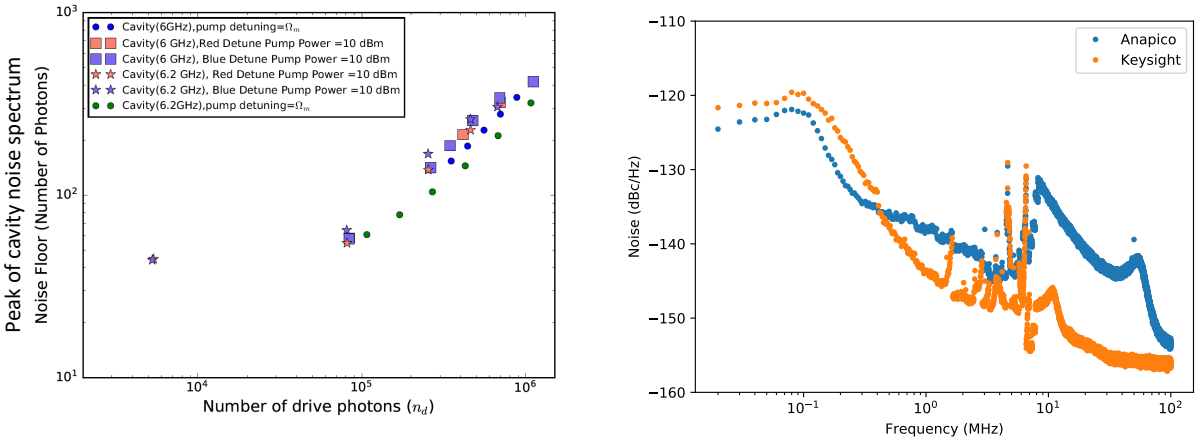

FIGURE 3.30: (left) Peak of the cavity spectral density versus the input drive photons in the cavity (right) Phase noise comparison of the Anapico and Keysight generators

number of drive photons is much less than $n_d << \sim 10^5$. The noise floor of the setup with 50 Ω termination on all input of the cryostat is also ~ 40. The increase in the noise floor with pump power led us to believe that there is some additional noise accompanying the pump signal which is populating the MWC. One of the plausible reasons for this behavior may be due to the phase noise of the microwave generator. We measured the phase noise of the Anapico microwave generator and compared it with the phase noise of the Keysight generator. For measuring the

phase noise, we applied a signal at 6.05 GHz with 9 dBm power and measured the spectrum in a span of 100 MHz. As evident from figure 3.30, the phase noise of the Anapico generator is much larger than the Keysight generator. We switched to the Keysight generator to pump the cavity. We did not see such behavior while pumping with the Keysight generator.

Chapter 4

Optomechanically induced transparency and absorption

4.1 Introduction

One of the fundamental processes occurring in nature is the interaction between matter and electromagnetic fields. The quantum theory developed in the early 1900s mainly resulted from the interaction of light with subatomic particles like electrons. The advent of the laser has led to further discoveries and applications. One such application is the laser cooling of atoms developed in the 1980s. Atoms and molecules moving with random motion with a certain velocity can be slowed in the direction of the incident laser beam under certain conditions. Applying laser fields in multiple directions allows 3-dimensional cooling. The work was awarded the Nobel prize in Physics in 1997 [2]. Furthermore, evaporative cooling was employed to cool the atoms even further. As a result of these cooling techniques, Ketterle reported the Bose-Einstein condensates (BEC) of Na atoms. This experimental evidence of BEC was awarded the Nobel prize in Physics in 2001 [3]. The field of cavity-QED deals with the interaction of electromagnetic field and matter inside a high Q-cavity. Various quantum optics experiments have been carried out demonstrating dressed states [81], Autler-Townes splitting [71], electromagnetically induced transparency [14] etc. by trapping atoms inside an optical cavity interacting with different modes of the electromagnetic field in the cavity.

Superconducting microwave circuits provide an alternative route to perform the quantum optics experiments using microwave photons, superconducting artificial atoms, and other quantum devices. The superconducting artificial atom or quantum bits/qubits based on the Josephson junction are building blocks of quantum information processing [6]. The superconducting qubits can be designed, fabricated, and tailored according to different research purposes in contrast to natural atoms. Various quantum optics experiments with atoms trapped inside an optical cavity can be manifested with this platform. Superconducting qubits coupled to transmission lines outperform different platforms (like trapped ions in an optical cavity) to

implement quantum algorithms. However, these qubits are prone to fluctuations from the environment or internal two-level defects in the material leading to memory loss. Massive efforts in the field have led to run quantum error correction algorithms, thus preserving the qubit's state and protecting it from bit error [37]. The superconducting circuits are also used as highly sensitive astrophysical detectors. KID's or kinetic inductive detectors based on superconducting circuits are promising candidates for millimeter and submillimeter astronomy and also for high-energy particles. NIKA2, an instrument based on these detectors, are currently installed at a 30 m telescope of IRAM in Spain [19].

Recently, the field of superconducting microwave optomechanics wherein the mechanical degree of freedom is coupled to an electromagnetic field has led to many fascinating results that we have already discussed in chapter 1. The field has also led to the development of various microwave components such as circulators [70], amplifiers [23], switches [39] etc. which are crucial components for measuring superconducting quantum devices. Amplifiers and notch filters can rely on optomechanically induced transparency and absorption, respectively. Optomechanically induced transparency and absorption (OMIT/OMIA) are phenomena observed in cavity optomechanical experiments when the cavity is probed using a weak field in the presence of a strong pump field. Also, optomechanically induced transparency is an analogue of electromagnetically induced transparency observed in a 3-level atomic system. We will commence this chapter by giving a brief introduction to electromagnetically induced transparency. A summary of different experiments done till now showing OMIT/OMIA and its applications will be discussed. We will then derive the formula for the transmission of a cavity coupled to a mechanical resonator in the presence of a strong pump field. Finally, we will show the results of our two-tone optomechanical measurements spanning a larger parameter space than has been covered in previous works. In particular, we vary probe frequency, pump frequency, pumping scheme (red/blue), probe power, pump power, and temperature. We demonstrate that the theoretical transmission derived from input/output theory is in excellent agreement with our measurements over the entire parameter range.

4.2 Electromagnetically induced transpareny

Optomechanical induced transparency (OMIT) in an optomechanical system is an analogue of electromagnetically induced transparency first observed in absorption spectra of gas-phase atomic medium [14]. In electromagnetically induced transparency, the absorption of the electromagnetic field is canceled by applying another electromagnetic field detuned adequately from the resonance of the cavity. Understanding the physics behind EMIT can simplify our

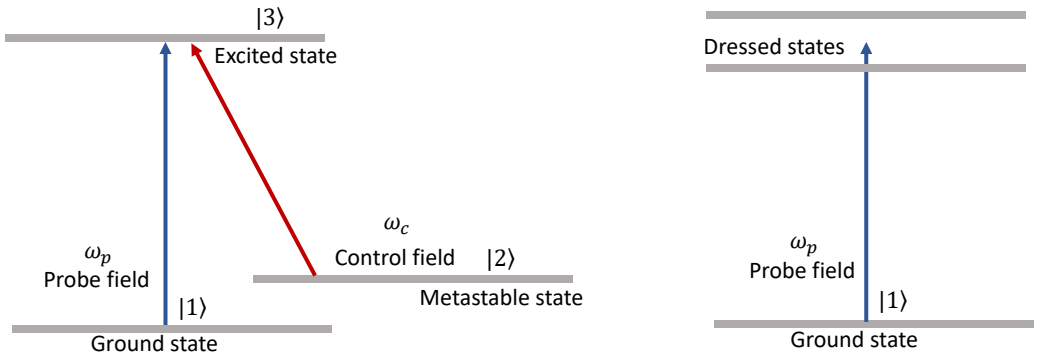

FIGURE 4.1: (left) Bare state picture of λ type three level system. After the control field is on we can transform the bare state picture of the system to dressed state system (right)

understanding of OMIT. EMIT has long been observed in atomic gases [33], atomic and molecular systems [52], solid-state systems [43], superconductors [4], plasmonics [86], photonic crystals [82], etc. In a gas phase medium consisting of a 3 level atomic ensemble [32], the absorption spectra are canceled by an auxiliary field due to quantum interference phenomena where the transition amplitudes between different pathways destructively interfere.

Consider a λ type 3 level atomic system shown in figure 4.1. $|1\rangle$ is the ground state, $|2\rangle$ is the metastable state, and $|3\rangle$ is the excited state. The transitions $|1\rangle$-$|3\rangle$ and $|2\rangle$-$|3\rangle$ are allowed and $|1\rangle$-$|2\rangle$ is dipole forbidden. The states $|1\rangle$ and $|3\rangle$ are coupled by weak probe field while the states $|2\rangle$ and $|3\rangle$ are coupled by strong control field. The strong control field coupling between $|2\rangle$ and $|3\rangle$ induces a dressed state as shown in figure 4.1. Once the control field is on, there is splitting in the excited state level, thus leading to the formation of so-called dark state. In other words, the contribution from these two split levels is equal and opposite in sign, thus leading to the cancellation of the response opening a transition window. The energy splitting between these two split levels is proportional to the amplitude of the control field. If we increase the amplitude of the control field, the transparency window in the response also increases. To discuss the mathematics and the derivation of the transmission spectrum is currently beyond the scope of this thesis. The optomechanically induced transparency where the MWC is coupled to NEMS can also be represented in the same picture.

In one of the early experimental evidence of EMIT shown in figure 4.2 Harris *et al.* [28] observed EMIT on collisionally broadened resonance line of PB vapor. They observed that by applying a 1064-nm laser beam, the transmission at 283 nm is increased by at least a factor of e^{10}, with nearly all of the Pb atoms remaining in the ground state.

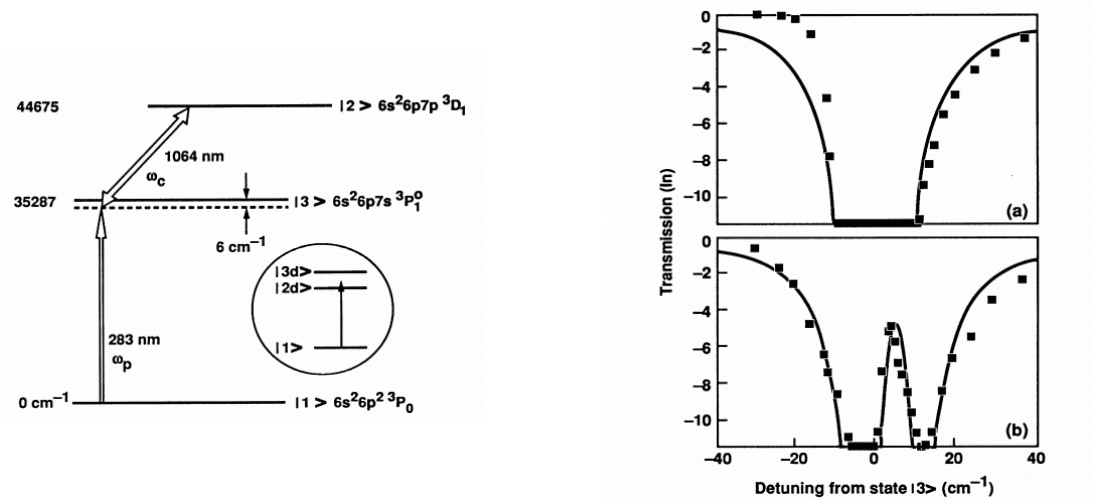

FIGURE 4.2: (left) Energy-level diagram of neutral Pb atoms (inset : Dressed state picture) (right) Transmission versus probe laser detuning at 18 torr. In the upper plot the control field is off while in lower plot the control field is on. The solid line represents the fitted transmission spectrum

4.3 Summary of previous works on OMIT and OMIA

In one of the early demonstrations of OMIT, Weis *et al.* [78] observed OMIT in toroidal whispering-gallery-mode microresonators illuminated by a laser operating at a wavelength of 775 nm. They measured the transmission of the cavity for different control/pump frequencies at constant control power of 0.5 mW. They varied the control power from 0.125 mW to 6.5 mW at constant control frequency. Their experimental observations were in agreement with their theoretical model. Following this work, Teufel *et al.* [74] performed a similar experiment but with the superconducting circuit, Al drum as the mechanical degree of freedom and microwaves. They performed the two-tone measurements and demonstrated the OMIT and subsequently split in the microwave cavity's transmission by entering the strong coupling regime. Shortly after that, an analysis of the use of OMIT for microwave amplification, as well as the observation of OMIA at microwave frequencies, was presented by Massel *et al.* [50] . Any detector or amplifier necessarily adds a certain amount of noise. This noise can be equal or at least the noise added by quantum fluctuations. Massel *et al.* studied the dependence of probe transmission on pump power and demonstrated an overall gain of 25 dB with 20 quanta of added noise. Hocke *et al.* [35] focused on microwave OMIA and reported transmission as a function of detuning and drive power up to mechanical parametric instability. Zhou *et al.* [88] returned to microwave OMIT and scanned the probe power, thereby driving the mechanical resonator strongly enough so that its Duffing non-linearity became significant. They also realized the slowing and advancing of microwave signals with millisecond distortion-free delay

and negligible losses. They also showed that by temporally modulating the electromechanical coupling and correspondingly the transparency window, switching of microwave signals could be demonstrated. Recent work has demonstrated the advantage of combining mechanical parametric amplification with OMIT [15] and microwave amplification in the absence of dynamical backaction responsible for amplification of mechanical motion [23].

4.4 Theory: OMIT/OMIA

As discussed before, OMIT and OMIA can be observed in systems where a mechanical resonator is coupled to an electromagnetic resonator (the cavity) so that the motion of the former changes the resonance frequency of the latter. The interaction between a single phonon and a single photon is characterized by g_0, the vacuum optomechanical coupling strength, which is the frequency shift of the cavity due to a zero-point motion of the mechanical resonator. When the cavity is driven by a pump at frequency ω_d and a probe at frequency ω_p (Fig. 4.3), there is a component of the resulting radiation pressure force at the difference frequency $\Omega = \omega_p - \omega_d$. We denote the mechanical resonance frequency by Ω_m. When $||\Omega| - \Omega_m|$ is less than or approximately equal to the mechanical linewidth, the response of the mechanical element is appreciable. Now its motion yields up-conversion or down-conversion of the photons by an amount $|\Omega|$, yielding sidebands in the microwave spectrum. One of the two sidebands of the pump is at a frequency that coincides with the probe frequency. Whether this is the upper or lower sideband depends on the sign of Ω. The probe and the coincident sideband interfere constructively or destructively depending on their relative phases, resulting in a change in the transmission of the probe relative to the value it would have in the absence of optomechanical coupling. This effect is most significant when the probe frequency is within about one-half linewidth κ_{total} of the cavity resonance frequency ω_c. This is equivalent to $|\Delta + \Omega| <\approx \frac{\kappa_{total}}{2}$, where we define $\Delta = \omega_d - \omega_c$.

The magnitude of the response of the mechanical resonator to the radiation pressure at the beat frequency Ω influences the probe transmission. The mechanical response depends not only on the difference between the driving frequency and the mechanical resonance $|\Omega| - \Omega_m$ and the intrinsic linewidth of the mechanical resonator Γ_m but also on dynamical backaction due to the pump [8]. The backaction yields an effective mechanical linewidth Γ_{eff}, which is greater than Γ_m for $\omega_c - \omega_d \approx \Omega_m$ ("red pumping") and less than Γ_m for $\omega_c + \omega_d \approx \Omega_m$ ("blue pumping").

We will now proceed to derive the probe transmission, which is generally denoted as S_{21}. S_{21} can be derived by solving the coupled quantum Langevin equation for cavity and mechanical resonator (as done in the chapter Theory: quantum noise in microwave optomechanics to derive

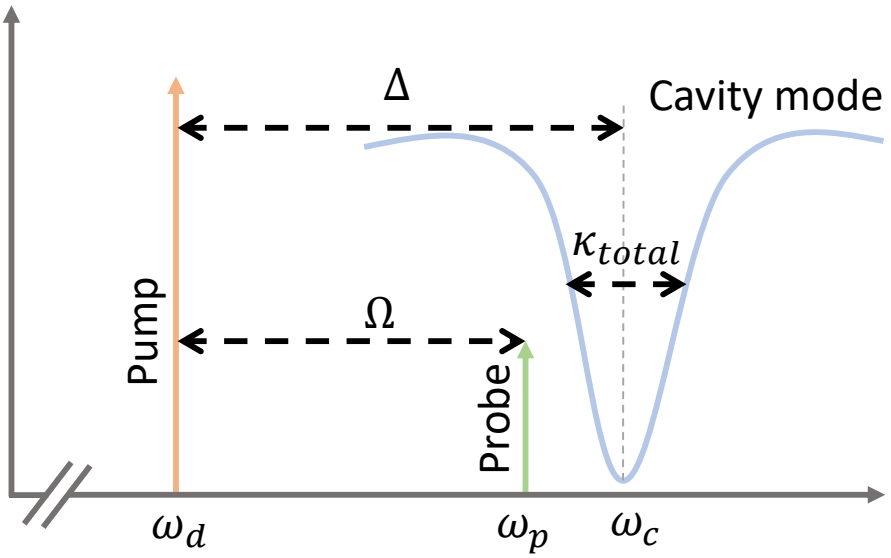

FIGURE 4.3: The pump and the probe scheme for two tone measurements for observing OMIT/OMIA.

the noise spectrum). We will use the quantum Langevin equation for the cavity and the classical equation of motion for the mechanical resonator. The quantum Langevin equation for MWC is given as,

$$\dot{a} = -\frac{i}{\hbar}[a, H_{sys}] - \frac{\kappa_{total}}{2}a - \sqrt{\kappa_l}\alpha_{in,l} - \sum_{k=l,r,0}\sqrt{\kappa_k}\delta a_{in,k} \tag{4.1}$$

where $H_{sys} = \hbar\omega_c a^\dagger a + \hbar\Omega_m b^\dagger b + \hbar g_0(b+b^\dagger)a^\dagger a$ and $g_0(b+b^\dagger) = Gx$. Putting H_{sys} in equation 4.1 we get,

$$\dot{a} = -(i\omega_c + \frac{\kappa_{total}}{2})a - iGxa - \sqrt{\kappa_l}\alpha_{in,l} - \sum_{k=l,r,0}\sqrt{\kappa_k}\delta a_{in,k} \tag{4.2}$$

In the above equation we have the input field as $a_{in,l} = \alpha_{in,l} + \delta a_{in,l}$ where $\alpha_{in,l}(t) = \alpha_{in}e^{-i\omega_d t}e^{-i\phi}$ is the driving field and $\delta a_{in,l}(t)$ is the fluctuating term. The cavity field can be written as $a = \alpha e^{-i\omega_d t} + \delta a$. Similarly we can write the classical equation of motion for NEMS as,

$$\frac{dx}{dt} = \frac{p}{m_{eff}} \tag{4.3}$$

$$\frac{dp}{dt} = -m_{eff}\Omega_m^2 x(t) - F_{RP} - \Gamma_m p \tag{4.4}$$

In the above equations, x and p are position and momentum operators of the mechanical degree of freedom with effective mass m_{eff}. F_{RP} is the radiation pressure force which is equal to $\hbar G a^\dagger a$. Analogous to cavity field, the displacement x can be written in terms of static displacement x_{shift} and fluctuation term δx. As done previously, we can solve for intracavity field α and

static mechanical displacement x_{shift}.

$$\alpha = -\frac{\kappa_l \alpha_{in} e^{-i\phi}}{i(\omega_c^{'} - \omega_d) + \frac{\kappa_{total}}{2}} \tag{4.5}$$

$$m_{eff}\Omega_m^2 x_{shift} + \hbar G|\alpha|^2 = 0 \tag{4.6}$$

where $\omega_c^{'} = \omega_c - G x_{shift}$. We can now write equations of motion for cavity and NEMS by considering the noise terms similar to what we did while computing the noise spectrum in previous chapter.

$$\delta\dot{a} = -i(\omega_c^{'} + \frac{\kappa_{total}}{2})\delta a - iG\delta x(\alpha e^{-i\omega_d t} + \delta a) - \sum_{k=l,r,0}\sqrt{\kappa_k}\delta a_{in,k}(t) \tag{4.7}$$

$$m_{eff}\left(\frac{d^2\delta x}{dt^2} + \Gamma_m\frac{d\delta x}{dt} + \Omega_m^2\delta x\right) = -\hbar G\alpha(\delta a e^{i\omega_d t} + \delta a^{\dagger} e^{-i\omega_d t}) \tag{4.8}$$

The time dependence of above equations can be eliminated by writing equations 4.7 and 4.8 in the frame rotating with ω_d. Thus equations 4.7 and 4.8 are modified as,

$$\delta\dot{a} = (i\Delta - \frac{\kappa_{total}}{2})\delta a - iG\delta x(\alpha + \delta a) - \sum_{k=l,r,0}\sqrt{\kappa_k}\delta a_{in,k} \tag{4.9}$$

$$m_{eff}\left(\frac{d^2\delta x}{dt^2} + \Gamma_m\frac{d\delta x}{dt} + \Omega_m^2\delta x\right) = -\hbar G\alpha(\delta a + \delta a^{\dagger}) \tag{4.10}$$

We will solve the above coupled equations in the presence of pump field at ω_d and a probe field at ω_p and neglect all the fluctuations. We denote the probe field as $\delta\beta$. The above coupled equations then become,

$$\delta\dot{a} = (i\Delta - \frac{\kappa_{total}}{2})\delta a - iG\delta x(\alpha + \delta a) - \sqrt{\kappa_l}\delta\beta \tag{4.11}$$

$$m_{eff}\left(\frac{d^2\delta x}{dt^2} + \Gamma_m\frac{d\delta x}{dt} + \Omega_m^2\delta x\right) = -\hbar G\alpha(\delta a + \delta a^{\dagger}) \tag{4.12}$$

For a given $\Omega = \omega_p - \omega_d$, and a probe field $\delta\beta = Be^{-i\Omega t}$ we use the ansatz,

$$\begin{aligned} \delta a &= A^- e^{-i\Omega t} + A^+ e^{i\Omega t} \\ \delta a^* &= (A^+)^* e^{-i\Omega t} + (A^-)^* e^{i\Omega t} \\ \delta x &= X^- e^{-i\Omega t} + X^+ e^{i\Omega t} \end{aligned} \tag{4.13}$$

Putting the above ansatz in the coupled equations 4.11 and 4.12 and writing only the terms with $e^{-\Omega t}$ we get the following eqautions,

$$\begin{aligned} A^{-}\left(-i(\Omega+\Delta)+\kappa_{total}/2\right) &= -iG\alpha X-\sqrt{\kappa_l}B \\ A^{+}\left(i(\Omega-\Delta)+\kappa_{total}/2\right) &= -iG\alpha X^{*} \\ m_{eff}\left(\Omega_m^2-\Omega^2-i\Gamma_m\Omega\right)X &= -\hbar G\alpha(A^{-}+(A^{+})^{*}) \end{aligned} \tag{4.14}$$

We can further define the cavity susceptibilities as $\chi_c(\Omega)$ and $\chi_a(\Omega)$ and mechanical susceptibility as $\chi_m(\Omega)$.

$$\begin{aligned} \chi_c(\Omega) &= \frac{\kappa_{total}}{2}-i(\Omega+\Delta) \\ \chi_a(\Omega) &= \frac{\kappa_{total}}{2}-i(\Omega-\Delta) \\ \chi_m(\Omega) &= \frac{\Gamma_m}{2}-i(\Omega-\Omega_m) \end{aligned} \tag{4.15}$$

Equation 4.14 can be rewritten with an approximation $\Omega\approx\Omega_m$ as,

$$\begin{aligned} \chi_c(\Omega)A^{-} &= -iG\alpha X+\sqrt{\kappa_l}B \\ \chi_m(\Omega)(A^{+})^{*} &= iG\alpha X \\ 2m_{eff}\Omega_m\chi_m(\Omega)X &= -i\hbar G\alpha(A^{-}+(A^{+})^{*} \end{aligned} \tag{4.16}$$

Solving the set of above equations we can obtain,

$$A^{-}=\sqrt{\kappa_l}B\frac{\chi_c(\Omega)(1-g_0^2\alpha^2\chi_m(\Omega)\chi_a(\Omega))}{1+g_0^2\alpha^2\chi_m(\Omega)(\chi_c(\Omega)-\chi_a(\Omega))} \tag{4.17}$$

Following the input-output relation we can thus write the probe transmission as,

$$S_{21}=1-\kappa_l\frac{\chi_c(\Omega)(1-g_0^2\alpha^2\chi_m(\Omega)\chi_a(\Omega))}{1+g_0^2\alpha^2\chi_m(\Omega)(\chi_c(\Omega)-\chi_a(\Omega))} \tag{4.18}$$

For the case of sideband resolved system we can neglect A^{+} and up with a simplified version of S_{21} which is,

$$S_{21}=1-\kappa_l\frac{\chi_c(\Omega)}{1+g_0^2\alpha^2\chi_m(\Omega)\chi_c(\Omega)} \tag{4.19}$$

Expanding the above equation we get,

$$S_{21}=1-\frac{\frac{\kappa_{ext}}{2}}{\frac{\kappa_{total}}{2}-i(\omega_p-\omega_c)+\frac{g_0^2\alpha^2}{\Gamma_m/2-i(\omega_p-\omega_d-\Omega_m)}} \tag{4.20}$$

We can do the similar analysis for blue pumping where $\Delta > 0$ and S_{21} for the same is,

$$S_{21} = 1 - \frac{\frac{\kappa_{ext}}{2}}{\frac{\kappa_{total}}{2} - i(\omega_p - \omega_c) - \frac{g_0^2\alpha^2}{\Gamma_m/2 - i(\omega_p - \omega_d + \Omega_m)}} \tag{4.21}$$

4.5 Experimental setup

Our optomechanical device and microwave measurement circuit are similar to ones used in previous works. A circuit diagram is shown in figure 4.4. The pump and probe tones are combined at room temperature. These signals then pass through attenuators, which decrease the thermal noise, and a bandpass filter before reaching the input port of the experimental cell. The pump signal is attenuated by approximately 59.5 ± 0.5 dB, while the probe tone is attenuated by approximately 56.5 ± 0.5 dB. The estimate of these attenuations was obtained by carefully measuring the attenuation of every single component in the driving side. The transmitted signal that exits the cell passes through two circulators, which prevent the noise traveling down the detection line from entering the output port of the cell. At the 4 kelvin plate, the pump signal that was transmitted through the cell is canceled to avoid saturating the amplifiers. The resulting signal passes through the series of high electron mobility transistor (HEMT) amplifier installed at 4-kelvin plate and room temperature before detecting the signal by the spectrum analyzer.

The experimental cell is a box made of annealed Cu. It is pressed against the mixing chamber plate of the cryogen-free dilution refrigerator. Inside the cell, the input and output coaxial transmission lines are soldered to gold coplanar waveguides (CPW) on a circuit board, which are in turn microbonded to the ends of a niobium CPW on a chip. The chip is made of silicon and is coated with 100 nm of high-stress silicon nitride. A $\frac{\lambda}{4}$ CPW resonator is also present on the chip and forms a cavity with resonance frequency $\frac{\omega_c}{2\pi} = 6$ GHz. The open end of the $\frac{\lambda}{4}$ resonator is precisely situated relative to the CPW feedline to achieve the desired coupling. The strength of the coupling is characterized by an external cavity linewidth $\frac{\kappa_{ext}}{2\pi} = 44$ kHz. The total cavity linewidth is $\frac{\kappa_{total}}{2\pi} \approx 100$ kHz, so that the coupling is nearly critical.

The mechanical element is a vibrating string made from silicon nitride at the open end of the cavity (Fig. 1c). Its geometry was defined by a 30 nm thick aluminum layer that served as a reactive ion etch (RIE) mask. After the anisotropic RIE, the string was released by selective XeF2 etching of the silicon substrate. The aluminum was not removed after etching, and it

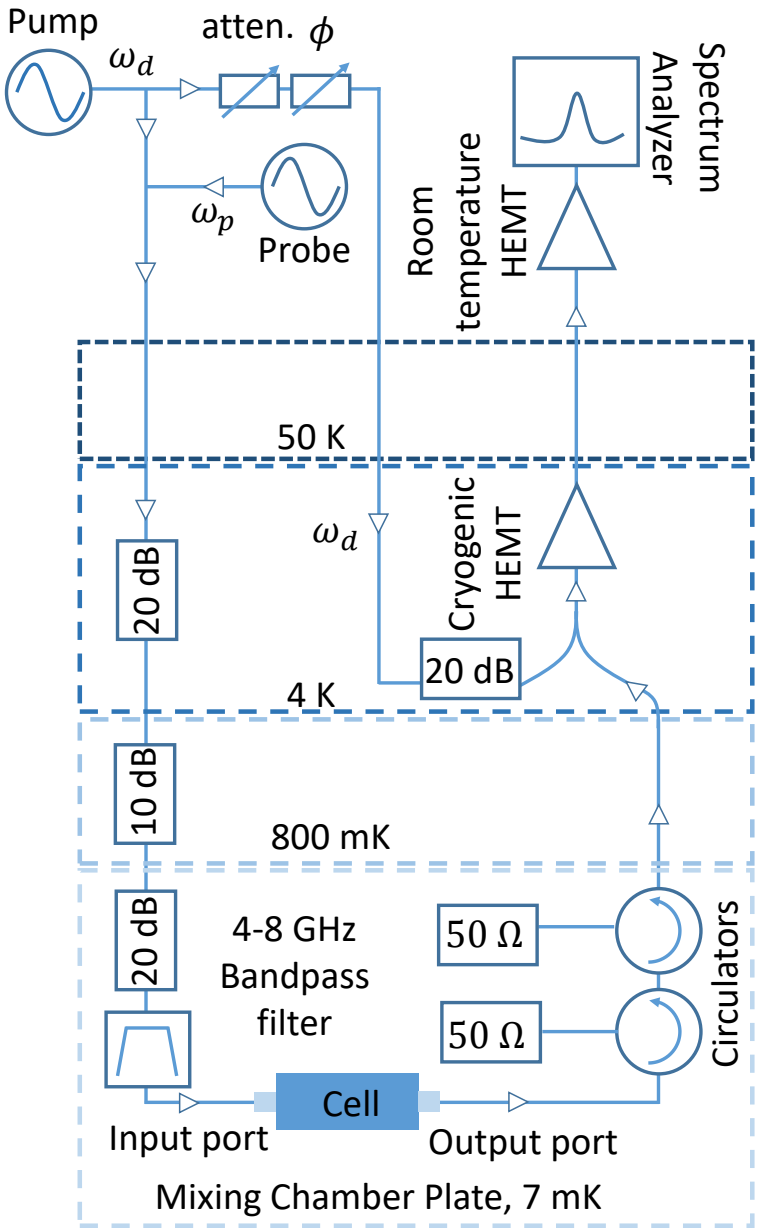

FIGURE 4.4: The microwave circuit

yields electrostatic coupling between the vibrating string and the cavity characterized by the coupling strength $\frac{g_0}{2\pi} = 0.56$ Hz. The string has a length of 50 μm and a resonance frequency $\frac{\Omega_m}{2\pi} = 3.8$ MHz. The detailed parameters for fabrication can be found in previous chapter.

4.6 Results and Discussion

The measurements were carried out at sample temperatures of 250, 350, and 450 mK. For each temperature, pump power, and probe power setting, the pump and probe frequencies were

scanned, and the probe transmission was measured. Figure 4.5 shows our measurements at 250 mK with red pumping yielding $n_{cav} = 1.3 \times 10^6$ and a probe power of -116 dBm at the input of the cell. The transmission measurements were made by setting ω_d and sweeping the probe frequency ω_p over a narrow range around $\omega_d + \Omega_m$ for red pumping and around $\omega_d - \Omega_m$ for blue pumping. The width of the probe frequency sweeps was comparable to the mechanical linewidth, so that it encompassed the OMIT/OMIA resonance. These measurements were made at a range of pump frequencies ω_d such that the set of center frequencies of the narrow probe frequency sweeps spanned the microwave resonance. These narrow sweeps appear as vertical lines on the scale of the main panel of figure 4.5; two of the sweeps are enlarged in the insets.

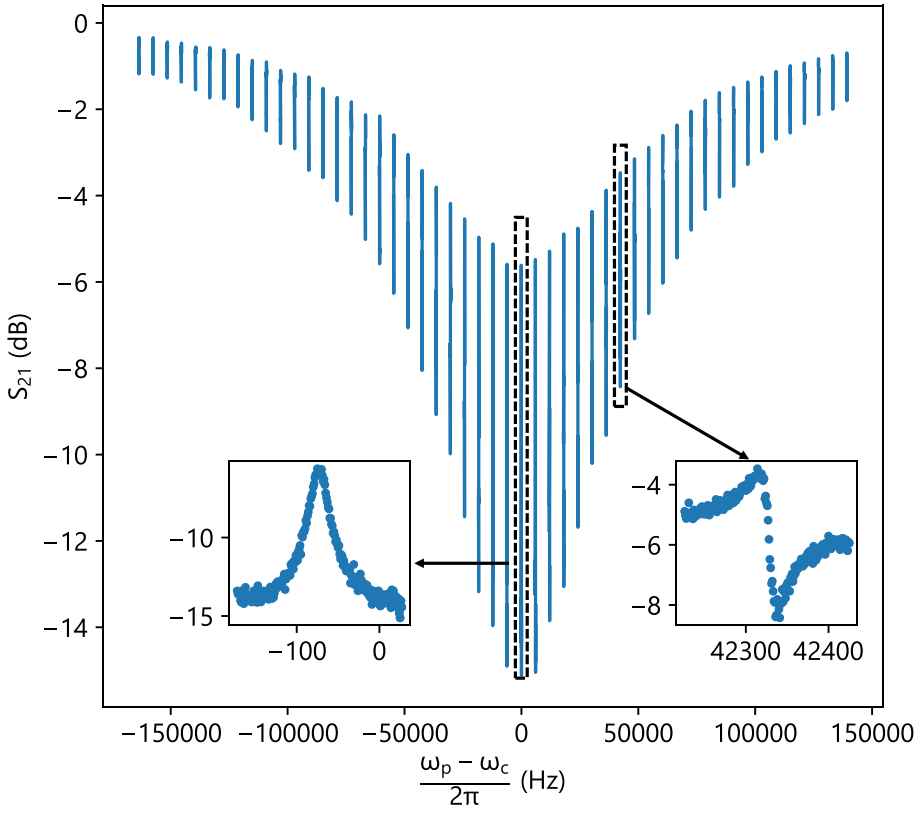

FIGURE 4.5: Probe transmission measurements at 250 mK with red pumping yielding $n_{cav} = 1.3 \times 10^6$ and a probe power of -116 dBm at the input of the cell. The narrow probe frequency sweeps appear as vertical lines. The insets show enlargements of the indicated sweeps.

Figure 4.6 shows OMIT at the microwave resonance. Any residual detuning is very small compared with the cavity linewidth. These data were acquired under red pumping ($\omega_d =$

$\omega_c - \Omega_m$), and the dependence on temperature, probe power and pump power is shown. The intracavity pump photon numbers and probe powers at the input of the cavity are based on a careful measurement of the attenuation of the transmission line connecting the generator to the microwave cavity. At constant temperature and probe power the amplitude of the OMIT resonance increases with pump power because (1) the mechanical mode is driven more strongly and (2) more pump photons are available for up-conversion to the probe frequency by interaction with the mechanical mode. The resulting upper sideband interferes constructively with the probe. The width of the OMIT resonance increases with pump power due to dynamical backaction on the mechanical mode. The curves represent fits of the theoretical $|S_{21}|$ (Equation 4.20) to the data. Single values of Ω_m and Γ_m were chosen for each temperature to optimize the fits of the theoretical transmission to the entirety of our measurements of this device. At 350 (450) mK, $\frac{\Omega_m}{2\pi}$ is higher than its 250 mK value by 7 (12) Hz. The intrinsic mechanical linewidths $\frac{\Gamma_m}{2\pi}$ at 250, 350 and 450 mK are 15.3, 20.0 and 26.8 Hz, respectively.The values of ω_c and κ_{total} were allowed to vary to account for the dependence of these parameters on cavity temperature and photon population. The dependence of κ_{total} on probe power is primarily responsible for the dependence of the transmission on probe power shown in figure 4.6.

Figure 4.7 shows OMIA on the microwave resonance at the same probe powers and temperatures as in Fig. 3. These data were acquired under blue pumping ($\omega_d = \omega_c + \Omega_m$). As for red pumping, the driving force acting on the string and the number of pump photons stored in the cavity increase with pump power. But for blue pumping the lower sideband interferes destructively with the probe, yielding decreased transmission of the probe in figure 4.7. Furthermore, the width of the optomechanical resonance decreases with pump power due to dynamical backaction on the mechanical mode. At pump powers that are higher than those shown in figure 4.7, Γ_{eff} vanishes and the mechanical mode undergoes self-sustained oscillations. The curves represent fits of the theoretical $|S_{21}|$ (equation 4.20) to the data, where the values of Ω_m and Γ_m at each temperature are the same as the ones used to fit the red pumping data (Figure 4.6).

The theoretical transmission is also in excellent agreement with our measurements made further from the microwave resonance. The top row of panels in figure 4.8 shows $|S_{21}|$ as a function of Ω and Δ at the maximum red pumping power ($n_{cav} = 1.3 \times 10^6$) and the specified temperatures and probe powers. Horizontal line cuts in this figure correspond to particular pump frequencies ω_d and narrow sweeps of ω_p centered on $\omega_d + \Omega_m$. Thus each spectrum appearing as a vertical line in figure 4.5 corresponds to a horizontal line-cut at a particular value of Δ in the upper-left panel of figure 4.10.

In figures 4.6 and 4.8, the OMIT signal decreases significantly, as expected, when the frequency of the upper mechanical sideband of the pump is not well-aligned with the microwave

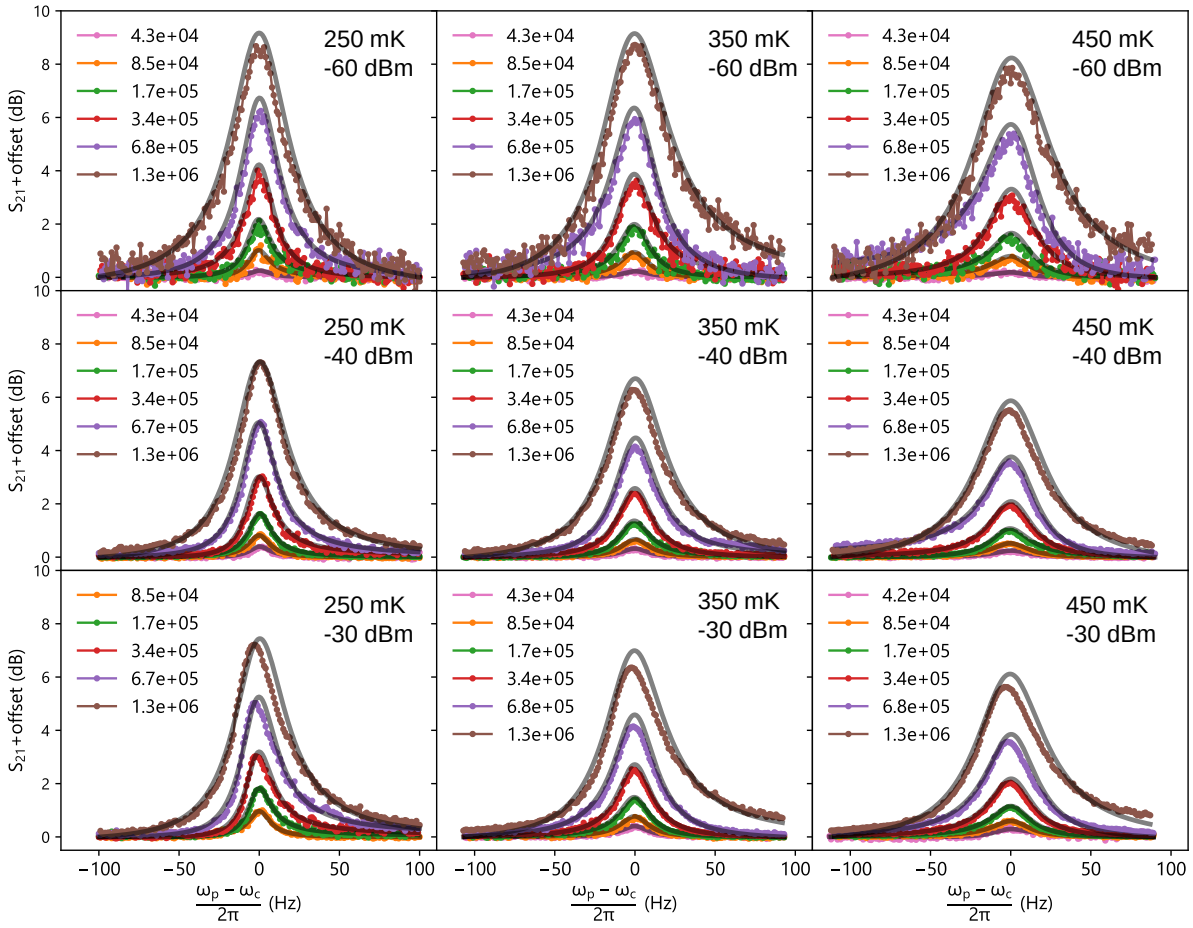

FIGURE 4.6: Main panel: Probe transmission measurements at the indicated temperatures and probe powers referenced to the input of the cavity. Red pumping was applied, yielding the specified intracavity pump photon numbers. The transmission curves are offset vertically for clarity. Grey curves are fits of equation 4.20 to the data.

resonance. In figure 4.6 this condition corresponds to the left and right extremities of the plot and in figure 4.8 it corresponds to the upper and lower extremities of each panel. The fact that the size of the OMIT resonance is figure 4.8 is largest for $|\Delta/\Omega_m + 1| <\approx 0.5\kappa_{total}/\Omega_m \approx 10^{-2}$ follows from the condition $|\Delta + \Omega| <\approx \kappa_{total}/2$.

The black dashed lines in figure 4.8 are at the optimal pump detuning $\Delta = \Omega_m$ and correspond to data shown in the top row and left column of panels of figure 4.6. Note that for the pump detuning $\omega_d = \omega_c - \Omega_m$ used in figure 4.6 the quantity on the x-axis of that figure $(\omega_p - \omega_c)$ is equivalent to the one on the x-axis of figure 4.8 $(\Omega - \Omega_m)$. Thus we have already demonstrated excellent agreement between theory and the data along the black dashed lines in figure 4.8. The panels in the bottom row of figure 4.8 demonstrate the same level of agreement for the case where the upper mechanical sideband of the pump is slightly detuned from the

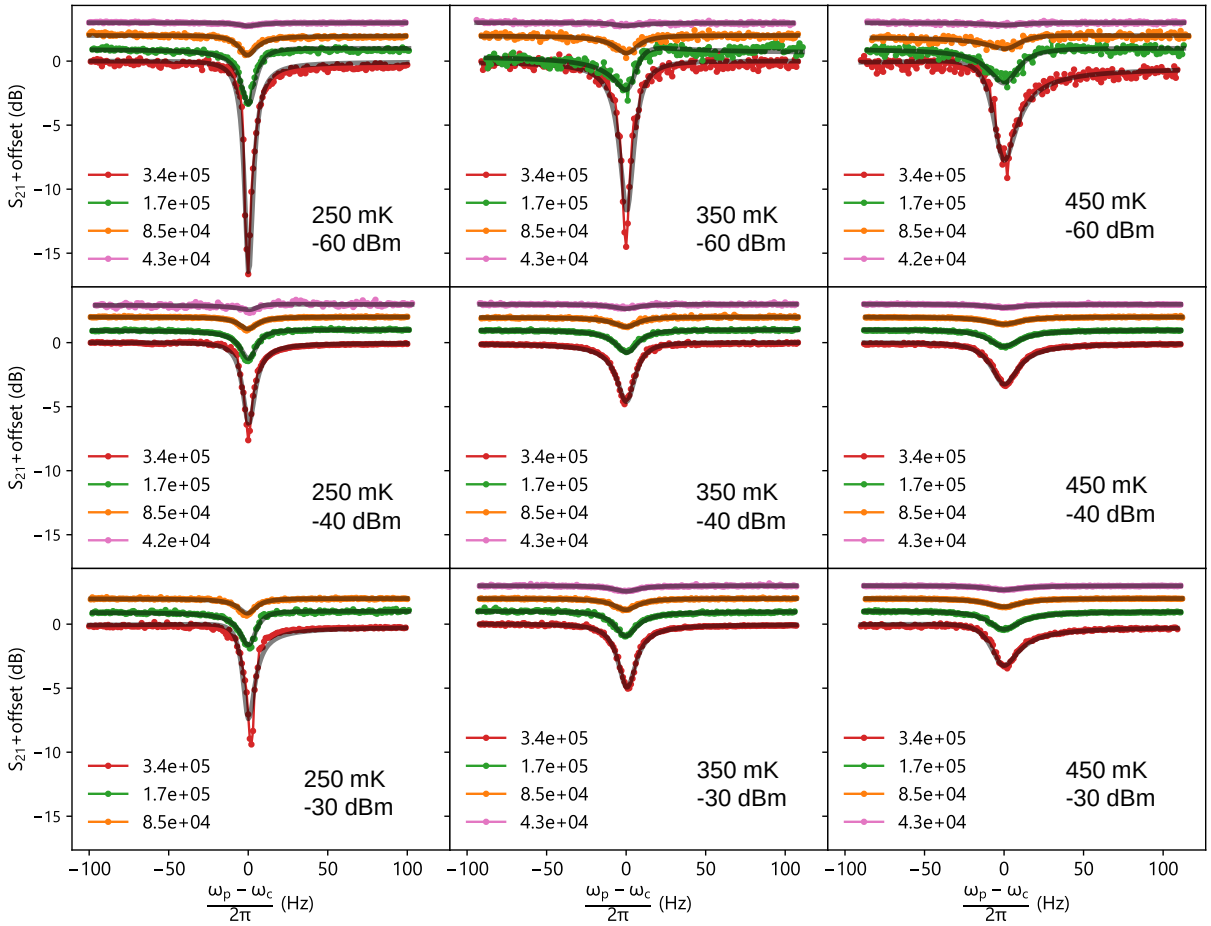

FIGURE 4.7: Probe transmission measurements at the indicated temperatures and probe powers referenced to the input of the cavity. Blue pumping was applied, yielding the specified intracavity pump photon numbers. The transmission curves are offset vertically for clarity. Grey curves are fits of equation 4.20 to the data.

microwave resonance. These panels show $|S_{21}|$ from equation 4.20 with the values of Ω_m and Γ_m corresponding to the temperatures given in the respective upper panels and the indicated best-fit values of κ_{total} and ω_c.

The top row of panels in figure 4.10 shows $|S_{21}|$ as a function of Ω and Δ at the maximum blue pumping power ($n_{cav} = 3.4 \times 10^5$) and the specified temperatures and probe powers. The panels in the bottom row of figure 4.10 show $|S_{21}|$ from equation 4.20 with the values of Ω_m and Γ_m corresponding to the temperatures given in the respective upper panels and the indicated best-fit values of κ_{total} and ω_c. The agreement between theory and experiment is again excellent.

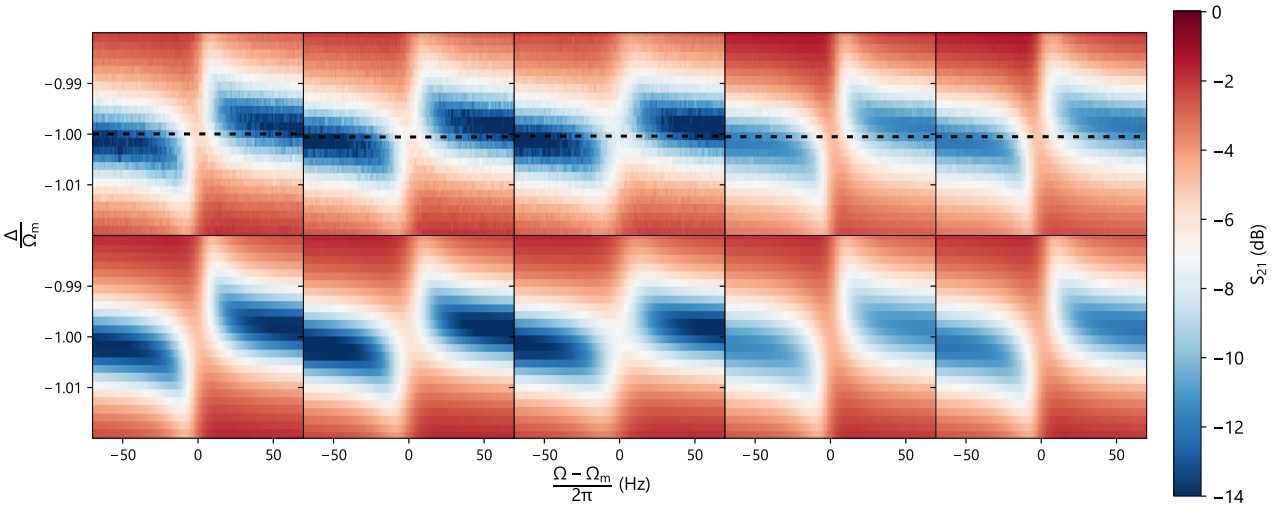

FIGURE 4.8: Measured (upper panel) and theoretical (lower panel) probe transmission at the maximum red pumping power ($n_{cav} = 1.3\times10^6$). From left to right the values of [temperature (mK), probe power (dBm),κ_{total} (kHz) and $\Delta\omega_c$(kHz)] are [250,- 116,84,0],[350,-116,82,52],[450,-116,83,93],[250,-96,96,-10],[250,-86,95,-9], where $\Delta\omega_c$ is the shift in ω_c relative to its value in the leftmost panels. The black dashed lines correspond to data shown in the top row and left column of panels of figure 4.6.

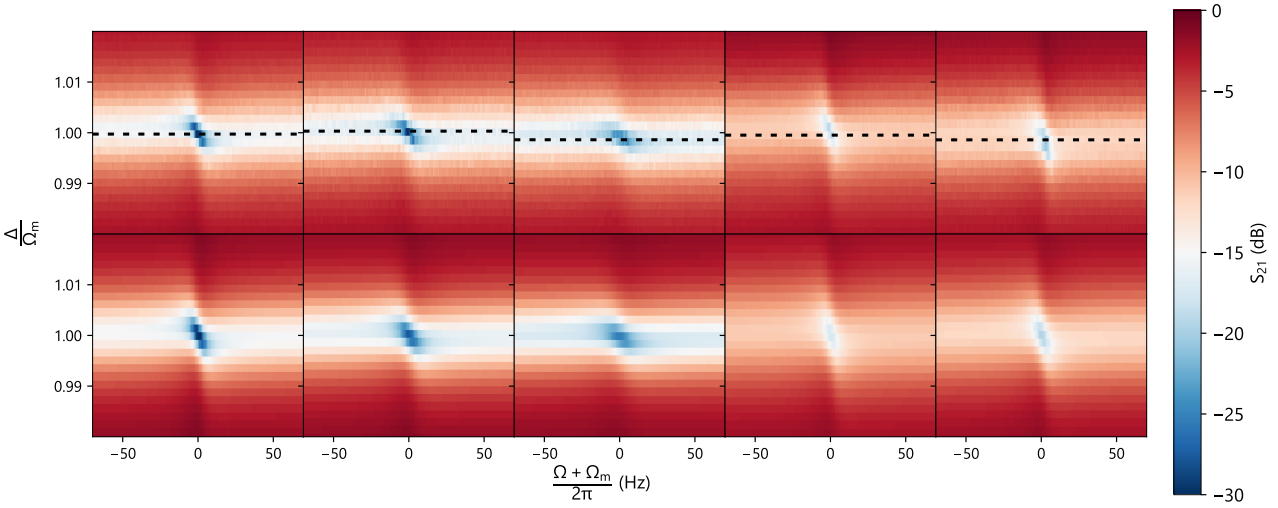

FIGURE 4.9: Measured (upper panel) and theoretical (lower panel) probe transmission at the maximum blue pumping power ($n_{cav} = 3.4 \times 10^5$). From left to right the values of [temperature (mK), probe power (dBm),κ_{total} (kHz) and $\Delta\omega_c$ (kHz)] are [250,- 116,83,0],[350,-116,80,37],[450,-116,78,80],[250,-96,103,-17],[250,-86,98,-19], where $\Delta\omega_c$ is the shift in ω_c relative to its value in the leftmost panels. The black dashed lines correspond to data shown in the top row and left column of panels of figure 4.7

4.6.1 Non-linear OMIA at high pump powers

Although we had an excellent agreement with theory and experiments for OMIT and OMIA measurements, we were unable to fit the OMIA data for high pump powers at 250 mK. As shown in figure 4.10 we observed duffing type non-linearity in transmission while pumping blue i.e. at $\omega_c + \Omega_m$. The pump power referenced to the output of the microwave generator was -4 dBm leading to $n_{cav} \sim 1.3 \times 10^6$ photons in the cavity. The probe power was -116 dBm at the input of the cell. The intrinsic linewidth was same as discussed before i.e. $\frac{\Gamma_m}{2\pi} = 15.3$ Hz. The transmission was linear while pumping red i.e. at $\omega_c - \Omega_m$ and there is an excellent agreement with the theory with the same pump and probe powers used. S_{21} can be derived

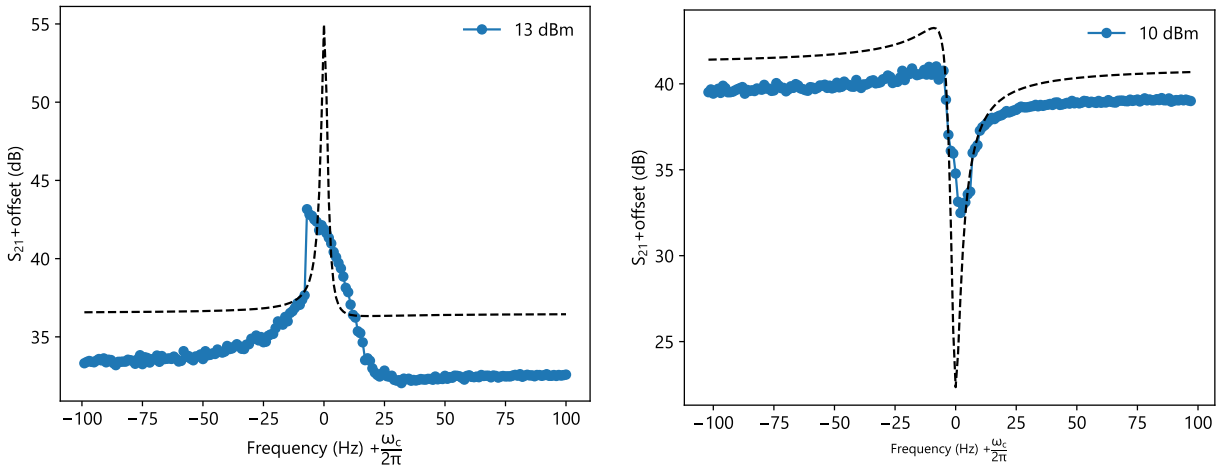

FIGURE 4.10: Probe transmission measurements at 250 mK and pump powers referenced to the generator indicated in the plot . Blue pumping was applied. The transmission curves are offset vertically for clarity. Dotted black curves are fits of equation 4.20 to the data

again by introducing a non-linear term in the mechanical equation of motion [88]. Eqaution 4.4 is now modified consisting of duffing nonlinear term as,

$$\frac{dp}{dt} = -m_{eff}\Omega_m^2 x(t) - F_{RP} - \Gamma_m p - Dx^3(t) \tag{4.22}$$

where D is the duffing non-linear parameter which depends on material and the geometry. Solving for intracavity field and static mechanical displacement x_{shift} as done previously in this chapter yields,

$$\alpha = -\frac{\kappa_l \alpha_{in} e^{-i\phi}}{i(\omega_c' - \omega_d) + \frac{\kappa_{total}}{2}} \tag{4.23}$$

$$m_{eff}\Omega_m^2 x_{shift} + \hbar G|\alpha|^2 + Dx_{shift}^3 = 0 \tag{4.24}$$

The dynamical equations in the frame rotating with ω_d are now given as,

$$\delta\dot{a} = (i\Delta - \frac{\kappa_{total}}{2})\delta a - iG\delta x(\alpha + \delta a) - \sqrt{\kappa_l}\delta\beta \tag{4.25}$$

$$m_{eff}\left(\frac{d^2\delta x}{dt^2} + \Gamma_m\frac{d\delta x}{dt} + \Omega_m^2\delta x\right) = -\hbar G\alpha(\delta a + \delta a^\dagger) - D\delta x^3 - 3Dx_{shift}^2\delta x - 3D\delta x^2 x_{shift} - \hbar G\delta a\delta a^\dagger \tag{4.26}$$

Using the same ansatz as described in equation 4.14 and writing only the terms with $e^{-i\Omega t}$ we get the following equations,

$$A^-\left(-i(\Omega + \Delta) + \kappa_{total}/2\right) = -iG\alpha X + \kappa_l B \tag{4.27}$$

where we have defined B before.

$$m_{eff}\left(\Omega_m^2 - \Omega^2 - i\Gamma_m\Omega\right)X + 3DX^3 = -A^-\alpha g_0\sqrt{2\Omega\hbar}m_{eff} \tag{4.28}$$

Using some algebra and putting the value of A^- from equation 4.27 in equation 4.28 we get the following equation of motion under blue pumping,

$$m_{eff}\left(\Omega_m^2 - \Omega^2 - i(\Gamma_m - \frac{4g^2}{\kappa_{total}})\Omega\right)X + 3DX^3 = \frac{2\hbar\alpha G\sqrt{\kappa_l}B}{\kappa_{total}} \tag{4.29}$$

Since under blue pumping, $\Gamma_{eff} = \Gamma_m - \dfrac{4g^2}{\kappa_{total}}$ we can further write the above equation as,

$$m_{eff}\left(\Omega_m^2 - \Omega^2 - i\Gamma_{eff}\Omega\right)X + 3DX^3 = \frac{2\hbar\alpha G\sqrt{\kappa_l}B}{\kappa_{total}} \tag{4.30}$$

Equation 4.30 is a general equation of motion with duffing nonlinear terms. The displacement of the mechanical resonator depends on Γ_{eff} rather than intrinsic linewidth Γ_m. Since for red pumping scheme, $\Gamma_{eff} = \Gamma_m + \dfrac{4g^2}{\kappa_{total}}$ which is greater than Γ_{eff} while pumping blue, we concluded that there is no nonlinearity under the same conditions while pumping red. We then tried to fit the data with the nonlinear theory and could not get a good fit. It would be interesting to acquire more data in the nonlinear regime to further study the nonlinearity in the OMIA measurements, which is the work for the future.

4.7 Conclusions

Nanomechanical resonators coupled to microwave cavities by radiation pressure constitute ideal systems for microwave amplification and absorption. The amplifiers or filters can have a very

low noise level or a very narrow bandwidth, and the gain or attenuation depends very strongly on pump power. Our measurements confirm the applicability of the theoretical transmission Eq. 1 to a larger parameter space than has been covered in previous works. We demonstrated excellent agreement with theory over a wide range of probe frequencies, pump frequencies, probe powers, pump powers and temperatures for both red and blue pumping, thereby facilitating further development of microwave devices based on nanomechanics.

Chapter 5

Anomalous force noise

The dependence of dissipation of the mechanical resonator at low temperatures (1 mK to 1 kelvin) is critical to test the validity of the tunneling two-level system (TTLS) model. The mechanical resonator with the fundamental resonance mode of 60 MHz will be in the ground state at approximately 5 mK. The chip with the mechanical resonator is typically measured by installing it at the mixing chamber of the dilution cryostat. The commercial Bluefors dilution cryostat has a base temperature of 7±1 mK subject to heat leaks. Therefore, the base temperature of the cryostat is not enough to measure the dissipation of the mechanical resonator in the desired regime of temperature (i.e., below 5 mK). To solve this issue, we are also trying to add a demagnetization stage in our cryostat. The demagnetization can lower the base temperature of our cryostat to 1 mK and below. Discussing the principles of the demagnetization stage is out of scope for this chapter. However, it is an essential step for our future endeavor to measure the dissipation of the mechanical resonator below 5 mK. The initial characterization of our mechanical resonator (nanobeam) is done using just the dilution unit of the cryostat. We started with the measurement of the noise spectrum of 50 μm × 300 nm × 90 nm silicon nitride nanobeam with 30 nm of a thin layer of Al coupled capacitively to the $\frac{\lambda}{4}$ CPW superconducting microwave resonator. The device works according to the optomechanical theory above 200 mK and departs from the theory below 200 mK. We will discuss this behavior later, but firstly, it is imperative to look into literature if there is any record of the departure of the behavior from the usual optomechanical theory for similar kinds of devices as ours.

In *chapter 2*, we discussed the various pumping schemes for the measurement of the mechanical noise spectrum. Pumping the microwave cavity with frequency $\omega_c+\Omega_m$ (blue-detuned) and $\omega_c-\Omega_m$ (red-detuned) leads to back action forces on the mechanical resonator. The back action forces change the mechanical properties, including the optical spring effect and changes in the linewidth of the mechanical mode. However, at low powers, the back action forces are small and mechanical properties extracted from the mechanical noise spectrum are intrinsic and only depend on the temperature at which the experiment is being conducted. The area under

the mechanical noise spectrum at low pump powers is linear and proportional to the temperature. Massel *et al.* [49] measured the mechanical noise spectrum of two mechanical resonators coupled to a single microwave cavity. These mechanical resonators were made of 150 nm thick Aluminum with fundamental modes at 32.1 MHz and 32.5 MHz. For the initial calibration of their mechanical resonators, they measured the area under the mechanical noise spectrum with red-detuned pumping at low powers. The area under the mechanical noise spectrum is linear with temperature, but according to them, the linearity holds to about 150 mK, below which they observed intermittent heating. Similar behavior was observed by Rocheleau *et al.* [63] where they measured the mechanical noise spectrum of SiN based nanobeam with Aluminum on top. They observed fluctuations in the area under the mechanical noise spectrum also below 150 mK, apparently due to non-thermal intermittent force noise. The dependence of the area under the mechanical noise spectrum with temperature for both the above-mentioned articles is shown in figure 5.1.

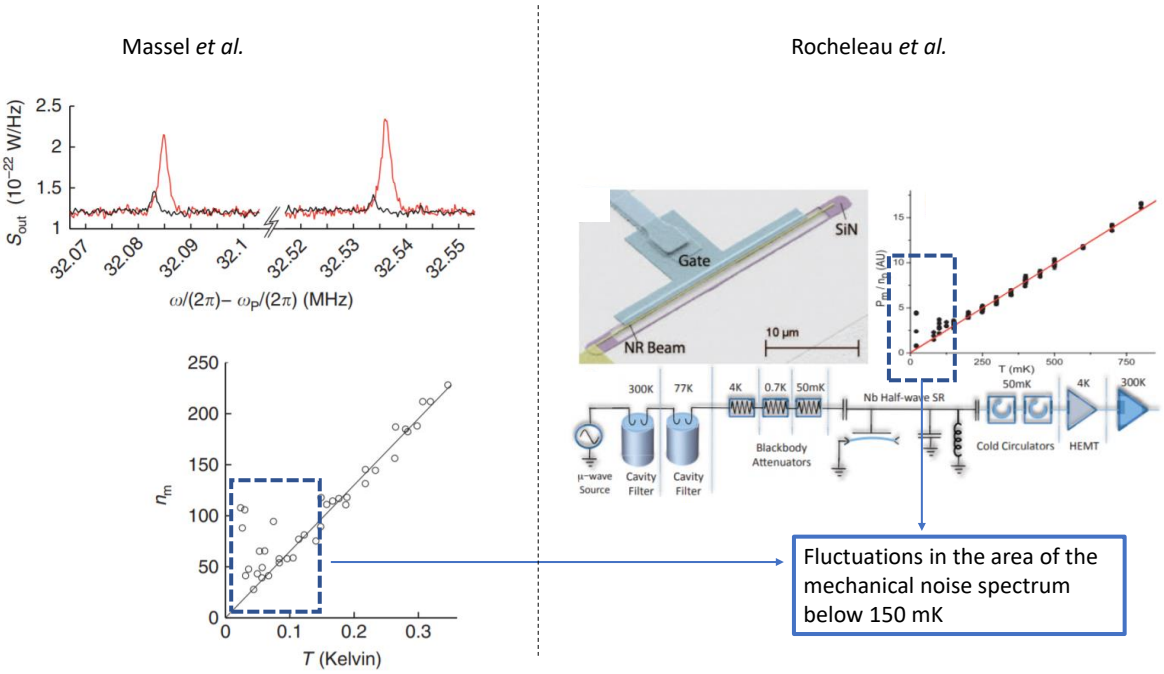

FIGURE 5.1: (left) Dependence of area under the mechanical noise spectrum with temperature taken from Massel *et al.* [49] (right) Dependence of area under the mechanical noise spectrum with temperature taken from Rocheleau *et al.* [63]

We observed similar behavior in our 50 μm $\times$ 300 nm $\times$ 90 nm silicon nitride nanobeam with 30 nm of a thin layer of Al coupled capacitively to the $\frac{\lambda}{4}$ CPW superconducting microwave resonator. The fluctuations in the area under the mechanical noise spectrum are due to huge

amplitude fluctuations. These fluctuations were observed by several other groups in the measurement of beam-based optomechanical devices with a thin layer of Aluminum. However, the amplitude fluctuations were never seen in the measurement of Al and SiN nanobeams via magnetomotive technique [36], [46], or laser-based measurements of Si beams [34]. In this chapter, we will discuss the features and characteristics of the amplitude fluctuations, which we call *spikes*, for the above-mentioned device.

5.1 Experimental setup

The cell made of annealed Cu containing the chip with the optomechanical device was installed at the mixing chamber plate of the commercial Bluefors dilution cryostat. The optomechanical device is the same device used for optomechanically induced transparency and absorption measurements (OMIT/OMIA). The reader can therefore consult *chapter 4* for details about the device. The pump and the probe signal were combined at room temperature before reaching the cell passing through a series of attenuators and a bandpass filter inside the cryostat as shown in figure 5.2. For in-cavity pumping, the pump signal is applied at ω_c, where ω_c is the resonance frequency of the microwave cavity. The modulation of the resonance frequency of the MWC due to thermal motion of the mechanical resonator leads to the generation of mechanical sidebands at $\omega_c \pm \Omega_m$, where Ω_m is the resonance frequency of the fundamental mode of the mechanical resonator. The pump signal transmitted by the cell is canceled at 4-kelvin plate to avoid the saturation of the cryogenic HEMT. The typical residual pump power reaching the cryogenic HEMT after cancellation is -30 dBm. The signal at $\omega_c \pm \Omega_m$ coming out the cryostat is further amplified by room temperature HEMT before down-conversion by mixing it with another microwave signal of frequency $\omega_c + \Omega_m + \delta$ at room temperature, where $\delta = 3$ MHz is an arbitrary detuning. The Keysight generator was used to pump the MWC. Anapico channel 2 was used to generate the local oscillator's frequency for the down-conversion of the signal. Anapico channel 1 was used to probe the transmission of the MWC. The down-converted signal is then fed to the Zurich Instrument's UHF lockin amplifier. The lockin amplifier can measure the noise spectrum using the spectrum mode. The signal is then demodulated at δ for measuring the signal originally at $\omega_c + \Omega_m$ and at $2\Omega_m + \delta$ for the signal at $\omega_c - \Omega_m$, where δ is some detuning frequency, 3 MHz in our case. The time constant of the lockin amplifier was set to 690.4 μs leading to 3 dB BW of 100 Hz and NEP BW of 113 Hz. Similar procedures were followed for the red and blue detuned pumping. The circuit diagram for the red detuned pumping is shown in figure 5.3.

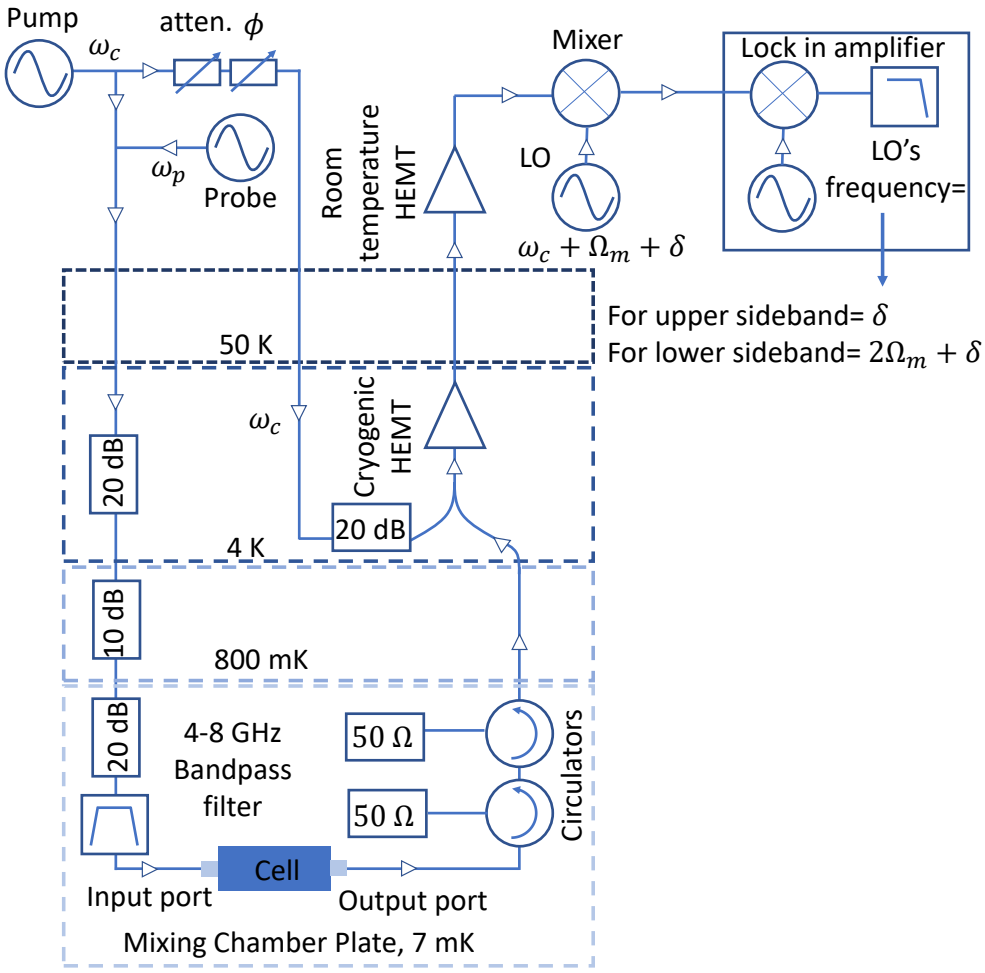

FIGURE 5.2: Circuit diagram for measurement of the device with in-cavity pumping

5.2 Introduction to *spikes*

We derived the output mechanical noise spectrum for in-cavity pumping in *chapter 2*. The output noise spectrum in the frame rotating with ω_c is given by,

$$S = \frac{16\Gamma_m\kappa_r n_b g^2}{\Gamma_m^2 + 4(\omega - \Omega_m)^2}\frac{1}{\kappa_{total}^2 + 4\Omega_m^2} + \frac{16\Gamma_m\kappa_r(n_b+1)g^2}{\Gamma_m^2 + 4(-\omega - \Omega_m)^2}\frac{1}{\kappa_{total}^2 + 4\Omega_m^2} \tag{5.1}$$

where Γ_m is the intrisic linewidth of the mechanical mode, κ_r is the coupling of any field coming from port 2 of the transmission line to the MWC, κ_{total} is the total linewidth of the MWC, Ω_m is the resonance frequency of the mechanical mode, n_b is the bose einstein occupancy of the mechanical resonator at temperature T, and $g = g_0\sqrt{n_d}$. g_0 is the vacuum optomechanical coupling and n_d is the number of drive photons inside the cavity. In classical regime, $n_b \approx n_b + 1$

and the output spectrum is modified in laboratory's frame as,

$$S = \frac{16\Gamma_m \kappa_r n_b g^2}{\Gamma_m^2 + 4(\omega_c - \omega - \Omega_m)^2} \frac{1}{\kappa_{total}^2 + 4\Omega_m^2} + \frac{16\Gamma_m \kappa_r n_b g^2}{\Gamma_m^2 + 4(\omega - \omega_c - \Omega_m)^2} \frac{1}{\kappa_{total}^2 + 4\Omega_m^2} \tag{5.2}$$

The left term of the above equation represents mechanical noise spectrum at $\omega_c + \Omega_m$ and the right terms represents the signal at $\omega_c - \Omega_m$. The area under both sidebands is equal and proportional to the temperature of the cryostat. One can further write the mechanical noise

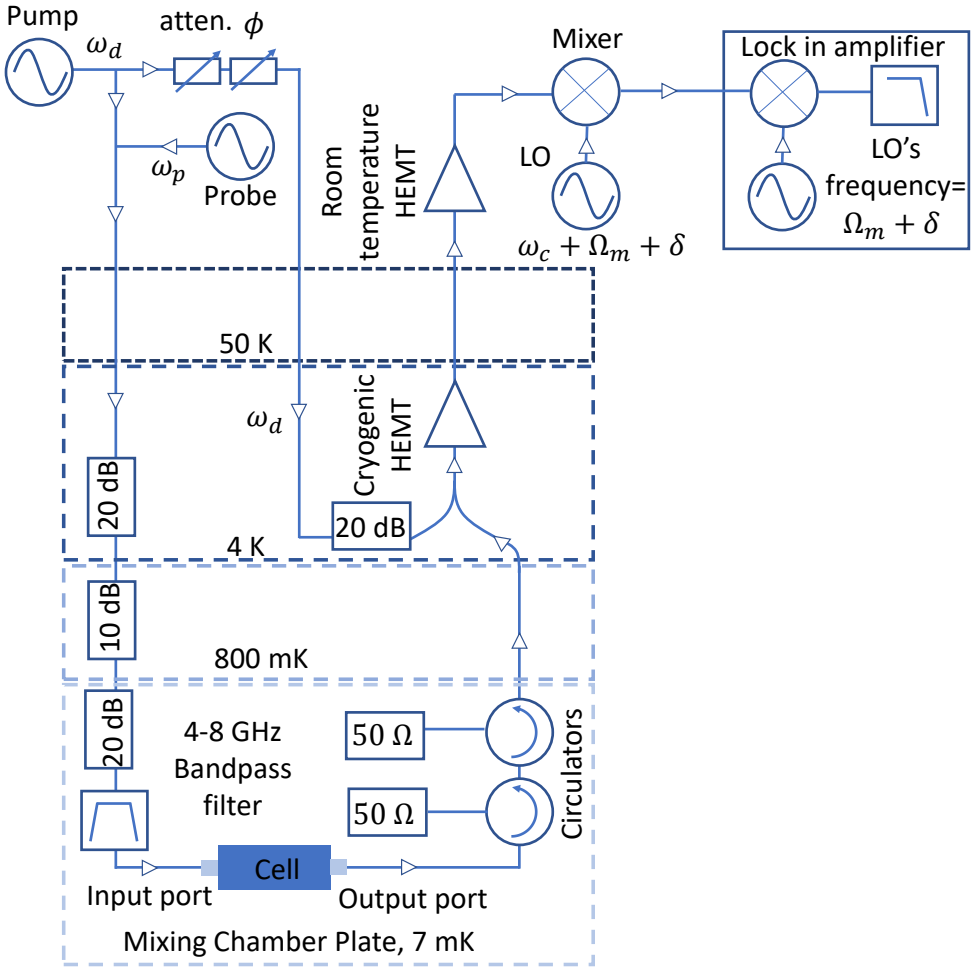

FIGURE 5.3: Circuit diagram for measurement of the device with red-detuned pumping

spectrum for each sideband in terms of single sided position spectral density as,

$$S = \frac{\kappa_{ext} G^2 n_d}{\kappa_{total}^2} S_x + nf \tag{5.3}$$

where $\kappa_{ext} = 2\kappa_r, G = g_0/x_{zpf}$, $S_x = 2S_{xx} = \frac{8k_bT}{m_{eff}\Omega_m^2} \frac{\Gamma_m}{\Gamma_m^2 + 4(\omega - \Omega_m)^2}$ is the single sided position spectral density and nf is the noise floor of the circuit. The typical mechanical

output noise spectrum transmitted from the MWC is shown in figure 5.4. The measurements were done using the spectrum mode of the Zurich Instrument's UHF lock-in amplifier. The raw data is acquired in Volts. Since we are interested in power spectral density, we convert the units from volts to Watts/Hz. The frequency range of the each spectra depends on the sampling rate. The sampling rate was set 429 samples/sec which is appropriately higher than demodulator's NEP BW to avoid aliasing effects. The number of samples were 1024 which leads to a resolution bandwidth (RSBW) of $\frac{\text{Sampling rate}}{\text{Number of samples}} = 0.418$ Hz. The PSD in Watts/Hz can thus be calculated as $\frac{V^2}{\text{RSBW} \times \text{WF} \times 50}$ where V is the raw data in volts, WF is the factor accommodating for the Hann window used to perform the fourier transform. The WF is 1.5 in our case. The onset of spikes below 200 mK hampers our measurements and makes

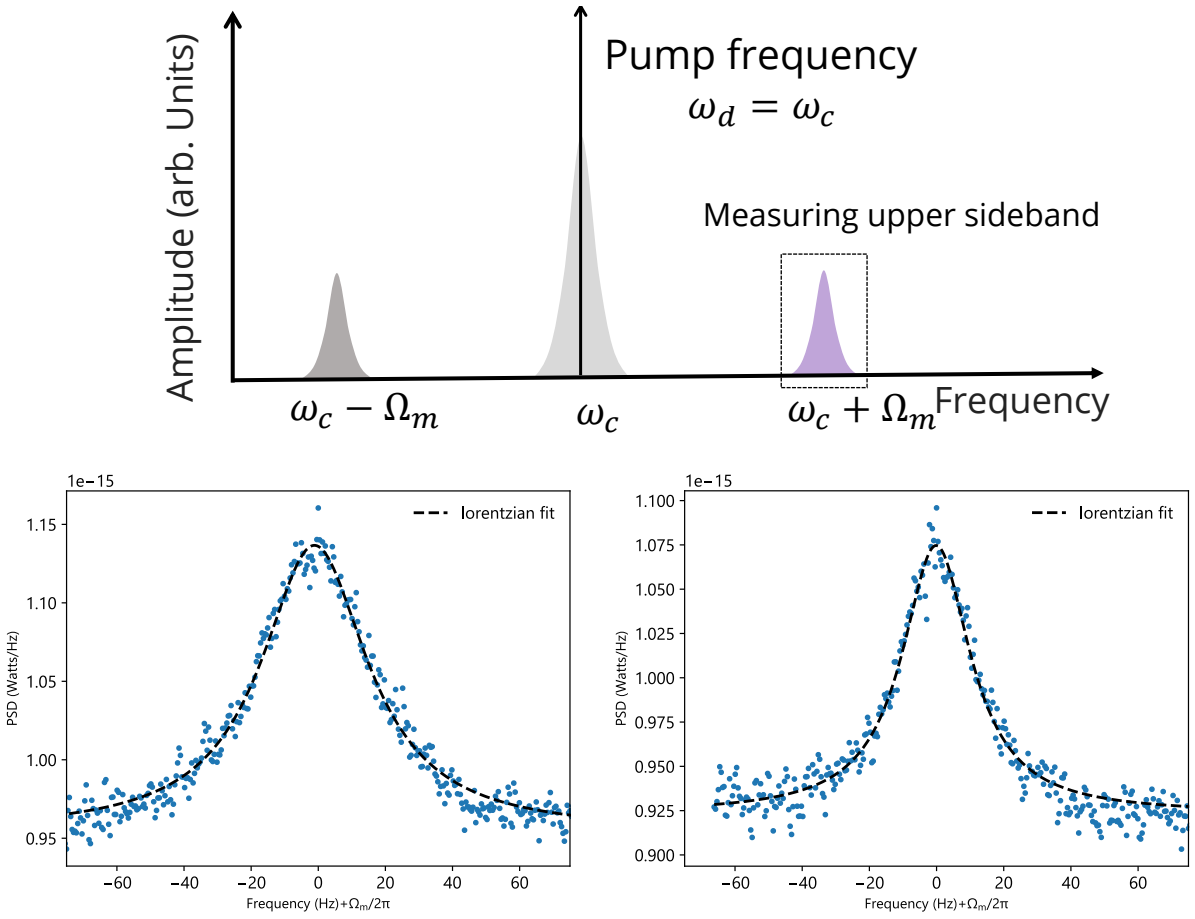

FIGURE 5.4: (upper) Sidebands generated at $\omega_c \pm \Omega_m$ while pumping the MWC at ω_c (bottom left) Mechanical sideband at $\omega_c + \Omega_m$ at 500 mK (bottom right) Mechanical sideband at $\omega_c + \Omega_m$ at 245 mK

it difficult to extract mechanical characteristics. Therefore, we use area under the mechanical sideband at $\omega_c + \Omega_m$ at 500 mK as calibration to compare the area under the curves below this temperature. The mechanical sideband at two different temperatures is shown in figure 5.4. It is also worthwhile to mention that the mechanical sideband plotted in figure 5.4 is the

average of 15000 individual spectra. Also, the measurements were done at a constant pump power of -4 dBm at the generator for both the temperatures. The area under the mechanical sidebands is calculated by extracting the linewidth and the height of the peak. Since the mechanical sidebands are lorentzian, the area is $\frac{\pi}{2} \times$ linewidth $\times$ height. The area under the mechanical sideband at 245 mK is 5.85 $\times$ 10^{-15} Watts and at 500 mK is 1.07$\times$ 10^{-14} Watts. The ratio of area under the curves is approximately the same as ratio of the temperatures. Let the temperature extracted from the mechanical sideband be denoted as T_{mode}. Since we have established the temperature of the cryostat T_{cryo} is equal to T_{mode} from our previous measurements at 500 mK and 245 mK, we can further extract the apparent temperature of the mode at lower temperature using a simple relation,

$$T_{mode} = \frac{A}{MP_{in}\frac{\Gamma_m}{\Gamma_{eff}}} \tag{5.4}$$

where A is the area under the mechanical sideband, P_{in} is the pump power applied, Γ_m is the intrinsic mechanical linewidth and Γ_{eff} is effective linewidth due to backaction forces and M is a constant discussed below. For in-cavity pumping $\Gamma_m = \Gamma_{eff}$, the above equation simplifies to $T_{mode} = \frac{A}{M}$. We also have omitted P_{in}, since all the measurements were taken at constant pump power. Using the same procedures we calculated T_{mode} at $T_{cryo} = 95$ mK. We calculated

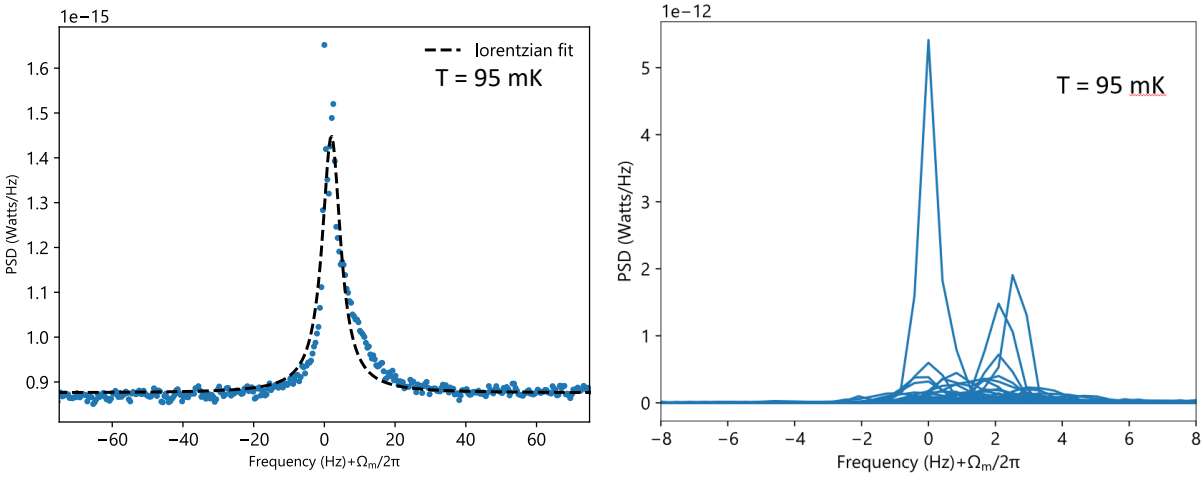

FIGURE 5.5: (left) Average of 15000 spectra taken at 95 mK leading to higher mode temperature (right) 15000 spectra superimposed on each other

the factor M at 500 mK. The factor M depends on the cavity parameters, attenuation and gain in the circuit. The cavity parameters may depend on T_{cryo}. We have ignored these effects in the calculation of T_{cryo} because the change in the cavity parameters with temperature is very small, as we shall see when we delve into the dependence of cavity parameters with temperature

in later sections. $T_{mode} = 265$ mK at $T_{cryo} = 95$ mK, where $M = 2.14 \times 10^{-14}$ Watts/kelvin. The average of 15000 spectra leading to mechanical sideband at 95 mK is shown in figure 5.5. This anomalous behavior is due to large amplitude fluctuations at the mechanical sideband frequency in some spectra. The plot of 15000 individual spectra is superimposed and also shown in figure 5.5. As evident from the large fluctuations in some of the spectrum, the area under the averaged spectra will be higher leading to larger area and in turn higher T_{mode}. The spikes were present at all temperatures below $T_{cryo} < 200$ mK at different pumping schemes (i.e. red-detuned, blue-detuned and in-cavity). To understand the characteristics of spikes and their source, we lowered the $T_{cryo} = 13$ mK and took data at different pump powers.

5.3 *Spikes* at 13 mK

In this section, we will discuss the dependence of the position spectral density of the mechanical sideband at $\omega_c + \Omega_m$ on the pump power applied at the generator. The measurements were done using in-cavity pumping where the pump frequency is at ω_c, where ω_c is the resonance frequency of the MWC. The lock-in settings for these measurements were discussed in the previous section. The temperature of the cryostat, T_{cryo} is always 13 mK unless stated otherwise. The time taken for each spectra is given by $\frac{\text{Number of samples}}{\text{Sampling rate}}$ which is approximately 2.8 secs. To characterize the time dependence of the spikes, we converted the power spectral density to apparent string amplitude. From equation 5.3, we can calculate single-sided position spectral density using the power spectral density.

$$S_x = \frac{S - nf}{\alpha n_d} \tag{5.5}$$

S and nf have the units of Watts/Hz. $n_d = \frac{2\kappa_{ext} P_{in}}{\hbar \omega_c \kappa_{total}^2}$ is the number of drive photons in the cavity and $\alpha = \frac{\hbar \omega_c \kappa_{ext} G^2}{\kappa_{total}^2 + 4\Omega_m^2}$. Following are the parameters used for calculating n_d and α.

Parameters	Values
$\frac{\kappa_{ext}}{2\pi}$	90 kHz
$\frac{\kappa_{total}}{2\pi}$	140 kHz
$\frac{\omega_c}{2\pi}$	6 GHz
$\frac{\Omega_m}{2\pi}$	3.8 MHz

κ_{ext} and κ_{total} do depend on P_{in} but the dependence is quite weak. $G = \frac{g_0}{x_{zpf}}$ where g_0 is the vacuum optomechanical coupling strength and x_{zpf} is the zero point motion of the mechanical resonator. g_0 can be calculated from the linewidth dependence of the mechanical mode with

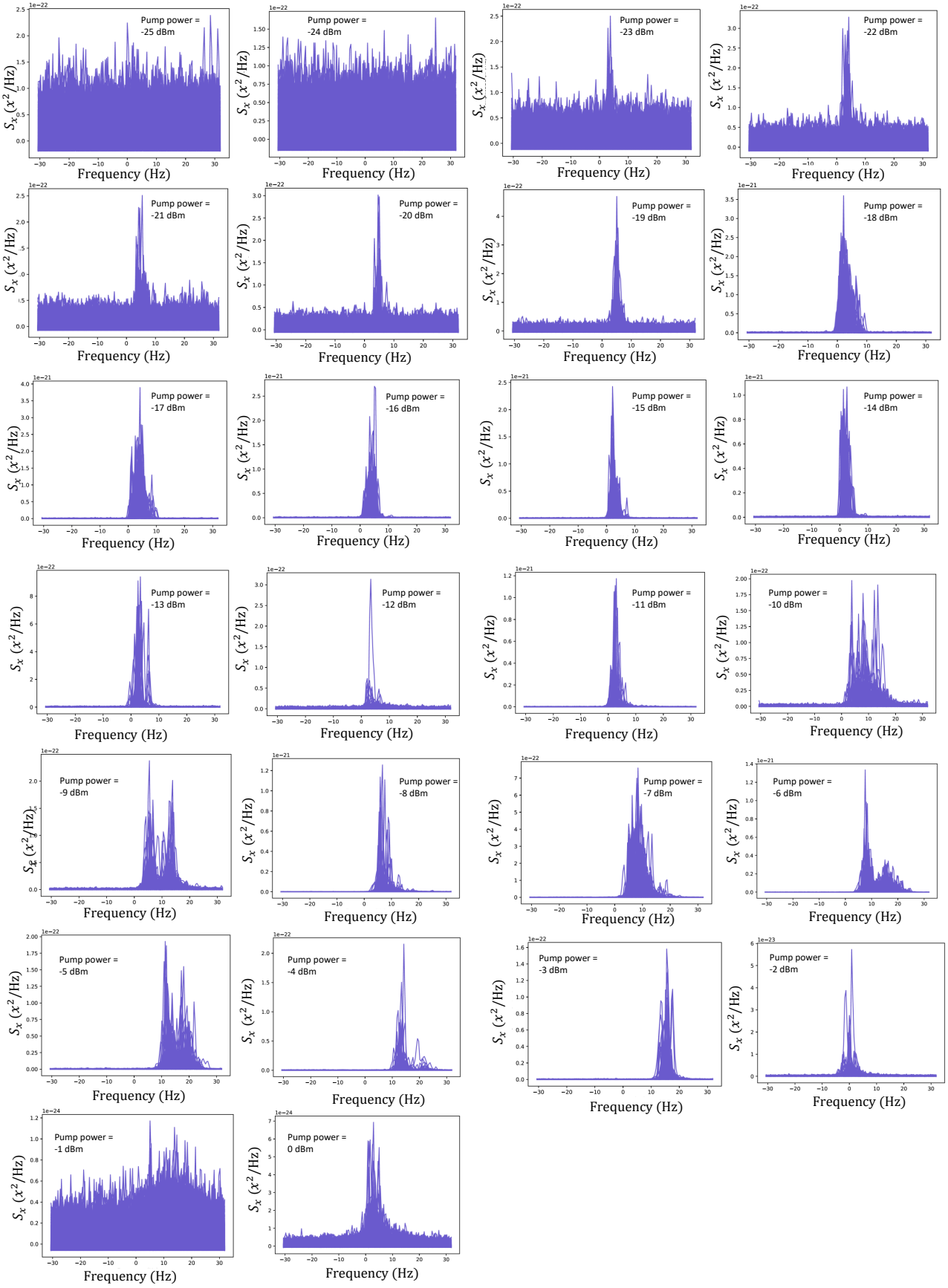

FIGURE 5.6: 3000 position spectra density superimposed for different pump powers at 10 mK. In these plots 0 in the x-axis is referenced to $\Omega_m/2\pi$ where Ω_m is the resonance frequency of the mechanical resonator

pump power and $x_{zpf} = \sqrt{\frac{\hbar}{2m_{eff}\Omega_m}}$. m_{eff} is the effective mass of the mechanical mode in consideration. $m_{eff} = \frac{m}{2}$ where $m = \rho \times l \times w \times t$. $l = 50\mu$m is the length of the string, $w = 300$nm is the width and $t = 120$ nm is the thickness. To calculate g_0 we pump the MWC at $\omega_c + \Omega_m$ and measure the mechanical sideband at ω_c. The circuit diagram for this measurement is shown in figure 5.3. The lock-in settings were same as mentioned before. The effective linewidth $\Gamma_{eff} = \Gamma_m - \frac{4g_0^2 n_d}{\kappa_{total}}$ depends on the number of drive photons inside the cavity. We can obtain the g_0 by simply linearly fitting the effective linewidth Γ_{eff} versus the pump power applied. The measurement was taken at 245 mK.

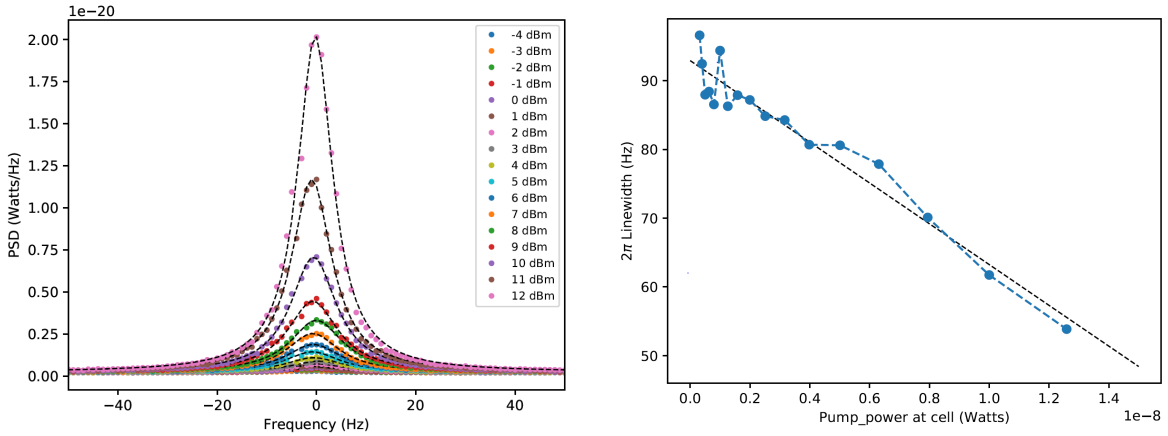

FIGURE 5.7: (left) Power spectral density at ω_c while pumping at $\omega_c + \Omega_m$ for different pump powers applied at the generator (right) Effective linewidth versus pump power applied the cell

The value of $\frac{g_0}{2\pi}$ obtained is 0.45 ± 0.05 Hz. To obtain the position spectral density in x^2/Hz we subtract the noise floor $nf = 1.68e-22$ Watts/Hz from the power spectral density. Also, $\alpha = 8.85 \times 10^{-6}$. The position spectra density was taken for different pump powers applied at the generator from -25 dBm to 0 dBm. Figure 5.6 shows 3000 position spectra superimposed for different pump powers. One can clearly see that there is a huge fluctuation in the amplitude. The amplitude of these fluctuations does not depend on the pump power applied at the generator. Also, these huge amplitude fluctuations are time-dependent, i.e., they come in sudden bursts and remain for some time. The apparent string vibration amplitude is calculated by integrating the position spectral density in a 60 Hz bandwidth discarding the negative points (which are obtained by subtracting the nf from power spectral density), and then taking its square root. The apparent string amplitude versus time for different pump powers in shown in figure 5.8. The time resolution of the plots is approximately 2.8 secs. One can infer that there is no apparent dependence of the string vibration amplitude on the pump powers. The maximum string vibration amplitude was approximately 50 pm. These measurements were taken in May

2020 after the 1st lockdown due to COVID-19. We were performing these measurements before the lockdown before abruptly warming up the cryostat. We obtained similar results, but the maximum string vibration extracted was about 300 pm.

The next step we followed is to check if these spikes were present at other frequencies. We started by checking the power spectral density at $\omega_c - \Omega_m$, the lower mechanical sideband. For the measurement of the lower sideband, the local oscillator's frequency in the lock-in amplifier was set to $2\omega_m + \delta$ as the downconverted signal is at $2\omega_m + \delta$ as shown in figure 5.2. Instead of looking at the time dependence of the string vibration amplitude, we plotted the integrated power versus time shown in figure 5.9. We again integrated the power spectral density in a 60 Hz bandwidth. The plots clearly show the spikes also at the lower sideband at $\omega_c - \Omega_m$. Evidently, the spikes are present at both the mechanical sideband frequencies, i.e., $\omega_c \pm \Omega_m$. This suggests that the spikes are caused by the vibration of the mechanical resonator. Although we checked for the spikes at $\omega_c \pm \Omega_m$, it is imperative to check the power spectral density in a broader bandwidth to look for spikes at other frequencies to strengthen our hypothesis. For these measurements, we set the bandwidth of the lock-in amplifier to 5642 Hz and the sampling rate to 27465 samples/sec leading to the resolution bandwidth of the spectra to be 0.2 Hz, and the time taken for each spectrum is 4.86 secs. Next, we measured the power spectral density at the upper sideband, i.e., at $\omega_c + \Omega_m$ for different pump powers (-10 dBm to 0 dBm) at the generator. We also calculated the apparent string amplitude and plotted it with time. Again, the spikes were present only at the mechanical sideband. Figure 5.10 shows the power spectral density and the corresponding string amplitude for a pump power of -10 dBm. We also checked for power spectral density for other pump powers and found the spikes present only at $\omega_c + \Omega_m$. The fact that the spikes only occur at the mechanical sidebands demonstrates that their mechanism must involve the motion of the string.

From equation 5.5, the spikes in the power spectral density must be caused by the spikes in either α, n_d (the number of photons inside the cavity due to pump) or S_x. To calculate n_d we kept S_x to be constant. The noise floor nf was subtracted from the power spectral density. The negative points were omitted. Therefore, the new power spectral density is $S_{new} = S - nf = S_x\alpha(n_d + \Delta n_d)$. Δn_d corresponds to hypothetical spikes in the number of photons inside the cavity. We calculated Δn_d for different pump powers applied at the generator. Figure 5.11 shows the power spectral density and the corresponding spikes in n_d at -7 dBm pump power. As shown in figure 5.11, for -7 dBm of pump power applied at the generator, the steady state number of photons circulating inside the cavity is $n_d \sim 6 \times 10^7$. The maximum spikes in n_d i.e. Δn_d is approximately 4×10^{12}. This would be an enormous spike in n_d considering that we already observe degradation of the cavity line shape at n_d= (figure 5.12).

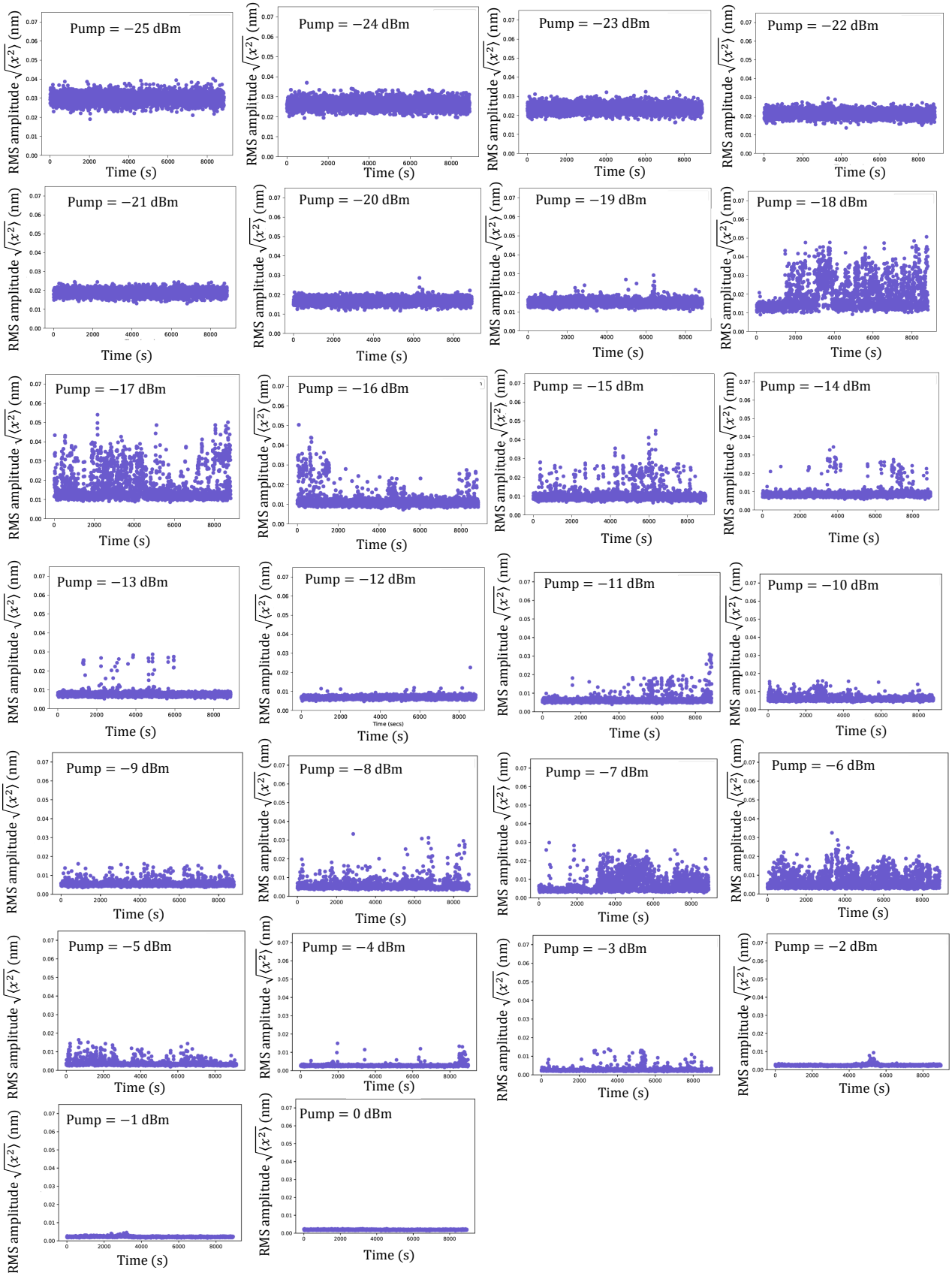

FIGURE 5.8: Apparent string amplitude versus time for different pump powers applied at the generator

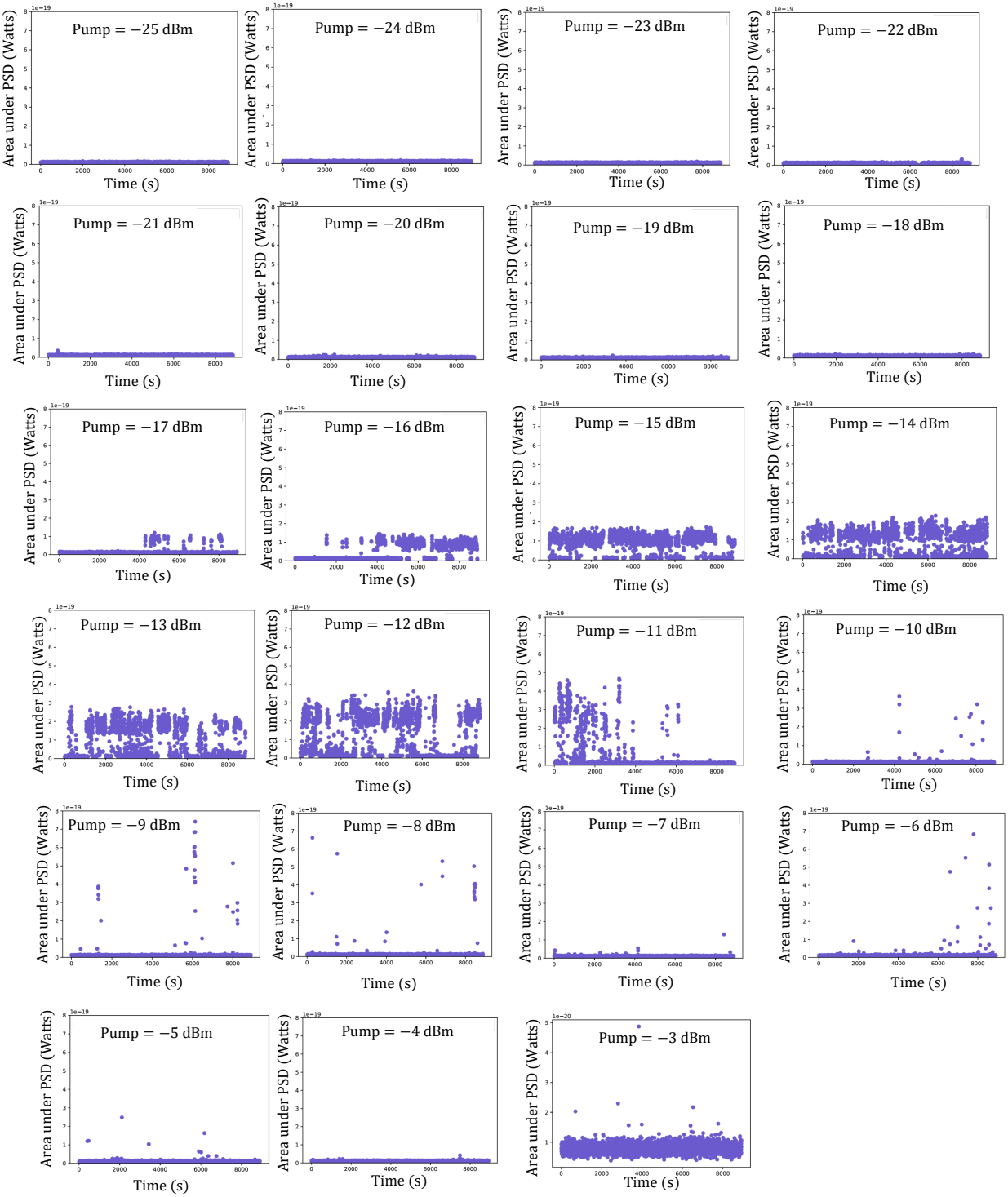

FIGURE 5.9: Integrated power from the power spectral density at the lower sideband i.e. at $\omega_c - \Omega_m$ versus time for different pump powers applied at the generator

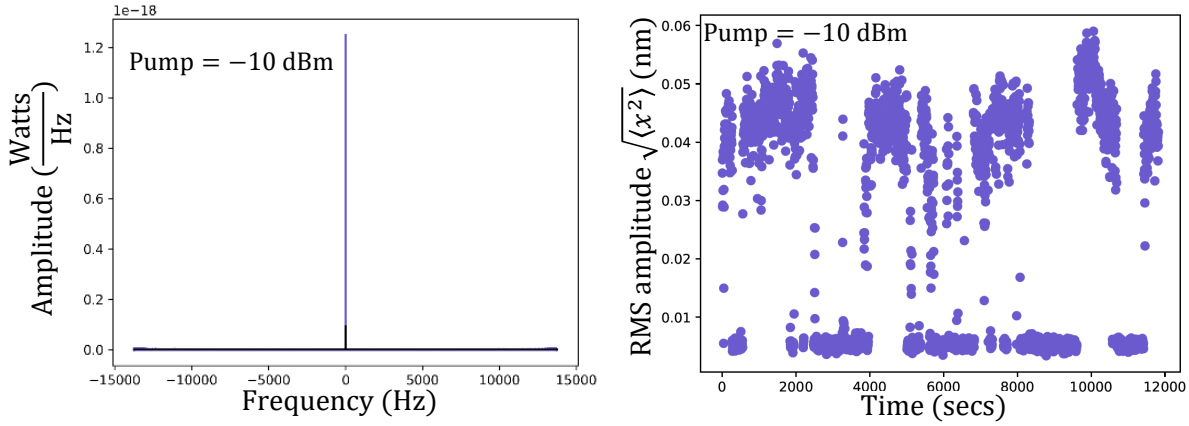

FIGURE 5.10: Power spectral density in a wide bandwidth at -10 dBm of pump power(blue curve shows the individual spectra superimposed and the black curve is the average of all the spectra) and the corresponding apparent string amplitude, again 0 in the x-axis of the power spectral density is referenced to Ω_m

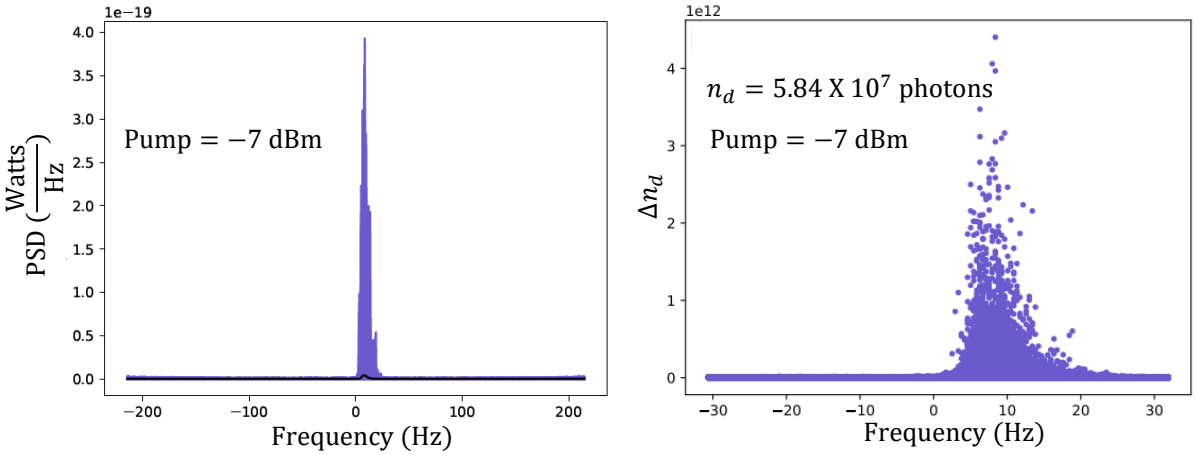

FIGURE 5.11: Individual power spectra density(blue curve) at -7 dBm of pump power (black curve is the average of all the spectra) and the corresponding spikes in n_d, again 0 in the x-axis of the power spectral density is referenced to $\omega_c + \Omega_m$

As expected, we don't observe such enormous spikes in the cavity population when looking at the microwave output spectrum at the cavity resonance. We don't see spikes in n_d so this leaves spikes in S_x. But where could such large spikes come from? A rms spike amplitude of 300 pm and an effective spring constant of 1 N/m corresponds to a potential energy of 5×10^{-20} J and a temperature of 6000 Kelvin. For comparison, -25 dBm pump power corresponds to $n_d = 10^6$ photons circulating in the cavity, which corresponds to 5×10^{-18} J. And a 3 MeV gamma ray corresponds to 5×10^{-13} J. Therefore, the spikes we observe at the mechanical sidebands must be caused by real spikes in the vibration amplitude of the string or spikes in the optomechanical

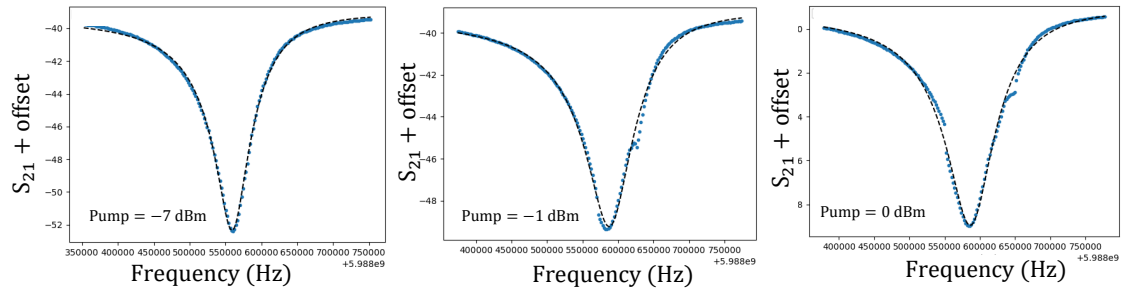

FIGURE 5.12: Typical transmission curves of the MWC at different pump powers applied at the generator. For pump power of -1 dBm and 0 dBm, one can clearly notice the distortion in the curve

gain that are not consistent with optomechanical theory (equation 5.5). We also see spikes with the other two pumping schemes, i.e., red and blue. We do not perform a similar analysis for these pumping schemes as we want to keep the back-action forces out of play.

5.4 Plausible sources of *spikes*

5.4.1 Impact of ionizing radiation

Vepsäläinen *et al.* [77] measured the impact of ionizing radiation from the environment on the coherence time of superconducting qubits. When the qubit is in excited state the probablity for qubit in excited state decays as $p(t) = e^{-\Gamma_1 t}$ where $\Gamma_1 = \frac{1}{T_1}$ is the relaxation rate corresponding to qubit's decoherence time T_1. According to them, the relaxation rate $\Gamma_1 = \Gamma_{qp} + \Gamma_{other}$ where Γ_{qp} is the relaxation rate contribution from the generation of quasi particles in the superconducting material and Γ_{other} corresponds to other loss channels (like two level fluctuators). The relaxation rate Γ_{qp} depends on the normalized quasi-particle density $x_{qp} = \frac{n_{qp}}{n_c}$ where n_{qp} is the number of quasi particles and n_c is the number of cooper pairs in the qubit. In order to calculate the number of quasi particles generated due to the background radiation, they measured the background radiation using NaI scintillation detector. They found the background radiation flux of approximately ~ 7 cm^2/s, 'consistent with typical values of concrete'. Nazaretski *et al.* [53] studied the acoustic properties of the torsional oscillator between 1 mK and 100 mK. They observed distorted lorentzian response of the oscillator below 10 mK as shown in figure 5.13 accompanied by random noise. They also attributed the random noise shown in figure 5.13 to the background radiation in the energy range of 0.05 to 2.65 MeV.

Can this background radiation be responsible for the spikes we see in our mechanical resonators? The area of the nanostring is very small $\sim 2{\times}10^{-7}$ cm^2. The total flux absorbed on

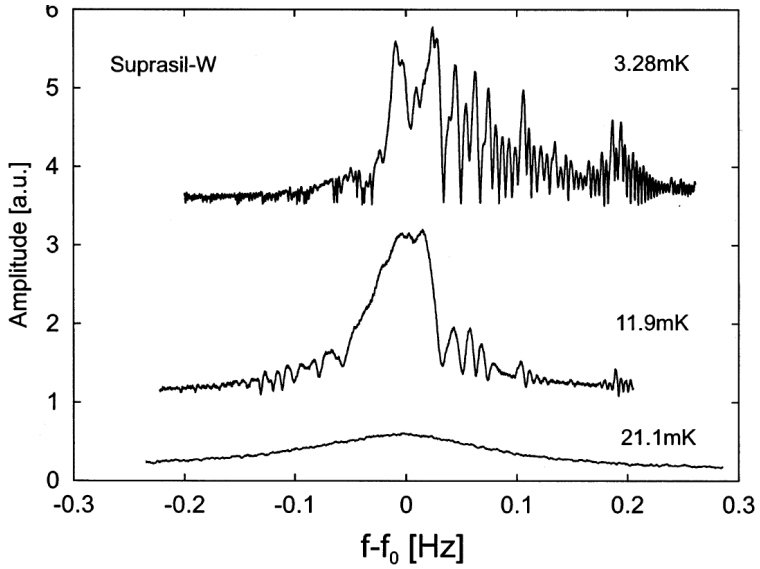

FIGURE 5.13: Non-Lorentzian response of the torsional detector due to background radiation taken from [53]

the string will be $\sim 1.4\times10^{-6}$/s. Thus gamma flux incident on the string cannot explain the frequency of spikes we observe. It is possible that gammas create phonons in the 1 cm^2 square chip, which in turn cause spikes in the string motion. Even so, the gamma flux may be too low to explain the frequency of spikes that we observe, since a significant fraction of the gammas have low energies and can be excluded by a modest thickness of Cu. The fact that the spikes are clustered in time (Figs. 5.8and 5.9) also seems inconsistent with an explanation in terms of background radiation.

5.4.2 Cracks in the chip

Åström *et al.* [9] discussed about the fracture processes observed with a cryogenic detector. In the early attempts for CRESST dark matter search using the sapphire detectors at low temperatures, they observed unexpected huge signal pulses. They traced back the occurrence of a random signal to fracture events in the sapphire due to tight clamping of the detectors. Working in the vicinity of 10 mK, CRESST cryogenic detector was well shielded against cosmic rays and carefully designed to minimize the effects of radioactive background. The sapphire crystal was held tightly using sapphire balls. They initially feared that this might be due to some radioactive contamination of an unknown type. Since the unexpected pulses they observed come in *sudden bursts* or *avalanches*, they disregarded the source to be of radioactive origin as they are poisson distributed in time. In our case, we also observed spiky events that come in *sudden bursts*. This led us to believe if our chip made of SiN/Si is also cracking due to clamping forces. However, instead of sapphire balls, we are using a thin indium sheet as a

clamp leading to uniform distribution of forces on the chip.

To delve more into the statistics of the avalanches, they plotted number of event per unit energy with energy and fitted the data with a simple power law distribution as,

$$\frac{dN}{dE} \propto E^{-\beta} \tag{5.6}$$

where $\beta \approx 1.9$. This power law is called Gutenberg-Richter law, often used for measurements of magnitudes in an earthquake event. Therefore, to probe our suspicion, we decided to do a similar analysis. Instead of measuring the power spectral density, we measured the fluctuation of RMS voltage measured by the lock-in amplifier with time. Using the same settings for the lock-in amplifier as described in the previous section, we measured the R^2 with time as shown in figure 5.14. The time-domain data was taken for 54000 secs with a 2 msec time resolution. We call each time-domain data for 54000 secs as a single run. R^2 is the integrated area under the power spectral density also shown in figure 5.14 at $\omega_c + \Omega_m$ from -BW to BW where BW = 113 Hz. Several runs were performed for few different temperatures, i.e., 7 mK, 13 mK, 25 mK, and 50 mK. The pump power applied at the generator was -4 dBm at ω_c.

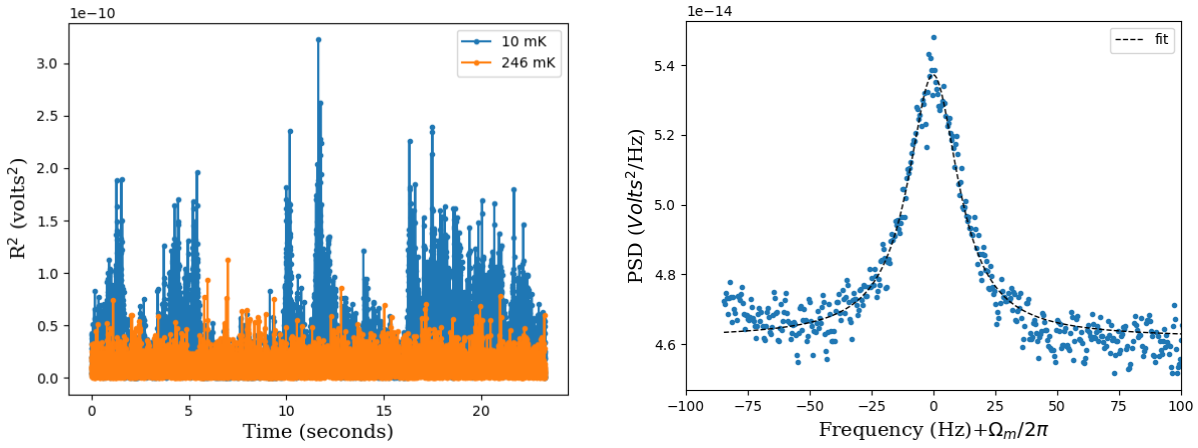

FIGURE 5.14: (left) Time domain data with time resolution of 2 msec at two different specified temperatures (right) The R^2 in the y-axis in left plot is the area under the mechanical sideband. The typical mechanical spectrum in frequency domain is shown in the figure

We then divided the amplitude R^2 in 200 equally sized bins of size 2 $\times 10^{-12}$ V^2 in the range of $[0.5 \times 10^{-10}]$ V^2. We counted the number of points in each bin and plotted the histograms for different runs and temperatures as shown in figure 5.15. The different runs at a particular temperature are shown in transparent colors, and the average of all the runs is shown in opaque. From the plots, it is evident that there are no reproducible statistics for

the distribution of the R^2 for different runs at a particular temperature. At 7 mK, there is a somewhat flat distribution of the R^2 in an intermediate range of amplitudes shown between dotted lines in figure 5.15 for some runs. This flatness of the distribution of R^2 or the change of slope in the distribution is also a feature at 13 mK shown between dotted lines. We do not observe such behavior at higher temperatures. Is this feature only observed at lower temperatures is subject to further theoretical inputs. Another interesting analysis is to plot the distribution of R^2 for all temperatures in the same plot to probe if the distribution depends on the temperature itself. Therefore, in figure 5.16 the distribution of R^2 is plotted for different temperatures. The distribution of R^2 for higher temperatures (247 mK, 173 mK, 95 mK) looks the same. Since the area under the power spectral density scales with the temperature, the average value of R^2 should scale with temperature. However, we found that the average value of R^2 was higher at 95 mK and 173 mK than 247 mK. This discrepancy can be due to the presence of smaller amplitudes of spikes at 95 and 173 mK, which is not resolvable in the figure 5.16. The distribution of R^2 for lower temperatures (50 mK, 25 mK, 13 mK, 7 mK) follows the trace of distribution of R^2 at 247 mK for lower amplitudes and then diverges. One can further conclude that the number of events with higher amplitudes of R^2 depends on temperature. The number of events with high amplitudes of R^2 is more at lower temperatures.

After considerable devotion of time to understand the dependence of the amplitude of spikes on different parameters, we did found some dependence on temperature. However, one can question if this dependence is reproducible. In figure 5.17, we have plotted the histograms of different runs at various temperatures. We can notice that it is not evident that the runs at lower temperatures have more number of points at higher amplitudes. The distribution at 7 mK and 13 mK for different runs are random, and there is no clear evidence that the number of events with higher amplitude at 7 mK is always more than at 13 mK and is the same for higher temperatures. To get a more accurate picture of the temperature dependence, one can certainly measure for a longer period of time. We did measure R^2 close to 75 hours at 7 mK and 165 hours at 13 mK. We can now compare our measurements with the data presented by Åström *et al.* [9]. Åström *et al.* plotted the distribution, which was reproducible and followed the simple power-law mentioned above in this section. Our distribution is far from the simple power-law dependence and is not reproducible. We certainly cannot discard cracking as one of the plausible sources of spikes since it may follow a different mechanism, and the distribution is not given by a simple power law.

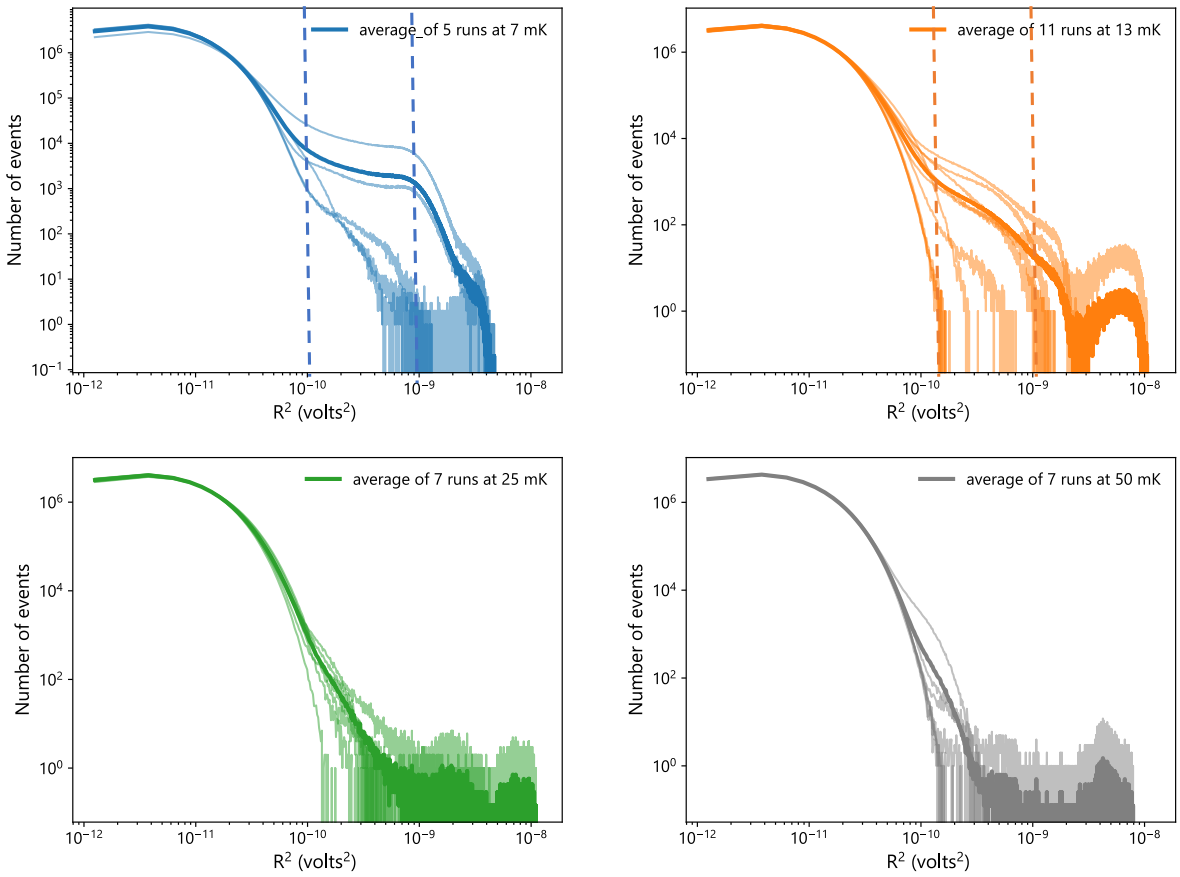

FIGURE 5.15: Distribution of R^2 at different specified temperatures. The transparent color represents different runs and the opaque color represents the average of all the runs

5.5 Conclusions

We reported very high amplitude fluctuations at the mechanical sidebands while pumping the MWC at ω_c, which were also observed at various other groups. These spikes were present only at the mechanical sidebands implying that there is some stochastic force noise acting on the mechanical resonator or that the standard theory of optomechanical transduction does not apply. The amplitude fluctuations appear below 200 mK. The source of the force noise is still unclear. Our analysis of ionizing radiations or cracks in the silicon chip due to clamping did not provide sufficient information to link these amplitude fluctuations to the formers. It is also tempting to connect these fluctuations/stochastic force noise to the TLSs present in the string, which is driven by the microwaves. One can also argue if there is any temperature-dependent non-linearity present in these devices leading to amplitude fluctuations. Also, these amplitude fluctuations are present only on devices made of Aluminum or having a thin layer of Aluminum.

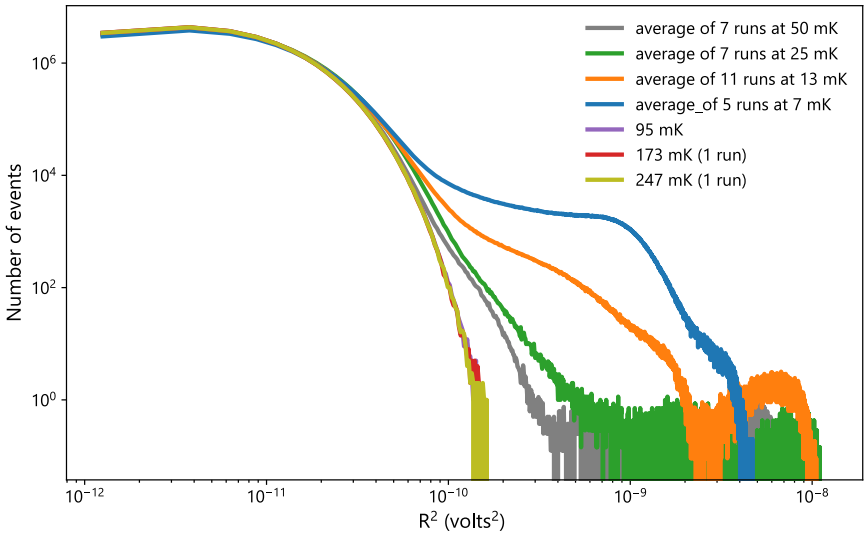

FIGURE 5.16: Distribution of R^2 at different specified temperatures plotted on same graph.

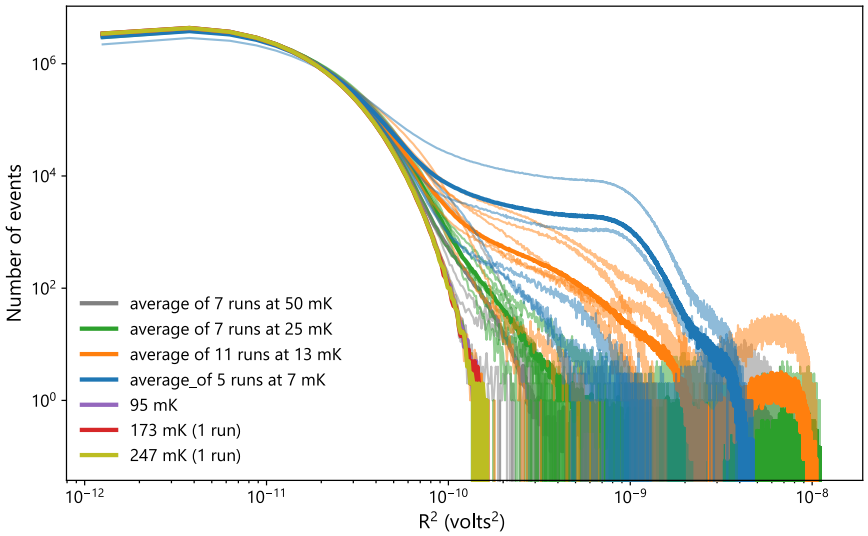

FIGURE 5.17: Distribution of R^2 for all the runs at different specified temperatures plotted on same graph. The transparent color represents different runs and the opaque color represents the average of all the runs

Thus, it becomes imperative to test devices made of other materials for the presence of spikes. We then created another platform to measure the nanobeams made of SiN without any metal present on them, which is the subject of interest for the next chapter.

Chapter 6

Dielectric actuation and detection of nanobeams made of SiN at low temperatures

The smaller dimensions of nanomechanical resonators make the transduction of the Brownian motion of mechanical resonators at low temperatures arduous. The recent field of cavity optomechanics wherein the mechanical resonator is coupled to an optical cavity, or superconducting microwave cavity, has paved the sensitive detection of its motion at low temperatures. However, microwave cavity optomechanical experiments have relied on the coupling of superconducting mechanical resonators to superconducting microwave cavities focusing on ground-state cooling [73], quantum non-demolition measurements [40], entanglement between different mechanical resonators [54], etc. Most of the achievements in the field of superconducting microwave cavity optomechanics were carried out with massive drums made of Aluminum coupled capacitively to the microwave cavity. In a recent experiment by Cattiaux *et al.* [20], the mechanical resonator (Aluminum drum) was cooled down to ~ 0.5 millikelvins, and the Brownian motion was measured successfully using the superconducting MWC. Although the use of mechanical drums made of superconducting material induces large coupling with the MWC favoring sensitive detection of its motion at low temperatures, it is generally marred with low-quality factors. To further increase the performance of such devices, one can benefit from high-quality factors of mechanical resonators made of pre-stressed Silicon Nitride. Typically, the mechanical resonators made of Silicon nitride are metalized (Al, Nb) and are capacitively coupled to the MWC. The detection of Brownian motion of the metalized (Al) doubly clamped SiN nanobeam coupled to the MWC is tarnished by huge amplitude fluctuations due to anomalous force noise below 200 mK as discussed in the *Chapter 5*. On the other hand, vacuum optomechanical coupling of non-metalized SiN nanobeam to the MWC is quite low. Pernpeintner *et al.* [57] extracted the vacuum coupling rate $\frac{g_0}{2\pi} = 11.5$ mHz by coupling 20 μm long bare SiN nanobeam to $\frac{\lambda}{2}$ MWC cavity. This coupling strength is much smaller compared to the coupling strength observed in metalized beam. For example, Sulkko *et al.* [72] measured $\frac{g_0}{2\pi} = 20$ Hz. Thus,

integrating bare SiN mechanical resonators into the electric circuit is still a challenging task. Recently flip-chip techniques are used to capacitively couple SiN membranes with a thin layer of Al to 3-d MWC [84].

Maillet *et al.* [47] reported the damping rate and frequency shift of high quality, metalized pre-stressed SiN nanobeams between 30 mK and 1 kelvin. The results supported the idea that electron-driven TLS relaxation is the dominant mechanism of damping. Their results may explain the several issues raised with the nanomechanical damping mechanisms at low temperatures. Thus, it becomes imperative to measure the mechanical characteristics of bare SiN mechanical resonators to test the validity of the TTLS model.

Faust *et al.* [25] presented an integrated NEMS transducer based on MWC dielectrically coupled to an array of doubly clamped pre-stressed SiN nanobeam. The MWC was based on strip resonator forming $\frac{\lambda}{4}$ geometry. One end of the strip was grounded and inductively coupled to the feedline, and the other end was wire bonded to another chip with an array of mechanical resonators. The MWC was fabricated using copper on a ceramic substrate. The mechanical resonator was actuated using a piezo inertial drive. The coupling of the mechanical resonator to the MWC induces periodic modulation of the microwave resonance frequency causing sidebands at $\omega_c \pm \Omega_m$ where ω_c and Ω_m are the microwave and mechanical resonance frequency, respectively. The scheme allows probing the motion of the mechanical resonator between 4 kelvin and room temperature. To further measure the motion of the mechanical resonator below 4 kelvin, superconducting microwave cavities are ideally suited. Pernpeintner *et al.* [57] integrated a pure insulating silicon nitride nanobeam to a superconducting coplanar waveguide microwave resonator. However, vacuum optomechanical coupling strength $g_0/2\pi$ was 11.5 mHz which is quite low. Unable to measure the thermal motion of the mechanical resonator at 500 mK, they excited the mechanical resonator with a piezo inertial drive. They could not carry out the measurements below 500 mK, possibly due to heat loads by piezo drive.

This chapter will discuss a novel scheme for detecting non-metalized doubly clamped SiN nanobeam coupled to a superconducting microwave cavity on a separate chip using wire bonds. The mechanical resonators will be placed between two metallic plates and will be driven using dielectric forces. This dual-chip dielectric actuation and detection using microwave cavity is related to the scheme presented by Faust *et al.* [25]. I will start this chapter by discussing various experimental tools and challenges. I will then report the measurements of 100 μm long metalized doubly clamped nanobeam using the dual chip technique before switching to bare SiN nanobeams. We again measured huge amplitude fluctuations in the long metalized nanobeam, which is the subject of discussion for later in this chapter.

6.1 Experimental tools

The foremost step is the design of the microwave cavity for the transduction of the motion of the mechanical resonator. The microwave cavity is based on the superconducting material. We made both Niobium and Aluminum microwave cavities. The section will start with the design issues of the microwave cavity before delving into the circuit for the measurement.

6.2 Superconducting microwave cavity

The superconducting microwave cavity was fabricated using either Al or Nb as superconducting material on an intrinsic Si wafer. For details on the fabrication methods, the reader can consult *chapter 3* for more information. The superconducting MWC was based on coplanar waveguide forming open $\frac{\lambda}{2}$ type geometry. The CPW resonator was in turn coupled to the CPW transmission line as shown in figure 6.1. S specifies the spacing between the central conductor and either of the ground plane, while W specifies the width of the central conductor. The parameters S= 94 μm and W=150 μm are chosen such that the impedance of the transmission line and the MWC is 50 Ω. The whole structure was made on 1 cm^2 chip. The larger dimension of the central conductor enables us to have enough space for wire bonding it to another chip with the mechanical resonator. The GDS image of the chip and the FEM simulation of the MWC is shown in figure 6.2.

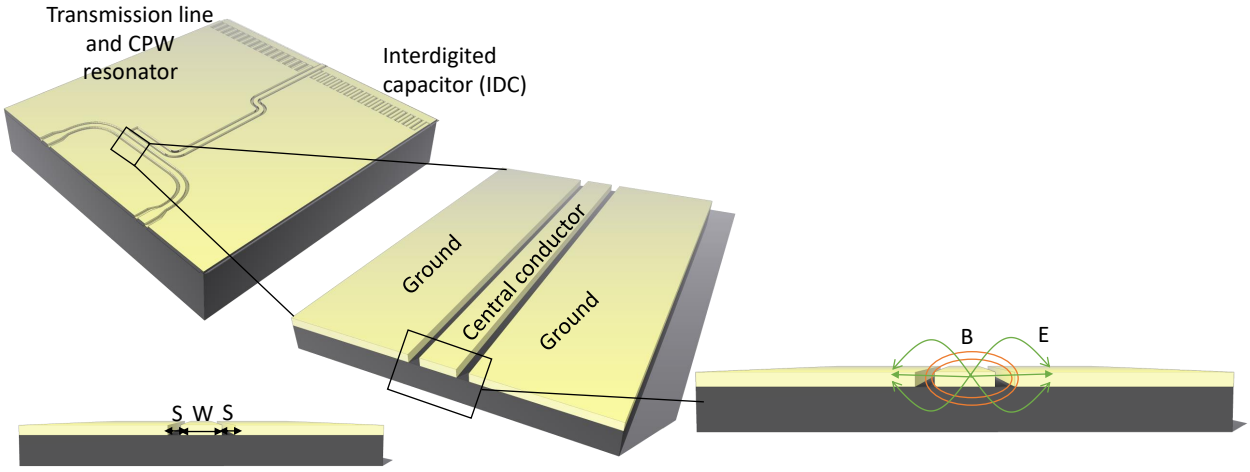

FIGURE 6.1: Design of the open $\frac{\lambda}{2}$ MWC coupled to the transmission line. The design was fabricated on 1 cm^2 chip. One end of the central conductor is coupled to the transmission line while the other end is for the wire bonding. There is also an interdigitated capacitor (IDC) running across the chip near one end of the central conductor. The paramenters S and W are chosen such that the impedance of the MWC is 50 Ω

As shown in the FEM simulation in figure 6.2, the voltages are maximum at two open ends of the central conductor on the MWC. One end of the central conductor is capacitively coupled to the transmission line for the transmission measurements at GHz frequencies, and another end is meant for the wire bonding to another chip with NEMS. From the simulation, we found the resonance frequency of the fundamental mode of the MWC to be at 6.2 GHz. The central conductor of the transmission is also widened at the two open ends to match with the dimension of the gold coplanar waveguides on a circuit board. The input and the output of the coaxial transmission line in the cryostat are soldered to the gold CPW.

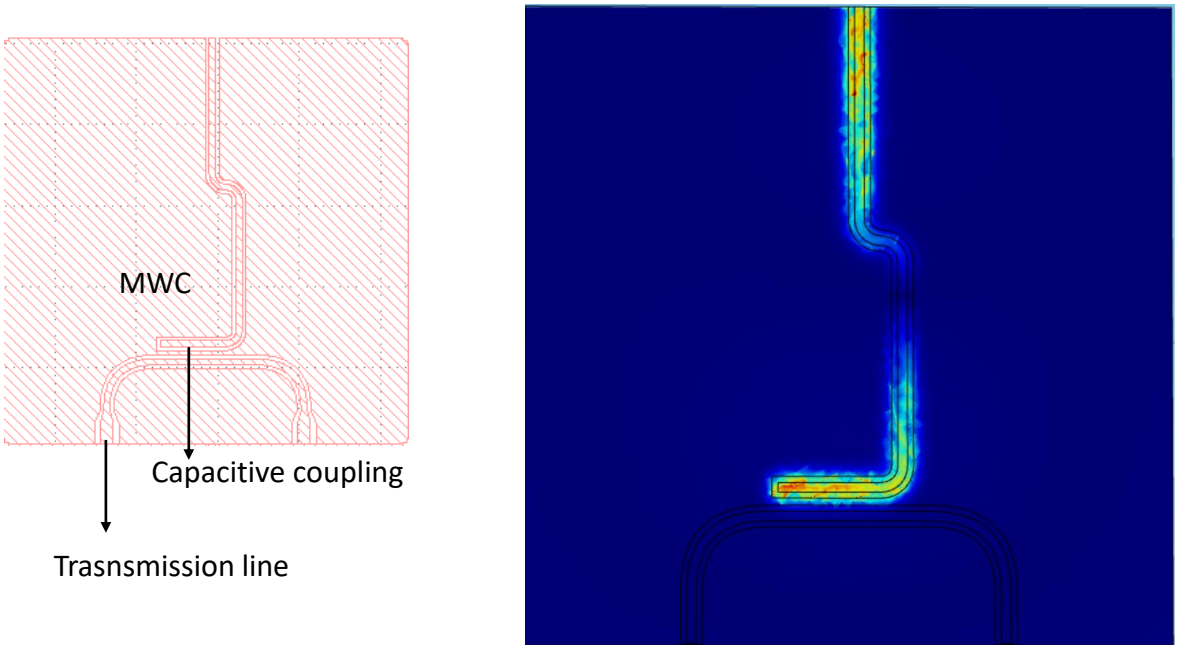

FIGURE 6.2: (left) The GDS file of the MWC which was used to perform laser lithography on 1 cm^2 chip(right) FEM simulation of the MWC showing the voltage distribution in the MWC at the fundamental mode of MW resonance. The resonance frequency was extracted to be 6.2 GHz. Blue color corresponds to minimum voltage and red the maximum

There is also an interdigitated capacitor (IDC) running across the chip near one end of the central conductor of the MWC shown in figure 6.1. The role of IDC is the subject of discussion for the upcoming sections. However, in this section, we will try to approximate the capacitance of the IDC using analytical solutions. The IDC is a multi-finger periodic structure that utilizes the capacitance across a narrow gap between two thin films. The gaps are essentially very long and folded to use a small amount of area, as shown in figure 6.3. The approximate solution of the total capacitance of an IDC of length l is given by [79],

$$C = \frac{\epsilon_{re} 10^{-3}}{18\pi} \frac{K(k)}{K'(k)} (N-1) l \text{ (pF)} \tag{6.1}$$

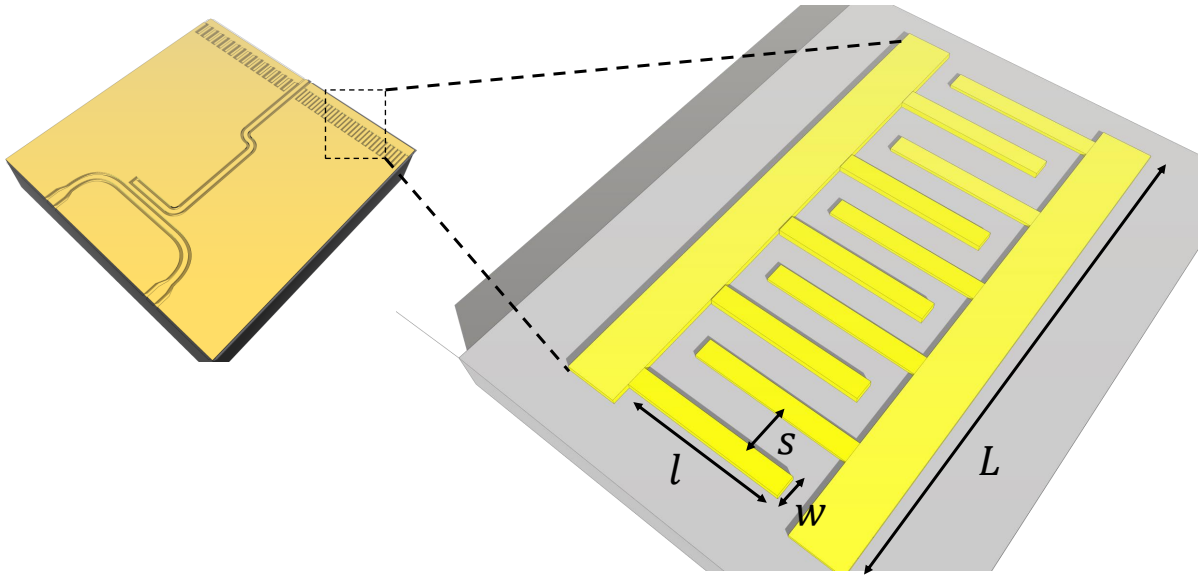

FIGURE 6.3: Schematic of the interdigitated capacitor

where C is the total capacitance, l is the length of IDC, N is the number of fingers. The spacing s between two fingers of IDC is same as the width of the finger w. The substrate is intrinsic Si with relative permittivity $\epsilon_r = 11.7$. The ratio $\frac{K(k)}{K'(k)} = \frac{\pi}{ln\left[2\frac{1+\sqrt{k'}}{1-\sqrt{k'}}\right]}$ where $k' = \sqrt{1-k^2}$ and $k = \tan^2[\frac{0.25\pi w}{w+s}]$. We fabricated IDCs with different dimensions giving us following capacitances,

l (μm)	w (μm)	g (μm)	N	C_{IDC} (pF)
780	90	90	90	68
650	100	100	64	25
600	100	100	49	14
400	100	100	49	9

6.3 NEMS

The NEMS under consideration in this chapter is doubly clamped pre-stressed Silicon nitride nanobeams. The two kinds of nanobeams are 1) 100 μm $\times$ 300 nm $\times$ 100 nm SiN nanobeam with 30 nm of thin Al layer. 2) a harp of SiN nanobeams with different lengths encompassed with Al electrodes on either side. The nanobeam with a thin layer of Al on top was fabricated using the usual step discussed in *chapter 3*. The device is shown in figure 6.4. This gate of this device was connected to one of the open ends of the central conductor of the MWC via wire bonds. The pads of the nanobeam were connected to an RF source such that the nanobeam is excited using a capacitive drive. The fabrication process was hampered due to the presence of the foils beneath the surface of SiN that appeared after XeF_2 Si etch that released the

string, as discussed in *chapter 3*. Therefore, the final etching step to release the structure was carried out at IEMN, Lille on a different XeF_2 machine that never produces 'foils'. The gap between the nanobeam and the gate was approximately $\sim$ 90 nm. These devices were fabricated very close to one of the edges of 1 cm^2 chip such that the length of the wire bonds from MWC to gate is small to minimize the extraneous inductance due to them. The extraneous inductance can modify the resonance frequency and the quality factor of the microwave cavity. .

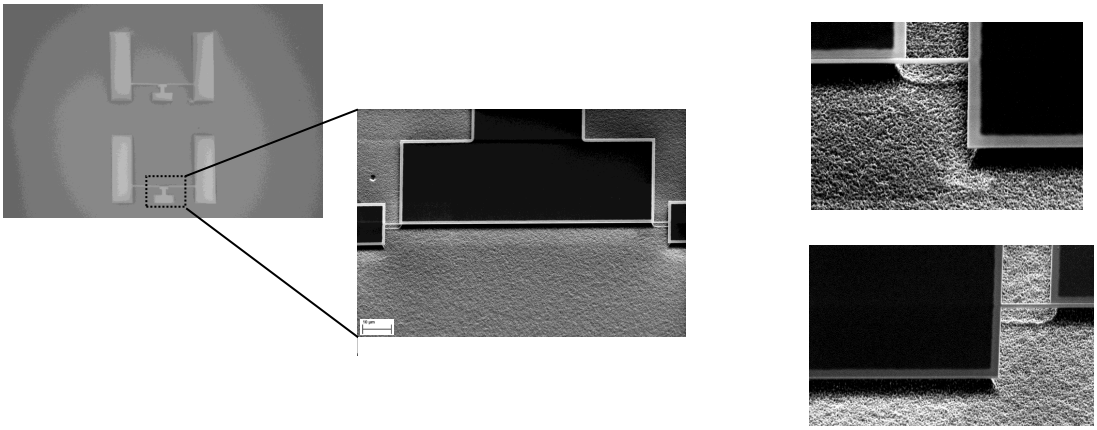

FIGURE 6.4: SEM image of the device used for measurement using capacitive drive and detection using microwave cavity. The devices were made very close to the edge of the chip. There were no foils beneath the surface of SiN in these devices. The nanobeam was 100 μm long, 300 nm wide and 100 nm thick with 30 nm of thin Al on top

The chip consisting of bare silicon nitride nanobeams was fabricated Klaß *et al.* at the University of Konstanz. However, the final release of the structure was intended to be done by us. The electrodes surrounding the nanobeam were 1 μm wide in the initial design. Performing the final etching in the XeF_2 dry etching machine led to the collapse of the electrodes, as shown in figure 6.5. The Silicon etching process in XeF_2 dry etching machine is calibrated to produce a minimum of 1 μm undercuts in the structures. The released nanobeams also possessed foils, as discussed previously. Therefore, it becomes essential to increase the width of the electrodes to prevent them from collapsing while etching. The adequate electrode width should be 3 μm and more.

For the reasons to be discussed in the next section, the gate capacitance C_g between two electrodes of the harp of nanobeams have to be much less than capacitance across the C_{IDC}. Therefore we calculated the approximate capacitance between the two electrodes of the harp using finite element method simulations. Figure 6.6 shows the finite element simulation between two electrodes of the harp for different thicknesses of the substrate. The left simulation

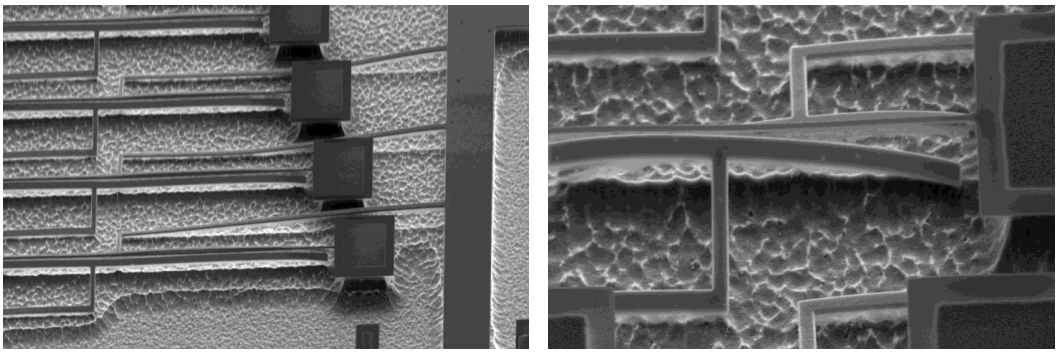

FIGURE 6.5: Collapse of the electrodes which encompasses the SiN nanobeams. The electrodes with width of 1 μm were too small to survive a single calibrated cycle of dry etching with XeF_2

in the figure has an electrode width of 3 μm with a substrate thickness of 20 μm. The spacing between two electrodes in the simulation was 600 nm. The static capacitance we get was 0.05 pF. The middle simulation is with 80 μm thick substrate, and the calculated capacitance was 0.053 pF. The substrate with a thickness of 160 μm has approximately the same capacitance.

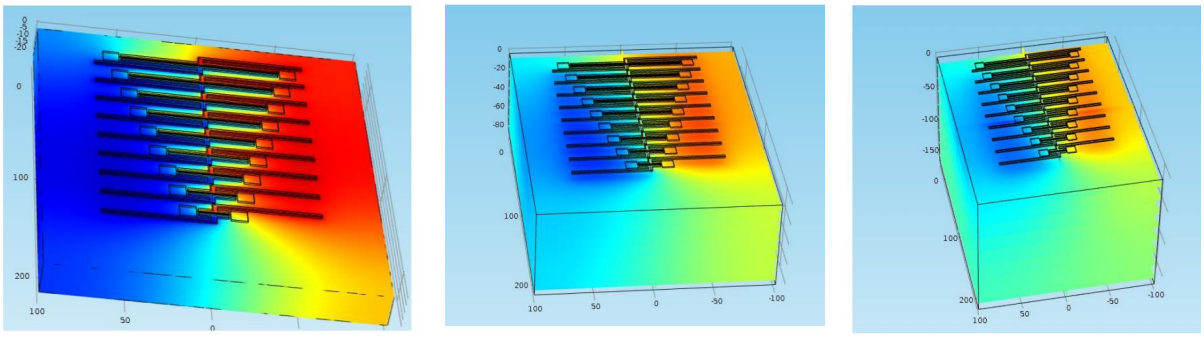

FIGURE 6.6: (left) FEM simulation to calculate the capacitance between electrodes with substrate thickness of 20 μm (middle) FEM simulation to calculate the capacitance between electrodes with substrate thickness of 80 μm (right) FEM simulation to calculate the capacitance between electrodes with substrate thickness of 160 μm. The blue color corresponds to ground or 0 Volt and red color corresponds to 1 Volt

The new chip with an electrode width of 6 μm was fabricated by Klaß *et al.*. This harp consists of 5 nanobeams made of bare silicon nitride with different lengths (80 μm, 70 μm, 60 μm, 50 μm, and 40 μm). The width of these nanobeams was approximately 350 nm, and they

are 100 nm thick. These devices were finally etched at IEMN, Lille, and SEM images are shown in figure 6.7.

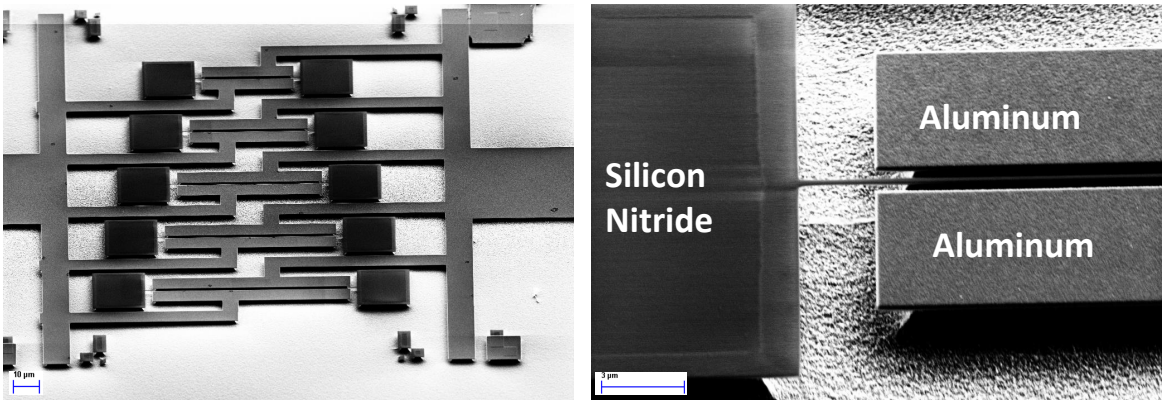

FIGURE 6.7: SEM image of the final device having an electrode thickness of 6 μm.

6.4 Electrical circuit

The cell made of annealed Cu containing two chips was installed at the mixing chamber plate of the Bluefors cryostat. Inside the cell, the chip consisting of a microwave cavity was placed in the space carved from the printed circuit board as shown in figure 6.8 (right). The printed circuit board was made from ROGERS polymer substrate optimized for operation with GHz frequencies. The coplanar waveguide made of gold was printed on the circuit board. The input and the output coaxial lines inside the fridge were soldered to the gold CPW. The transmission line on the PCB was, in turn, wire bonded to the transmission line on the chip. The chip consisting of a mechanical resonator was placed very near to the chip with the MWC, also shown in figure 6.8. Both the chips were clamped using a copper piece with a thin layer of Indium between the copper and the chip.

One end of the central conductor of the MWC was wire bonded to the gate electrode of the mechanical resonator. The upper part of the IDC was wire bonded to the Al pad of the nanobeam. The Cu pad on the PCB designed for the RF drive is also connected to the upper part of the IDC. This scheme of wire bonds is clearly shown in figure 6.8. We always make an effort to keep the wire bonds as short as possible to prevent spurious inductances.

The IDC acts as a capacitive ground for microwaves and allows us for actuation and detection dielectrically or capacitively using a pair of electrodes. The drive and detection circuit is shown in figure 6.9. The capacitance of the IDC was chosed so that it was approximately a

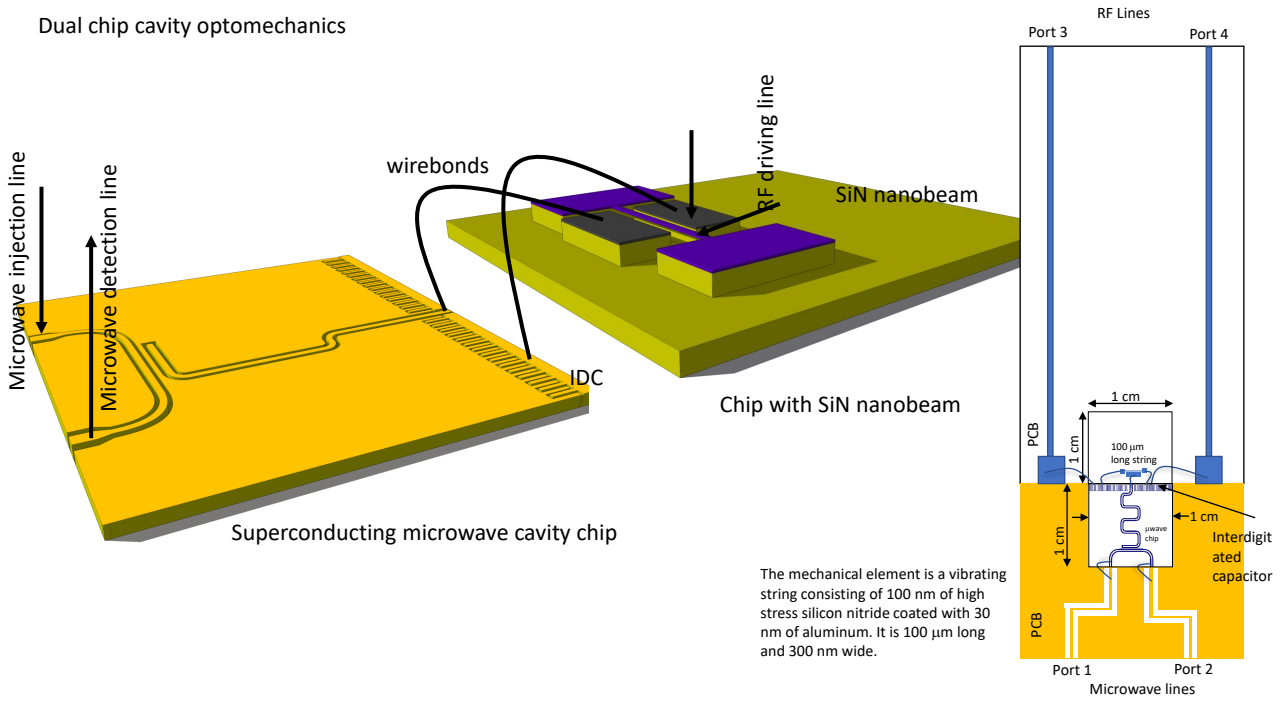

FIGURE 6.8: (left) Schematic of the measurement circuit inside the cell installed at the mixing chamber plate for measurement of the bare SiN string. (right) Schematic showing the two chips which are placed very close to each other to shorten the length of the wirebonds reducing spurious inductance. The NEMS chip contains the metalized string

short circuit at the microwave resonance and approximately an open circuit at the mechanical resonance, thereby enabling the RF drive of the string. Since the impedance of the IDC was low compared with that of the gate capacitor, motion of the sting caused a significant change in the total capacitance of the microwave resonator (figure 6.9). The Keysight microwave generator generated the microwave pump tone at ω_c, where ω_c is the resonance frequency of the cavity. The pump tone was kept at a constant pump power of 16 dBm. The pump tone was divided into two microwave lines. One of the lines acts as a local oscillator for the mixer at room temperature for the downconversion of the signal. The other line is attenuated (attenuation depends on how much power we want at the cell level), which is further split into two lines. The line going inside the cryostat to the mixing chamber plate can be combined with a weak probe signal to measure the transmission of the cavity. The transmitted pump signal from the cell at ω_c was canceled by combining with another line at the 4-kelvin plate to avoid the saturation of the cryogenic HEMT. Due to the motion of nanobeam with a fundamental resonance frequency at Ω_m, the signal at ω_c is periodically modulated, causing sidebands at $\omega_c \pm \Omega_m$. The sideabands were further amplified using room temperature HEMT before being downconverted at the mixer. The details about the attenuation in the coaxial line inside the cryostat and the gain of HEMTs were given in *Chapter 3*. The downconverted signal at Ω_m was fed to the Zurich

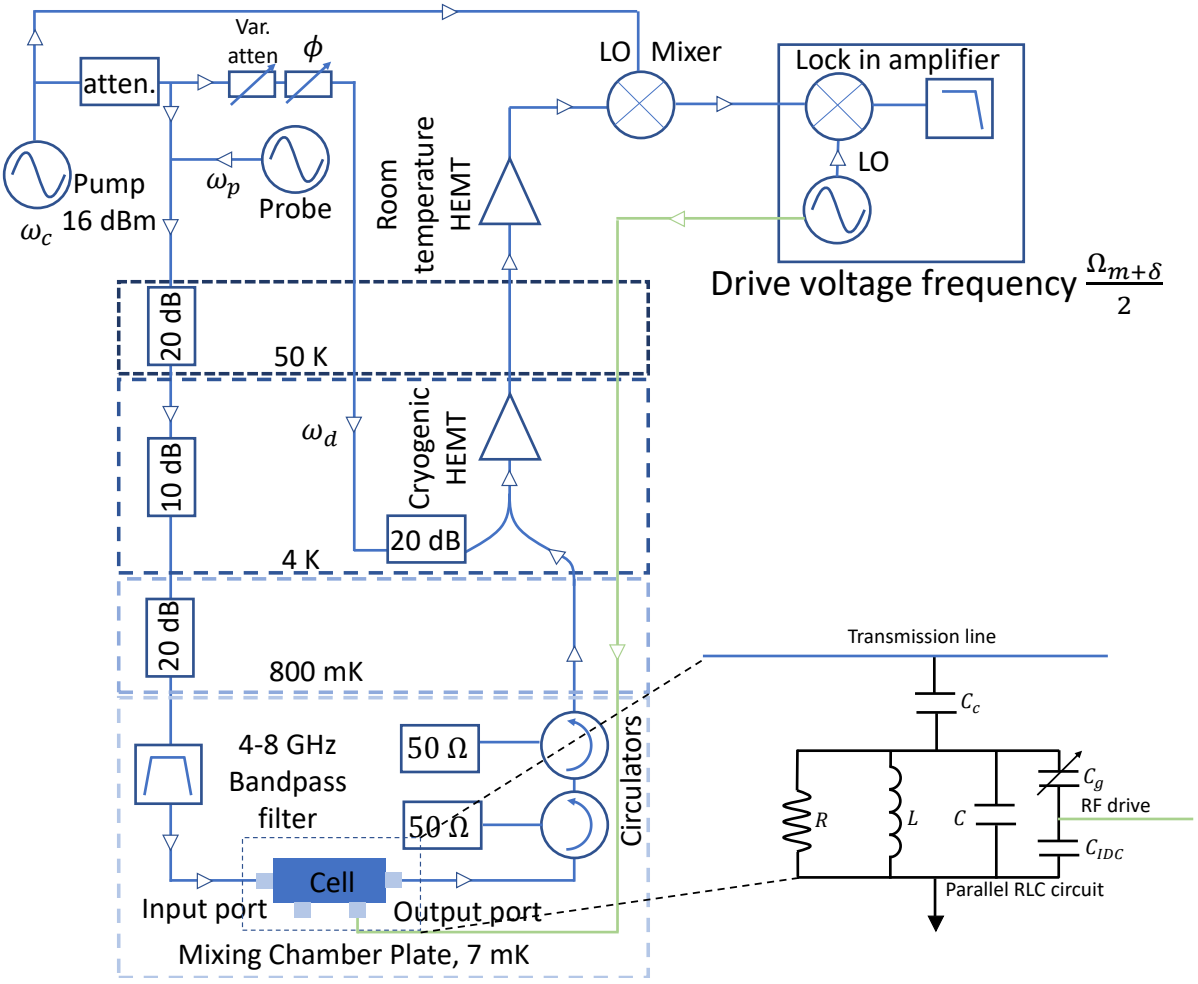

FIGURE 6.9: Circuit diagram for the measurement of the mechanical sideband. The circuit was similar to measurements used in previous chapters. The green line is the therocoaxial line for feeding an RF signal to the mechanical resonator

instruments UHF lockin amplifier. A signal oscillator inside the lockin amplifier was used to generate the RF drive at Ω (close to half the mechanical resonance frequency) and the reference at 2Ω going into the lockin's mixer. The RF signal from room temperature to the cell was fed using a thermocoaxial cable (shown in green in the circuit diagram), having a capacitance of 600 pF and resistance of 150 Ω.

According to the simple circuit model of figure 6.9, the change in the capacitance of the microwave cavity due to the motion of nanobeam $\frac{dC}{dx}$ is attenuated by a factor $\frac{1}{(1+\frac{C_g}{C_{IDC}})^2}$ where C_g is the gate capacitance between two electrodes and C_{IDC} is the capacitance across the interdigitated capacitor. Therefore, as long as $C_{IDC} >> C_g$, the impedance of the IDC should not degrade the detection sensitivity. However, we have not ruled out the possibility that the IDC degrades the quality factor of the microwave cavity. The calculated approximate

solution of the capacitance across IDC was $\sim$ 60 pF, which is much greater than the simulated gate capacitance across the electrodes.

6.5 Measurement of 100 μm SiN nanobeam with 30 nm of Al

The pre-stressed SiN nanobeam with a thin layer of Aluminum was fabricated on a 1 cm^2 chip. The nanobeams were 100 μm long, 100 nm thick, and 300 nm wide with 30 nm of Aluminum on top. The gap between nanobeams and the gate is close to $\sim$ 90 nm. Before wire bonding the chip containing the NEMS to the central conductor of the MWC, we measured the transmission of the microwave cavity. We found the resonance frequency of the MWC, $\frac{\omega_c}{2\pi} = 6.23$ GHz at 4 kelvin. The resonance frequency extracted from the transmission measurements was similar to the value obtained using FEM simulation on COMSOL. After wire bonding to the gate of the nanobeam, the resonance frequency of the MWC decreased to 5.8 GHz, which is expected due to spurious inductance added by wire bonds and added capacitance by pads and nanobeam. The MWC used in this measurement was made from Niobium deposited using ultra-high vacuum e-beam evaporator. The cavity parameters extracted from the transmission measurement at 95 mK is also shown in figure 6.10. We measured the transmission of the MWC at vari-

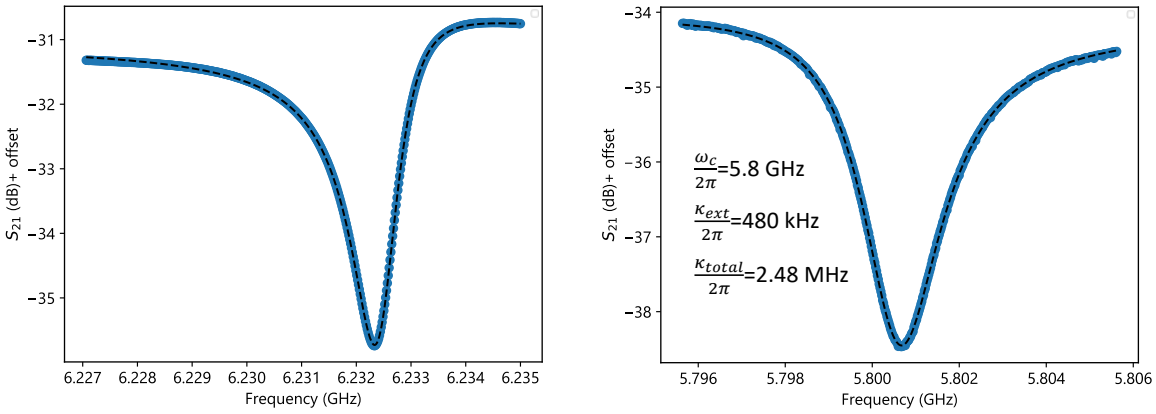

FIGURE 6.10: (left) Transmission measurement of the MWC when not connected to another chip with nanobeam. The resonance frequency extracted was 6.23 GHz. (right) Transmission measurement of the MWC when connected to the gate of the nanobeam. The resonance frequency decreased to 5.8 GHz

ous temperatures from 500 mK to the base temperature and found the resonance frequency to be approximately the same. After characterizing the MWC, we pumped the MWC at ω_c while nanobeam is grounded. The in-cavity scheme will lead to the generation of mechanical sidebands at $\omega_c \pm \Omega_m$ due to periodic modulation of the MWC by the thermal motion of the

mechanical resonator coupled to it. Ω_m is the resonance frequency of the fundamental mode of the mechanical resonator. Using the circuit shown in figure 6.9, we can measure both the sidebands. The upper sideband was measured using the spectrum mode of the Zurich Instrument's UHF lockin amplifier. The sampling rate was set to 1716 samples/sec, which sets the span of the spectrum. The lockin amplifier's NEP bandwidth was set to 565 Hz. The mechanical sideband was measured at different temperatures (495 mK, 405 mK, 318 mK, 231 mK, 187 mK, 140 mK, 95 mk, 48 mK), and the power spectral density was plotted as shown in figure 6.11. The pump power applied by the Keysight generator was kept the same. As mentioned in previous chapters, the area under the mechanical sideband while pumping in-cavity is proportional to the temperature; we plotted the area under the mechanical sideband versus temperature to check for the linearity. The plot is also shown in figure 6.11. At 495 mK, the resonance frequency of the mechanical resonator $\Omega_m/2\pi$ was 2.39 MHz, and linewidth $\Gamma_m/2\pi$ was 89 Hz. The linewidth and the resonance frequency decreased with a decrease in temperature.

The area under the mechanical sideband is linear in temperature at high temperatures, but departs from linearity below 200 mK. In the plot of the area under the mechanical sideband versus the temperature shown in figure 6.11, blue dots represents the points where the area is linear with temperature and the orange dots are the one which departs from the linearity. We have discussed this behavior with another device in *Chapter 5*. To check if the elevated area under the sideband below 200 mK is due to the presence of amplitude fluctuations or *spikes*, we plotted the individual superimposed spectra, and indeed, we found spikes also shown in figure 6.11.

Therefore, we cannot use this device to measure the linewidth and the change in resonance frequency with temperature (below 200 mK) due to spikes whose origin remains elusive to us. However, the device can be used to test the RF drive capability of our platform. The MWC is again pumped at ω_c. The oscillator of lockin amplifier is used to produce a sinusoidal output signal at $\frac{\Omega_{m+\delta}}{2}$ which is fed to the mechanical resonator using thermocoaxial cable installed in the cryostat where $\Omega_{m+\delta}$ is the frequency in the vicinity of Ω_m and δ depends on the linewidth of the mechanical resonator. The force exerted on the mechanical resonator due to the mechanical RF drive of $V_{ac}\cos\left[\frac{\Omega_{m+\delta}}{2}t\right]$ is proportional to $\left(V_{ac}\cos\left[\frac{\Omega_{m+\delta}}{2}t\right]\right)^2$ where V_{ac} is the RMS amplitude of the RF signal.
The term $\left(V_{ac}\cos\left[\frac{\Omega_{m+\delta}}{2}t\right]\right)^2$ when expanded has term $V_{ac}^2\cos\left[\Omega_{m+\delta}t\right]$ which excites the mechanical resonator. The oscillation of the mechancial resonator with frequency $\Omega_{m+\delta}$ leads to periodic modulation of the MWC's resonance frequency leading to generation of the sidebands at $\omega_c \pm \Omega_{m+\delta}$. The siganl transmitted by the cell was down-converted using a mixer to produce the signals at $\Omega_{m+\delta}$ and $-\Omega_{m+\delta}$ which is fed to lockin amplifier. The second harmonic of the oscillator (used to generate the RF signal) is used to demodulate the signal inside the lockin

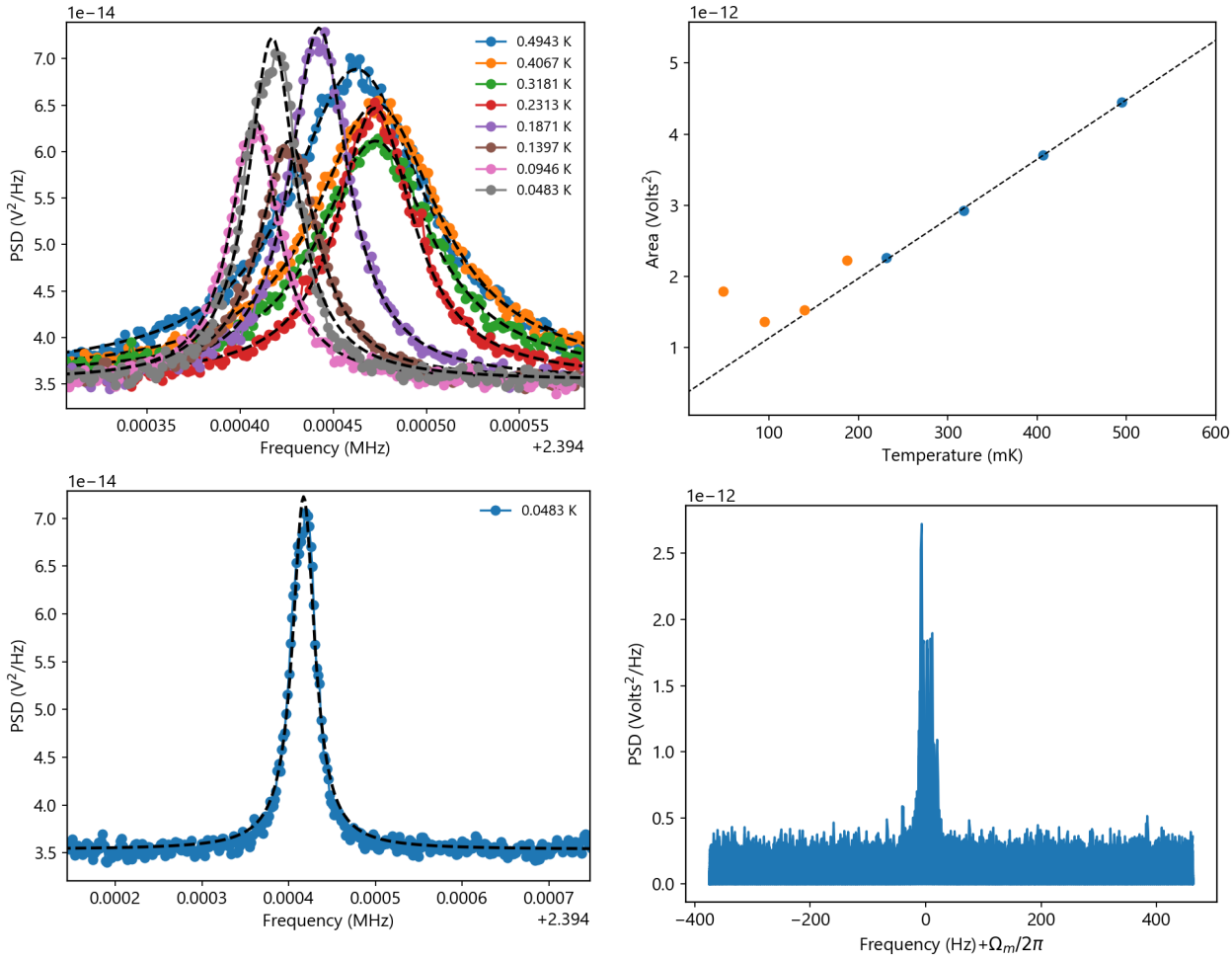

FIGURE 6.11: (top left) Mechanical noise spectrum at $\omega_c+\Omega_m$ while pumping the MWC at ω_c for specified temperatures. (top right) Area under the mechanical sideband versus the temperature. The orange points shows the departure of linearity below 200 mK (bottom left) Mechanical noise spectrum at 48 mK. The increased area under the noise spectrum is due to the presence of amplitude fluctuations or *spikes* (bottom right) The individual spectra were plotted at 48 mK showing spikes

amplifier. The RF frequency generated from the oscillator was swept from $\frac{\Omega_{m-\delta}}{2}$ to $\frac{\Omega_{m+\delta}}{2}$.

Figure 6.12 shows the mechanical response of the signal at two different values of V_{ac}. The V_{ac} applied 2.6 mVolts and 1.96 mVolts. Normalizing the drive level leads to the overlap of the signal for two different levels demonstrating linear response. The measurements were done at 495 mK and 230 mK. The response of the mechanical drive becomes very noisy near the mechanical resonance frequency below 200 mK as shown in figure 6.13 possibly due to spikes. We then tried applying $V_{dc} + V_{ac}\cos[\Omega_{m+\delta}]$ as RF drive to see how the resonance frequency

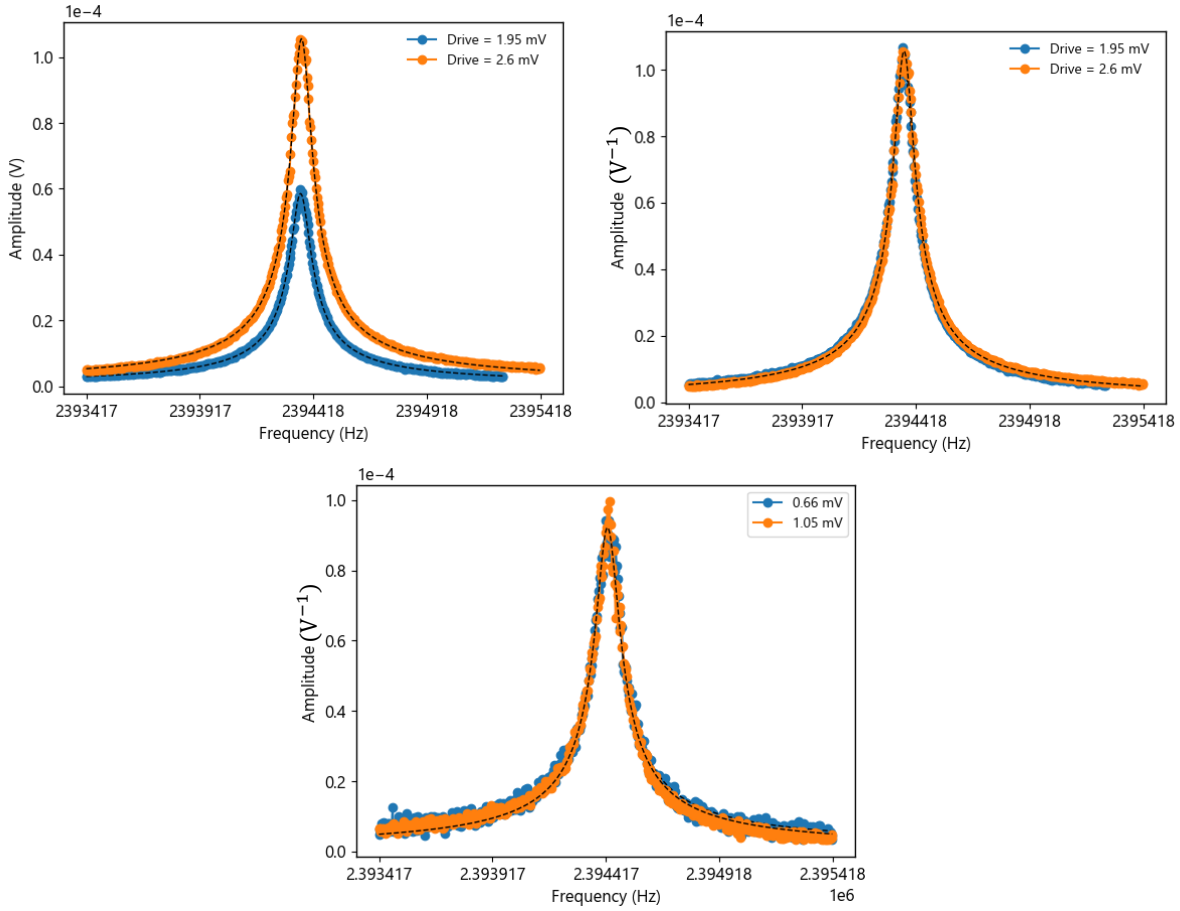

FIGURE 6.12: (top left) Mechanical response of the nanobeam at 495 mK when it is capacitively driven with an RF signal. The plots are the mechanical response at two different amplitude of RF signal (top right) The two plots on the top left plot were normalized by the square of the driving voltage, demonstrating linearity (bottom middle) The linearity was also demonstrated at 243 mK

varies with variation in V_{dc} (DC RF voltage). Applying V_{dc} can nullify any inbuilt charge in the nanobeam.

6.6 Measurement of non-metalized SiN strings below 500 mK

The typical actuation schemes of nanomechanical resonators are capacitive [65], piezoelectric [48], magnetomotive [38], electrothermal [10], etc. These actuation schemes are highly integrable and efficient but put many constraints on material choice and geometry. For example,

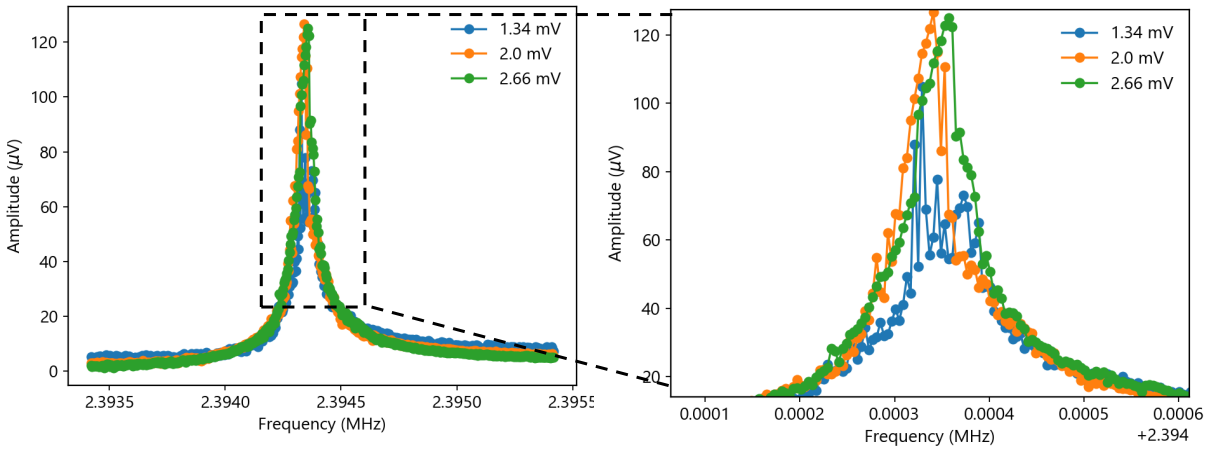

FIGURE 6.13: Mechanical response of the metalized string at different drive levels at 187 mK

capacitive actuation relies on the interaction between two metallic plates. The magnetomotive actuation is also based on the current passing through NEMS made entirely of metal or metalized dielectrics. The internal piezoelectric actuation scheme demands the material used for fabricating NEMS to be piezoelectric. Since the dissipation of metalized SiN strings is primarily due to the presence of metal [47], it is important to measure the NEMS made of non-metalized SiN. Unterreithmeier *et al.* [76] first measured the SiN strings actuated via dielectric forces. A polarizable material experiences an attractive force in an inhomogeneous electric field directed towards maximum field strength. Here, the doubly clamped pre-stressed SiN string acts as a polarizable material as shown in figure 6.7. The inhomogeneous field is created by two Aluminum electrodes also shown in figure 6.7. An AC voltage $V_{ac}\cos(\frac{\Omega t}{2})$ was applied to one of the electrode resulting in oscillating force component that drives the string perpendicular to the chip plane, where $\Omega \approx \Omega_m$ and Ω_m is the resonance frequency of the string. The circuit diagram for the measurement of SiN string is shown in figure 6.9. We measured the transmission of the MWC before and after bonding the electrode of SiN strings to the central conductor of the MWC. Unlike in the case of the metalized string, the microwave cavity's linewidth increased considerably upon bonding the NEMS chip to the cavity chip as shown in the plot 6.14 (there are offsets in both x and y). The reason for this is uncertain. We observed similar broadening of the microwave resonance with two different NEMS chips (K1 and K3) with bare SiN strings. The resonance frequency shifted from 6.1855 GHz before bonding to 6.607 GHz after wire bonding. Because the devices on chip K3 were close to the edge of the chip, we used much shorter wirebonds to connect chip K3 than to connect chip K1, but this did not improve the Q of the microwave resonance.

We are using 16 dBm microwave pump on the cavity resonance (ω_c). We tried increasing

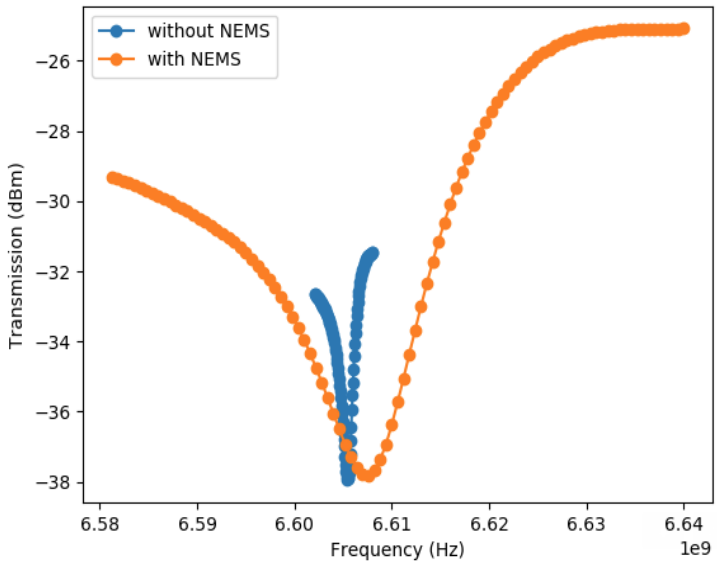

FIGURE 6.14: Transmission of the MWC before and after bonding to the chip with the bare SiN string (sample K1)

the microwave drive from 16 dBm to 18 dBm but this caused the noise level measured by the lockin amplifier to increase. Drive levels above 16 dBm also make the opposition line unstable, leading to saturation of the HEMT. The power into the cell is about -46 dBm, corresponding to about 25 nW. Applying an RF drive $V_{ac}\cos(\frac{\Omega t}{2})$ where $V_{ac} = 200$ mV and Ω was swept from 3.161 to 3.167 MHz, we found the signal corresponding to the resonance of the longest string i.e. 81 μm. However, we were not able to resolve the signal in linear regime by applying lower drive voltage. The measurements were done at the mixing chamber plate temperature of 284 mK. The plot 6.15 shows the signal at different drive levels. Even at 35 mV rms drive, the resonance may remain non-linear. The measurement at 35 mV was averaged over 12 hours. Also, it's not clear why the offset depends on drive level shown in plot 6.15. Using the same procedures, we found the resonance frequency of strings with different lengths. For the string of length 61 μm, we have to increase the maximum drive voltage to 600 mV and to 700 mV for string lengths of 51 μm and 41 μm. The resonance frequency was approximated by plotting the jump frequency of the non-linear response of the string against the square of the driving voltage as shown in figure 6.15. The typical response of the strings of different lengths at different voltages are shown in figures 6.16, 6.17, 6.18, 6.19, 6.20. The figures also comprise the plot showing the jump frequency of the non-linear response against the square of the driving voltage.

The jump frequency at the lowest drive voltage for strings of different lengths was plotted against the length of the string shown in figure 6.21. The experimental data were compared with the resonance frequency of strings of different lengths extracted from the numerical solution of the Euler-Bernoulli's beam discussed by Bokaian *et al.* [13]. The experimental data were also

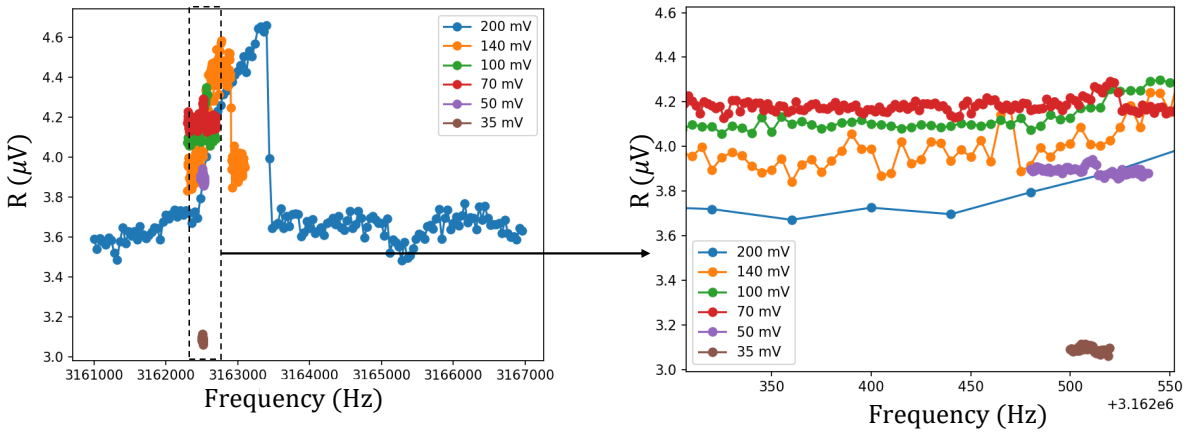

FIGURE 6.15: (left)Response of 81 μm string (right) The offset depends on the drive level

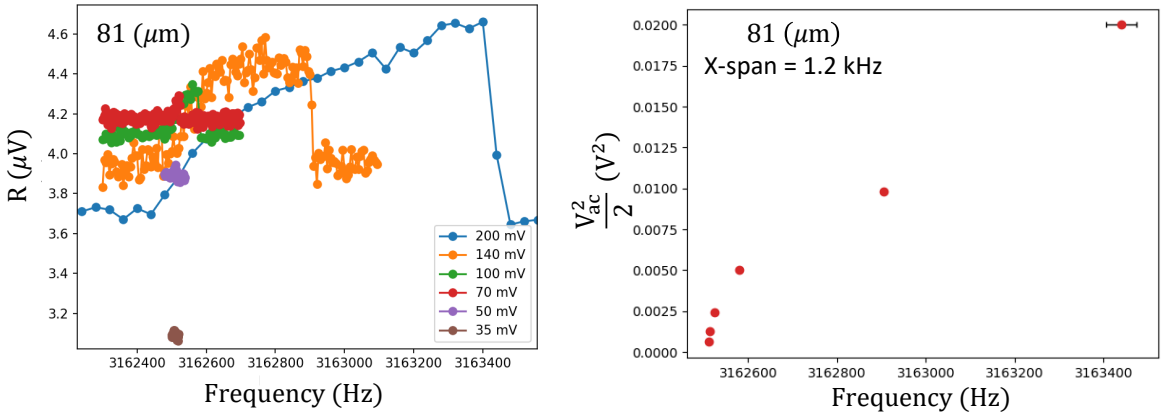

FIGURE 6.16: (left)Response of 81 μm string (right) Jump frequency against the square of the driving voltage

compared with the FEM simulation done in COMSOL.

6.7 Conclusions

In this chapter, we presented a scheme to measure the motion of the non-metalized SiN string below 500 mK. The polarizable SiN string is driven out off to the chip plane using an inhomogeneous electric field between two electrodes. We were able to measure all the SiN strings of different lengths shown in figure 6.7 although in the non-linear regime at 284 mK. We also measured the strings at a mixing chamber temperature of 13 mK in the non-linear regime and

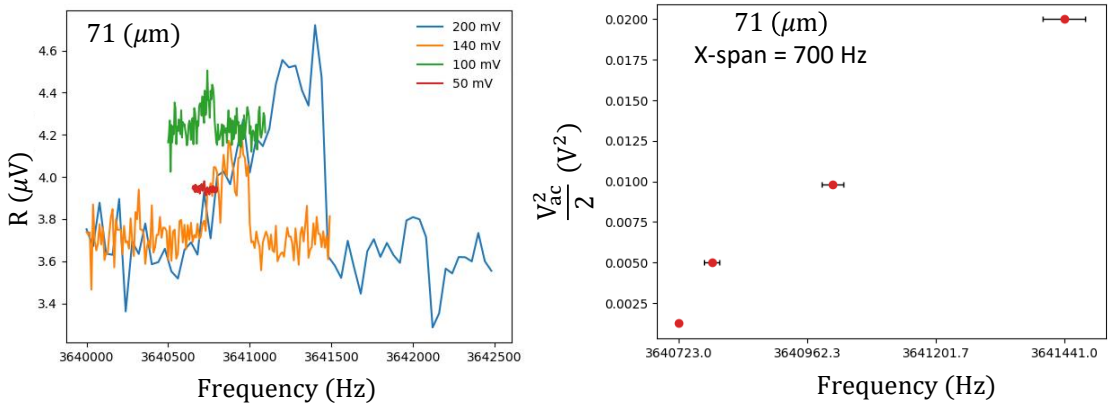

FIGURE 6.17: (left)Response of 71 μm string (right) Jump frequency against the square of the driving voltage

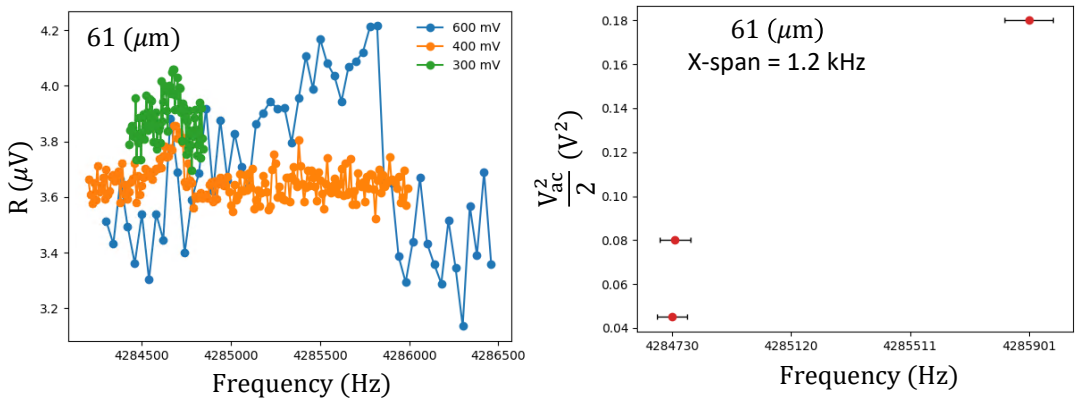

FIGURE 6.18: (left)Response of 61 μm string (right) Jump frequency against the square of the driving voltage

found no signs of *spikes*. The resonance frequency of different strings was plotted against their length. The experimental data were compared with the numerical solution of Euler-Bernoulli's beam equation and FEM simulation. We also measured a 100 μm metalized SiN string using the dual-chip scheme and observed its response. The mechanical spectrum was again tarnished by the presence of *spikes*. We can measure the non-metalized SiN string in the linear regime by increasing the coupling between the string and the MWC. The coupling can be increased by reducing the gap between the string and the electrodes.

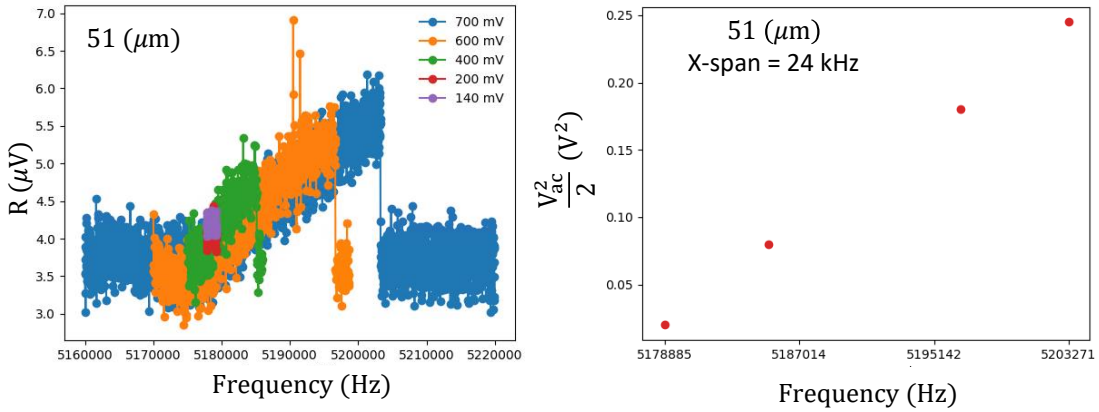

FIGURE 6.19: (left)Response of 51 μm string (right) Jump frequency against the square of the driving voltage

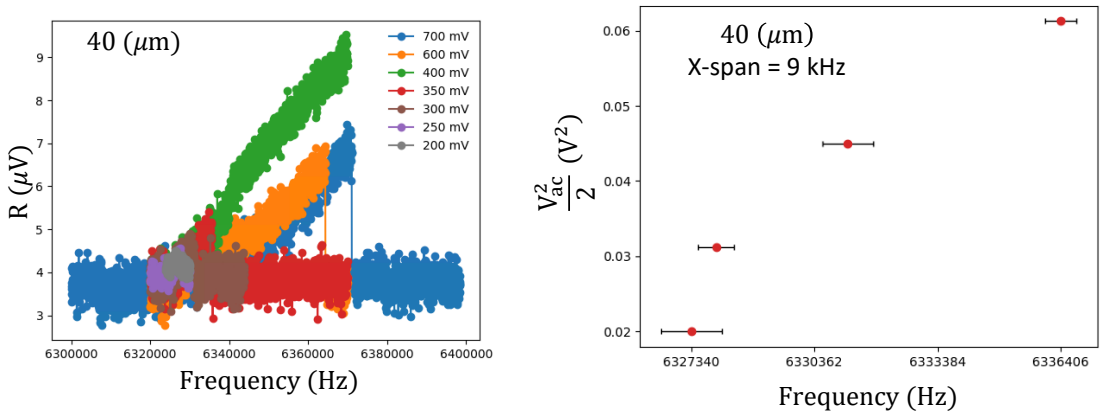

FIGURE 6.20: (left)Response of 41 μm string (right) Jump frequency against the square of the driving voltage

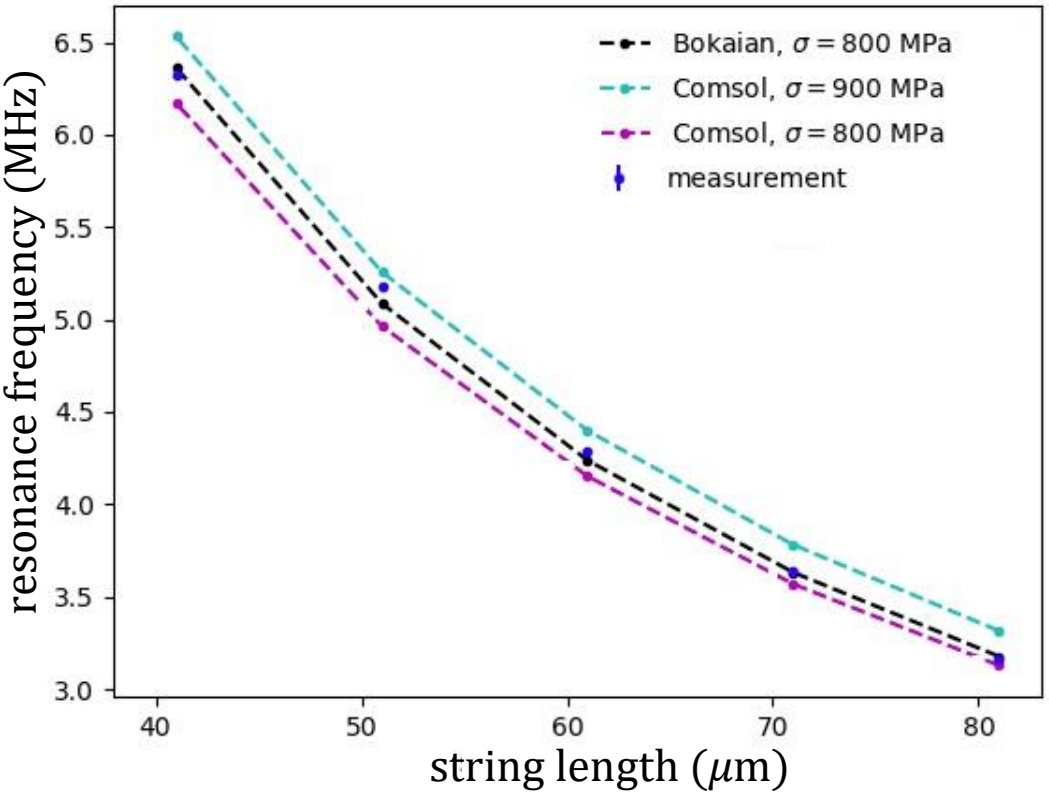

FIGURE 6.21: Jump frequency at the lowest drive voltage for strings of different lengths versus the length of the string. The experimental data was compared with the numerical solution (Bokaian *et al.*) considering the stress in the string to be 900 MPa.

Bibliography

[1] https://ark.intel.com/content/www/us/en/ark/products/126699/intel-core-i9-7980xe-extreme-edition-processor-24-75m-cache-up-to-4-20-ghz.html.

[2] https://www.nobelprize.org/prizes/physics/1997/summary/.

[3] https://www.nobelprize.org/prizes/physics/2001/summary/.

[4] AA Abdumalikov Jr, O Astafiev, Alexandre M Zagoskin, Yu A Pashkin, Y Nakamura, and Jaw Shen Tsai. Electromagnetically induced transparency on a single artificial atom. *Physical review letters*, 104(19):193601, 2010.

[5] P W Anderson, Bertrand I Halperin, and C M Varma. Anomalous low-temperature thermal properties of glasses and spin glasses. *Philosophical Magazine*, 25(1):1–9, 1972.

[6] Frank Arute, Kunal Arya, Ryan Babbush, Dave Bacon, Joseph C Bardin, Rami Barends, Rupak Biswas, Sergio Boixo, Fernando GSL Brandao, David A Buell, et al. Quantum supremacy using a programmable superconducting processor. *Nature*, 574(7779):505–510, 2019.

[7] Neil W Ashcroft, N David Mermin, et al. Solid state physics, 1976.

[8] Markus Aspelmeyer, Tobias J Kippenberg, and Florian Marquardt. Cavity optomechanics. *Reviews of Modern Physics*, 86(4):1391, 2014.

[9] J Åström, PCF Di Stefano, F Pröbst, L Stodolsky, J Timonen, C Bucci, S Cooper, C Cozzini, Fv Feilitzsch, H Kraus, et al. Fracture processes observed with a cryogenic detector. *Physics Letters A*, 356(4-5):262–266, 2006.

[10] I Bargatin, I Kozinsky, and ML Roukes. Efficient electrothermal actuation of multiple modes of high-frequency nanoelectromechanical resonators. *Applied Physics Letters*, 90(9):093116, 2007.

[11] AJ Barlow, J Lamb, and AJ Matheson. Viscous behaviour of supercooled liquids. *Proceedings of the Royal Society of London. Series A. Mathematical and Physical Sciences*, 292(1430):322–342, 1966.

[12] Shabir Barzanjeh, Matthias Wulf, Matilda Peruzzo, Mahmoud Kalaee, PB Dieterle, Oskar Painter, and Johannes M Fink. Mechanical on-chip microwave circulator. *Nature communications*, 8(1):1–7, 2017.

[13] A. Bokaian. Natural frequencies of beams under tensile axial loads. *Journal of Sound and Vibration*, 142(3):481 – 498, 1990.

[14] K-J Boller, A Imamoğlu, and Stephen E Harris. Observation of electromagnetically induced transparency. *Physical Review Letters*, 66(20):2593, 1991.

[15] Daniel Bothner, Shun Yanai, Agustin Iniguez-Rabago, Mingyun Yuan, Ya M Blanter, and Gary A Steele. Cavity electromechanics with parametric mechanical driving. *Nature communications*, 11(1):1–9, 2020.

[16] AL Burin and Yu Kagan. Low-energy collective excitations in glasses. new relaxation mechanism for ultralow temperatures. *Soviet Journal of Experimental and Theoretical Physics*, 80(4):761–768, 1995.

[17] AL Burin, Yu Kagan, LA Maksimov, and I Ya Polishchuk. Dephasing rate in dielectric glasses at ultralow temperatures. *Physical review letters*, 80(13):2945, 1998.

[18] David G Cahill and Robert O Pohl. Lattice vibrations and heat transport in crystals and glasses. *Annual review of physical chemistry*, 39(1):93–121, 1988.

[19] M Calvo, J Goupy, A Benoit, O Bourrion, A Catalano, A Monfardini, et al. Superconducting kinetic inductance detectors for astronomy and particle physics. *Nuclear Instruments and Methods in Physics Research Section A: Accelerators, Spectrometers, Detectors and Associated Equipment*, 824:173–176, 2016.

[20] D Cattiaux, I Golokolenov, S Kumar, M Sillanpaa, L Mercier de Lepinay, RR Gazizulin, X Zhou, AD Armour, O Bourgeois, A Fefferman, et al. A macroscopic object passively cooled into its quantum ground state of motion. *arXiv preprint arXiv:2104.09541*, 2021.

[21] AN Cleland and ML Roukes. External control of dissipation in a nanometer-scale radiofrequency mechanical resonator. *Sensors and Actuators A: Physical*, 72(3):256–261, 1999.

[22] Aashish A Clerk, Michel H Devoret, Steven M Girvin, Florian Marquardt, and Robert J Schoelkopf. Introduction to quantum noise, measurement, and amplification. *Reviews of Modern Physics*, 82(2):1155, 2010.

[23] Martijn A Cohen, Daniel Bothner, Yaroslav M Blanter, and Gary A Steele. Optomechanical microwave amplification without mechanical amplification. *Physical Review Applied*, 13(1):014028, 2020.

[24] Peter Debye. Zur theorie der spezifischen wärmen. *Annalen der Physik*, 344(14):789–839, 1912.

[25] Thomas Faust, Peter Krenn, Stephan Manus, Jörg Peter Kotthaus, and Eva Maria Weig. Microwave cavity-enhanced transduction for plug and play nanomechanics at room temperature. *Nature communications*, 3(1):1–6, 2012.

[26] AD Fefferman, RO Pohl, AT Zehnder, and JM Parpia. Acoustic properties of amorphous silica between 1 and 500 mk. *Physical review letters*, 100(19):195501, 2008.

[27] Andrew Fefferman. The low temperature acoustic properties of amorphous silica and polycrystalline aluminum. 2009.

[28] JE Field, KH Hahn, and SE Harris. Observation of electromagnetically induced transparency in collisionally broadened lead vapor. *Physical review letters*, 67(22):3062, 1991.

[29] Crispin Gardiner and Peter Zoller. *Quantum noise: a handbook of Markovian and non-Markovian quantum stochastic methods with applications to quantum optics*. Springer Science & Business Media, 2004.

[30] Crispin W Gardiner and Matthew J Collett. Input and output in damped quantum systems: Quantum stochastic differential equations and the master equation. *Physical Review A*, 31(6):3761, 1985.

[31] Ramesh Garg, Inder Bahl, and Maurizio Bozzi. *Microstrip lines and slotlines*. Artech house, 2013.

[32] Stephen E Harris, JE Field, and A Imamoğlu. Nonlinear optical processes using electromagnetically induced transparency. *Physical Review Letters*, 64(10):1107, 1990.

[33] Lene Vestergaard Hau, Stephen E Harris, Zachary Dutton, and Cyrus H Behroozi. Light speed reduction to 17 metres per second in an ultracold atomic gas. *Nature*, 397(6720):594–598, 1999.

[34] BD Hauer, PH Kim, C Doolin, F Souris, and JP Davis. Two-level system damping in a quasi-one-dimensional optomechanical resonator. *Physical Review B*, 98(21):214303, 2018.

[35] Fredrik Hocke, Xiaoqing Zhou, Albert Schliesser, Tobias J Kippenberg, Hans Huebl, and Rudolf Gross. Electromechanically induced absorption in a circuit nano-electromechanical system. *New Journal of Physics*, 14(12):123037, 2012.

[36] F Hoehne, Yu A Pashkin, O Astafiev, L Faoro, LB Ioffe, Y Nakamura, and Jaw Shen Tsai. Damping in high-frequency metallic nanomechanical resonators. *Physical Review B*, 81(18):184112, 2010.

[37] Julian Kelly, Rami Barends, Austin G Fowler, Anthony Megrant, Evan Jeffrey, Theodore C White, Daniel Sank, Josh Y Mutus, Brooks Campbell, Yu Chen, et al. State preservation by repetitive error detection in a superconducting quantum circuit. *Nature*, 519(7541):66–69, 2015.

[38] Robert G Knobel and Andrew N Cleland. Nanometre-scale displacement sensing using a single electron transistor. *Nature*, 424(6946):291–293, 2003.

[39] David P Lake, Matthew Mitchell, and Paul E Barclay. Demonstration of all-optical switching with dichromatic cavity optomechanics. In *Frontiers in Optics*, pages FW7B–2. Optical Society of America, 2018.

[40] Florent Lecocq, Jeremy B Clark, Raymond W Simmonds, Jose Aumentado, and John D Teufel. Quantum nondemolition measurement of a nonclassical state of a massive object. *Physical Review X*, 5(4):041037, 2015.

[41] Anthony J Leggett. Amorphous materials at low temperatures: why are they so similar? *Physica B: Condensed Matter*, 169(1-4):322–327, 1991.

[42] Anthony J Leggett and Dervis C Vural. "tunneling two-level systems" model of the low-temperature properties of glasses: Are "smoking-gun" tests possible? *The Journal of Physical Chemistry B*, 117(42):12966–12971, 2013.

[43] Jevon J Longdell, Elliot Fraval, Matthew J Sellars, and Neil B Manson. Stopped light with storage times greater than one second using electromagnetically induced transparency in a solid. *Physical review letters*, 95(6):063601, 2005.

[44] Vassiliy Lubchenko and Peter G Wolynes. Theory of structural glasses and supercooled liquids. *Annu. Rev. Phys. Chem.*, 58:235–266, 2007.

[45] Annina Luck. *Nuclear spin dominated relaxation of atomic tunneling systems in glasses*. PhD thesis, 2016.

[46] Olivier Maillet. *Stochastic and non-linear processes in nano-electro-mechanical systems*. PhD thesis, Université Grenoble Alpes, 2018.

[47] Olivier Maillet, Dylan Cattiaux, Xin Zhou, Rasul R Gazizulin, Olivier Bourgeois, Andrew D Fefferman, and Eddy Collin. Nanomechanical damping via electron-assisted relaxation of two-level systems. *arXiv preprint arXiv:2009.03804*, 2020.

[48] Sotiris C Masmanidis, Rassul B Karabalin, Iwijn De Vlaminck, Gustaaf Borghs, Mark R Freeman, and Michael L Roukes. Multifunctional nanomechanical systems via tunably coupled piezoelectric actuation. *Science*, 317(5839):780–783, 2007.

[49] Francesco Massel, Sung Un Cho, Juha-Matti Pirkkalainen, Pertti J Hakonen, Tero T Heikkilä, and Mika A Sillanpää. Multimode circuit optomechanics near the quantum limit. *Nature communications*, 3(1):1–6, 2012.

[50] Francesco Massel, TT Heikkilä, J-M Pirkkalainen, Sung-Un Cho, Heini Saloniemi, Pertti J Hakonen, and Mika A Sillanpää. Microwave amplification with nanomechanical resonators. *Nature*, 480(7377):351–354, 2011.

[51] Michael Metcalfe. Applications of cavity optomechanics. *Applied Physics Reviews*, 1(3):031105, 2014.

[52] Martin Mücke, Eden Figueroa, Joerg Bochmann, Carolin Hahn, Karim Murr, Stephan Ritter, Celso J Villas-Boas, and Gerhard Rempe. Electromagnetically induced transparency with single atoms in a cavity. *Nature*, 465(7299):755–758, 2010.

[53] E Nazaretski, RD Merithew, VO Kostroun, AT Zehnder, RO Pohl, and JM Parpia. Effect of low-level radiation on the low temperature acoustic behavior of a- sio 2. *Physical review letters*, 92(24):245502, 2004.

[54] CF Ockeloen-Korppi, E Damskägg, J-M Pirkkalainen, M Asjad, AA Clerk, F Massel, MJ Woolley, and MA Sillanpää. Stabilized entanglement of massive mechanical oscillators. *Nature*, 556(7702):478–482, 2018.

[55] Agustin Palacios-Laloy. *Superconducting qubit in a resonator: test of the Legget-Garg inequality and single-shot readout*. PhD thesis, Université Pierre et Marie Curie-Paris VI, 2010.

[56] TA Palomaki, JW Harlow, JD Teufel, RW Simmonds, and Konrad W Lehnert. Coherent state transfer between itinerant microwave fields and a mechanical oscillator. *Nature*, 495(7440):210–214, 2013.

[57] Matthias Pernpeintner, Thomas Faust, Fredrik Hocke, Jörg Peter Kotthaus, Eva Maria Weig, Hans Huebl, and Rudolf Gross. Circuit electromechanics with a non-metallized nanobeam. *Applied Physics Letters*, 105(12):123106, 2014.

[58] William A Phillips. Tunneling states in amorphous solids. *Journal of low temperature physics*, 7(3):351–360, 1972.

[59] William A Phillips. Two-level states in glasses. *Reports on Progress in Physics*, 50(12):1657, 1987.

[60] Robert O Pohl, Xiao Liu, and EunJoo Thompson. Low-temperature thermal conductivity and acoustic attenuation in amorphous solids. *Reviews of Modern Physics*, 74(4):991, 2002.

[61] David M Pozar. *Microwave engineering*. John wiley & sons, 2011.

[62] Tomás Ramos, Vivishek Sudhir, Kai Stannigel, Peter Zoller, and Tobias J Kippenberg. Nonlinear quantum optomechanics via individual intrinsic two-level defects. *Physical review letters*, 110(19):193602, 2013.

[63] T Rocheleau, T Ndukum, C Macklin, JB Hertzberg, AA Clerk, and KC Schwab. Preparation and detection of a mechanical resonator near the ground state of motion. *Nature*, 463(7277):72–75, 2010.

[64] Tristan Rocheleau. Quantum-limited mechanical resonator measurement and back-action cooling to near the quantum ground state. 2011.

[65] D Rugar and P Grütter. Mechanical parametric amplification and thermomechanical noise squeezing. *Physical Review Letters*, 67(6):699, 1991.

[66] Amir H Safavi-Naeini, Thiago P Mayer Alegre, Martin Winger, and Oskar Painter. Optomechanics in an ultrahigh-q two-dimensional photonic crystal cavity. *Applied Physics Letters*, 97(18):181106, 2010.

[67] Albert Schliesser and Tobias J Kippenberg. Cavity optomechanics with whispering-gallery mode optical micro-resonators. *Advances In Atomic, Molecular, and Optical Physics*, 58:207–323, 2010.

[68] Silvan Schmid, Luis Guillermo Villanueva, and Michael Lee Roukes. *Fundamentals of nanomechanical resonators*, volume 49. Springer, 2016.

[69] James Sethna et al. *Statistical mechanics: entropy, order parameters, and complexity*, volume 14. Oxford University Press, 2006.

[70] Zhen Shen, Yan-Lei Zhang, Yuan Chen, Fang-Wen Sun, Xu-Bo Zou, Guang-Can Guo, Chang-Ling Zou, and Chun-Hua Dong. Reconfigurable optomechanical circulator and directional amplifier. *Nature communications*, 9(1):1–6, 2018.

[71] Ryo Shimano and Makoto Kuwata-Gonokami. Observation of autler-townes splitting of biexcitons in cucl. *Physical review letters*, 72(4):530, 1994.

[72] Jaakko Sulkko, Mika A Sillanpaa, Pasi Hakkinen, Lorenz Lechner, Meri Helle, Andrew Fefferman, Jeevak Parpia, and Pertti J Hakonen. Strong gate coupling of high-q nanomechanical resonators. *Nano letters*, 10(12):4884–4889, 2010.

[73] John D Teufel, Tobias Donner, Dale Li, Jennifer W Harlow, MS Allman, Katarina Cicak, Adam J Sirois, Jed D Whittaker, Konrad W Lehnert, and Raymond W Simmonds. Sideband cooling of micromechanical motion to the quantum ground state. *Nature*, 475(7356):359–363, 2011.

[74] John D Teufel, Dale Li, MS Allman, K Cicak, AJ Sirois, JD Whittaker, and RW Simmonds. Circuit cavity electromechanics in the strong-coupling regime. *Nature*, 471(7337):204–208, 2011.

[75] KA Topp and David G Cahill. Elastic properties of several amorphous solids and disordered crystals below 100 k. *Zeitschrift für Physik B Condensed Matter*, 101(2):235–245, 1996.

[76] Quirin P Unterreithmeier, Eva M Weig, and Jörg P Kotthaus. Universal transduction scheme for nanomechanical systems based on dielectric forces. *Nature*, 458(7241):1001–1004, 2009.

[77] Antti P Vepsäläinen, Amir H Karamlou, John L Orrell, Akshunna S Dogra, Ben Loer, Francisca Vasconcelos, David K Kim, Alexander J Melville, Bethany M Niedzielski, Jonilyn L Yoder, et al. Impact of ionizing radiation on superconducting qubit coherence. *Nature*, 584(7822):551–556, 2020.

[78] Stefan Weis, Rémi Rivière, Samuel Deléglise, Emanuel Gavartin, Olivier Arcizet, Albert Schliesser, and Tobias J Kippenberg. Optomechanically induced transparency. *Science*, 330(6010):1520–1523, 2010.

[79] Withawat Withayachumnankul, Christophe Fumeaux, and Derek Abbott. Compact electric-lc resonators for metamaterials. *Optics Express*, 18(25):25912–25921, 2010.

[80] Emma Edwina Wollman, CU Lei, AJ Weinstein, J Suh, A Kronwald, F Marquardt, Aashish A Clerk, and KC Schwab. Quantum squeezing of motion in a mechanical resonator. *Science*, 349(6251):952–955, 2015.

[81] Min Yan, Edward G Rickey, and Yifu Zhu. Observation of doubly dressed states in cold atoms. *Physical Review A*, 64(1):013412, 2001.

[82] Xiaodong Yang, Mingbin Yu, Dim-Lee Kwong, and Chee Wei Wong. All-optical analog to electromagnetically induced transparency in multiple coupled photonic crystal cavities. *Physical review letters*, 102(17):173902, 2009.

[83] CC Yu and AJ Leggett. Low temperature properties of amorphous materials: Through a glass darkly. *Comments Cond. Mat. Phys*, 14(4):231–51, 1988.

[84] Mingyun Yuan, Vibhor Singh, Yaroslav M Blanter, and Gary A Steele. Large cooperativity and microkelvin cooling with a three-dimensional optomechanical cavity. *Nature communications*, 6(1):1–6, 2015.

[85] RC Zeller and RO Pohl. Thermal conductivity and specific heat of noncrystalline solids. *Physical Review B*, 4(6):2029, 1971.

[86] Shuang Zhang, Dentcho A Genov, Yuan Wang, Ming Liu, and Xiang Zhang. Plasmon-induced transparency in metamaterials. *Physical review letters*, 101(4):047401, 2008.

[87] X Zhou, D Cattiaux, RR Gazizulin, A Luck, O Maillet, T Crozes, J-F Motte, O Bourgeois, A Fefferman, and E Collin. On-chip thermometry for microwave optomechanics implemented in a nuclear demagnetization cryostat. *Physical Review Applied*, 12(4):044066, 2019.

[88] Xiaoqing Zhou, Fredrik Hocke, Albert Schliesser, Achim Marx, Hans Huebl, Rudolf Gross, and Tobias J Kippenberg. Slowing, advancing and switching of microwave signals using circuit nanoelectromechanics. *Nature Physics*, 9(3):179–184, 2013.